Modeling battery intercalation materials with the multiphase-field method

Zur Erlangung des akademischen Grades eines
Doktors der Ingenieurwissenschaften (Dr.-Ing.)
von der KIT-Fakultät für Maschinenbau des
Karlsruher Instituts für Technologie (KIT)

angenommene
Dissertation
von

M.Sc. Simon Daubner

Tag der mündlichen Prüfung:	14. September 2023
Referentin:	Prof. Dr. Britta Nestler
Korreferent:	Prof. Dr. Marc Kamlah

Abstract

The multiphase field method holds great potential to accelerate future materials research through simulation studies - for example in the field of battery materials. Through appropriate modeling, fundamental mechanisms of diffusion, phase transformation and reaction kinetics can be investigated, thus providing insight into possible kinetic limitations or degradation mechanisms. In the last decade, the phase-field method has been increasingly used to simulate phase transformations in the active material on the electrode level. However, these studies are mostly limited to single crystals with one coherent phase transformation. A consistent description of materials with multiple phase transformations and polycrystalline morphology has not yet been developed.

In the introduction of this work, relevant mechanisms that significantly influence the kinetics of charging and discharging at the particle level are discussed. Based on this, a multiphase-field model for intercalation materials is formulated, which includes phase transformations coupled with ion diffusion and an elastic deformation of the crystal lattice. The intercalation reaction is applied as a boundary condition and correlates with the local chemical potential of sodium at the particle surface. Assuming a globally constant charge rate, the effective overpotential can be determined and compared with experiments. Polycrystalline agglomerates can be described in a natural way including the effects of grain boundaries by the underlying multiphase-field formulation. Since this model formulation has not yet been applied to battery materials modeling, this work investigates and validates individual energy contributions in detail. New implementations are tested numerically and build upon previous developments of the simulation software PACE3D, which has been developed for more than 20 years at the chair

of Prof. Britta Nestler. Additionally, the detailed discussion in the validation chapters is intended to facilitate the implementation of the same model or similar formulations in other research codes.

In the second part of this work, the versatile capabilities and potentials of the developed model are tested and discussed on the basis of several examples. First, based on the well-researched cathode material lithium iron phosphate, a comparison of the model with an established approach based on the Cahn-Hilliard model is drawn. Furthermore, the underlying assumptions of the simulations are discussed in detail. The results confirm previous research findings and, moreover, show the influence of polycrystals on the intercalation behavior. While the phase transformation occurs preferentially grain by grain at slow charge rates, simultaneous transformation of many grains is enforced at high rates. In addition, high tensile stresses can be observed at grain boundaries of randomly oriented polycrystals, which contribute to mechanical degradation. The final two use cases illustrate new directions in the field of battery modeling. The cathode material $Na_XNi_{1/3}Mn_{2/3}O_2$ is a promising candidate for future sodium-ion batteries. However, it exhibits poor cycling stability which is partially attributed to a phase transformation at high potentials associated with a highly anisotropic deformation of the crystal lattice. The simulations provide insight into the interplay between phase transformation, mechanical deformation and diffusion. They reveal that mechanics contributes significantly to the effective capacity at slow to moderate charge rates. High tensile stresses, however, are indicative of cracking in the material. The study on polycrystalline NMC agglomerates emphasizes the influence of microstructure on the overall battery charging behavior. Directional grain structures can improve ion transport and contribute to a more homogeneous concentration distribution in the particle, which positively affects the cycle and rate stability of the material. Future research could investigate the potential of similar microstructures for other cathode materials to accelerate materials research with respect to batteries.

Kurzfassung

Die Multiphasenfeld-Methode birgt großes Potential, die zukünftige Materialforschung durch Simulationsstudien zu beschleunigen - so auch im Bereich der Batteriematerialien. Durch geeignete Modellierung können grundlegende Mechanismen der Diffusion, Phasenumwandlung und Reaktionskinetik untersucht werden und so Aufschluss über mögliche kinetische Limitierungen oder Degradationsmechanismen geben. In den letzten zehn Jahren wurde die Phasenfeld-Methode immer häufiger für die Simulation von Phasenumwandlungen im Aktivmaterial auf Elektrodenebene eingesetzt, wobei diese Studien sich meist auf Einkristalle mit einer kohärenten Phasenumwandlung beschränken. Eine konsistente Beschreibung von Materialien mit mehreren Phasenumwandlungen und polykristalliner Morphologie fehlte bisher.

In der vorliegenden Arbeit werden zunächst die relevanten Mechanismen diskutiert, welche auf Partikelebene maßgeblich die Kinetik das Laden und Entladens beeinflussen. Basierend darauf wird ein Multiphasenfeld-Modell für Interkalationsmaterialien formuliert, welches Phasenumwandlungen gekoppelt mit Ionen-Diffusion und einer elastischen Deformation des Kristallgitters umfasst. Die Interkalationsreaktion wird als Randbedingung aufgebracht und korreliert mit dem lokalen chemischen Potential des Natriums an der Partikeloberfläche. Unter der Annahme einer global konstanten Laderate, kann das effektive Überpotential bestimmt und mit Experimenten verglichen werden. Polykristalline Agglomerate können durch die zugrundeliegende Multiphasenfeld-Formulierung auf natürliche Weise inklusive der Effekte von Korngrenzen beschrieben werden. Da

diese Modellformulierung bisher nicht für die Modellierung von Batteriematerialien angewendet wurde, werden die einzelnen Energiebeiträge detailliert untersucht und validiert. Neue Implementierungen werden numerisch getestet und bauen auf den bisherigen Entwicklungen der Simulations-Software PACE3D auf, welche seit mehr als 20 Jahren am Lehrstuhl von Prof. Britta Nestler entwickelt wird. Die ausführliche Diskussion in den Validierungskapiteln soll gleichzeitig auch die Umsetzung desselben Modells oder ähnlicher Formulierungen in anderen Forschungscodes erleichtern.

Im zweiten Teil der Arbeit werden die vielseitigen Anwendungsmöglichkeiten und Potentiale des entwickelten Modells anhand mehrerer Beispiele erprobt und diskutiert. Zunächst wird auf Basis des gut erforschten Kathodenmaterials Lithiumeisenphosphat ein Vergleich des Modells mit einem etablierten Ansatz basierend auf dem Cahn-Hilliard Modell gezogen. Des Weiteren werden die zugrundeliegenden Annahmen der Simulationen ausführlich diskutiert. Die Ergebnisse bestätigen bisherige Forschungsergebnisse und zeigen darüber hinaus den Einfluss von Polykristallen auf das Interkalationsverhalten. Während die Phasenumwandlung bei langsamen Laderaten bevorzugt Korn für Korn erfolgt, wird bei hohen Raten eine gleichzeitige Umwandlung vieler Körner erzwungen. Außerdem können in zufällig orientierten Polykristallen starke Spannung an Korngrenzen beobachtet werden, welche zur mechanischen Degradation beitragen. Die anderen beiden Anwendungsfälle zeigen neue Wege im Bereich der Batteriemodellierung auf. Das Kathodenmaterial $Na_XNi_{1/3}Mn_{2/3}O_2$ ist ein vielversprechender Kandidat für zukünftige Natrium-Ionen Batterien. Allerdings weist es eine schlechte Zyklenfestigkeit auf, was unter anderem auf eine Phasenumwandlung bei hohen Potentialen zurückgeführt wird, welche mit einer stark anisotropen Deformation des Kristallgitters einhergeht. Die Simulationen geben Einblick in das Zusammenspiel von Phasenumwandlung, mechanischer Deformation und Diffusion. Dabei zeigt sich, dass die Mechanik bei langsamen bis moderaten Laderaten maßgeblich zur nutzbaren Kapazität beiträgt. Hohe Zugspannungen sind jedoch ein Indiz für Rissbildung im Material. Die Studie zu polykristallinen NMC Agglomeraten unterstreicht den Einfluss der Mikrostruktur auf das gesamte

Ladeverhalten der Batterie. Gerichtete Kornstrukturen können den Ionentransport verbessern und zu einer homogeneren Konzentrationsverteilung im Partikel beitragen. Dies wirkt sich wiederum positiv auf die Langlebigkeit und Ratenfestigkeit des Materials aus. Zukünftige Forschungsarbeiten könnten die Potentiale ähnlicher Mikrostrukturen für andere Kathodenmaterialien untersuchen, um die Materialforschung im Batteriebereich zu beschleunigen.

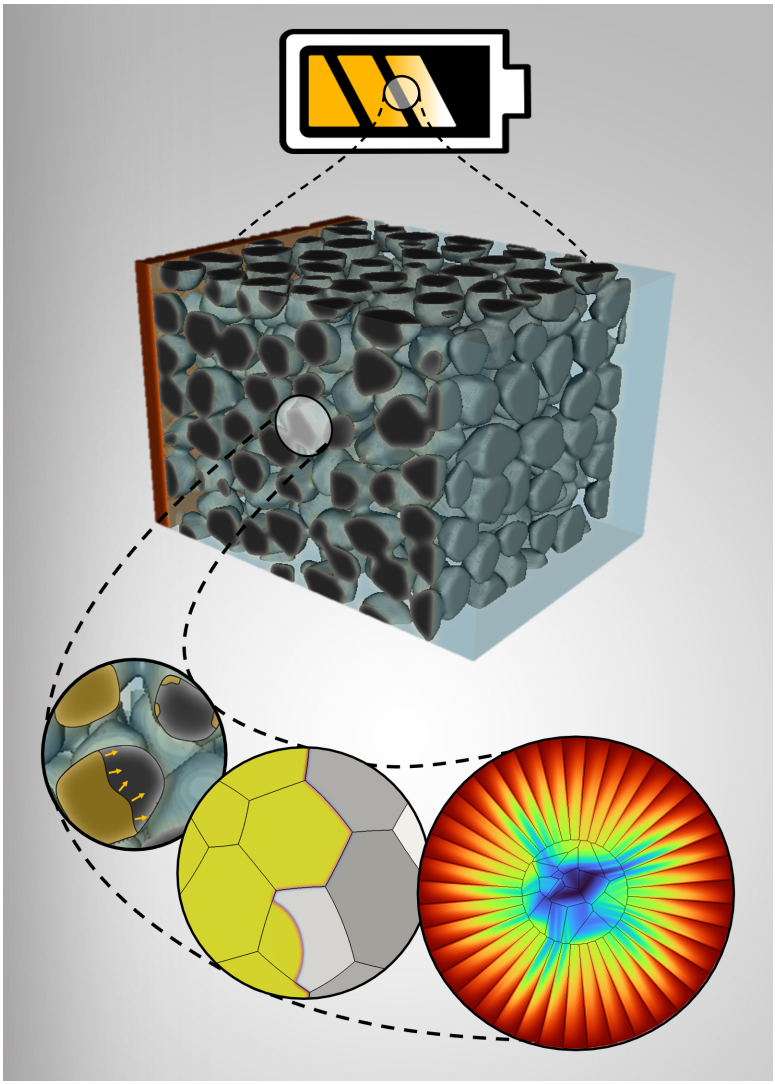


Figure 1: Phase-field simulations applied on the single particle and agglomerate scale. Selected results from this work illustrate phase transformations and ion transport in polycrystalline battery particles.

Acknowledgment

An dieser Stelle möchte ich mich zunächst bei Prof. Britta Nestler bedanken, die es mir ermöglicht hat in ihrer Gruppe zu forschen und mich über die letzten vier Jahre betreut hat - mit viel Freiheit in der Ausgestaltung meiner Forschung, der Möglichkeit Verantwortung am Institut zu übernehmen und einem starken Rückhalt bei inhaltlichen und organisatorischen Angelegenheiten. Ebenso gilt mein Dank Prof. Marc Kamlah für die Übernahme des Korreferats und darüber hinaus für die stets offene Tür, wenn ich mit Fragen inhaltlicher Art oder Kooperationen angeklopft habe.

Special thanks to Prof. Martin Bazant and his group at MIT, who welcomed me with great hospitality for a three-month stay in 2022. A special shout-out to Alex, Nic, Debbie, Pedro and Tammo for scientific discussions and for showing me around Boston and its surroundings. I thankfully acknowledge the funding for this research stay that was provided through the graduate school for electrochemical energy storage (GS-ESS).

Diese ganze Arbeit wäre nicht das, was sie ist, ohne meine Kollegen. Meinen Vorgängern danke ich für ihre Entwicklungen am Code, allen voran Ephraim Schoof. Wer hätte gedacht, dass die martensitische Umwandlung und polykristalline Batteriematerialien so viele Gemeinsamkeiten haben. Danke dir auch in den Rollen als Ansprechpartner, Vorbild und Kollege! Mein Dank gilt auch der ganzen Steinbeis-Crew: meinen Zimmerkollegen Paul und Andreas, Martin, Michael, Lukas, Marcel, Christof, ... danke für die Zeit und die Gespräche bei Kaffee und Bier. Daniel, du führst diese Gruppe mit viel Herzblut und ich möchte dir danken für den Rückhalt und deine Unterstützung. Für organisatorische Probleme gibt es zum Glück unser Sekretariat. An dieser Stelle gilt mein besonderer

Dank Inken für ihren Einsatz in der Vorbereitung des Forschungsaufenthaltes und Vieles mehr.

I feel very priviledged that I was able to meet a lot of interesting discussion partners and could establish some research collaborations along the way. First and foremost, I want to acknowledge my project funding through the POLiS Cluster of Excellence which is funded through DFG. This agglomerate of battery scientists gave me endless opportunities to discuss and collaborate and I can't name them all here. I want to mention some people that became more than colleagues to me - Manuel, Cornelius, Lukas and Johanna, thank you for your time! Others I met more by chance but, nevertheless, they had an impact on my research. Thank you Martin for sharing your expertise about multi-order parameter models and thank you Pierfrancesco for your enthusiasm in discussing battery models.

Zu guter Letzt möchte ich mich herzlich bei meiner Familie und meinen Freunden bedanken, die mich nicht nur durch die Promotionszeit begleitet haben, sondern schon viel länger begleiten. Danke Beate und Markus für eure Sicht aufs Leben, eure Begeisterung und bedingungslosen Rückhalt. Ihr seid mein sicherer Hafen. Danke Andi, Yannis, Björn, Fabio und Larissa. Danke Benni - du warst oft ein paar Schritte weiter auf demselben Weg und nicht nur dadurch ein unentbehrlicher Diskussionspartner. Danke Teagan fürs Korrekturlesen und so Vieles mehr. Du hast mich oft genug nach anstrengenden Tagen aus meinen Gedanken über die Forschung wieder in die Wirklichkeit geholt.

Karlsruhe, im Mai 2023 *Simon Daubner*

List of Symbols

Physics Constants

e	elementary charge
F	Faraday constant
k_B	Boltzmann constant
N_A	Avogadro constant
R	Ideal gas constant

Variables

c	composition (molar fraction / site filling fraction)
$\mathbb{C}$	stiffness tensor
$\mathbb{D}$	diffusion tensor
D	scalar diffusivity
$\mathscr{F}$	energy functional
f	energy density contribution
h	interpolation function
I	applied current (= global intercalation flux)
j_0	exchange current density
k_0	intercalation rate constant
$\mathbb{M}$	chemical mobility tensor
$M_{\alpha\beta}$	mobility of α-β phase transition

N	total amount of phases
$\tilde{N}$	amount of locally present phases
R	reaction term
T	temperature (assumed constant at 300 K)
X	average site filling fraction
z	charge number
V	applied voltage
$V_{\text{cell}}^{\ominus}$	reference cell voltage
$A^{\alpha}, B^{\alpha}, c_{\text{min}}^{\alpha}$	fitting parameters for quadratic chemical free energy
$K^{\alpha}, B^{\alpha}, \mu_0^{\alpha}$	fitting parameters for logarithmic chemical free energy
Δx	grid spacing
$\Delta^{\alpha\beta}$	bulk driving force acting on $\alpha\beta$-interface
ε	scaling parameter for width of diffuse interface
$\boldsymbol{\epsilon}$	total strain (tensor)
$\boldsymbol{\epsilon}^{\text{el}}$	elastic strain
$\boldsymbol{\epsilon}^{*}$	eigenstrain (tensor)
η	overpotential
γ	interfacial energy
κ	long-range interaction parameter
λ	Lagrange multiplier
μ	diffusion potential
$\mu^{\ominus}$	reference potential
$\tilde{\mu}$	electro-chemical potential
$\boldsymbol{\nabla}(\cdot)$	gradient operator
$\boldsymbol{\nabla} \cdot (\cdot)$	divergence operator

Φ	electro-static potential
ϕ	tuple of phase fractions
ϕ_α	volume fraction of α-phase
σ	stress tensor
θ, ψ, φ	rotation angles

Super- and subscripts

$\square^{\mathrm{A}}$	related to anode
$\square^{\mathrm{C}}$	related to cathode
$\square_{\mathrm{bulk}}$	bulk contribution
$\square_{\mathrm{chem}}$	(electro-)chemical contribution
$\square_{\mathrm{int}}$	interfacial contribution
$\square_{\mathrm{max}}$	maximal
$\square_{\mathrm{surf}}$	related to surface of active electrode material
$\square_{\alpha\beta}$, $\square^{\alpha\beta}$	related to $\alpha\beta$-interface
$\square_\alpha$, $\square^\alpha$	related to α-phase
$\square_i$	related to i-th species
$\square_{ij}$	related to interaction of i and j species

Abbreviations

C-rate	charging rate
DFT	density functionl theory
FIB-SEM	focused ion beam - scanning electron microscopy
GITT	galvanostatic intermittend titration technique
GITT	potentiostatic intermittend titration technique
LCO	lithium cobald oxide ($LiCoO_2$)

LFP	lithium iron phosphate (Li_XFePO_4)
LIB	lithium-ion battery
MEP	minimum energy path
MOP	multi-order parameter (model)
MPF	multiphase-field (model)
NMC	layered nickel manganese oxide (e.g. $Li_XNi_{0.8}Mn_{0.1}Co_{0.1}O_2$)
OCV	open circuit voltage
P2D	pseudo-2D model
PDE	partial differential equation

Contents

Abstract i

Kurzfassung iii

Acknowledgment vii

List of Symbols viii

1 Introduction 1
1.1 Intercalation batteries - a materials perspective 1
1.1.1 Ionic transport in intercalation compounds 3
1.1.2 Phase transformations 6
1.1.3 Mechanical degradation 7
1.2 Battery modeling 9
1.3 Phase-field models for battery modeling 13
1.4 Research motivation 16
1.5 Structure of this work 18

I Model formulation and validation **21**

2 Multiphase-field model for intercalation battery materials . . **23**
2.1 Brief history of (multi)phase-field models 23
2.2 Energy functional 25
2.3 Phase-evolution equations 27
2.4 Diffusion within the active material 34
2.5 Mechanical equilibrium 36

2.6 Electro-chemical surface reaction 39
2.7 Numerical implementation 44
2.8 Remarks 46

3 Benchmarking interfacial forces 47
3.1 Model formulation 49
3.1.1 Gradient energy formulations 50
3.1.2 Potential energy formulations 52
3.1.3 Multiphase-field evolution equations 57
3.2 Simulation studies 59
3.2.1 Simulation setup 59
3.2.2 Static triple junction 60
3.2.3 Steady-state motion of a triple junction 64
3.3 Discussion 67

4 Phase nucleation driven by chemical forces 69
4.1 Free energy landscape 69
4.2 Stability analysis in a two-phase system 71
4.3 Phase separation in a two-phase model system 75
4.4 Heterogeneous nucleation in pre-existing grain boundaries 79
4.5 Multi-grain intercalation 85
4.6 Discussion 87

5 Implementation of anisotropic diffusion 89
5.1 Discretization stencils 89
5.2 Discrete boundary conditions 91
5.3 Quantifying the numerical error for bulk diffusion 94

II Application to battery materials 99

6 Intercalation in $LiFePO_4$ 101
6.1 Materials and methods 104
6.1.1 Material data for $LiFePO_4$ 104

6.1.2 Cahn-Hilliard model . . . 106
6.1.3 Modeling assumptions . . . 107
6.2 Results and discussion . . . 108
6.2.1 Dimensionality reduction . . . 108
6.2.2 Bulk kinetics . . . 110
6.2.3 Galvanostatic charge and discharge . . . 117
6.2.4 Multigrain systems . . . 123
6.3 Conclusion . . . 127

7 Phase transitions in the layered oxide $Na_XNi_{1/3}Mn_{2/3}O_2$ . . . 129
7.1 Material data . . . 131
7.2 Electro-chemical model . . . 133
7.2.1 Gibbs free energy fitting . . . 133
7.2.2 Dimensionality study . . . 135
7.2.3 Influence of diffusivity and charge transfer . . . 139
7.3 Electro-chemo-mechanical model . . . 142
7.3.1 Material-specific input data . . . 142
7.3.2 Kinetics of phase transformations . . . 143
7.4 Conclusion . . . 146

8 Anisotropic ion diffusion in polycrystalline battery materials 147
8.1 Materials and Methods . . . 149
8.1.1 Multi-phase diffusion . . . 149
8.1.2 Anisotropic diffusion tensor . . . 150
8.1.3 Simulation parameters for high-nickel NMC . . . 152
8.2 Results . . . 154
8.3 Discussion . . . 159
8.4 Conclusion . . . 161

9 Conclusion . . . 163
9.1 Summary . . . 163
9.2 Outlook . . . 166

A Phase-field derivations **169**
A.1 Two-phase energy functional 169
A.2 Interfacial properties 170
A.3 Functional derivatives 170

B Gibbs simplex constraint **173**

C Chemical free energies **177**

List of Publications **181**

List of Figures **183**

List of Tables **187**

Bibliography **189**

1 Introduction

1.1 Intercalation batteries - a materials perspective

Undeniably, the lithium-ion battery is a cornerstone of today's society and has influenced many areas of public life. This fact was acknowledged by the bestowal of the 2019 Nobel Prize in Chemistry to the three researchers John B. Goodenough, M. Stanley Whittingham and Akira Yoshino "for their contributions to the development of the lithium-ion battery. This rechargeable battery laid the foundation of wireless electronics such as mobile phones and laptops. It also makes a fossil fuel-free world possible, as it is used for everything from powering electric cars to storing energy from renewable sources." [1].

The development of the lithium-ion battery (LIB) is not only a story of electrochemistry but also of material science. Finding electrode materials that deliver high energy density and can be reversibly charged and discharged has been the goal since the beginning and still is today. The basic working principle of the lithium-ion cell is the so-called rocking chair mechanism, which means that lithium ions can be reversibly inserted and extracted from both electrodes and are shutteled between the anode and the cathode during cycling. On the anode side, graphite has been investigated since the 1970s and has been used in commercial cells since 1994 [2]. Graphite remains the dominant anode material for applications ranging from portable electronics to electric vehicles despite extensive research on alternatives such as silicon, sulfur and lithium metal anodes [2].

The improvement of LIBs over the last 30 years was instead driven by changes in electrolyte additives, new cathode materials and engineering concepts which led to a rather linear increase in cell performance [3]. In 2010, $LiCoO_2$ was the most commonly used cathode material in LIBs [4], but the global ramp-up of electric vehicle production led to new demands in terms of price, resource availability and sustainability. LIB sales have more than tripled between 2010 and 2016 [3] and the market is still growing exponentially. Material abundance, chemical toxicity and recycling are very present issues in the public discourse and society is quite unwilling to compromise on upcoming technologies in the face of advancing climate change [5]. To that end, the global availability of lithium and cobald as well as their mining conditions are rather problematic which leads to increased interest in 'next-generation' batteries, often called 'post-lithium batteries' [3]. The research in the field of post-lithium systems covers a wide range of cell chemistries such as sodium, magnesium [6], fluorine [7] and many others. For the context of this work, I focus on intercalation batteries with monovalent ions.

Lithium and sodium intercalation batteries both rely on the same basic principle for charge storage. The ions are reversibly stored in a host material and can be inserted or removed depending on the surface overpotential. Sodium ions have a larger ionic radius compared to lithium (1.02 Å vs. 0.76 Å) which influences phase stability, crystallographic structure and transport properties. Hence, sodium intercalation materials often exhibit pronounced steps in the open circuit potential indicating a tendency towards electronic or structural phase transitions [8] due to the strong lattice distortion upon insertion and extraction of ions. Depending on the applied voltage, the occurring phase transitions can be partially irreversible which crucially limits cell stability and performance and, thus, needs to be investigated in more detail.

While lithium-ion cells are today's state of the art, it is expected that the emergence of new cell chemistries will lead to more technological diversity for battery systems. However, any new development will be benchmarked against LIBs in terms of e.g. energy density, cycle life, sustainability and cost, which are moving targets given the continuous improvement of lithium-ion technology [3].

1.1.1 Ionic transport in intercalation compounds

There are many ways to categorize and describe electrode materials for lithium- and sodium-ion batteries. From a material science perspective, it seems natural to start with the properties of perfect single crystals and then look at technically relevant microstructures. From the modeling perspective, I will focus on physical properties such as ion diffusion in the host structure, concentration-dependent changes in lattice constants and phase transformations rather than electro-chemical metrics such as specific capacity. Anisotropies that are intrinsic to the crystal structure will be used to group and discuss intercalation compounds.

Three representative intercalation compounds are the olivine $LiFePO_4$, the layered $LiCoO_2$ and spinel $LiMn_2O_4$ as shown in Fig. 1.1. Li_XFePO_4 (LFP) is a structure in which lithium resides in one-dimensional channels. Therefore, the bulk diffusion is strongly anisotropic with fast diffusion in the b-direction (along the channels) while hopping across channels is rather unlikely in a perfect crystal structure but can be mediated through crystal defects [9]. In the $LiCoO_2$ (LCO) layered oxide, lithium resides between layers of transition metal oxide sheets (Fig. 1.1 b). Lithium diffusion is restricted to the layers in a defect-free crystal and still varies by orders of magnitude between the parallel und normal direction of the sheets in real systems [10]. In the $LiMn_2O_4$ spinel, Li interstitial sites form a three-dimensional network that results in isotropic diffusion [11].

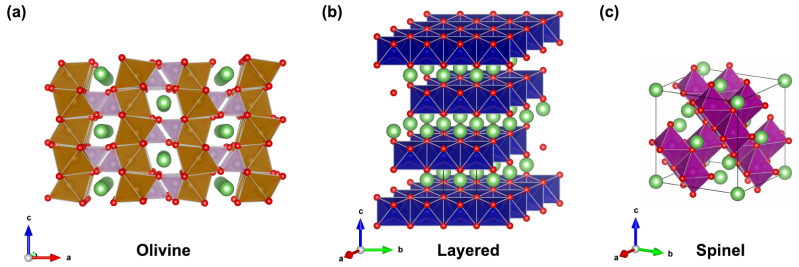
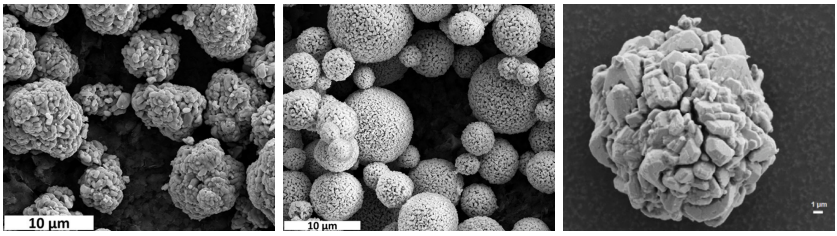


Figure 1.1: Crystal structure of three canonical intercalation cathodes for LIBs, namely a) $LiFePO_4$, b) $LiCoO_2$ and c) $LiMn_2O_4$. Green spheres represent lithium ions. Reprinted with permission from Van Der Ven *et al.* [12]. Copyright 2023 American Chemical Society.

Besides the correlation of diffusivity and anisotropy of the crystal structure, there is a compositional dependence on the fraction of intercalated ions in the host structure. The interlayer diffusivity in LCO varies depending on X in Li_XCoO_2 with a maximum around $X = 0.5$ and two to three orders slower diffusion in the empty ($X \to 0$) and full ($X \to 1$) state [13]. One reason is that the migration barrier scales with the distance between layers which becomes smaller at low lithium content [14]. Furthermore, the lowest energy path for lithium migration is a di-vacancy hop, which becomes much less probable at high lithium content such that in order to diffuse, another mechanism with higher energy barrier needs to be activated [13]. The same holds true for similar layered structures with the generalized formula A_XMO_2 where A is the intercalated ion and M stands for one or various transition metals such as Ni, Mn or Co [15]. The high-nickel $Li_XNi_{0.8}Mn_{0.1}Co_{0.1}O_2$ (NMC811) exhibits a strong decrease of chemical diffusivity for $X < 0.3$ and $X > 0.9$ [16]. Diffusion in $Na_XNi_{1/3}Mn_{2/3}O_2$ also depends strongly on sodium content and the crystallographic phase. At low sodium content ($X < 0.33$) there is a phase transition from the P2 to O2 structural polymorph which is accompanied by a reduction of the interlayer distance. Consequently, the energetic barrier for sodium ion diffusion in the O2 phase is higher which results in slower diffusion [17].

Apart from the crystal structure, ion transport in electrode particles is strongly influenced by the **morphology**. Within this work, the term morphology is used to describe the structural appearance of crystalline materials on the mesoscale (i.e. single crystals with more than 100 nm and secondary particles up to 15 μm). Layered-oxides based on nickel, manganese and cobald (NMC) are state-of-the-art cathode materials for commercial lithium-ion cells in high-capacity applications such as electric vehicles. Typically, NMCs form hierarchical structures of many primary crystals agglomerated in a spherical secondary particle (see Fig. 1.2), sometimes referred to as *meatball structure* [18, 19]. As the primary crystals are typically randomly oriented, stresses arise due to misorientation of neighboring grains that can lead to fracture and eventually disintegration of the secondary structure [19] (see also Section 1.1.3). Similar secondary morphologies can be obtained for the P2-type $Na_XNi_{1/4}Mn_{3/4}O_2$ [20].



(a) **(b)** **(c)**

Figure 1.2: Secondary particle morphologies of a) as-prepared NCM111 and b) nano-porous NMC111 after spraydrying reproduced from Müller *et al.* [21] published under a CC BY-NC-ND licence. The $Na_XNi_{1/4}Mn_{3/4}O_2$ particle shown in c) is reproduced from Pfeiffer *et al.* [20] and has been published under the CC BY licence.

Ionic transport can be altered in polycrystalline materials through microstructure design such as tailoring crystallographic orientations [22] or introducing nanoporosity as in Fig. 1.2b [21]. Particles consisting of radially aligned grains show excellent rate performance and improved cyclic stability [22]. This can be attributed to less tortuous pathways for ion transport and the increase of small-angle grain boundaries, which lead to an overall reduction of accumulated stress in grain boundaries. The same applies for the nano-porous particle morphology, as the open-pored structure significantly reduces diffusion paths within the active material compared to close-packed spherical structures. Additionally, the pores buffer the breathing (cycling expansion and contraction) of the material, thus limiting stress accumulation and subsequent fracture [21].

In conclusion, the modeling of ion diffusion in battery intercalation compounds needs to reflect the material-specific crystyllography and the anisotropy of diffusion barriers that might arise from it. Furthermore, the microstructure of secondary particles strongly affects the ion transport alongside other key properties such as mechanical degradation. Model simplifications such as the assumption of spherical symmetry in cell models should be based on homogenization of the actual microstructure (more details can be found in Section 1.2).

1.1.2 Phase transformations

First order phase transformations as well as charge orderings that are continuous second order transformations cause plateaus in the voltage profile due to the coexistence of two states of minimal energy. This was discussed by Delmas *et al.* [23] in 1999 and led to a variety of electro-chemical measurement methods to characterize electrode materials during intercalation. Steps and plateaus can be found in a large number of technically relevant electrode materials, ranging from graphite, lithium-iron phosphate (LFP) to high-nickel NMCs for LIBs. In sodium intercalation compounds, steps and plateaus are even more pronounced due to strong lattice distortion resulting from the larger ionic radius of sodium.

In recent years, LFP has transformed from a material with strong scientific interest and low market share ('drosophila of phase separation' [24]) to the second-most employed cathode material for electric vehicles after NMC-based cell chemistries in 2022. It undergoes a first order phase transformation with low miscibility in the end-member states, i.e. there is a long plateau over almost the whole compositional range of $X \in [0, 1]$ [25]. The layered oxide Li_XCoO_2 undergoes a phase transition at low lithium content [14] while Li_XNiO_2 exhibits four structurally different phases in the full range of $X \in [0, 1]$ [26, 27]. As previously mentioned, graphite is the dominant anode material for LIBs [2]. It exhibits a staging phenomenon characterized by a stepwise filling of graphite layers which manifests itself through plateaus in the open-circuit voltage (OCV) [28]. Promising cathode materials for sodium-ion batteries typically exhibit phase transitions and charge ordering, e.g. the layered oxides $Na_XNi_{1/3}Mn_{2/3}O_2$ [29, 30] and $Na_XNi_{1/4}Mn_{3/4}O_2$ [20], olivine $NaFePO_4$ [31], $Na_3V_2(PO_4)_3$ [32].

This list is far from complete, yet it highlights that reversible phase transformations during cycling are not an exotic execption but a common phenomenon in intercalation compounds. The nature of these materials can only be modeled and understood if phase transformations are accounted for.

1.1.3 Mechanical degradation

The intercalation of ions is often accompanied by volumetric changes of the insertion host material, which is material specific (e.g. volume change of $\approx 1.2\%$ in NMC111 [18], $\approx 6.9\%$ in LFP [33], $\approx 20\%$ in $Na_XNi_{1/3}Mn_{2/3}O_2$ [30]). This results in two effects, the first of which is a "breathing" of the electrode, i.e. overall expansion and shrinkage of the particles within one eletrode during charge and discharge. This effect is mitigated by the porous nature of electrodes and the viscosity of the binder [34]. However, continued cycling can lead to gradual degradation through contact loss between the binder and the active material [34]. Secondly, and probably more important in terms of degradation, stresses arise in particles (both single crystals and agglomerates) due to concentration gradients or due to a lattice mismatch between crystallographic phases that form during cycling. This induces an electro-chemo-mechanical fatigue either through disintegration of agglomerated structures [18, 19, 35] or crack formation in primary crystals [34].

Secondary particles such as the ones shown in Fig. 1.2 tend to form intergranular cracks if the primary crystals undergo significant expansion and contraction [18]. This effect is strongly interconnected with the anisotropic nature of these materials as layered oxides typically exhibit much stronger changes in the c-axis (perpendicular to the transition metal oxide sheets). In the randomly oriented arrangement of primary crystals, large stresses arise at grain boundaries where crystals with a strong misorientation meet [18, 36]. Accordingly, small-angle grain boundaries are not strained as much because neighboring grains expand in a similar way.

For single crystal electrodes, a clear trend between particle size and crack formation has been observed [34]. Larger crystals are more prone to cracking for several reasons. The stored elastic energy resulting from strain scales with the volume of the particle, as opposed to crack surface energy which scales with area. Thus, in larger particles more stored elastic energy can be released via formation of crack surfaces. Furthermore, the probability of crystal defects is higher

in larger crystals, which lowers the energetic barrier for crack nucleation. If the intercalation of ions becomes diffusion limited at high C-rates, concentration gradients develop, additionally contributing to lattice strain. Larger particles enter the diffusion limited regime much earlier as the diffusion relaxation time scales with the square of the average diffusion length [37].

The direct consequence of fracture on the battery performance is ambiguous for the following reasons. First of all, the increase in surface that is accessible for ion insertion improves the rate performance [38]. At the same time, the creation of new surfaces in combination with other surface degradation mechanisms such as surface densification leads to continuous degradation [27, 39, 40]. The disintegration of agglomerated particles can result in the loss of electrical contact, which leads to a fraction of active material that is dead in the sense that it no longer contributes to the reversible capacity [35]. This effect is even more pronounced in solid state batteries as the solid electrolyte cannot compensate the loss of contact [41].

To summarize this section, it should be noted that mechanical degradation is an important issue, especially in electrode materials undergoing phase transformations. Consequently, the modeling therof should include elastic deformations and the coupled effects of diffusion and strain. Furthermore, it is crucial that the anisotropic nature of crystalline materials is accounted for if the simulations aim at understanding degradation mechanisms such as a correct prediction of fracture. A homogenized modeling of spherical particles with volumetric expansion can only account for the collective behaviour of the electrode and is, thus, able to account for the breathing but not for particle degradation. Cracking and disintegration of agglomerates can only be captured if grain boundaries in the polycrystal are accounted for.

1.2 Battery modeling

The research on new electrode materials for LIBs and next-generation batteries is very interdisciplinary. Experimental methods from various fields are combined with simulation techniques to develop a deeper understanding of the physical processes that determine battery performance and lifetime. The simulation methods which have been applied in the field of intercalation batteries cover length scales ranging from atomic resolution to cell and pack models. Typically, the considered length scale correlates with the timescale that is accessible by the respective method as shown in Fig. 1.3.

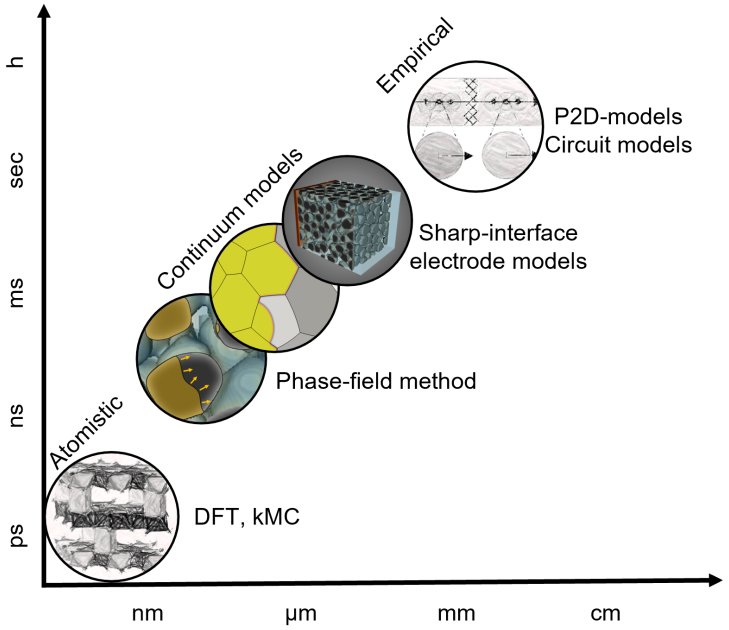


Figure 1.3: Methods for battery simulation across the scales. The phase-field method on the mesoscale bridges the gap between atomistic models to empirical cell models.

On the smallest scale, we find ab-initio methods which means that only physical constants are used as an input. The computational accessability of quantum chemistry has been propelled by the research of Kohn and Pople, which resulted in the development of density functional theory (DFT) and the bestowal of the 1998 Nobel Prize in Chemistry "to Walter Kohn for his development of the density-functional theory and to John Pople for his development of computational methods in quantum chemistry" [42]. DFT has also been used in the context of battery material science to study many aspects of intercalation compounds.

Some physical properties of battery electrode materials are intrinsically difficult to measure experimentally. Diffusivity measurements, for example, yield an apparent diffusivity of intercalated ions that depends on the electrode microstructure and the multi-particle nature of electrodes. DFT can be used to compute diffusivities from migration barriers via the nudged elastic band method (e.g. for LFP [9, 43] and graphite [44]). Furthermore, the energy above hull yields information about stable states and, thus, possible two-phase coexistence. In that regard, ab-initio calculations are well-established to compute phase diagrams [45], ordering effects [30, 46, 47] and open circuit voltages [11, 44]. The calculation of elastic constants [48] in combination with anisotropic chemical interfacial energies [49] has be used to estimate the thermodynamically stable interface orientation of the phase-separated state in LFP nanocrystals. The computation of surface energies yields insights into the equilibrium crystal shape (Wulff shape) of faceted crystals [50, 51]. A comprehensive review of DFT studies in the context of lithium and sodium intercalation compounds can be found in the work by Islam and Fisher [11]. Furthermore, DFT can be used to parametrize kinetic Monte Carlo (kMC) models which are able to describe ion diffusivity in a crystalline host structure on longer time scales and at higher temperatures (e.g. room temperature) [13, 52].

While DFT is a powerful method to study the properties of crystalline bulk materials, several drawbacks arise from the computational cost involved in resolving atoms and electron densities. The system size is typically limited to a periodic supercell with few hundred atoms such that phase transformations and complex

interfaces are out of scope. Thus, other simulation methods are necessary to describe the spatial and temporal scale of nucleation and growth of new phases, the interplay of chemical and mechanical driving forces as well as the collective behaviour of many interconnected particles.

On the particle to cell scale, continuum theories are employed, typically involving more assumptions and input parameters. The discrete atomic representation of a material is replaced by a continuum field with a set of physical properties. Physical processes such as ion transport within the electrolyte and electrode materials, stress evolution and phase transformations are then described by partial differential equations (PDEs) [53–56]. Two classes of continuum models can be distinguished in this context, namely spatially resolved models and effective transport models.

The first class of models is based on spatially resolved microstructures which can be artificially generated or included from microscopy data such as FIB-SEM measurements [57, 58]. Some studies focus on the microstructure of secondary particles [59–61] while others are concerned with the porous electrode morphology without resolving grain structures of agglomerates [56, 58, 62–65]. This can be explained by the fact that the smallest resolved feature typically dictates the maximal resolved length scale in terms of computational times. The advantage of explicitly resolving the microstructure is that these models are able to capture local variations in electrical potential and ion flux which can be crucial for the prediction of degradation mechanisms that can result in failure [58].

The second class of model formulations is based on a homogenization of porous electrode structures such that ion transport can be described on a one-dimensional line from the anode, through the separator, to the cathode. These models are typically called “Newman-type model” or “Doyle-Fuller-Newman (DFN) model” according to their origins [53, 66]. Alternatively, the term “pseudo-2D model (P2D)” [67, 68] is used to emphasize the two resolved length scales in this model formulation, i.e. the cross section through the cell and the length scale for diffusion in the active material particles. Compared to spatially resolved models,

this approach is computationally cheap and well-suited for battery lifetime prediction or real-time estimation of state-of-charge. Geometric information of the porous electrode microstructure is included in terms of effective parameters such as porosity and tortuosity, both of which can be determined from representative volume elements (e.g. based on FIB-SEM data [69]). There are open-source code projects such as PyBaMM [70] and MPET [71] that aim at unifying individual efforts and accelerating battery modeling research by reducing duplicate code development. Oftentimes, simulations are based on the assumption of spherical particles and a constant diffusivity in the solid [53] which calls for an appropriate homogenization of the secondary particle microstructure to yield physically meaningful results. A comparison of spatially resolved simulations with a lower dimensional DFN model has been carried out by Wiedemann *et al.* [58]. An extensive overview of continuum models in general can be found in Grazioli *et al.* [67], in which various assumptions and modeling details found in literature are discussed.

Phase-field models play a vital role for the simulation of electrode materials that undergo phase transformations upon cycling. They can be employed in both classes of continuum models, either for spatially resolved particles [72] or in homogenized models [73]. Furthermore, the multiphase-field method provides a framework to study coupled multi-physics in polycrystalline battery materials in a thermodynamically consistent framework. In the following section, state-of-the-art phase-field models for intercalation compounds are discussed in more detail.

1.3 Phase-field models for battery modeling

As elaborated in Sec. 1.1.2, there are many battery intercalation compounds which exhibit phase transitions during cycling. This includes first-order phase transformations which typically entail a change in the host crystal structure and, furthermore, second-order continuous phase separations such as charge ordering. Therefore, attempts have been made to model phase transitions in a thermodynamic framework which encompasses electrical, chemical and mechanical driving forces.

Originally introduced to the field of battery simulation by the studies of Han *et al.* [74] and Guyer *et al.* [75], the phase-field method is well-established nowadays and has been applied in numerous works investigating electrodeposition [76–81] and intercalation in phase separating electrode materials [72, 82–98]. For the scope of this work, I will mainly focus on intercalation models and only briefly comment on modeling dendrite formation simulations.

The first application of a Cahn-Hilliard type phase-field model to describe ion diffusion in an electrode was shown by Han *et al.* [74]. Singh *et al.* [82] then employed this formulation to model the phase transition in Li_XFePO_4 single crystals based on a depth-averaging in the b-direction. This dimensionality reduction is motivated from the assumption of surface reaction limitation and fast bulk diffusion in the 1D channels along the b-direction for LFP. As a result, concentration evolution is described by a reaction equation that has later been called “Allen-Cahn reaction (ACR) model” [99]. The model predicts intercalation waves sweeping across the single-crystal as a result of diffusion anisotropy and the surface reaction rate given by the Butler-Volmer (BV) equation. This approach has been used to study the suppression of phase separation for high fluxes [83] and the pattern formation on an active facet of nano-sized single crystal including the effect of coherency strain [84] and surface wetting [100]. In a recent work [72], pattern formation depending on particle size was studied. Another approach, often referred to as Cahn-Hilliard reaction (CHR) model [99], uses the BV equation as a boundary condition while computing the flux inside

the particle based on the conservative Cahn-Hilliard equation. Tang et al. [85] showed that the interface evolution is dependent on both surface flux and bulk diffusion. The recent works of Hong *et al.* [86, 87] show how larger overpotentials shift the interface motion from surface reaction limitation to a hybrid or mainly bulk-diffusion limited case.

Huttin and Kamlah [88] studied intercalation in spherical particles reduced to one dimension by radial symmetry with constant boundary flux. Their original work was based on small deformations and later extended to large deformation mechanics [89]. Subsequent studies comprise the intercalation simulation in $NaFePO_4$, a promising candidate for post-lithium batteries, [90] and a comparison of miscibility gaps for various cathode materials [91]. Zhao et al. [92] introduced concentration-dependent elastic properties and performed simulations in spheroidal three-dimensional particles. In their later work [93], surface reaction was accounted for by the BV equation rather than constant flux, and diffusion-induced cracking was investigated. All these works focus on the influence of strongly coupled chemo-mechanics on diffusion and are characterized by sophisticated treatment of large deformation mechanics with the finite element method. Furthermore, degradation due to fracture was studied with the phase-field method in isotropic spherical particles [101], LFP single-crystals [102, 103] as well as polycrystalline NMC particles [104].

Several other studies focus on incorporating realistic particle shapes into simulations. For example, Santoki et al. [94] studied the intercalation in an arbitrarily-shaped particle in three dimensions. Constant boundary flux was applied based on the smoothed boundary method, which has also been previously used to study spherical particles in 2D [95]. More complex geometries have also been studied, such as the agglomerate of three spherical particles neglecting internal interfaces [96] and two touching nanowires [97]. Wu et al. [98] performed simulations with particle shapes reconstructed from x-ray tomography. They discuss the importance of realistic shapes as higher stress arises during insertion compared to simulations with idealised particles.

In the context of the phase-field method, the most studied electrode material is LFP [72, 74, 82–87, 95, 98–100, 103, 105–110], which is most likely chosen for the following reasons. First of all, there is technological relevance as discussed in Sec. 1.1.2 and, secondly, Li_XFePO_4 is a very prototypical phase-separating material in the sense that it exhibits a large miscibility gap resulting in a long voltage plateau in the compositional range $X \in [0, 1]$. The free energy is well described by the regular solution model, which has also been used in the original works of Cahn and Hilliard [111–113]. Furthermore, there is a multitude of published experimental results and simulations on atomistic scales which can be used to parametrize phase-field models. Other phase-field studies comprise the electrode materials $Li_XMn_2O_4$ [88–90, 94, 101, 102], Na_XFePO_4 [90, 114, 115] and NMC [104]. A special variant of the Cahn-Hilliard model with across-layer interactions was used to model the staging in graphite [73, 116–118]. There are many other lithium and sodium intercalation compounds that undergo phase transformations which have not yet been modelled. This raises the question if the existing approaches are too restrictive to model other materials which cannot be described by a regular solution free energy. Within this work, the multiphase-field approach is used to introduce additional degrees of freedom and allow for an arbitrary number of phases which can be parametrized with phase-specific free energy functions. This model aproach is compared with the established Cahn-Hilliard approach for the well-studied LFP cathode material in Chapter 6.

As mentioned earlier, several phase-field works are concerned with the electrodeposition of lithium metal and the growth of dendritic structures. To the best of my knowledge, none of the dendrite shapes predicted by phase-field simulations resemble the needle-like structures that are typically observed in experiments [119]. Differences are also found for mossy lithium growth [120]. The differences could trace back to the fact that the phase-field formulations are based on a driving force based on the electric field while experimental results suggest that crystal defects and grain boundaries determine the growth behaviour rather than the electric field [119, 120].

1.4 Research motivation

Because experimental observations provide evidence that multi-particle interaction noticeably affects the intercalation behaviour [121], the need for extending existing phase-field techniques to multi-particle systems has been reported [122]. So far, phase-field simulations of intercalation are mostly restricted to single crystals or single particles. Possible reasons are, first of all, the limitations linked to the Cahn-Hilliard approach used in basically all phase-field intercalation simulations on LFP, $Li_XMn_2O_4$, Na_XFePO_4 and graphite. The underlaying evolution equation is a fourth order PDE which is computationally challenging. Furthermore, the Cahn-Hilliard approach is a microscopic theory in the sense that all the parameters involved are motivated from atomic interactions on the nanometer-scale. The gradient term describes long range interactions in the crystal lattice while the regular solution free energy includes the mixing entropy between intercalated ions and vacancies as well as the enthalpic contribution which covers repulsive forces between ions. As a result, this model is able to predict interfacial energies between stable phases and the length scale of the transition region in between. For electrode materials, the interfacial width is in the range of nanometers which needs to be resolved by spatial discretization. This smallest resolved feature limits the overall simulation size to single nano-particles with a length of 20-500 nm due to computational cost, as shown on the left-hand side of Fig. 1.4.

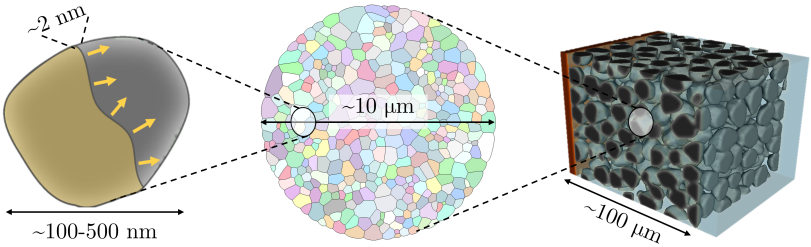


Figure 1.4: Relevant length scales from single particles to one electrode layer.

Common multiphase-field models based on the works of Steinbach *et al.* [123] and Nestler *et al.* [124] address these two issues very naturally. They are mesoscopic models in the sense that the interfacial width can be re-scaled while recovering a physical interfacial energy. All equations are formulated in terms of N phases which includes polycrystalline materials and makes them an attractive choice to model battery electrode materials.

To correctly describe the multi-physics involved in the intercalation of lithium or sodium into electrode materials, further requirements arise. Ideally, the model should

- be able to describe phase transformations, ion diffusion, mechanical deformation and the intercalation reaction;
- be thermodynamically consistent, i.e. recover the equilibrium states in the bulk of the material and non-equilibrium kinetics should be driven by energy minimization;
- cover material anisotropies with regard to ion migration, lattice expansion and interfacial energies;
- cover length scales from 100 nm to 10 µm to be able to simulate single crystals as well as agglomerates.

As illustrated in Fig. 1.4, the simulation of single particles and agglomerates already involves multiple length scales. Nevertheless, the phase-field method acts on the mesoscale between atomistic and more coarse-grained models. Thermodynamic consistency on all modeling scales and an effective parameter transfer for scale bridging are vital to get predictive cell models on the macroscopic scale [125]. Thus, the goal of this work is not only to investigate the multiphase-field method as a tool for battery simulation, but also to discuss linkages to the adjacent length scales.

1.5 Structure of this work

The overarching goal of my research during the last four years was the development of a multiphase-field model that is suitable for the investigation of phase transitions in polycrystalline battery materials under the influence of electrical, chemical and mechanical forces. This has led to the following publications, which cover individual aspects of this thesis and are partially reproduced in Chapters 3 to 8:

1. **S. Daubner**, P G Kubendran Amos, E. Schoof, J. Santoki, D. Schneider, and B. Nestler. Multiphase-field modeling of spinodal decomposition during intercalation in an Allen-Cahn framework. Physical Review Materials, 5(3):035406, 2021.

2. **S. Daubner**, M. Weichel, D. Schneider, and B. Nestler. Modeling intercalation in cathode materials with phase-field methods: Assumptions and implications using the example of LiFePO4. Electrochimica Acta, 421:140516, 2022

3. **S. Daubner**, P. W. Hoffrogge, M. Minar, and B. Nestler. Triple junction benchmark for multiphase-field and multi-order parameter models. Computational Materials Science, 219:111995, 2023.

4. **S. Daubner**, M. Weichel, P. W. Hoffrogge, D. Schneider, and B. Nestler. Modeling anisotropic transport in polycrystalline battery materials. Batteries, 9(6), 310, 2023.

5. **S. Daubner**, M. Dillenz, L. F. Pfeiffer, C. Gauckler, M. Rosin, N. Burgard, J. Martin, P. Axmann, M. Sotoudeh, A. Groß, D. Schneider, and B. Nestler. Combined study of phase transitions in the P2-type $Na_XNi_{1/3}Mn_{2/3}O_2$ cathode material: experimental, ab-initio and multiphase-field results. Submitted.

These indiviual works are put into context by explaining how they contributed to the overaching research question within this thesis by a discussion section at the

end of each chapter. Only parts that are relevant for the modeling of battery intercalation materials with the multiphase-field method are taken from the original publications and discussed in this work. I have been involved in other publications during the course of my research in the group of Prof. Nestler which are not included in this thesis but are listed here for completeness:

6. X. Liu, D. Schneider, **S. Daubner**, and B. Nestler. Simulating mechanical wave propagation within the framework of phase-field modelling. Computer Methods in Applied Mechanics and Engineering, 381:113842, 2021.

7. M. Reder, D. Schneider, F. Wang, **S. Daubner**, and B. Nestler. Phase-field formulation of a fictitious domain method for particulate flows interacting with complex and evolving geometries. International Journal for Numerical Methods in Fluids, 93(8):2486–2507, 2021.

8. J. Santoki, **S. Daubner**, D. Schneider, M. Kamlah, and B. Nestler. Effect of tortuosity, porosity, and particle size on phase-separation dynamics of ellipsoid-like particles of porous electrodes: Cahn–Hilliard-type phase-field simulations. Modelling and Simulation in Materials Science and Engineering, 29(6):065010, 2021.

9. **S. Daubner**, M. Reder, N. Prajapati, D. Schneider, and B. Nestler. Multiphase-field modelling of anisotropic elasticity at finite deformation in Eulerian space. Journal of Computational Science, 66:101930, 2023.

10. Q. Huang, **S. Daubner**, S. Zhang, D. Schneider, B. Nestler, H. Mao, S. Liu, and Y. Du. Phase-field simulation for voltage profile of LixSn nanoparticle during lithiation/delithiation. Computational Materials Science, 220:112047, 2023.

The literature overview given in the introduction illuminates general aspects of electrode materials from a materials science perspective. Afterwards, the state of the art of battery modeling from the atomistic to the cell scale is reviewed with a special emphasis on the application of phase-field methods to the simulation

of intercalation materials. From this introduction I derive open research questions and formulate the overarching goal of my research. Chapter 2 presents the developed model in a consolidated manner. It is based on the validation works within the previously mentioned publications. The model section is followed by three validation chapters, each of them elaborating on specific aspects of the suggested model. The goal is to provide a comprehensive overview of how to select an appropriate phase-field model and energetic terms for the simulation of battery materials. Due to the complex multi-physics, the individual energetic terms have been validated in a gradual manner, starting with interfacial forces which are the basis of the multiphase-field method in Chapter 3. In Daubner *et al.* [126], various formulations for interfacial energies are discussed and evaluated for multiphase-field and multi-order parameter models. The results for MPF formulations are re-printed in Chapter 3. This chapter is closed by a discussion of implications for the modeling of polycrystalline battery materials. The analysis is then extended to the interplay of interfacial with chemical driving forces and their influence on nucleation of new phases and spontaneous phase separation in Chapter 4. Part I of this thesis is closed with numerical details about the implementation of anisotropic fluxes in Chapter 5.

The second part of this thesis comprises three application examples covering different aspects of the presented multiphase-field model. In Chapter 6, the well-established Cahn-Hilliard model is compared with the multi-phase formulation and various modeling assumptions are discussed in detail for LFP. Subsequently, the sodium intercalation compound $Na_XNi_{1/3}Mn_{2/3}O_2$ is studied in Chapter 7. The effects of hierarchical secondary microstructures on effective ion transport are discussed in Chapter 8. The main outcomes and potential future investigations are summarized in the final Chapter 9.

Part I

Model formulation and validation

2 Multiphase-field model for intercalation battery materials

2.1 Brief history of (multi)phase-field models[1]

»Over the last decades, phase-field methods have been established as the method of choice for the simulation of microstructures with evolving interfaces. A general feature of phase-field approaches is the diffuse interface between coexisting phases. The term phase refers to thermodynamically distinct states that occur in a phase diagram as a function of temperature, pressure, composition, and so on. In the phase-field community, the usage of this term extends to differentiate between crystalline polymorphs or grains with different orientations. The diffuse interface is characterized by a continuous and steep transition of the phase-field variable, which generally could be molar fraction c [111], an order parameter η [127–129] or the volume fraction ϕ [123, 124] of the respective phase. In many fundamental works of the phase-field method, such as those by van der Waals [130], Ginzburg and Landau [131] and Cahn and Hilliard [111], the diffusiveness of interfaces is considered a natural property of the transition region between stable phases which holds true on a small scale. Cahn and Hilliard introduce the gradient term $\kappa(\nabla c)^2$ to account for long-range interactions while the second contribution, the regular solution free energy, has a strong foundation in chemistry. As a result, the interfacial energy, which is defined as the excess Gibbs free energy per unit area in the diffuse region, can be predicted as a function of temperature. In many applications, the phase-field method is primarily used due

[1] The content of this section is taken verbatim from the article Daubner *et al.* [126].

to its strength to describe curved and evolving surfaces but the physical length scale of the diffuse interface is well below the microstructural scale of interest. This introduces the notion of diffuse representation of sharp-interface problems which calls for effective re-scaling of the diffuse interfacial width while preserving its physical interfacial energy to correctly model the interplay of curvature driven phase transformations with other coupled multi-physics.

Another reason for the success of phase-field methods is the thermodynamically-sound framework of defining the overall system free energy (or entropy) functional and, consequently, deriving the kinetic evolution equations from variational principles. This allows for modeling of multi-physics interaction, including various coupled effects such as thermal, chemical, mechanical, electrical or magnetic bulk driving forces or coupling with fluid mechanics. Hence, the range of applications is broad nowadays, including fluid-fluid interfaces such as demixing or spinodal decomposition of emulsions (oil-water systems) [132] and multi-phase flows of two immiscible fluids [133]. Problems with fluid-solid interfaces include solidification from a melt which can result in dendritic growth for pure substances [134] or lamellae for eutectic systems [124, 135, 136] as well as growth or dissolution of crystals from supersaturated solutions [137, 138]. Solid-solid interfaces and phase transformations, on the other hand, can be found in many applications associated with steels and alloys, such as recrystalization, grain coarsening and martensitic transformations [139, 140]. Additionally, in fields like microstructure evolution in fuel cells [141], intercalation in battery materials [36, 100] and many others, the phase-field method continues to acquire increasing interest. For all these applications, the simulation outcome heavily depends on the correct modeling of competing driving forces and, irrespective of the possibly coupled multiphysics, always depends on interfacial energies and, thus, curvature driving forces.

Generalizations of the phase-field method to multi-phase systems were developed in two different ways, both acting as a nucleus for the growth of scientific communities. In 1994, Chen and Yang [128] published a model employing many non-conserved order parameters evolving through time-dependent Ginzburg-Landau

equations and started the model branch of **multi-order parameter models** (also called continuum-field models). The work by Steinbach *et al.* [123] in 1996 marks the beginning of **multiphase-field models** which are characterized by the notion of phase-fields ϕ representing the volume fraction. Both branches have been further developed since.«

This work is based on the ongoing development of multiphase-field models based on [123]. Relevant details are the gradient term formulation following [142], the re-scaling of interfacial width [124], the evolution equation proposed in [143] and the derivation of chemical driving forces within the framework of a grand-potential functional [144, 145]. The treatment of phase transformations in poly-crystalline samples as well as the corresponding noise term for phase nucleation are based on the works of Schoof [140, 146]. The following sections provide detailed insights into the model formulation und the corresponding numerical implementation.

2.2 Energy functional

A multiphase-field (MPF) model is formulated for a tuple of N phase variables $\boldsymbol{\phi} = \{\phi_\alpha, \phi_\beta, \dots\}$ where ϕ_α denotes the volume fraction of the α-phase and thus $\phi_\alpha \in [0,1]$ and $\sum_\alpha^N \phi_\alpha = 1$ should be fulfilled [124, 142, 147, 148]. The evolution of phases in battery materials is governed by the complex interplay of electro-chemo-mechanical as well as interfacial driving forces. Thus, the free energy functional $\mathscr{F}$ can be expressed as

$$\begin{aligned}
\mathscr{F} &= \mathscr{F}_{\text{int}}(\boldsymbol{\phi}, \boldsymbol{\nabla}\boldsymbol{\phi}) + \mathscr{F}_{\text{bulk}}(\boldsymbol{\phi}, \boldsymbol{c}, \boldsymbol{\epsilon}) && (2.1)\\
&= \int_V f_{\text{int}}(\boldsymbol{\phi}, \boldsymbol{\nabla}\boldsymbol{\phi})\mathrm{d}V + \int_V f_{\text{bulk}}(\boldsymbol{\phi}, \boldsymbol{c}, \boldsymbol{\epsilon})\mathrm{d}V && (2.2)\\
&= \int_V f_{\text{grad}}(\boldsymbol{\nabla}\boldsymbol{\phi}) + f_{\text{ob}}(\boldsymbol{\phi})\mathrm{d}V + \int_V f_{\text{chem}}(\boldsymbol{\phi}, \boldsymbol{c}, \Phi) + f_{\text{elast}}(\boldsymbol{\phi}, \boldsymbol{\epsilon})\mathrm{d}V, && (2.3)
\end{aligned}$$

consisting of interfacial and bulk contributions. The interfacial energy f_{int} comprises two terms, first the gradient energy density [142]

$$f_{\text{grad}}(\nabla\phi) = -\varepsilon \sum_{\alpha} \sum_{\beta>\alpha} \gamma_{\alpha\beta} \nabla\phi_\alpha \cdot \nabla\phi_\beta \tag{2.4}$$

with the numerical parameter ε linked to interface width and the interfacial energy $\gamma_{\alpha\beta}$ between two phases ϕ_α and ϕ_β. The nabla symbol is used $\nabla(\cdot)$ for the gradient operator. The second term f_{ob} is the multi-obstacle potential energy density

$$f_{\text{ob}}(\phi) = \frac{16}{\varepsilon\pi^2} \sum_{\alpha} \sum_{\beta>\alpha}^{N} \gamma_{\alpha\beta} \phi_\alpha \phi_\beta, \tag{2.5}$$

which, in combination with Eq. (2.4), prevents the non-physical formation of ghost phases in two-phase interfaces (see Chapter 3). The driving force for intercalation in Li/Na-ion batteries, which are based on the rocking-chair principle, is given by the difference between chemical potentials of Li/Na in the anode and cathode. During charge or discharge, electrons are moving through an outer circuit while Li^+/Na^+ ions are shuttled through the electrolyte. Thus, the discussion of equilibrium states includes consideration of the electro-chemical potentials of charged species (see Section 2.6). Under the assumptions of fast electronic transport and charge neutrality on the mesoscopic length scale, it is sufficient to model the energetic landscape of intercalated Li/Na atoms in the host structure. The chemical energy density depends on the site filling fraction in the host structure c and is expressed as the linear interpolation of phase-specific contributions

$$f_{\text{chem}}(\phi, c) = \sum_{\alpha}^{N} f_{\text{chem}}^{\alpha}(c^\alpha)\phi_\alpha \tag{2.6}$$

weighted by the local volume fractions ϕ_α. The phase-specific molar fractions $c^\alpha(\mu)$ are related by equal diffusional potential in the diffuse interface while the average is defined as $c = \sum c^\alpha \phi_\alpha$. The fitting of phase-dependent chemical energies f_{chem}^{α} needs to fulfill the invertibility criterion [145] (for more details

see Appendix C). In this work, two formulations are used, namely the quadratric fit for computational efficiency and a logarithmic expression based on an ideal solution

$$f^{\alpha}_{\text{quad}} = A^{\alpha}(c^{\alpha} - c^{\alpha}_{\text{min}})^2 + B^{\alpha}, \tag{2.7}$$

$$f^{\alpha}_{\text{ideal}} = \mu^{\alpha}_0 c^{\alpha} + K^{\alpha} c^{\alpha} \ln(c^{\alpha}) + K^{\alpha}(c_{\text{max}} - c^{\alpha}) \ln(c_{\text{max}} - c^{\alpha}) + B^{\alpha}. \tag{2.8}$$

For the mechanical part, only elastic deformation due to a change in lattice constants is considered. The corresponding energy contribution f_{elast} includes phase-dependent eigenstrains $\boldsymbol{\epsilon}^*_{\alpha}$ and is formulated following [149] as

$$f_{\text{elast}}(\boldsymbol{\phi}, \boldsymbol{\epsilon}) = \frac{1}{2}\boldsymbol{\epsilon}^{\text{el}} : \mathbb{C} : \boldsymbol{\epsilon}^{\text{el}} = \frac{1}{2}[\boldsymbol{\epsilon} - \boldsymbol{\epsilon}^*] : \mathbb{C} : [\boldsymbol{\epsilon} - \boldsymbol{\epsilon}^*]. \tag{2.9}$$

The effective stiffness is defined as the linear interpolation of stiffnesses $\mathbb{C} = \sum_{\alpha} \mathbb{C}_{\alpha} \phi_{\alpha}$ and the effective eigenstrain $\boldsymbol{\epsilon}^* = \sum \boldsymbol{\epsilon}^*_{\alpha} \phi_{\alpha}$ is given by linear interpolation as well. A discussion regarding this choice of interpolation coupled with chemical driving forces can be found in [150, 151].

2.3 Phase-evolution equations

The kinetics of phase transformations are described by N coupled evolution equations (**Allen-Cahn equations**) for the non-conserved fields ϕ_{α}. Following Hamilton's principle, the equilibrium solution of the total energy Eq. (2.3) is given by $\delta \mathscr{F} = 0$. Furthermore, linear relaxation of the system free energy towards its minimum is assumed. The evolution of phase ϕ_{α} is then governed by

$$\frac{\partial \phi_{\alpha}}{\partial t} = -L \left(\frac{\partial f}{\partial \phi_{\alpha}} - \boldsymbol{\nabla} \cdot \frac{\partial f}{\partial \boldsymbol{\nabla} \phi_{\alpha}} \right), \tag{2.10}$$

where f denotes the total energy density and L is the kinetic coefficient in the sense of a relaxation rate. Throughout this work $\boldsymbol{\nabla} \cdot (\cdot)$ denotes the divergence operator.

For sake of compact notation, the functional derivative is introduced [152, Eq. 13.63]

$$\frac{\delta(\cdot)}{\delta\phi_\alpha} = \left(\frac{\partial(\cdot)}{\partial\phi_\alpha} - \boldsymbol{\nabla}\cdot\frac{\partial(\cdot)}{\partial\boldsymbol{\nabla}\phi_\alpha}\right). \tag{2.11}$$

The notion of ϕ_α representing the volume fraction of phase α makes it necessary to fulfill the Gibbs simplex constraint

$$\boldsymbol{\phi} \in \mathbb{R}^N : \sum_{\alpha=1}^{N} \phi_\alpha = 1, \quad 0 \leq \phi_\alpha \quad \forall\alpha. \tag{2.12}$$

The constraints of all ϕ_α summing up to one and all phase fractions being larger than zero, implicitly ensures $\phi_\alpha \in [0,1]\ \forall\alpha = 1,\ldots,N$. If the initial conditions fullfill Eq. (2.12), the two conditions $\sum_{\alpha=1}^{N} \partial\phi_\alpha/\partial t = 0$ and $0 \leq \phi_\alpha$ need to be ensured during the phase-field evolution. The first condition is ensured by a correct formulation of the evolution equations. One option is the introduction of a Langrange multiplier [124]

$$\frac{\partial\phi_\alpha}{\partial t} = -L\frac{\delta f}{\delta\phi_\alpha} - \lambda. \tag{2.13}$$

Another option is a suitable choice of the mobility matrix. This results in the sum over two-phase interactions as introduced by Steinbach and Pezolla [142]

$$\frac{\partial\phi_\alpha}{\partial t} = -\frac{1}{\tilde{N}\varepsilon}\sum_{\beta\neq\alpha}^{\tilde{N}} M_{\alpha\beta}\left(\frac{\delta f}{\delta\phi_\alpha} - \frac{\delta f}{\delta\phi_\beta}\right) \tag{2.14}$$

where $\tilde{N} \leq N$ denotes the amount of locally present phases and ε scales the interfacial width. Following [153], the mobility matrix $M_{\alpha\beta}$ must be symmetric and all rows and columns should sum up to zero. If all entries $M_{\alpha\beta}$, $\alpha \neq \beta$ are chosen such that they match the experimental interfacial velocity of the $\alpha\beta$-phase pair and $M_{\alpha\beta} = M_{\beta\alpha}$, the main diagonal of the mobility matrix is given by $M_{\alpha\alpha} = -\sum_\alpha M_{\alpha\beta}$. A significant difference between the two evolution equations is that the kinetic coefficient L in Eq. (2.13) needs to be interpolated from

pair-wise mobilities while Eq. (2.14) directly incorporates the physical parameters $M_{\alpha\beta}$ which is preferable if they are pair-wise different. This is especially relevant in the context of intercalation in polycrystalline structures where the pre-existing grain boundaries should be immobile or much less mobile compared to the phase transitions happening within the grains. The second criterion, $0 \leq \phi_\alpha$, is either fulfilled by construction of the energetic landscape [154] as discussed in Fig. 3.2 or needs to be enforced explicitly via algebraic constraints or projection schemes as discussed in Appendix B. Within this work, the multi-obstacle potential (Eq. (2.5)) is employed together with the projection scheme outlined in Algorithm 1.

If Eq. (2.14) is solved for a two-phase case solely driven by interfacial forces, the combination of Eq. (2.4) and (2.5) results in a diffuse transition from $\phi_\alpha = 0$ to $\phi_\alpha = 1$, as shown in Fig. 2.1a for a flat interface. For a one-dimensional case, the equilibrium solution can be obtained analytically as $\phi_\alpha(x) = 0.5 + 0.5\sin(4x/\varepsilon\pi)$, which also results in the interfacial energy and width of the diffuse interphase given in Appendix A.2. The results in Fig. 2.1b reveal two

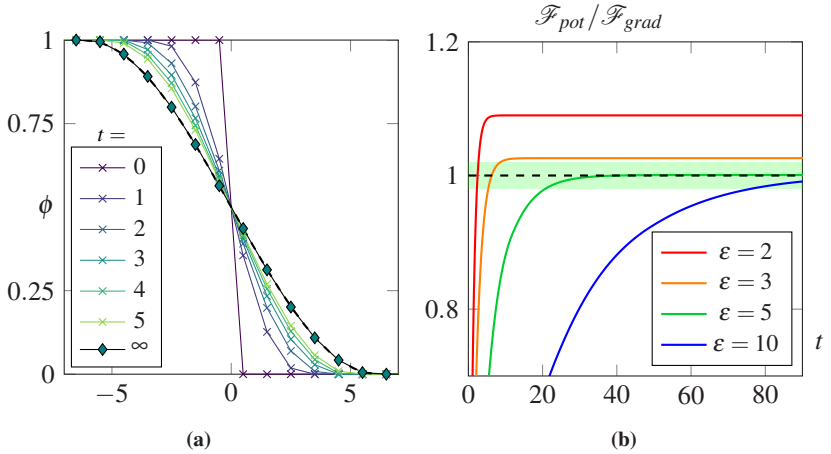


Figure 2.1: Evolution of a one-dimensional diffuse interface towards the equilibrium solution. The diffuse transition is shown in a) for grid spacing $\Delta x = 1$ and $\varepsilon = 5$ while the ratio of interfacial forces in b) is used as a metric for convergence.

fundamental properties of the diffuse interface. First of all, the time it takes for convergence towards an equilibrium interface depends on the parameter ε and, thus, the width of the interface. The formation process must be resolved on a smaller timescale than the physical processes of interest. For this reason, PACE3D [155, 156] includes an implementation to pre-process interfaces by solving a modified version of Eq. (2.14) to start with close-to-equilibrium diffuse interfaces. Secondly, the ratio of interfacial forces only converges to 1 if the interface is resolved with enough grid points. Strong deviation can be observed for $\varepsilon = 2\Delta x$ where Δx denotes the grid spacing, i.e. the distance between two grid points. Therefore, throughout this work a minimal resolution of $\varepsilon = 4\Delta x$ is used.

If a constant bulk driving force is now added to the system (e.g. $f_{\text{bulk}} = f^{\alpha}\phi_{\alpha}$, $f^{\alpha} = \text{const.}$), one would expect from consideration of the corresponding sharp interface problem that the diffuse interphase moves with constant velocity along its normal direction while keeping its equilibrium profile. This is, however, not the case which can be shown mathematically [143]. In fact, the representation of a surface by the volumetric transition region of the phase variable ϕ_{α} must

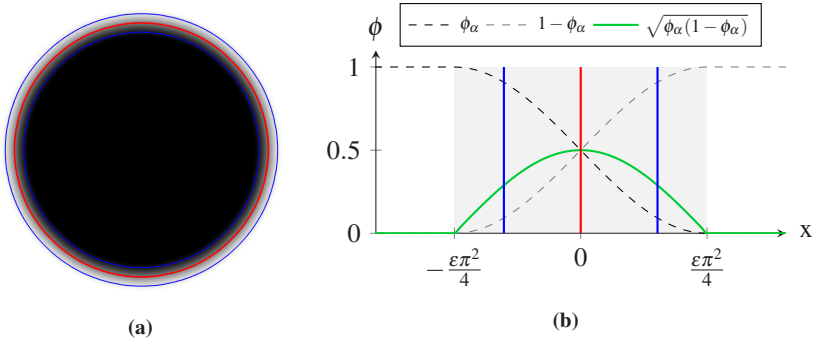


Figure 2.2: Diffuse representation of a sharp interface problem with the phase-field method given exemplarily for a circle. Isolines of $\phi_{\alpha} = 0.1$ and 0.9 are marked in blue. The isoline $\phi_{\alpha} = 0.5$ is drawn in red and represents the corresponding sharp interface problem. Interfacial profile and gradient approximation in radial direction are shown in b)

be accompanied by a consistent application of forces across the diffuse interface. Just as the surface of a body is accurately recovered by the volume integral $S = \int |\nabla\phi_\alpha| \mathrm{d}V$, any force f^α acting on this surface needs to be smeared by $|\nabla\phi_\alpha| f^\alpha$ [141, 157]. Employing the equilibrium solution for the obstacle potential in Appendix A.2, the norm of the gradient $|\nabla\phi_\alpha|$ can be replaced in the two-phase case by $\frac{4}{\varepsilon\pi}\sqrt{\phi_\alpha(1-\phi_\alpha)}$. Inspired by this consideration, the evolution equation Eq. (2.14) can be modified, treating interfacial terms as before but adjusting all pair-wise bulk driving forces with a factor accounting for the diffuseness of interfaces. The evolution of phase variables is then governed by [143, 158]

$$\frac{\partial\phi_\alpha}{\partial t} = -\frac{1}{\tilde{N}\varepsilon}\sum_{\beta\neq\alpha}^{\tilde{N}} M_{\alpha\beta}\left(\frac{\delta f_{\mathrm{int}}}{\delta\phi_\alpha} - \frac{\delta f_{\mathrm{int}}}{\delta\phi_\beta} + \frac{8}{\pi}\sqrt{\phi_\alpha\phi_\beta}\Delta^{\alpha\beta}\right), \tag{2.15}$$

in which the abbreviation $\Delta^{\alpha\beta} = \delta f_{\mathrm{bulk}}/\delta\phi_\alpha - \delta f_{\mathrm{bulk}}/\delta\phi_\beta$ has been introduced. Eq. (2.15) can also be motivated by an interpolation function h_{ob} for bulk driving forces that ensures the correct traveling wave solution for a binary interface [110, Eq. 14]. The derivative of this interpolation function $\partial h_{\mathrm{ob}}(\phi)/\partial\phi = \frac{8}{\pi}\sqrt{\phi(1-\phi)}$ is then generalized for the multi-phase case. Note that no matter how Eq. (2.15) is derived, it is no longer fully variational.

The functional derivatives of the free energy contributions (2.4)-(2.9) yield

$$\begin{aligned}
-\nabla\cdot\frac{\partial f_{\mathrm{grad}}}{\partial\nabla\phi_\alpha} &= \sum_{\beta\neq\alpha}^{N}\varepsilon\gamma_{\alpha\beta}\nabla^2\phi_\beta,\\
\frac{\partial f_{\mathrm{ob}}}{\partial\phi_\alpha} &= \frac{16}{\varepsilon\pi^2}\sum_{\beta\neq\alpha}^{N}\gamma_{\alpha\beta}\phi_\beta,\\
\frac{\partial f_{\mathrm{chem}}}{\partial\phi_\alpha} &= f^\alpha_{\mathrm{chem}} + \sum_{\beta}^{N}\frac{\partial f^\beta_{\mathrm{chem}}}{\partial c^\beta}\frac{\partial c^\beta}{\partial\phi_\alpha}\phi_\beta = f^\alpha_{\mathrm{chem}} - \mu c^\alpha,\\
\frac{\partial f_{\mathrm{elast}}}{\partial\phi_\alpha} &= \frac{1}{2}\boldsymbol{\epsilon}^{\mathrm{el}} : \frac{\partial\mathbb{C}}{\partial\phi_\alpha} : \boldsymbol{\epsilon}^{\mathrm{el}} + \frac{\partial\boldsymbol{\epsilon}^{\mathrm{el}}}{\partial\phi_\alpha} : \mathbb{C} : \boldsymbol{\epsilon}^{\mathrm{el}}.
\end{aligned}$$

For the re-formulation of the chemical contribution, the constraint of equal phase diffusion potentials in the interface $\mu = \partial f^\alpha/\partial c^\alpha = \cdots = f^N/\partial c^N$ and the definition of the mean composition have been used. The interpolation of energies yields the definition $c = \sum_\alpha^N c^\alpha \phi_\alpha$ for the mean composition [145].

Furthermore, the mean composition should not depend on phase fractions, i.e.

$$\frac{\partial c}{\partial \phi_\alpha} = c^\alpha + \sum_\beta^N \frac{\partial c^\beta}{\partial \phi_\alpha}\phi_\beta = 0 \quad \rightarrow \quad \sum_\beta^N \frac{\partial c^\beta}{\partial \phi_\alpha}\phi_\beta = -c^\alpha.$$

The evolution of phase α is then goverend by

$$\frac{\partial \phi_\alpha}{\partial t} = -\frac{1}{\tilde{N}\varepsilon}\sum_{\beta\neq\alpha}^{\tilde{N}} M_{\alpha\beta}\left(\gamma_{\alpha\beta} I_{\text{dual}} + I_{\text{triple}} + \frac{8}{\pi}\sqrt{\phi_\alpha\phi_\beta}\left(\Delta^{\alpha\beta}_{\text{chem}} + \Delta^{\alpha\beta}_{\text{elast}}\right)\right)$$

where the symmetry $\gamma_{\alpha\beta} = \gamma_{\beta\alpha}$ has been included. The individual contributions are given as

$$I_{\text{dual}} = \varepsilon\left(\nabla^2\phi_\beta - \nabla^2\phi_\alpha\right) + \frac{16}{\varepsilon\pi^2}\left(\phi_\beta - \phi_\alpha\right), \tag{2.16}$$

$$I_{\text{triple}} = \varepsilon\sum_{\gamma\neq\beta\neq\alpha}^{N}(\gamma_{\alpha\gamma} - \gamma_{\beta\gamma})\left(\nabla^2\phi_\gamma + \frac{16}{(\varepsilon\pi)^2}\phi_\gamma\right), \tag{2.17}$$

$$\Delta^{\alpha\beta}_{\text{chem}} = (f^\alpha_{\text{chem}} - \mu c^\alpha) - \left(f^\beta_{\text{chem}} - \mu c^\beta\right), \tag{2.18}$$

$$\Delta^{\alpha\beta}_{\text{elast}} = \frac{1}{2}\boldsymbol{\epsilon}^{\text{el}} : \left(\mathbb{C}_\alpha - \mathbb{C}_\beta\right) : \boldsymbol{\epsilon}^{\text{el}} - \left(\boldsymbol{\epsilon}^*_\alpha - \boldsymbol{\epsilon}^*_\beta\right) : \mathbb{C} : \boldsymbol{\epsilon}^{\text{el}}. \tag{2.19}$$

Note that even if there is an immobile phase ϕ_γ, the evolution of ϕ_α and ϕ_β is influenced by ϕ_γ via I_{triple}. The triple phase contribution scales with the difference in interfacial energies $\gamma_{\alpha\gamma} - \gamma_{\beta\gamma}$ and ensures correct angles in multi-junctions according to Young's law. Thus, the model is e.g. able to naturally account for correct wetting behaviour on a substrate. If $\gamma_{\alpha\gamma} - \gamma_{\beta\gamma} \approx 0$, the triple phase contribution I_{triple} becomes negligibly small. Furthermore, it is computationally beneficial to skip the computation of I_{triple} which led to the so-called antisymmetric approximation [158, 159]. Note that this simplification can result in a strong

deviation of multi-junction angles and dynamics if the ratio between pairwise interfacial energies becomes large.

Nucleation

For the nucleation of new phases in combination with the multi-obstacle potential (Eq. (2.5)), a noise term is necessary in order to enable growth of phases that are initially not present. Consequently, a term representing thermal fluctuations is included in the evolution equation [140]

$$\frac{\partial \phi_\alpha}{\partial t} = -\frac{1}{\tilde{N}\varepsilon} \sum_{\beta \neq \alpha}^{\tilde{N}} M_{\alpha\beta} \left(\frac{\delta f_{\text{int}}}{\delta \phi_\alpha} - \frac{\delta f_{\text{int}}}{\delta \phi_\beta} + \frac{8}{\pi} \sqrt{\phi_\alpha \phi_\beta} \Delta^{\alpha\beta} \right) + \frac{\partial \zeta}{\partial \phi_\alpha}, \tag{2.20}$$

which is only active in the interface regions assuming heterogeneous nucleation at structural defects such as grain or phase boundaries in polycrystalline materials [160]. This assumption is discussed in more detail in Sec. 4.4. The noise term is formulated as

$$\zeta = \sum_{\alpha<\beta<\gamma}^{N} A \cdot D \cdot \phi_\alpha \phi_\beta \phi_\gamma \tag{2.21}$$

with an amplitude A and random distribution D. As the computation of ion diffusion is based on the diffusion potential μ (Section 2.4), a correction of μ is included to ensure that c is unaffected by the noise [136]. Otherwise, the inclusion of noise in ϕ could result in a numerical leakage of the conserved quantitiy c. The choice of Eq. (2.21) and the corresponding necessary noise amplitude A are discussed in more detail in Chapter 4.

2.4 Diffusion within the active material

In the general case, the diffusion of K species with molar fractions c_i is given by a set of $K-1$ independent partial differential equations driven by the phase diffusion potentials μ_j

$$\frac{\partial c_i}{\partial t} = \nabla \cdot \left(\sum_{j=1}^{K-1} \mathbb{M}_{ij}(\phi, c_i) \nabla \mu_j \right) + R_i. \tag{2.22}$$

and the reaction term R_i. The mean mobility comprises the individual phase mobilities $\mathbb{M}_{ij} = \sum_\alpha^N \mathbb{M}_{ij}^\alpha \phi_\alpha$, where each $\mathbb{M}_{ij}^\alpha$ is defined as $\mathbb{M}_{ij}^\alpha = \mathbb{D}_{ij}^\alpha \partial c_i^\alpha / \partial \mu_j$ in the general case. The thermodynamic pre-factors $\partial c_i^\alpha / \partial \mu_j$ depend on the choice of chemical phase energies f_{chem}^α. In equilibrium, the diffusion potentials of two adjacent phases must be equal ($\mu_i^\alpha = \mu_i^\beta$) and this constraint is generally applied to diffuse interface regions. This can be motivated from the fact, that interfaces can be interpreted as a phenomenological superposition of multiple phases and, according to the introduced separation of interfacial and bulk contributions in Eq. (2.1), the equilibrium interfacial profile obtained from f_{grad} and f_{ob} should not be altered by bulk driving forces [144]. The chemical driving force for phase transformations is given by the pairwise difference of grand chemical potentials $(f_{\text{chem}}^\alpha - \mu c^\alpha) - (f_{\text{chem}}^\beta - \mu c^\beta)$ (Eq. (2.18)), which needs to be constant across the diffuse interface [145]. This condition is fulfilled if $\mu = \mu_i^\alpha = \cdots = \mu_i^N$. Instead of solving for $K \times N$ molar fractions and applying the $K \times N - 1$ constraints, the evolution equations (2.22) can be re-written in terms of diffusional potential following [145]. From $c_i = \sum_\alpha^N c_i^\alpha \phi_\alpha$ it follows that

$$\frac{\partial c_i}{\partial t} = \sum_\alpha^N \frac{\partial c_i^\alpha}{\partial \mu_k} \frac{\partial \mu_k}{\partial t} \phi_\alpha + \sum_\alpha^N c_i^\alpha \frac{\partial \phi_\alpha}{\partial t} \tag{2.23}$$

and, thus, the expression

$$\frac{\partial \mu_k}{\partial t} = \left[\sum_\alpha^N \frac{\partial c_i^\alpha}{\partial \mu_k} \phi_\alpha \right]^{-1} \left(\nabla \cdot \left(\sum_{j=1}^{K-1} \mathbb{M}_{ij} \nabla \mu_j \right) + R_i - \sum_\alpha^N c_i^\alpha \frac{\partial \phi_\alpha}{\partial t} \right) \tag{2.24}$$

is obtained for the evolution of the diffusion potentials.

The diffusion of ions inside the intercalation compound is treated in the sense of interstitial diffusion inside a lattice with the two species ions and vacancies. The maximal concentration of intercalated ions $c_{\max}$ is given by the number of interstitial sites per unit cell volume. The sum of ions and vacancies $c_{\text{ion}} + c_{\text{v}} = c_{\max}$ can be considered constant under the assumption that the host structure does not change significantly. The field variable is normalized by its maximal value such that equations are formulated in terms of the molar fraction $c_{\text{ion}}/c_{\max}$, which is equivalent to the local site filling fraction of vacancies within the host structure (e.g. x in Li_xFePO_4). Eq. (2.24) can thus be simplified to

$$\frac{\partial \mu}{\partial t} = \left[\sum_{\alpha}^{N} \frac{\partial c^{\alpha}}{\partial \mu}\phi_{\alpha}\right]^{-1} \left(\nabla \cdot (\mathbb{M}\nabla\mu) + R - \sum_{\alpha}^{N} c^{\alpha}\frac{\partial \phi_{\alpha}}{\partial t}\right). \tag{2.25}$$

The ion concentration in the active material can change due to an insertion reaction at the electrode-electrolyte interface, which is given by a surface reaction term or, under specific assumptions (see Section 6.2.1), as a bulk source term. Electro-chemical reactions are discussed in Sec. 2.6.

For many applications, diffusion is assumed to be ideal and isotropic which results in a scalar mobility $\mathscr{M} = \sum_{\alpha}^{N}(D^{\alpha}\partial c^{\alpha}/\partial\mu)\phi_{\alpha}$ based on scalar diffusivities D^{α} per phase. More generally, anisotropic diffusion is described by a second order tensor $\mathbb{D}^{\alpha}$. As discussed in Section 1.1.1, many battery materials exhibit strongly anisotropic properties in terms of diffusivity, surface energies, mechanical stiffness and lattice expansion. For orthorhombic materials with strong anisotropy, the diffusion tensor in the lattice coordinate system can be expressed by a diagonal tensor with three independent entries

$$\mathbb{D}_{123} = \begin{bmatrix} D_{11} & 0 & 0 \\ 0 & D_{22} & 0 \\ 0 & 0 & D_{33} \end{bmatrix}.$$

Every grain has an individual orientation that can be described by Euler angles or quaternions with respect to the global coordinate system. Rotation of the diffusion tensor from the material to the reference coordinate system can be achieved using rotation matrices such as

$$\boldsymbol{R}_x = \begin{bmatrix} 1 & 0 & 0 \\ 0 & \cos\theta & -\sin\theta \\ 0 & \sin\theta & \cos\theta \end{bmatrix}, \boldsymbol{R}_y = \begin{bmatrix} \cos\psi & 0 & \sin\psi \\ 0 & 1 & 0 \\ -\sin\psi & 0 & \cos\psi \end{bmatrix}, \boldsymbol{R}_z = \begin{bmatrix} \cos\varphi & -\sin\varphi & 0 \\ \sin\varphi & \cos\varphi & 0 \\ 0 & 0 & 1 \end{bmatrix}$$

which, in the XYZ-convention, yields the rotation transformation

$$\mathbb{D}^{\alpha}_{xyz} = \boldsymbol{R}^{\alpha}_z \boldsymbol{R}^{\alpha}_y \boldsymbol{R}^{\alpha}_x \mathbb{D}_{123} (\boldsymbol{R}^{\alpha}_x)^T (\boldsymbol{R}^{\alpha}_y)^T (\boldsymbol{R}^{\alpha}_z)^T .$$

Alternatively, the rotation can be computed based on quaternions, which are more robust for arbitrary rotations [161, 162] and, moreover, allow for straight-forward interpolation of intermediate configurations.

2.5 Mechanical equilibrium

The **kinematics** of a continuous body $\mathscr{B}$ can be described by the mapping from the reference to the current configuration $\boldsymbol{x} = \chi(\boldsymbol{X},t)$, in which $\boldsymbol{x}$ denotes the current position of a material point and $\boldsymbol{X}$ the initial position. The displacment of each material point is defined by the vector pointing from the initial to the current position $\boldsymbol{u}(\boldsymbol{X},t) = \chi(\boldsymbol{X},t) - \boldsymbol{X}$. The deformation is described by the deformation gradient $\boldsymbol{F} = \boldsymbol{\nabla}\chi$ containing rigid body rotations as well as strain. An appropriate strain measure needs to be independent of rigid body motion, which leads to formulations for material laws based on e.g. the right Cauchy-Green tensor $\boldsymbol{C} = \boldsymbol{F}^{\mathrm{T}}\boldsymbol{F}$ or the Green strain tensor $\boldsymbol{E} = \frac{1}{2}(\boldsymbol{F}^{\mathrm{T}}\boldsymbol{F} - \mathbf{1})$. In the limit of small strain $\boldsymbol{\epsilon}$, the linearized approximation

$$\boldsymbol{\epsilon} = \frac{1}{2}(\boldsymbol{\nabla}\boldsymbol{u} + (\boldsymbol{\nabla}\boldsymbol{u})^{\mathrm{T}}) \tag{2.26}$$

holds. Within this work, only small deformations are considered. However, the inclusion of large deformations within the multiphase-field approach is also possible [163].

The evolution of mechanical stress is governed by the **momentum balance**. Under the assuption that mechanical relaxation processes are much faster than diffusional ones, equilibrium of the static momentum balance is required at any given time such that the stress tensor $\boldsymbol{\sigma}$ fulfills

$$\boldsymbol{\nabla} \cdot \boldsymbol{\sigma} + \boldsymbol{b} = \mathbf{0} \tag{2.27}$$

with applied body forces $\boldsymbol{b}$. Furthermore, symmetry of $\boldsymbol{\sigma}$ is obtained from the balance of angular momentum $\boldsymbol{\sigma} = \boldsymbol{\sigma}^{\mathrm{T}}$. To close the system of equations, an assumption about the rheological behaviour of the continuous body needs to be introduced which is typically called **material law**. The postulated elastic energy density (2.9) defines the material law through the relation

$$\boldsymbol{\sigma} = \frac{\partial f_{\mathrm{elast}}}{\partial \boldsymbol{\epsilon}^{\mathrm{el}}} = \mathbb{C} : [\boldsymbol{\epsilon} - \boldsymbol{\epsilon}^*] \tag{2.28}$$

in which the additive superposition of strains $\boldsymbol{\epsilon} = \boldsymbol{\epsilon}^{\mathrm{el}} + \boldsymbol{\epsilon}^*$ was implicitely imposed. $\boldsymbol{\epsilon}$ denotes the total, $\boldsymbol{\epsilon}^{\mathrm{el}}$ the elastic and $\boldsymbol{\epsilon}^*$ eigenstrains, respectively.

Within the diffuse interface region, an interpolation of phase-specific quantities needs to be employed. From the Hill-Mandel condition [164], it follows that a homogenization of the phase-dependent stress and strain contributions by interpolation with the volume fraction ϕ_α

$$\boldsymbol{\sigma} = \sum_\alpha \boldsymbol{\sigma}_\alpha \phi_\alpha \quad \text{and} \quad \boldsymbol{\epsilon} = \sum_\alpha \boldsymbol{\epsilon}_\alpha \phi_\alpha$$

defines the effective quantities $\boldsymbol{\sigma}$ and $\boldsymbol{\epsilon}$. Two well-known averaging schemes are the Voigt-Taylor (VT) interpolation based on the assumption of uniform strains $\boldsymbol{\epsilon} = \boldsymbol{\epsilon}_\alpha, \forall \alpha$ and the Reuss-Sachs scheme, which assumes uniform stress among all phases $\boldsymbol{\sigma} = \boldsymbol{\sigma}_\alpha, \forall \alpha$. These two interpolations define the upper and lower bounds of admissible interpolation schemes. Eq. (2.9), on the other hand, follows the

microelasticity approach of Khachaturyan [149] assuming linear interpolation of stiffnesses $\mathbb{C} = \sum \mathbb{C}_\alpha \phi_\alpha$ and linear interpolation of eigenstrains $\boldsymbol{\epsilon}^* = \sum \boldsymbol{\epsilon}^*_\alpha \phi_\alpha$, resulting in the effective stress

$$\boldsymbol{\sigma} = \mathbb{C} : [\boldsymbol{\epsilon} - \boldsymbol{\epsilon}^*] = \left(\sum_\alpha \mathbb{C}_\alpha \phi_\alpha \right) : [\boldsymbol{\epsilon} - \sum_\alpha \boldsymbol{\epsilon}^*_\alpha \phi_\alpha].$$

The elastic energy (2.9) cannot be expressed as an average of phase-specific energies and, thus, this approach is not a homogenization in the spirit of the Hill-Mandel condition. All three approaches have been compared for the case of an elasto-plastic precipitate in an elastic matrix driven by chemo-mechanical forces. The comparison showed that the Reuss-Sachs interpolation does not correctly account for the coupling of chemical and mechanical forces while the other two yielded almost identical results [150].

All three interpolation schemes discussed above do not reproduce the momentum balance at singular surfaces for a finite width of the diffuse interface [165]. Interpolation schemes that correctly account for the Hadamard condition and avoid excess energies in the diffuse interface have been developed [165–167]. They are based on a split of normal and tangential contributions, which makes it necessary to compute the surface normal of an interface from the gradient of the phase-field, e.g. $\boldsymbol{n} = \boldsymbol{\nabla}\phi_\alpha / |\boldsymbol{\nabla}\phi_\alpha|$. However, this approach poses a numerical challenge for nucleation of new phases when interfaces are not yet fully developed. The VT and Khachaturyan approaches are more stable but alter the interfacial energy. This excess energy is larger in the case of VT interpolation [151]. For this reason, the microelasticity theory (i.e. Khachaturyan interpolation) is employed throughout this work although I am aware of the drawbacks arising from the interdependence between interfacial width $l(\varepsilon)$ and excess energy.

2.6 Electro-chemical surface reaction

All model derivations and assumptions in this section are discussed for a Na-ion intercalation battery. However, the results are also applicable to Li-ion batteries.

In a sodium ion cell, sodium *atoms* are stored in both the anode and the cathode. However, oxidation and reduction reactions are necessary at both electrode-electrolyte interfaces during operation of the cell such that ions can be solvated in the electrolyte and travel to the other electrode while electrons are moving through an external circuit. The driving force for an electric current is the difference of electro-chemical potentials of the electrons between the anode (A) and cathode (C) side which corresponds to the voltage difference measured by a potentiometer [168]

$$F\Delta V = \tilde{\mu}_{e^-}^{\mathrm{A}} - \tilde{\mu}_{e^-}^{\mathrm{C}}. \tag{2.29}$$

F denotes the Faraday constant. In other words, the measured potential can be interpreted as the voltage that must be applied to a battery to stop the current. These potentials are actually measured at contacts to the current collectors (cc) on both sides but in equilibrium $\tilde{\mu}_{e^-}^{\mathrm{cc,A}} = \tilde{\mu}_{e^-}^{\mathrm{A}}$ must hold as the electrode and respective current collector are electrically connected. Note that the measured potential difference is not generally equal to the difference in (inner) electrostatic potentials. If we measure the potential difference with two copper wires, the chemical potentials of electrons are identical and thus

$$\begin{aligned}\Delta V &= \frac{\tilde{\mu}_{e^-}^{\mathrm{wire,A}} - \tilde{\mu}_{e^-}^{\mathrm{wire,C}}}{F} \\ &= \frac{\mu_{e^-}^{\mathrm{copper}} - F\Phi^{wire,A} - \mu_{e^-}^{\mathrm{copper}} + F\Phi^{wire,C}}{F} \\ &= \Phi^{wire,C} - \Phi^{wire,A}\end{aligned}$$

holds. Typically, the anode and cathode are two different materials and, as a result, their inner electro-static potentials cannot be directly measured.

Under open-circuit conditions, the electrochemical potential of sodium ions must be equal across the cell

$$\tilde{\mu}^{\mathrm{C}}_{\mathrm{Na}^+} = \tilde{\mu}^{\mathrm{elyte}}_{\mathrm{Na}^+} = \tilde{\mu}^{\mathrm{A}}_{\mathrm{Na}^+} \tag{2.30}$$

as the electrolyte is able to shuttle Na^+ ions until equilibrium is established. The Na chemical potential can be expressed as the sum of electrochemical potentials of the ion and respective electron

$$\mu_{\mathrm{Na}} = \tilde{\mu}_{\mathrm{Na}^+} + \tilde{\mu}_{e^-} \tag{2.31}$$

and, consequently, the resulting open-circuit voltage can be expressed as

$$V_{\mathrm{OC}} = \frac{\tilde{\mu}^{\mathrm{A}}_{e^-} - \tilde{\mu}^{\mathrm{C}}_{e^-}}{F} = \frac{\mu^{\mathrm{A}}_{\mathrm{Na}} - \tilde{\mu}^{\mathrm{A}}_{\mathrm{Na}^+} - \mu^{\mathrm{C}}_{\mathrm{Na}} + \tilde{\mu}^{\mathrm{C}}_{\mathrm{Na}^+}}{F} = \frac{\mu^{\mathrm{A}}_{\mathrm{Na}} - \mu^{\mathrm{C}}_{\mathrm{Na}}}{F}. \tag{2.32}$$

This is equal to the change in Gibbs free energy when transferring an ion from the anode to the cathode and can be approximated by balancing the total energies obtained with DFT [169].

The simulation studies in Chapters 6, 7 and 8 consider the intercalation of lithium/sodium into cathode materials, which are cycled against the respective metal counter electrode (analogous to a half-cell setup). At constant temperature and pressure, the chemical potential of metallic sodium is constant ($\mu^{\mathrm{A}}_{\mathrm{Na}} = \mu^{\ominus,\mathrm{A}}_{\mathrm{Na}}$) while the chemical potential in the cathode depends on the site filling fraction of vacancies

$$\mu^{\mathrm{C}}_{\mathrm{Na}}(c) = \mu^{\ominus,\mathrm{C}}_{\mathrm{Na}} + \mu(c). \tag{2.33}$$

In the continuum approximation, the diffusion potential μ is related to the partial derivative of the Gibbs free energy density with respect to the site filling fraction $\mu = \partial f / \partial c$ [158, 170]. Within the multiphase-field approach presented in Section 2.2, $\mu = \partial f^\alpha / \partial c^\alpha = \cdots = f^N / \partial c^N$ holds for the phase-specific contributions. Under these assumptions, Eq. (2.32) can be expressed as

$$V_{\mathrm{OC}}(X) = V^{\ominus}_{\mathrm{cell}} - \frac{\mu}{F}. \tag{2.34}$$

where the reference cell voltage $V_{\text{cell}}^{\ominus} = (\mu_{\text{Na}}^{\ominus,\text{A}} - \mu_{\text{Na}}^{\ominus,\text{C}})/F$ is independent of c and thus constant. $X \in [0,1]$ denotes the average site filling fraction $X = \frac{1}{V_{\text{E}}} \int c_{\text{ion}} \text{d}V_{\text{E}}$ in the active electrode material volume V_{E}. Even though the local composition may vary across the active material due to phase transformations, the chemical potentials are equal in equilibrium. This thermodynamic background facilitates the comparison of experimental results that are close to equilibrium (i.e. low C-rate) with total energies calculated by DFT [169]. Furthermore, both can be used as an input to formulate the chemical Gibbs free energy density f_{chem} for phase-field simulations which is discussed for $\text{Na}_X\text{Ni}_{1/3}\text{Mn}_{2/3}\text{O}_2$ in Section 7.2.1.

Kinetic processes that dominate the charge and discharge of intercalation compounds include interfacial ion transfer as well as ion and electron transport in the bulk and possible phase transformations. The intercalation reaction into the active material such as

$$X \cdot \text{Na}^+ + X \cdot e^- + \text{TM}\,\text{O}_2 \rightleftharpoons \text{Na}_X\text{TM}\,\text{O}_2, \tag{2.35}$$

is typically modelled by the Butler-Volmer equation [168, Eq. 9.13] such that the electrical flux into or out of the electrode is given by

$$j_{\text{N}} = j_0(c_{\text{surf}}) \left(\exp\left(\alpha \frac{e\eta}{k_{\text{B}}T} \right) - \exp\left(-(1-\alpha) \frac{e\eta}{k_{\text{B}}T} \right) \right) \tag{2.36}$$

with the exchange current density j_0 and the so-called overpotential η. k_{B} denotes the Boltzmann constant, e the elemental charge and T the ambient temperature. For symmetry of the forward and backward reaction ($\alpha = 0.5$)), Eq. (2.36) reduces to

$$j_{\text{N}} = 2 j_0(c_{\text{surf}}) \sinh\left(\frac{e\eta}{2k_{\text{B}}T} \right). \tag{2.37}$$

In the non-equilibrium case, a gradient in chemical potential can arise in the cathode from the surface into the bulk of active particles due to diffusion limitation and $\nabla\mu$ is the respective driving force for diffusion as discussed in Section 2.4. The overpotential η is the driving force for intercalation, which is given by the

difference of electrochemical potentials of Na^+ ions at the electrolyte-electrode interface

$$\eta = (\tilde{\mu}^{\text{elyte}}_{\text{Na}^+} - \tilde{\mu}^{\text{C}}_{\text{Na}^+,\text{surf}})/F.$$

Assuming fast ion transport in the electrolyte and fast reaction kinetics at the metal electrode, $\tilde{\mu}^{\text{elyte}}_{\text{Na}^+} \approx \tilde{\mu}^{\text{A}}_{\text{Na}^+}$ holds and thus

$$\eta = \frac{\tilde{\mu}^{\text{A}}_{\text{Na}^+} - \tilde{\mu}^{\text{C}}_{\text{Na}^+,\text{surf}}}{F} = \frac{\mu^{\text{A}}_{\text{Na}} - \mu^{\text{C}}_{\text{Na,surf}}}{F} - \frac{\tilde{\mu}^{\text{A}}_{e^-} - \tilde{\mu}^{\text{C}}_{e^-,\text{surf}}}{F}.$$

Furthermore, assuming good electronic wiring in the cathode and fast electron conduction compared to the time scales of ion intercalation and diffusion, $\tilde{\mu}^{\text{C}}_{e^-}$ takes the same value across the cathode. With the definition in Eq. (2.29) and the previously used expressions for chemical potential, this yields

$$\eta = \frac{\mu^{\text{A}}_{\text{Na}} - \mu^{\text{C}}_{\text{Na,surf}}}{F} - V = V^{\ominus}_{\text{cell}} - V - \frac{\mu_{\text{surf}}}{F} \tag{2.38}$$

where the V is the applied voltage. μ_{surf} is the diffusion potential of sodium at the surface of the active material and will be spatially resolved in simulations. In combination with Eq. (2.37), this yields

$$j_{\text{N}} = 2 j_0(c_{\text{surf}}) \sinh\left(\frac{e}{2k_{\text{B}}T}(V^{\ominus}_{\text{cell}} - V) - \frac{\mu_{\text{surf}}}{2RT}\right) \tag{2.39}$$

and, thus, the surface reaction depends on the surface concentration and chemical potential of intercalated ions. The previously discussed model assumptions lead to the notion of the *nano-battery model* sketched in Fig. 2.3

In the classical Butler-Volmer equation, the exchange current density is assumed to take the form $j_0 = k_0\sqrt{c_{\text{surf}}(1-c_{\text{surf}})}$. A derivation of reaction kinetics from Marcus theory leads to a different pre-factor [99, 108], which introduces an asymmetry into the charge-discharge behaviour. A skewed $j_0(c_{\text{surf}})$ relation can amplify reaction heterogeneities during charge but suppresses them during discharge [171]. The rate constant k_0 is material specific [172] and associated with the energetic barrier to be overcome for desolvation and intercalation of ions. k_0

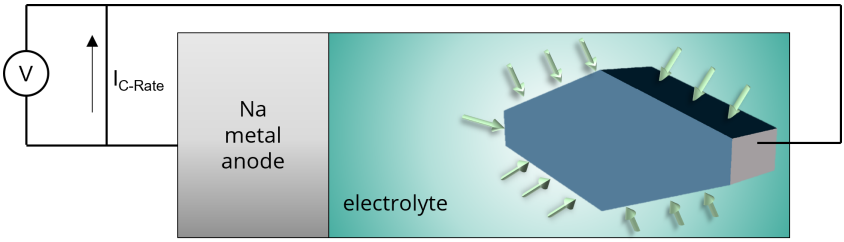


Figure 2.3: Nano-battery model consisting of a single cathode particle cycled against Na metal anode assuming fast transport in the electrolyte and fast reaction kinetics at the anode side.

and consequently j_N have dimensions [A/m^2] and the surface reaction is given by $R_{\text{surf}}(c,t) = j_N/F$ in [mol/(s m^2)] with F being the Faraday constant.

The assumption of galvanostatic (dis-)charge (i.e. battery is charged with a constant flux) can be modeled employing Eq. (2.39) on the surface while restricting the global flux [108]

$$I = \int_{\partial\mathscr{B}} \frac{1}{F}\, \boldsymbol{j}\cdot\boldsymbol{n}\,\mathrm{d}A \stackrel{!}{=} c_{\max}\,\text{C-rate}\int_{\mathscr{B}} 1\,\mathrm{d}V \quad \left[\frac{\text{mol}}{\text{s}}\right]. \tag{2.40}$$

Eq. (2.40) can be utilized to compute the applied voltage V of the nanoparticle battery under the assumptions stated before. Inserting Eq. (2.36) as the surface flux and employing the definition of overpotential in Eq. (2.38), yields

$$\frac{k_0}{F}\int_{\partial\mathscr{B}} \sqrt{c(1-c)}\left[\exp\left(\frac{e}{2k_{\mathrm{B}}T}(V_{\text{cell}}^{\ominus}-V)-\frac{\mu}{2RT}\right)\right.$$
$$\left.-\exp\left(-\frac{e}{2k_{\mathrm{B}}T}(V_{\text{cell}}^{\ominus}-V)+\frac{\mu}{2RT}\right)\right]\mathrm{d}A \stackrel{!}{=} I.$$

Substituting $y = \exp(\frac{e}{2k_{\mathrm{B}}T}(V_{\text{cell}}^{\ominus}-V))$ and multiplying both sides by y leads to

$$y^2\int \frac{k_0}{F}\sqrt{c(1-c)}\exp\left(-\frac{\mu}{2RT}\right)\mathrm{d}A - \int \frac{k_0}{F}\sqrt{c(1-c)}\exp\left(\frac{\mu}{2RT}\right)\mathrm{d}A - Iy \stackrel{!}{=} 0.$$

With abbreviations for both integrals

$$\text{int}^- = \int \frac{k_0}{F}\sqrt{c(1-c)}\exp\left(-\frac{\mu}{2RT}\right)\mathrm{d}A,$$
$$\text{int}^+ = \int \frac{k_0}{F}\sqrt{c(1-c)}\exp\left(\frac{\mu}{2RT}\right)\mathrm{d}A,$$

the quadratic formula for y can be solved and expressed as

$$y = \frac{1}{2\,\text{int}^-}\left[I \pm \sqrt{I^2 + 4\,\text{int}^-\,\text{int}^+}\right].$$

The second solution $I - \sqrt{I^2+\ldots}$ is unphysical (y must be positive for V to be existent) and, therefore, the applied voltage of the nanoparticle battery is

$$V = V_{\text{cell}}^{\ominus} - \frac{2k_{\text{B}}T}{e}\ln(y). \tag{2.41}$$

It is common practive in experimental setups to limit the voltage window with a lower and upper cut-off voltage. After computation of Eq. (2.41), the applied voltage in simulations is limited to the given interval by

$$V^* = \min(\max(V_{\text{lower}}^{\text{cut-off}}, V), V_{\text{upper}}^{\text{cut-off}}).$$

Cut-off voltages are chosen in accordance with experiments in Chapters 6 and 7.

2.7 Numerical implementation

All simulations are conducted using codes based on finite difference stencils and an explicit Euler time-stepping. MPF simulations were performed using PACE3D [155, 156] which is an in-house code. The PACE3D (Parallel Algorithms for Crystal Evolution in 3D) framework has been developed by the group of Prof. Nestler for over 20 years and comprises a set of modules covering phase evolutions, diffusional and thermal processes, solid mechanics, fluid mechanics,

magnetism and electrical fields. The battery-specific part of the model formulation presented in Section 2.6 has been implemented as a new module inside the framework and, consequently, has been applied in combination with phase, concentration and stress evolution. Coupling with other effects such as plasticity, fracture or temperature evolution are possible in the future.

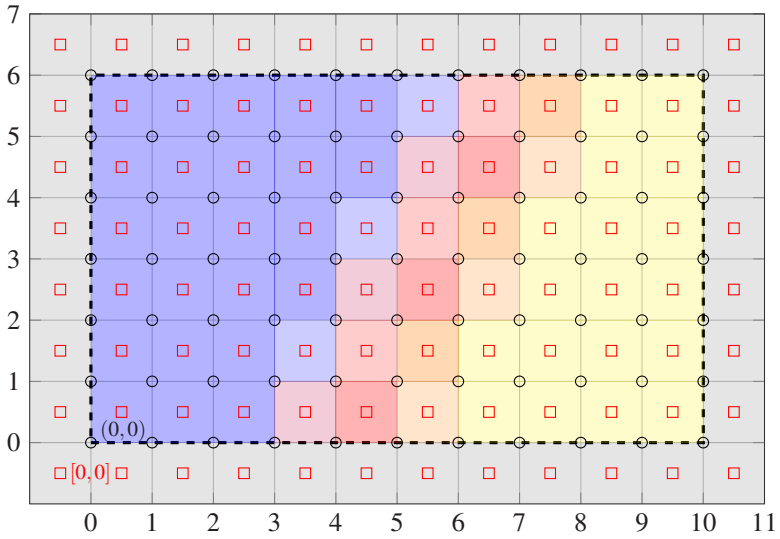


Figure 2.4: Discretisation of spatial domain

The spatial domain is discretized by a regular grid as shown in Fig. 2.4. Boundary conditions are applied using ghost cells (gray) such that all spatial gradients or the laplacian can be evaluated with stencils of second order precision in the physical domain (colored cells).

More details concerning the numerical implementation for anisotropic fluxes are given in Chapter 5. A domain decomposition is implemented in PACE3D using MPI (message passing interface) [156]. Each subdomain can be assigned to a MPI process, which allows for massive parallelization and computational speed-up [135]. To handle a large amount of phases in a computationally-efficient way,

a locally-reduced order parameter (LROP) scheme is employed [173, 174]. Under the assumption that at most $N_{\text{LROP}} << N_{\text{phases}}$ phases are locally present, the computation time and memory space can be significantly reduced if N_{LROP} phases are stored by index and value. The concept is similar to the idea of storing a sparse matrix as tuples of the two indices and a value.

2.8 Remarks

The model presented in this chapter has been carefully selected based on state-of-the-art multiphase-field models and the following validation chapters. Modeling aspects are discussed in detail and have partially been published in Daubner *et al.* [126], Daubner *et al.* [36] and Daubner *et al.* [110].

Future model improvements might encompass a strongly coupled chemo-mechanical energy formulation such that eigenstrains explicitely depend on the local composition and the ion flux has a contribution stemming from elastic deformation [175]. Currently, both influences are considered but coupled through the phase fields ϕ, which results in elimination of cross-terms in the evolution equations of μ and σ. On the other hand, the simplification is the basis for the re-formulation of Eq. (2.22) to Eq. (2.24) and, thus, contributes to the computational performance of the proposed model formulation.

Depending on the electrode material of interest, other possible model extensions comprise the inclusion of plasticity, large deformations or fracture. It has been shown experimentally [18, 35] as well as through simulations [19] that mechanical degradation is one of the most prominent mechanisms for irreversible capacity loss. At the same time, the complex effects of mechanical forces interacting with ion insertion and diffsion are not well-understood and mechanics can lead to unexpected behaviour. Fracture of larger agglomerates can shorten the average diffusion path length and lead to a higher rate performance [38]. Furthermore, the studies in Chapter 7 suggest that elastically stored energy dictates the direction of phase transformations and, thus, contributes to a higher accessible capacity.

3 Benchmarking interfacial forces[1]

»Multi-phase field formulations have historically been developed by various research groups, each of them following their own notation and advancing their own branch of model development. There has been little effort to address the mutual comparison of phase-field formulations. The work by Moelans, Wendler and Nestler [176] compares two phase-field models, employing a steady-state triple junction amongst others but is limited to dihedral angles in the range $\theta \in [89, 140]$. Toth *et al.* [153] were the first, to the best of our knowledge, to define a list of criteria that should be fulfilled for any multiphase-field formulation. Using these criteria, the authors compare established models with a newly developed one. For the scope of this work, we employ some of the criteria and only consider model formulations which fulfill the following conditions [153]:

- In accordance with the "principle of formal indistinguishability", physical results should be independent of the labeling of variables (i.e. independent of the order of computation).
- Over time, the total free energy should decrease monotonically (second law of thermodynamics) and tend towards the equilibrium solution which minimizes the free energy of the system.
- The model should be general in the sense that adding or removing a new phase is straight-forward and it should be possible to recover the respective

[1] The content of this chapter is taken verbatim from the article Daubner *et al.* [126]. While the original article includes a detailed derivation of analytical solutions and the comparison of multi-order parameter models, only the parts that are specific to multiphase-field models are included in this dissertation.

models from each other, e.g. all formulations naturally reduce to the well-known equations of a two-phase interface for $N = 2$.

The goal of this work is to shed some light on the similarities and differences among various branches of multi-phase field (MPF) models, performed in three consecutive steps. Commonly used gradient and potential energy contributions are compared using a unified notation. Subsequently, we specify the evolution equations, underlying assumptions as well as the inclusion of physical model parameters for MPF models (Sec. 3.1.3). Multiple authors have previously used a triple junction setup to validate their specific modeling approach [154, 176–180] which is well-suited for the following reasons:

- All critical modeling choices for extension from the binary to the multi-phase case have to be made to arrive at a triple junction. It should then be straight-forward to increase the number of phases to N.
- The energetic landscape of the potential term can still be visualized employing the Gibbs simplex constraint, similar to a ternary diagram (see [154] and Sec. 3.1.2).
- Triple junction angles are analytically known from Young's law.
- The occurance of ghost phases can be quantified.
- The simulation setup is simple enough (concerning initial and boundary conditions, domain size, computational effort) to be suitable for benchmarking.

The steady-state motion of the triple junction has often been compared with an analytical solution derived from a small-slope approximation [176, 181] without discussing the limits of this approximation. Especially at high ratios of pair-wise different interfacial energies, the approximate solution deviates strongly from the mathematically exact solution [182, 183] which impacts the drawn conclusions. This issue has been addressed in a recent note by Eiken [184].

3.1 Model formulation

In a general sense, the energy functional can be formulated as

$$\mathscr{F}(\phi, \nabla\phi, \dots) = \mathscr{F}_{\text{int}}(\phi, \nabla\phi) + \mathscr{F}_{\text{bulk}}(\phi, \dots) \tag{3.1}$$

where we assume a separation of interfacial and bulk energy terms following the notion discussed in the introduction that sharp interfaces can be replaced by a diffuse representation well above the atomic scale of diffuse transition regions. The interfacial term represents the surface energy of phases in contact with each other. In a sharp interface representation, this energy contribution is constrained to surfaces but in the context of the phase-field approach, it turns into a volumetric contribution smeared over the diffuse interface region such that $\mathscr{F}_{\text{int}} = \int_V f_{\text{int}} \mathrm{d}V$ holds. The integral should converge to the same energy even for finite interfacial widths. The bulk contribution can possibly contain chemical, mechanical, thermal, electrical or other driving forces for phase transformation but is not subject of the following investigations. The interfacial volume integral of phase-field formulations is generally constructed as the sum over two contributions

$$\mathscr{F}_{\text{int}}(\phi, \nabla\phi) = \int_V f_{\text{grad}}(\phi, \nabla\phi) + f_{\text{pot}}(\phi) \mathrm{d}V \tag{3.2}$$

namely a gradient term and a potential term (also called homogeneous free energy [178] or barrier function [153]) which will be discussed in detail in the following sections.

3.1.1 Gradient energy formulations

As a generalization of the two-phase case $\kappa|\nabla\phi|^2$, we formulate the gradient term for multiple phases $\alpha,\beta,\ldots N$ as

$$f_{\text{grad}}(\nabla\phi) = \frac{1}{2}\sum_{\alpha}\sum_{\beta}(\nabla\phi_\alpha : \kappa_{\alpha\beta} : \nabla\phi_\beta) \tag{3.3}$$

$$\overset{\text{isotropic}}{=} \frac{1}{2}\sum_{\alpha}\sum_{\beta}\kappa_{\alpha\beta}(\nabla\phi_\alpha \cdot \nabla\phi_\beta) \tag{3.4}$$

where $\kappa_{\alpha\beta}$ could be a tensor including directional dependence of interfacial energies. For isotropic systems, it reduces to a scalar $\kappa_{\alpha\beta}$. Note that there are various other ways to include anisotropic surface energies within phase-field formulations [153, 185]. Some model formulations only employ the main diagonal of the $\kappa_{\alpha\beta}$-matrix, i.e. $\kappa_{\alpha\beta} = 0, \forall\alpha \neq \beta$ which results in

$$f_{\text{grad}}(\nabla\phi) = \frac{1}{2}\sum_{\alpha}\kappa_\alpha|\nabla\phi_\alpha|^2. \tag{3.5}$$

This formulation carries the problem that for a number of phases $N > 3$ there are less parameters κ_α than possibly different pairwise interfacial energies $\gamma_{\alpha\beta}$ which leads to the alternative formulation based on interpolation of the pairwise parameters $\kappa_{\alpha\beta}$

$$f_{\text{grad}}^{\text{interpolate}}(\phi,\nabla\phi) = \frac{\tilde{\kappa}}{2}\sum_{\alpha}|\nabla\phi_\alpha|^2 \quad \text{where } \tilde{\kappa} = \frac{\sum\kappa_{\alpha\beta}h_{\alpha\beta}(\phi)}{\sum h_{\alpha\beta}(\phi)}. \tag{3.6}$$

A popular choice is $h_{\alpha\beta} = \phi_\alpha^2\phi_\beta^2$ [153, 178, 186], but generally the definition of an appropriate interpolation function can be challenging. Due to the interpolation, this formulation is not only a function of gradients $\nabla\phi_\alpha$ but also the ϕ_α-values. Alternatively, setting the main diagonal to zero $\kappa_{\alpha\alpha} = 0$ leads to a second set of frequently used gradient formulations [142]. As the interfacial energy $\gamma_{\alpha\beta}$

between two phases should be independent of the labeling of variables (see principle of formal indistinguishability [153]), we enforce symmetry $\kappa_{\alpha\beta} = \kappa_{\beta\alpha}$. The gradient term can thus be written as the summation over pairwise dot products

$$f_{\text{grad}}^{\text{dot}}(\nabla\phi) = -\sum_{\alpha}\sum_{\beta>\alpha}\kappa_{\alpha\beta}\nabla\phi_{\alpha}\cdot\nabla\phi_{\beta} \tag{3.7}$$

where the minus sign is introduced for convenience of the $\kappa_{\alpha\beta}$ fitting values. Note that the factor $1/2$ is consumed by assumption of symmetry and reduction to the upper right entries of the matrix ($\sum_{\beta>\alpha}$). Another formulation of the gradient term which has been used in works of Steinbach [123], Tiaden [159] and Nestler [124, 156]

$$f_{\text{grad}}^{\text{weighted}}(\phi,\nabla\phi) = \sum_{\alpha}\sum_{\beta>\alpha}\kappa_{\alpha\beta}|\phi_{\alpha}\nabla\phi_{\beta} - \phi_{\beta}\nabla\phi_{\alpha}|^2 \tag{3.8}$$

cannot be derived from the postulated Eq. (3.4) but is closely related to formulation Eq. (3.7) in the sense that terms are introduced as pairwise interactions with parameters $\kappa_{\alpha\beta}$. It includes a generalized gradient based on an antisymmetric weighting of the two gradients for each two-phase interface and traces back to the theory of irreducible representation (see Landau and Lifschitz [187]). An important feature that both equations 3.7 and 3.8 share is that the $\alpha\beta$ term vanishes in all other interfaces where one of the two phases is inactive ($\phi_{\alpha} = 0$ and $\nabla\phi_{\alpha} = 0$ or $\phi_{\beta} = 0$ and $\nabla\phi_{\beta} = 0$). This ensures that the interfacial energies are mutually decoupled, which simplifies the parameterization of the model. All the above mentioned formulations reduce to $\kappa|\nabla\phi_{\alpha}|^2$ in two-phase interfaces if $\phi_{\beta} = 1 - \phi_{\alpha}$ (which implies $\nabla\phi_{\beta} = -\nabla\phi_{\alpha}$) is fulfilled.

3.1.2 Potential energy formulations

The double-well and double-obstacle formulations which have typically been used for phase-field models with one parameter $f_{\text{well}}(\phi) = \Omega\phi^2(1-\phi)^2$ and $f_{\text{ob}}(\phi) = \Omega\phi(1-\phi)$ can be generalized intuitively in two possible ways. The first one is motivated by setting $\phi = \phi_\alpha$ and defining the second phase as $\phi_\beta = 1-\phi$ which results in

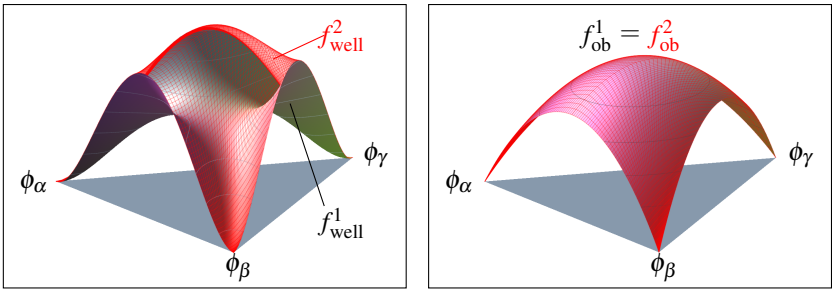
$$f^1_{\text{well}}(\phi) = \sum_\alpha \sum_{\beta>\alpha} \Omega_{\alpha\beta}\phi^2_\alpha\phi^2_\beta \quad \text{and} \quad f^1_{\text{ob}}(\phi) = \sum_\alpha \sum_{\beta>\alpha} \Omega_{\alpha\beta}\phi_\alpha\phi_\beta.$$

The second option is a summation over all occurring phases where we set $\phi = \phi_\alpha$ in the single phase terms

$$f^2_{\text{well}}(\phi) = \frac{1}{2}\sum_\alpha \Omega_\alpha\phi^2_\alpha(1-\phi_\alpha)^2 \quad \text{and} \quad f^2_{\text{ob}}(\phi) = \frac{1}{2}\sum_\alpha \Omega_\alpha\phi_\alpha(1-\phi_\alpha).$$

Other formulations are generally possible under the constraint that they naturally reduce to the double-well or obstacle potential within each two-phase interface to reproduce the physical interfacial energy $\gamma_{\alpha\beta}$ of each $\alpha\beta$-phase pair. This implicitly requires the additional criterion that two-phase interfaces should represent a stable equilibrium and thus be free of additional phases [153]. The occurrence of additional phases is often referred to as "spurious phases" or "ghost phases" as they are unphysical and alter the resulting interfacial energy. For a more detailed investigation of the above free energy formulations, a three-phase system is considered in the following paragraph.

As mentioned by Folch and Plapp [154], the visualization of the energy landscape over the Gibbs simplex of a triple junction (similar to a ternary diagram) is helpful to aquire geometric intuition. As we make use of the sum constraint $\sum\phi_\alpha = 1$ for parametrization, the energies shown in Fig. 3.1 are exact for multiphase-field models while differences can arise for multi-order parameter models. However, as the models discussed in this paper assume stable states of η at 0 and 1, most conclusions hold true for both classes of model formulations. By plotting the above formulations with the same value of Ω for all phases (or phase pairs),



(a) multi-well potential **(b)** multi-obstacle potential

Figure 3.1: Energetic landscape of the multi-well and multi-obstacle potentials shown for a three-phase system over the Gibbs simplex of a triple junction. Formulations f^1_{well} and f^1_{ob} are represented by surfaces with contour lines while f^2_{well} and f^2_{ob} are drawn by red wireframe plots.

we can immediately see that the first generalization of the multi-well potential exhibits a saddle at the triple point $\phi_\alpha = \phi_\beta = \phi_\gamma = 1/3$ while for the second approach, the energy of dual interphases is lower than anywhere in the triple phase region. For the obstacle potential, both formulations yield identical results and the energies of two-phase interfaces are generally lower than triple junctions. Differences will be discussed in more detail within the following subsections.

3.1.2.1 Multi-well energies

Throughout the phase-field community, several multi-phase extensions of the well-potential have been applied. Folch and Plapp [154] use formulation $f^2_{\text{well}}(\boldsymbol{\phi})$ for a ternary system. From Fig 3.1a, it is clear that formulation f^1_{well}, which is purely based on $\phi^2_\alpha \phi^2_\beta$ terms, suffers from low energy in the triple junction. As the three-phase case becomes energetically favorable compared to two-phase interfaces, models based on this approach suffer from ghost phases and distorted interfacial energies. Some multi-well formulations try to circumvent this issue by adding additional terms that penalize higher-order junctions through single

phase contributions that need to be constructed such that they reduce correctly in the two-phase case [153, 178]

$$f_{\text{well}}^{\text{Moelans}} = \tilde{\Omega}\left(\sum_{\alpha}\sum_{\beta>\alpha}\chi_{\alpha\beta}\phi_\alpha^2\phi_\beta^2 + \sum_{\alpha}\left(\frac{\phi_\alpha^4}{4} - \frac{\phi_\alpha^2}{2}\right) + \frac{1}{4}\right) \tag{3.9}$$

$$f_{\text{well}}^{\text{Toth}} = \tilde{\Omega}\left(\frac{1}{2}\sum_{\alpha}\sum_{\beta>\alpha}\phi_\alpha^2\phi_\beta^2 + \sum_{\alpha}\left(\frac{\phi_\alpha^4}{4} - \frac{\phi_\alpha^3}{3}\right) + \frac{1}{12}\right). \tag{3.10}$$

Alternatively, triple-phase terms can be added [177]

$$f_{\text{well}}^{\text{Garcke}} = \sum_{\alpha}\sum_{\beta>\alpha}\Omega_{\alpha\beta}\phi_\alpha^2\phi_\beta^2 + \sum_{\alpha}\sum_{\beta>\alpha}\sum_{\gamma>\beta}\Omega_{\alpha\beta\gamma}\phi_\alpha^2\phi_\beta^2\phi_\gamma^2 \tag{3.11}$$

to alter the triple junction energy. Other higher-order monomials have been used in works of Steinbach *et al.* [123] and Tiaden *et al.* [159]. The similarity between the potentials (3.10) and (3.9) is most apparent when both are written for a homogeneous system (as in ideal grain growth)

$$f_{\text{well}}^{\text{Moelans}} = \Omega\left(\chi^{\text{M}}\sum_{\alpha}\sum_{\beta>\alpha}\phi_\alpha^2\phi_\beta^2 + \sum_{\alpha}\left(\frac{\phi_\alpha^4}{4} - \frac{\phi_\alpha^2}{2}\right) + \frac{1}{4}\right) \tag{3.12}$$

$$f_{\text{well}}^{\text{Toth}} = \Omega\left(\chi^{\text{T}}\sum_{\alpha}\sum_{\beta>\alpha}\phi_\alpha^2\phi_\beta^2 + \sum_{\alpha}\left(\frac{\phi_\alpha^4}{4} - \frac{\phi_\alpha^3}{3}\right) + \frac{1}{12}\right). \tag{3.13}$$

The formulations only differ in the polynomial contributions, but interestingly, they reduce to the same expression in the two-phase interface such that the condition $\Omega(2\chi+1) = 2\Omega_{\text{ref}}$ should be fulfilled (see Appendix A). The parameter χ performs a weighting between the dual terms and single-phase monomials. Fig. 3.2 shows the energetic landscape over the triple junction for both formulations with constant Ω_{ref} but varying values of χ.

To predict the energy barrier and phase fractions in an interface between two phases, we compute the connecting minimum energy path (MEP) between global minima via the nudged elastic band method [188, 189]. Results are shown in

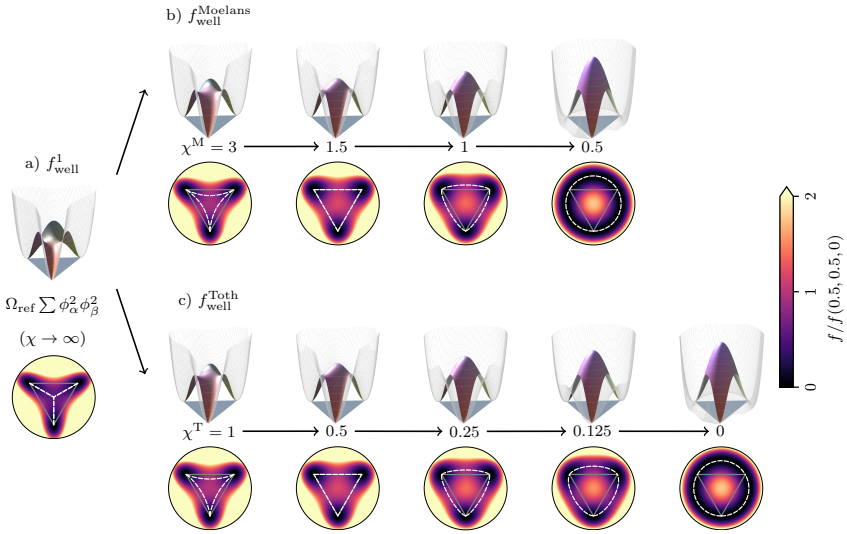


Figure 3.2: Multi-well formulations (3.12) and (3.13) drawn over the Gibbs simplex of a triple junction for different values of χ. Energy values inside the sum constraint are shown as colored surfaces with contour lines while values outside are shown by gray wireframe plots. The 2D-colorplots additionally show the minimum-energy path (MEP) between the bulk phases as a white dashed line. The MEP is calculated numerically using the nudged elastic band method [188, 189].

Fig. 3.2 as white dashed lines in the two-dimensional colorplots. Only for the special values of $\chi^{\text{M}} = 1.5$ and $\chi^{\text{T}} = 0.5$, the behavior of a two-phase system is reproduced. For other values of χ, we expect ghost phases as the minimum energy path involves nonzero values of a third phase. The illustration underlines that not only the values of the potential function within the Gibbs simplex constraint are relevant but also the position of the saddle point which defines the energetic barrier. The saddle point that separates α and β phases is located at $\phi_\alpha = \phi_\beta = (1-x)/2$ and $\phi_\gamma = x$, where x depends on the value of χ. In the limit of $\chi \to \infty$, both model formulations reduce to the binary terms in f_{well}^{1} and the saddle is located at $[1/3, 1/3, 1/3]$. Decreasing the value of χ leads to higher triple point energies until, eventually, two-phase interfaces become energetically favorable and thus a stable solution of the system. The two energy landscapes

are identical with formulation f_{well}^2 for the values $\chi^{\text{M}} = 1.5$ and $\chi^{\text{T}} = 0.5$. The saddle point lies on the two-phase interface at $[1/2, 1/2, 0]$ which makes these cases attractive in the sense that they are naturally bounded to the Gibbs simplex and make projection algorithms as discussed in Appendix B redundant. Formulation (3.12) has an infinite amount of stable solutions that lie on a circle around the Gibbs triangle for $\chi = 0.5$ [129] and, thus, is limited to $\chi \geq 0.5$. The formulation $f_{\text{well}}^{\text{Toth}}$ only reaches this limiting case asymptotically for $\chi \to 0$ which allows a wider range of input parameters. Note that for values smaller than 0.5, the saddle point is located at $x < 0$ which lowers the simulated interfacial energy for multi-order parameter models and, in the case of multi-phase field models, needs explicit handling of the Gibbs simplex constraint.

Hence, it seems beneficial to limit the value χ to a small range of values around 1.5 for Eq. (3.12) and 0.5 for Eq. (3.13), respectively, to reach the desired features of multi-well formulations. Moelans *et al.* studied the influence of χ^{M} (there called *overlap parameter*) on the shape of equilibrium phase field profiles and the interfacial energy in two-phase interfaces in more detail in the context of MOP models [178]. If interfacial energies are pair-wise different, this inhomogeneity can be introduced in Eqs. (3.12) and (3.13) either via the potential barrier height $\tilde{\Omega} = (\sum_\alpha \sum_{\beta>\alpha} \Omega_{\alpha\beta} \phi_\alpha^2 \phi_\beta^2)/(\sum_\alpha \sum_{\beta>\alpha} \phi_\alpha^2 \phi_\beta^2)$ or via the weighting parameter $\tilde{\chi} = (\sum_\alpha \sum_{\beta>\alpha} \chi_{\alpha\beta} \phi_\alpha^2 \phi_\beta^2)/(\sum_\alpha \sum_{\beta>\alpha} \phi_\alpha^2 \phi_\beta^2)$. Implications of these two choices are discussed in [178].

The third formulation Eq. (3.11) raises the energy in the triple junction, but only in the limit of $\Omega_{\alpha\beta\gamma} \to \infty$ are two-phase interfaces energetically favorable. For finite values of $\Omega_{\alpha\beta\gamma}$, a small fraction of ghost phases remains as can be observed from the simulations in Sec. 3.2. An additional problem with the triplet terms $\Omega_{\alpha\beta\gamma}\phi_\alpha^2\phi_\beta^2\phi_\gamma^2$ is the great number of numerical fitting parameters that results from many phase variables N as it scales with $\propto N^3$. Furthermore, these numerical parameters might cause issues in applications that employ heterogeneous nucleation mechanisms (e.g. martensitic transformations [140] or battery materials [110]) as they crucially influence the nucleation barriers of new phases within existing interfaces.

3.1.2.2 Multi-obstacle energies

In the case of the obstacle potential, both generalizations shown in Fig. 3.1b are identical which traces back to the re-formulation

$$\frac{1}{2}\sum_{\alpha}\Omega\phi_\alpha(1-\phi_\alpha) = \frac{1}{2}\sum_{\alpha}\Omega\phi_\alpha\sum_{\beta\neq\alpha}\phi_\beta = \Omega\sum_{\alpha}\sum_{\beta>\alpha}\phi_\alpha\phi_\beta.$$

This generally holds as long as Ω is identical for all phase-pairs. Formulation f_{ob}^2 suffers from the problem that there are less parameters Ω_α than possible phase-pairs for $N > 3$ which is why we restrict all following simulation examples including the obstacle potential to

$$f_{\mathrm{ob}}(\boldsymbol{\phi}) = \sum_{\alpha}\sum_{\beta>\alpha}\Omega_{\alpha\beta}\phi_\alpha\phi_\beta \tag{3.14}$$

which has been extensively used in works from the groups of Steinbach [142] and Nestler [124].

3.1.3 Multiphase-field evolution equations

The phase evolution equation (2.15) reduces to Eq. (2.14) in the absence of bulk driving forces. Therefore, we employ the sum over binary interactions as introduced by Steinbach and Pezolla [142]

$$\frac{\partial\phi_\alpha}{\partial t} = -\frac{1}{\tilde{N}\varepsilon}\sum_{\beta\neq\alpha}^{\tilde{N}}M_{\alpha\beta}\left(\frac{\delta f}{\delta\phi_\alpha}-\frac{\delta f}{\delta\phi_\beta}\right) \tag{3.15}$$

in this chapter. The criterion, $0 \leq \phi_\alpha$ from the Gibbs simplex constraint (2.12), is either fulfilled by construction of the energetic landscape [154] as discussed in Fig. 3.2 or needs to be enforced explicitly via algebraic constraints or projection schemes as discussed in Appendix B.

The interfacial energy terms in MPF formulations are typically formulated as the summation of binary terms which, in combination with the two-phase interface solutions from A.2, allows for re-formulation of simulation parameters. The replacement of $\kappa_{\alpha\beta} = \varepsilon\gamma_{\alpha\beta}$ and $\Omega_{\alpha\beta} = K\gamma_{\alpha\beta}/\varepsilon$ leads to an effective decoupling of interfacial energy and width which allows to keep the width of the diffuse interface constant throughout all phase pairs [124].

In this work we employ and compare the formulations

$$f_{\text{well}}^{\text{Moelans}} = \frac{9}{\varepsilon}\sum_{\alpha}\sum_{\beta>\alpha}\frac{3\gamma_{\alpha\beta}}{4}\phi_\alpha^2\phi_\beta^2 + \frac{9}{2\varepsilon}\tilde{\gamma}\left(\frac{1}{4}+\sum_{\alpha}\left(\frac{\phi_\alpha^4}{4}-\frac{\phi_\alpha^2}{2}\right)\right) \tag{3.16}$$

$$f_{\text{well}}^{\text{Toth}} = \frac{9}{\varepsilon}\sum_{\alpha}\sum_{\beta>\alpha}\frac{\gamma_{\alpha\beta}}{2}\phi_\alpha^2\phi_\beta^2 + \frac{9}{\varepsilon}\tilde{\gamma}\left(\frac{1}{12}+\sum_{\alpha}\left(\frac{\phi_\alpha^4}{4}-\frac{\phi_\alpha^3}{3}\right)\right) \tag{3.17}$$

$$f_{\text{well}}^{\text{Garcke}} = \frac{9}{\varepsilon}\sum_{\alpha}\sum_{\beta>\alpha}\gamma_{\alpha\beta}\phi_\alpha^2\phi_\beta^2 + \frac{9}{\varepsilon}\sum_{\alpha}\sum_{\beta>\alpha}\sum_{\gamma>\beta}\gamma_{\alpha\beta\gamma}\phi_\alpha^2\phi_\beta^2\phi_\gamma^2 \tag{3.18}$$

$$f_{\text{ob}} = \frac{16}{\varepsilon\pi^2}\sum_{\alpha}\sum_{\beta>\alpha}\gamma_{\alpha\beta}\phi_\alpha\phi_\beta \tag{3.19}$$

where the prefactors $K = 9$ for the multi-well and $K = 16/\pi^2$ for the multi-obstacle formulation ensure that the parameter $\gamma_{\alpha\beta}$ corresponds to the physical interfacial energy of the α-β phase pair. The interpolated value $\tilde{\gamma}$ is given by $\tilde{\gamma} = (\sum_\alpha\sum_{\beta>\alpha}\gamma_{\alpha\beta}\phi_\alpha^2\phi_\beta^2)/(\sum_\alpha\sum_{\beta>\alpha}\phi_\alpha^2\phi_\beta^2)$. Eq. (3.16)-(3.19) will be studied in combination with the two gradient formulations Eq. (3.7) and (3.8). The factors in Eqs. (3.16) and (3.17) are chosen such that in every two-phase interface $\chi^{\text{M}} = 1.5$ and $\chi^{\text{T}} = 0.5$ are fulfilled.

3.2 Simulation studies

3.2.1 Simulation setup

For our benchmark problem, we start with physical values in the order of typical microstructure simulations listed in Table 3.1 and make them non-dimensional, as would be common practice for any application to a specific material system. Three reference quantities are applied to de-dimensionalize the problem, namely the reference time $t_{\mathrm{ref}} = 100\,\mathrm{s}$, length $x_{\mathrm{ref}} = 1\,\mu\mathrm{m} = 10^{-6}\,\mathrm{m}$ and energy $\Omega_{\mathrm{ref}} = 10^6\,\mathrm{J/m^3}$, which yields

$$\tilde{W} = \frac{W}{x_{\mathrm{ref}}}, \quad \tilde{\gamma}_{\alpha\beta} = \frac{\gamma_{\alpha\beta}}{\Omega_{\mathrm{ref}} x_{\mathrm{ref}}} \quad \text{and} \quad \tilde{M} = M \frac{\Omega_{\mathrm{ref}} t_{\mathrm{ref}}}{x_{\mathrm{ref}}}. \tag{3.20}$$

Note that the choice of parameters is somewhat arbitrary and the simulation results could be re-scaled differently by changing the reference values.

The initial conditions of the problem are identical for the two following subproblems and can be summarized as follows: We start with initially sharp interfaces and fill $0 \leq x \leq W$ and $80 < y \leq 100$ with $\phi_0 = 1$ and, furthermore, $0 \leq x \leq W/2$ and $0 \leq y \leq 80$ with $\phi_\alpha = 1$ and the other half $W/2 < x \leq W, 0 \leq y \leq 80$ with $\phi_\beta = 1$. The respective other phases are equal to zero. A similar validation example has been used in [190]. For all cases, we employ Neumann boundary conditions (BCs) $\nabla\phi_\alpha \cdot \vec{n} = 0$, $\forall\alpha$ at the top and bottom of the domain. At the left and right domain boundary

- Dirichlet BCs are used for sub-problem (1) according to the initial setup, i.e. phase boundaries are pinned at $[0, 80]$ and $[W, 80]$;
- Neumann BCs with $\nabla\phi_\alpha \cdot \vec{n} = 0$, $\forall\alpha$ are used for subproblem (2) which in this case reflects mirror symmetry. Alternatively, the domain length can be doubled to $2W$ in combination with periodic BCs.

All simulations are conducted using codes based on finite difference stencils and an explicit Euler time-stepping. MPF simulations were performed using

Table 3.1: Set of simulation parameters

Parameter	Symbol	Physical value	Nondimensional
Width of domain	W	$100\,\mu$m	100
Height of domain	H	$[100,\ldots,400]\,\mu$m	[100,...,400]
Spatial resolution	Δx	$W/$cells	1
Interfacial energy	$\gamma_{\alpha 0} = \gamma_{\beta 0} = \gamma_0$	$1.0\,\mathrm{J/m^2}$	1.0
	$\gamma_{\alpha\beta}$	$[0.1,\ldots,2.0]\,\mathrm{J/m^2}$	[0.01,2.0]
Mobility	$M_{\alpha 0} = M_{\beta 0}$	$10^{-14}\,\mathrm{m^4/(Js)}$	1
	$M_{\alpha\beta}$	$10^{-14}\,\mathrm{m^4/(Js)}$	1

PACE3D [155, 156] which is an in-house code. Furthermore, all the models (MOP as well as MPF) were implemented for the specific case of three phases in MATLAB together with the necessary post-processing tools to acquire the metrics presented in the following sections. The MATLAB code has been made publicly available [191].

3.2.2 Static triple junction

The first benchmark case employed in this work is a triple junction that reaches a static equilibrium as sketched in Fig. 3.3. Below, the metrics for quantitative comparison of the various model formulations with the analytical considerations [126, Sec. 3.1] are defined:

- The **total interfacial energy** is computed as the energy density integral over the simulation domain, and its total value is compared to the sharp interface solution
  $E_{\mathrm{total}} = l_{\alpha\beta}\gamma_{\alpha\beta} + 2l_0\gamma_0 = W\left(\frac{H}{W}\gamma_{\alpha\beta} + \sqrt{\gamma_0^2 - \frac{\gamma_{\alpha\beta}^2}{4}}\right)$ [126, Eq. 34].
  Convergence to equilibrium state is quantified by the relative energy change over time $\varepsilon = |\mathscr{F}^n - \mathscr{F}^{n-1}|/\mathscr{F}^n$ and all the simulations presented are below a threshold of $\varepsilon = 10^{-5}$;

- The **dihedral angle** θ of the triple junction is computed from the position of the triple point $\theta = 2\arctan\left(W/2h_{\mathrm{GB}}\right)$ [126, Eq. 30] and compared with the analytical solution from Young's law $\theta = \theta_{\alpha\beta} = 2\arccos\left(\frac{\gamma_{\alpha\beta}}{2\gamma_0}\right)$ [126, Eq. 29]. The numerical triple point is defined as the intersection of isolines $\phi_0 = \phi_\alpha$ and $\phi_0 = \phi_\beta$;
- Spurious occurance of ϕ_α, ϕ_β and ϕ_0 in the respective other two-phase interface is quantified as the **maximum value of the phase** as shown in Fig. 3.3.

As the domain height H limits the range of observable triple junction angles, we conduct simulation studies with $H = 100$ and $H = 200$. The results are equal within the applicable range of $\gamma_{\alpha\beta}$ values. The temporal evolution towards equilibrium is shown exemplarily in Fig. 3.3.

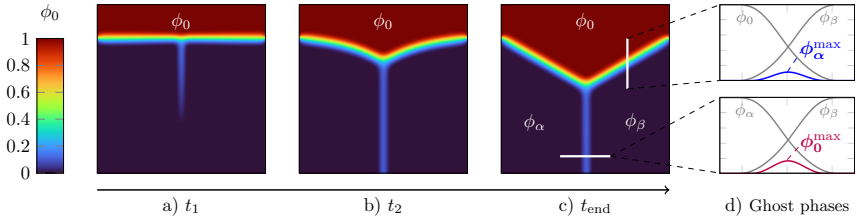


Figure 3.3: Evolution of phase ϕ_0 towards static equilibrium shown exemplarily for $\gamma_{\alpha\beta} = \gamma_0$ and domain size 100×100. Subfigures show a) state close to the initial conditions, b) an in-between state and c) the final state in equilibrium. Spurious phases are quantified by occurance in the respective other two-phase interface as sketched by linescans in c) and the detailed plots in d).

An overview of model combinations employed in this work with references to the original works is given in Table 3.2.

For the multiphase-field method, we compare the eight possible combinations of the gradient formulations Eq. (3.7) and (3.8) and the potentials Eq. (3.16)-(3.19). The numerical parameter ε scales the width of the diffuse interface and is set to 5, which corresponds to $10-12$ grid points within the diffuse interface region. To check the influence of ε with regard to the overall domain width W, a

Table 3.2: Overview of MPF model combinations employed in this work with references to original works. All new combinations are marked as such.

	$f_{\text{well}}^{\text{Moelans}}$	$f_{\text{well}}^{\text{Toth}}$ *	$f_{\text{well}}^{\text{Garcke}}$	f_{obstacle}
$f_{\text{grad}}^{\text{dot}}$ Eq. (3.7)	new	new	new	[142, 158]
$f_{\text{grad}}^{\text{weighted}}$ Eq. (3.8)	new	new	[124, 177]	[124, 177]

* In the original work [153], this potential term has been combined with the gradient term $f_{\text{grad}}^{\text{interpolate}}$ within the MPF framework. This combination is not covered within this paper.

comparative study has been carried out with a grid resolution of 0.5 which corresponds to a 200×400 grid and $\varepsilon = 2.5$. The differences in total energy and dihedral angle were found to be below 1%. The results in Fig. 3.4 clearly show that the deviations of the dihedral angle and total free energy from the analytic solutions are directly linked to the occurrence of spurious phases. Generally, all combinations including the gradient term $f_{\text{grad}}^{\text{weighted}}$ (denoted by circular markers) show larger deviation from the analytical solutions and higher fractions of ghost phases. We conclude that the driving force resulting from the functional derivative of Eq. (3.8) is one possible source of spurious phase generation. Furthermore, it should be noted that the implementation of the functional derivative of $f_{\text{grad}}^{\text{weighted}}$ contains about 20 times more arithmetic operations, thus resulting in simulation times that are significantly longer than the equivalent potential term combined with the gradient formulation $f_{\text{grad}}^{\text{dot}}$.

As discussed in Sec. 3.1.2, the potential formulation $f_{\text{well}}^{\text{Garcke}}$ tends to energetically favor triple phase regions over two-phase interphases which results in spurious phases and a deviation from the analytical solutions. The fraction of ghost phases can be reduced by increasing the numerical parameter $\Omega_{\alpha\beta\gamma}$ which scales the triplet energy contribution. The parameter study in Fig. 3.5 shows that for small values of $\Omega_{\alpha\beta\gamma}$, a high fraction of spurious phases distorts the equilibrium solutions. Very high values of $\Omega_{\alpha\beta\gamma}$ result in numerical pinning (i.e. the triple junction does not move) such that the resulting dihedral angle is $\approx 180^\circ$ for all $\gamma_{\alpha\beta} \in [0,2]$. For this benchmark, we found that a value of $\Omega_{\alpha\beta\gamma} = 100\,\Omega_{\alpha\beta}$ yields the best solution (see results Fig. 3.5). Nevertheless, the combination of $f_{\text{grad}}^{\text{dot}}$ and

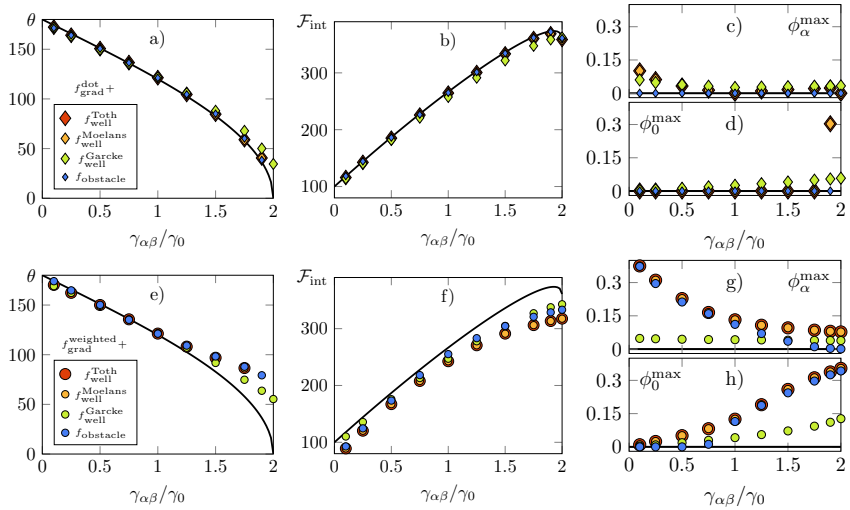


Figure 3.4: MPF comparison of metrics for the static triple junction with 100×200 domain size. Combinations including $f_{\text{grad}}^{\text{dot}}$ are marked by diamonds and shown in a)-d) while $f_{\text{grad}}^{\text{weighted}}$ is denoted by circles in subfigures e)-h). The potential terms are color coded as indicated by the legend ($f_{\text{well}}^{\text{Toth}}$=red,$f_{\text{well}}^{\text{Moelans}}$=orange,$f_{\text{well}}^{\text{Garcke}}$=green,$f_{\text{obstacle}}$=blue). Analytical solutions are shown as black lines.

$f_{\text{well}}^{\text{Garcke}}$ generally exhibits larger deviation from the analytical solution than combination with the other two potential terms. This can be traced back to the higher amount of spurious phases resulting from the potential term. Only three combinations effectively suppress spurious phases over a large range of $\gamma_{\alpha\beta}/\gamma_0$-ratios, namely the gradient term $f_{\text{grad}}^{\text{dot}}$ in combination with the well potentials $f_{\text{well}}^{\text{Toth}}$ and $f_{\text{well}}^{\text{Moelans}}$ or with the obstacle potential f_{obstacle}. Consequently, these are also the only three combinations which correctly capture de-wetting of the α and β phase for $\gamma_{\alpha\beta}/\gamma_0 = 2$. Results obtained from $f_{\text{well}}^{\text{Toth}}$ and $f_{\text{well}}^{\text{Moelans}}$ differ less than 1% due to the fact that for $\chi^{\text{T}} = 0.5$ and $\chi^{\text{M}} = 1.5$ the energetic landscapes are identical.

There are many works that employ the second gradient formulation $f_{\text{grad}}^{\text{weighted}}$ in combination with a modified obstacle potential [124, 135, 190]. Similarly to the study in Fig. 3.5, a triplet term $\Omega_{\alpha\beta\gamma}\phi_\alpha\phi_\beta\phi_\gamma$ can be introduced to counteract the spurious phases generated from the functional derivative of the gradient term.

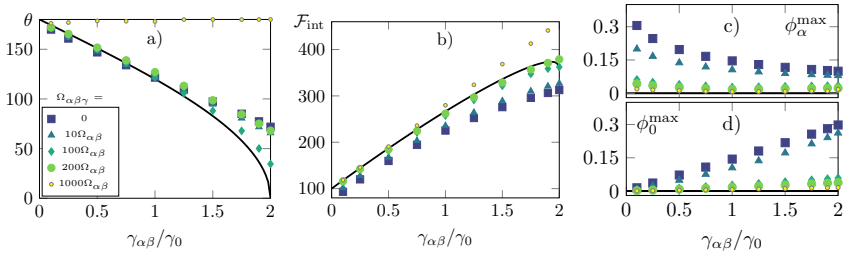


Figure 3.5: Influence of numerical parameter $\Omega_{\alpha\beta\gamma}$ in $f_{\text{well}}^{\text{Garcke}}$ (Eq. (3.11)) on spurious phase generation and model error. Simulations were performed employing $f_{\text{grad}}^{\text{dot}}$. Analytical solutions are shown as black lines.

The publication by Hötzer *et al.* [190] is dedicated to the calibration of the numerical parameter $\Omega_{\alpha\beta\gamma}$, in which the authors conclude that, first of all, it largely influences the equilibrium contact angles and, secondly, strongly depends on the specific pair-wise interfacial energies in every triple junction. This, together with the fact that for many phases N there could theoretically be $\propto N^3$ fitting parameters $\Omega_{\alpha\beta\gamma}$, makes this approach very complicated and numerically inefficient. Note that the initial problem is the occurance of spurious phases which can more efficiently be addressed by replacing $f_{\text{grad}}^{\text{weighted}}$ with $f_{\text{grad}}^{\text{dot}}$.

3.2.3 Steady-state motion of a triple junction

The second benchmark is a triple junction in steady-state motion which results from the first benchmark with modified BCs on the left and right boundary as sketched in Fig. 3.6.

The relevant metrics for quantitative comparison are:

- The **dihedral angle** is computed from the height of the profile h_{GB} using the analytic expression (3.21). h_{GB} is measured as the distance between the interface position at the left boundary $y_{\phi_0=\phi_\alpha}^{x=0}$ (or right boundary as the problem setup is symmetric) and the y-coordinate of the triple point.

Convergence to steady-state is quantified by the temporal change of the profile height with respect to the domain width $\varepsilon = |h_{\mathrm{GB}}^{n} - h_{\mathrm{GB}}^{n-1}|/W$;

- The **velocity** is measured as the temporal change of the y-coordinate of the interface at the left boundary $V = |(y_{\phi_0=\phi_\alpha}^{x=0})^{n} - (y_{\phi_0=\phi_\alpha}^{x=0})^{n-1}|/\Delta t$;
- The **(mis-)match of numerical results for the grain boundary geometry** with regard to the analytical solution (Eq. (3.23)) is quantified by a relative error measure introduced by the L^2-norm as
  $\mathrm{L2} = \|y_{\mathrm{numeric}} - y_{\mathrm{analytic}}\|_2 = \frac{1}{W}\sqrt{\frac{1}{N}\sum_{i=1}^{N}(y_i^{\mathrm{numeric}} - y_i^{\mathrm{analytic}})^2}$
  where y_{numeric} and y_{analytic} are both discrete representations evaluated at the same nodes in x-direction. The reference for the y-values of the GB profile is set to zero at the left and right boundary, i.e. $y_{\phi_0=\phi_\alpha}^{x=0} = 0$.

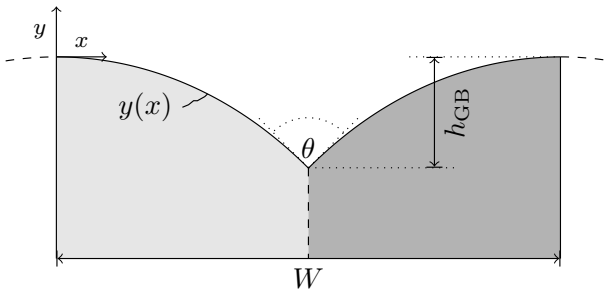


Figure 3.6: Steady-state triple junction

The dihedral angle can again be expressed in terms of the surface energy ratio $\gamma_{\alpha\beta}/\gamma_0$ or the grain boundary profile height $h_{\mathrm{GB}} = y_{\phi_0=\phi_\alpha}(x=0) - y_{\mathrm{TP}}$[2]

$$\text{analytical: } \theta = 2\arccos\left(\frac{\gamma_{\alpha\beta}}{2\gamma_0}\right), \quad \text{numerical: } \frac{h_{\mathrm{GB}}}{W} = \frac{\ln(\sin(\theta/2))}{\theta - \pi}. \tag{3.21}$$

[2] Detailed analytical considerations are given in [126, Sec. 3.1]

Note that in order to obtain the numerical solution for θ from the triple point position, the implicit expression above needs to be solved using Newton iterations [126]. The analytical steady-state velocity can be expressed in terms of the surface energy ratio $\gamma_{\alpha\beta}/\gamma_0$ as

$$V = \frac{M_0\gamma_0}{W}\left(\pi - 2\arccos\left(\frac{\gamma_{\alpha\beta}}{2\gamma_0}\right)\right). \tag{3.22}$$

The analytical solution of the grain boundary geometry is given by

$$y(x) = \begin{cases} \frac{W}{\pi-\theta}\ln\left(\cos\left(\frac{\pi-\theta}{W}x\right)\right) & 0 \le x < 0.5 \\ \frac{W}{\pi-\theta}\ln\left(\cos\left(\frac{\pi-\theta}{W}(x-W)\right)\right) & 0.5 \le x \le 1\,. \end{cases} \tag{3.23}$$

On the MPF side, we compare four model variants, namely all four potential terms Eqs. (3.16)-(3.19) in combination with $f_{\text{grad}}^{\text{dot}}$. At this point we exclude the other gradient term $f_{\text{grad}}^{\text{weighted}}$ due to the previous results. Similar to the previous benchmark, the well-potential $f_{\text{well}}^{\text{Garcke}}$ shows the largest deviation from the analytical solution due to appearance of spurious phases (see Fig. 3.7).

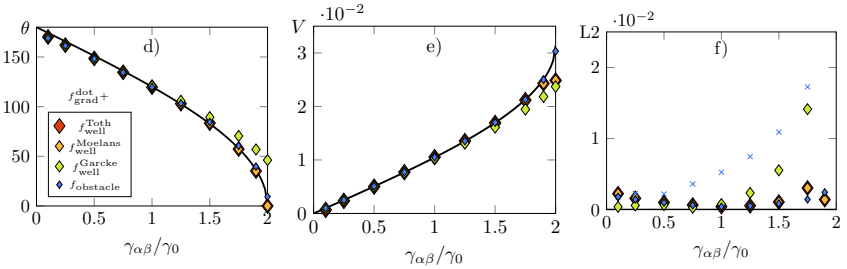


Figure 3.7: MPF comparison of metrics for the steady-state triple junction. The potential terms are color coded as indicated by the legend ($f_{\text{well}}^{\text{Toth}}$=red, $f_{\text{well}}^{\text{Moelans}}$=orange, $f_{\text{well}}^{\text{Garcke}}$=blue, f_{obstacle}=green). All MPF simulations are done in combination with the gradient term $f_{\text{grad}}^{\text{dot}}$. Analytical solutions are shown as black lines.

Furthermore, the triplet term scaled by $\Omega_{\alpha\beta\gamma}$ exhibits a drag force on the triple junction as discussed by Eiken [184]. As discussed before, large values of $\Omega_{\alpha\beta\gamma}$ (yellow dots in Fig. 3.5) lead to pinning of the triple junction which is the extreme case of this drag effect. The other three model combinations yield a close match with the analytical solutions. One peculiarity of the obstacle potential can be seen in the L2-norm results in Fig. 3.7. Due to the finite interface width, the choice of $\varepsilon = 5\Delta x$ can lead to 12 or 13 grid points within the diffuse interface where the second is slightly favorable energetically. This leads to a symmetry breaking force and the x-position of the TP tends to stabilize at 49.5 or 50.5. This numerical issue can be circumvented if ε is chosen such that the interface width to Δx ratio corresponds to an integer, e.g. $\varepsilon = 4 \cdot 12\Delta x/\pi^2 \approx 4.8634\Delta x$. The results for the dihedral angle and velocity are almost identical but the L2-norm differs drastically due to the shift in GB geometry. To illustrate the effect we plot results obtained with $\varepsilon = 4.8634\Delta x$ as blue diamonds and $\varepsilon = 5\Delta x$ using blue crosses.

3.3 Discussion

The systematic combination of various gradient and potential formulations yields new insights into the influence on generation of spurious phases which we identify as the main source for model error. The proposed benchmark is simple enough to be highly reproducible and yet captures most critical aspects of capillary effects in multi-phase systems. Possible sources for ghost phases can come from both the gradient and potential energy contribution and are unraveled by systematic combination of these terms. For the MPF models, the studies reveal that $f_{\text{grad}}^{\text{weighted}}$ generally performs worse than $f_{\text{grad}}^{\text{dot}}$ as it introduces an additional source of spurious phases. The two well-potentials $f_{\text{pot}}^{\text{Toth}}$ and $f_{\text{pot}}^{\text{Moelans}}$ yield almost the same results and, overall, coincide with analytical solutions. The third well-potential $f_{\text{pot}}^{\text{Garcke}}$ leads to a higher fraction of ghost phases and, thus, deviates more strongly from the reference solution. The obstacle potential results in a close match with analytical solutions and, in our case, comes with an advantage

in computational efficiency. The first reason for this is the simple form of the respective variational derivative and, secondly, as the equilibrium profile is given by a sinus function, the interface has a finite width and computation of phase evolution can be reduced to cells that exhibit a spatial gradient in phase-field values. Note that this computational advantage cannot be generalized because computational efficiency results from a complex interplay of numerical implementation, time stepping and the inclusion of the Gibbs simplex constraint.«

In the context of polycrystalline battery materials, the phase-field variables are used to parametrize grains with different orientations as well as various phases within these grains that differ in stoichiometry or their respective crystal lattice. As grain boundary energies differ strongly from interfacial energies between coherent phases, the model should be capable of correctly reproducing high ratios of $\gamma_{\alpha\beta}/\gamma_0$. Furthermore, the dynamics of grain boundaries and phase transformations within the grains take place on different time scales. At room temperature, the secondary particle morphology is conserved (unless fracture is modelled) i.e. the mobility of grain boundaries is approximately equal to zero. First and second order phase transformations of the host material, on the other hand, are on the timescale of ion mobility in the electrode material. The phase evolution equation (2.15) can correctly model systems with strongly varying interfacial mobilities as long as there are no spurious phases in binary interfaces and multijunctions. The presence of spurious phases alters the effective interfacial mobility and will, most likely, lead to an unphysical grain coarsening in the particle microstructures under investigation.

Based on this benchmark case, the interfacial energy contributions (2.4) and (2.5) were chosen in combination with the phase evolution equation (2.15).

4 Phase nucleation driven by chemical forces[1]

In continuation of the validation of interfacial energy contributions in the previous chapter, I now want to elucidate the interplay of chemical and interfacial forces. In the context of battery materials, it is necessary to investigate, first, if phase nucleation induced by the intercalation of ions can be modelled and, secondly, if a moving phase transformation front is correctly reproduced. For this reason, a stability analysis is performed to characterize the nucleation behaviour in the bulk and at grain boundaries and, subsequently, the model is tested for an exemplary polycrystalline cathode material.

4.1 Free energy landscape

»The bulk energy term is expressed as the interpolation of phase-dependent chemical free energy contributions

$$f_{\text{chem}}(\boldsymbol{\phi}, \boldsymbol{c}) = \sum_{\alpha}^{N} f_{\text{chem}}^{\alpha}(\boldsymbol{c}^{\alpha}) h^{\alpha}(\boldsymbol{\phi}), \tag{4.1}$$

[1] The content of this chapter is based on the article Daubner *et al.* [110]. Sections that are taken verbatim from the publication have been marked. While the original article includes a comparison with the Cahn-Hilliard model, only the parts that are specific to multiphase-field models are included in this dissertation. The MPF model in the publication differs slightly from the model presented in Chapter 2 in terms of interpolation functions (compare Eq. (2.6) and (4.1)).

where each f^α depends on a local phase dependent composition $\boldsymbol{c}^\alpha$ which is given as molar fraction. The mean compositions are defined by interpolation $c_i = \sum_\alpha^N c_i^\alpha h^\alpha(\phi)$ which follows from interpolation of chemical energies [145] and fulfill the constraint $\sum_i^K c_i = 1$. The formulation of interpolation functions $h^\alpha(\phi)$ poses a problem with thermodynamical consistency at multiple junctions. Following [167], we introduce normalised interpolation functions

$$h^\alpha(\phi) := \frac{h(\phi_\alpha)}{\sum_\beta h(\phi_\beta)}, \tag{4.2}$$

$$h_{\text{well}}(\phi_\alpha) = \phi_\alpha^2(3-2\phi_\alpha) \tag{4.3}$$

$$h_{\text{ob}}(\phi_\alpha) = \frac{1}{2} + \frac{2}{\pi}\left((2\phi_\alpha - 1)\sqrt{\phi_\alpha(1-\phi_\alpha)} + \frac{1}{2}\arcsin(2\phi_\alpha - 1)\right) \tag{4.4}$$

and adjust our choice to the potential formulation to ensure correct kinetics of the traveling wave solution in the dual-phase case [143]. More detailed discussion of interpolation functions in the multiphase context can be found in [186].

The chemical free energies f^α can be fitted by incorporation of CALPHAD data. In this work we use a quadratic fitting for numerical efficiency and furthermore to fulfill the invertibility criterion used for the derivation of the grand-potential model [145]. The chemical energy of each component in phase α is formulated dependent on the phase-dependent mole fraction c_i^α of species i and three fitting parameters A_i^α, B_i^α and $c_{i,\min}^\alpha$. The free energy of phase α can then be expressed as the sum over all species contributions«

$$f_{\text{chem}}^\alpha(\boldsymbol{c}^\alpha) = \sum_i^K A_i^\alpha \left(c_i^\alpha - c_{i,\min}^\alpha\right)^2 + B_i^\alpha. \tag{4.5}$$

The repulsive species interaction that leads to a miscibility gap is imposed by the potential energy. This term can be interpreted as an additional phase-mixture contribution which represents the activation energy to be overcome for the phase transformation [192]. For a dual interface this can be written as

$$f^{\alpha\beta} = f_{\text{chem}}^\alpha(c^\alpha)h^\alpha(\phi) + f_{\text{chem}}^\beta(c^\beta)\left(1-h^\alpha(\phi)\right) + \Delta f_{\text{mixing}}^{\alpha\beta} \tag{4.6}$$

with the phase-mixture contribution $\Delta f^{\alpha\beta}_{\text{mixing}} = f_{\text{well}}$ or f_{ob} (see two-phase energies in Appendix A.1). More generally, the homogenous free energy landscape is given by the sum $f_{\text{chem}} + f_{\text{pot}}$ which is a function of phase variables and phase-dependent concentrations or, in the case of the grand canonical potential, a function of phase variables and the chemical potential μ [145]. In the following only one diffusing species with mole fraction c is considered.

4.2 Stability analysis in a two-phase system

»The phase-dependent mole fractions in the diffuse interface are linked by the assumption of equal phase diffusion potentials for all phases [193] which yields

$$\mu = \frac{\partial f^{\alpha}}{\partial c^{\alpha}} = \frac{\partial f^{\beta}}{\partial c^{\beta}} = \frac{\partial f_{\text{chem}}}{\partial c}. \tag{4.7}$$

From Eq. (4.5) and (4.7) we get the equality $2A^{\alpha}(c^{\alpha} - c^{\alpha}_{\text{min}}) = 2A^{\beta}(c^{\beta} - c^{\beta}_{\text{min}})$. Furthermore, applying the relation $c = c^{\alpha}h(\phi) + c^{\beta}h(1-\phi)$ for the mean concentration which can be derived from the interpolation of chemical energy densities (4.1) [145], we express the phase-dependent chemical energy density Eq. (4.5) in terms of variables c, ϕ

$$f^{\alpha}_{\text{chem}}(c,\phi) = A^{\alpha}\left(\frac{c - \left(c^{\alpha}_{\text{min}}h(\phi) + c^{\beta}_{\text{min}}h(1-\phi)\right)}{h(\phi) + \frac{A^{\alpha}}{A^{\beta}}h(1-\phi)}\right)^2 + B^{\alpha}. \tag{4.8}$$

By inserting Eq. (4.8) into Eq. (4.1) and using the symmetry of interpolation function $h(1-\phi) = 1 - h(\phi)$, the free-energy density is expressed as

$$\begin{aligned} f_{\text{chem}}(c,\phi) = &\frac{A^{\alpha}A^{\beta}\left(c - \left[c^{\alpha}_{\text{min}}h(\phi) + c^{\beta}_{\text{min}}(1-h(\phi))\right]\right)^2}{A^{\beta}h(\phi) + A^{\alpha}(1-h(\phi))} \\ &+ \left(B^{\alpha} - B^{\beta}\right)h(\phi) + B^{\beta}. \end{aligned} \tag{4.9}$$

Without loss of generality, we set the reference of energy level to $B^\beta = 0$ and rename $B^\alpha = B$. By introducing the term $c_{\min}(\phi) = \left[c^\alpha_{\min} h(\phi) + c^\beta_{\min}(1-h(\phi))\right]$ and assuming a simplified system with $A^\alpha = A^\beta = A$ the free-energy density takes the form

$$f_{\text{chem}}(c,\phi) = A[c - c_{\min}(\phi)]^2 + Bh(\phi). \tag{4.10}$$

To investigate the stability, we first need to examine the stationary solutions of the given system of evolution equations in the two phase case

$$\varepsilon\dot{\phi} = -M\left(\frac{\delta\mathscr{F}}{\delta\phi}\right), \qquad \frac{\partial c}{\partial t} = \nabla\cdot\left(D(\phi)\nabla\left(\frac{\delta\mathscr{F}}{\delta c}\right)\right). \tag{4.11}$$

The coupled system of equations is then given by

$$\begin{bmatrix}\dot{\phi}\\ \dot{c}\end{bmatrix} = \begin{bmatrix}\frac{M}{\varepsilon}\left(2\varepsilon\gamma_{\alpha\beta}\nabla^2\phi - \frac{\partial f_{\text{pot}}}{\partial\phi} + (2A\Delta c_{\min}(c - c_{\min}(\phi)) - B)\frac{\partial h}{\partial\phi}\right)\\ D\left(\nabla^2 c - \Delta c_{\min}\frac{\partial h}{\partial\phi}\nabla^2\phi - \Delta c_{\min}\frac{\partial^2 h}{\partial\phi^2}(\nabla\phi)^2\right)\end{bmatrix} \tag{4.12}$$

with $\Delta c_{\min} = c^\alpha_{\min} - c^\beta_{\min}$. To investigate the stability of these stationary solutions, we introduce the sytem variable vetor $y = [\phi, c]^T$ and linearize the given system around the critical point $P_0 = (\phi_0, c_0)$ following the approach in [194]

$$\dot{y} = \begin{bmatrix}-\frac{1}{\varepsilon\tau} & 0\\ 0 & \frac{D\nabla^2}{2A}\end{bmatrix}\left(\begin{bmatrix}-2\varepsilon\gamma_{\alpha\beta} & 0\\ 0 & 0\end{bmatrix}_{P_0}\nabla^2 y + \begin{bmatrix}\frac{\partial^2 f_{\text{pot}}}{\partial\phi^2} + \frac{\partial^2 f_{\text{chem}}}{\partial\phi^2} & \frac{\partial^2 f_{\text{chem}}}{\partial\phi\partial c}\\ \frac{\partial^2 f_{\text{chem}}}{\partial\phi\partial c} & \frac{\partial^2 f_{\text{chem}}}{\partial c^2}\end{bmatrix}_{P_0} y\right).$$

We then transform our system into Fourier space with $\frac{\partial^n y}{\partial x^n} = (ik)^n\hat{y}(k)$

$$\frac{\partial\hat{y}}{\partial t} = -\begin{bmatrix}1/\varepsilon\tau & 0\\ 0 & Dk^2/2A\end{bmatrix}\begin{bmatrix}2\varepsilon\gamma_{\alpha\beta}k^2 + \frac{\partial^2 f_{\text{pot}}}{\partial\phi^2} + \frac{\partial^2 f_{\text{chem}}}{\partial\phi^2} & \frac{\partial^2 f_{\text{chem}}}{\partial\phi\partial c}\\ \frac{\partial^2 f_{\text{chem}}}{\partial\phi\partial c} & \frac{\partial^2 f_{\text{chem}}}{\partial c^2}\end{bmatrix}_{P_0}\hat{y}.$$

As the gradient in ϕ is negligibly small initially, the gradient energy contribution can be neglected $|\nabla\phi|^2 \approx 0$, which yields

$$\frac{\partial \hat{y}}{\partial t} = -\tilde{M} \begin{bmatrix} \frac{\partial^2 f_{\text{pot}}}{\partial \phi^2} + \frac{\partial^2 f_{\text{chem}}}{\partial \phi^2} & \frac{\partial^2 f_{\text{chem}}}{\partial \phi \partial c} \\ \frac{\partial^2 f_{\text{chem}}}{\partial \phi \partial c} & \frac{\partial^2 f_{\text{chem}}}{\partial c^2} \end{bmatrix}_{P_0} \hat{y} = -\tilde{M} H_f \hat{y}$$

with the system matrix $A = -\tilde{M}H_f$. The mobility matrix $\tilde{M}$ is diagonal and has two constant positive entries. The system is stable if the system matrix is negative definite which is fulfilled if the Hessian matrix H_f is positive definite. We investigate the stability concerning small pertubations around a constant value of c by first looking at the determinant

$$\det(H_f) = \left[\frac{\partial^2 f_{\text{pot}}}{\partial \phi^2} + \frac{\partial^2 f_{\text{chem}}}{\partial \phi^2}\right]\left[\frac{\partial^2 f_{\text{chem}}}{\partial c^2}\right] - \left[\frac{\partial^2 f_{\text{chem}}}{\partial c \partial \phi}\right]^2 = \lambda_1 \lambda_2. \tag{4.13}$$

The entries of the Hessian matrix are

$$\frac{\partial^2 f_{\text{tot}}}{\partial \phi^2} = \frac{\partial^2 f_{\text{pot}}}{\partial \phi^2} + 2A\left(\Delta c_{\min}\right)^2 \left(\frac{\partial h}{\partial \phi}\right)^2 - 2A[c - c_{\min}(\phi)]\Delta c_{\min}\frac{\partial^2 h}{\partial \phi^2} + B\frac{\partial^2 h}{\partial \phi^2}$$

$$\frac{\partial^2 f_{\text{chem}}}{\partial c^2} = 2A, \qquad \frac{\partial^2 f_{\text{chem}}}{\partial c \partial \phi} = -2A\Delta c_{\min}\frac{\partial h(\phi)}{\partial \phi}$$

Double-well potential

Examination of stationary solutions $[\dot{\phi}, \dot{c}]^T = 0$ for $\nabla\phi \approx 0$ and thus ϕ constant in the whole domain, yields

$$-\frac{18\gamma_{\alpha\beta}}{\varepsilon}\phi(1-\phi)(1-2\phi) + \left(2A\Delta c_{\min}(c - c_{\min}(\phi)) - B\right)\frac{\partial h}{\partial \phi} \stackrel{!}{=} 0 \tag{4.14}$$

with $\partial h/\partial\phi = 6\phi(1-\phi)$, which results in $c_{\text{stat}} = c_0$ for $\phi = 0$ or $\phi = 1$ and

$$c_{\text{stat}} = c_{\min}^{\beta} + \Delta c_{\min}\phi^2(3-2\phi) + \frac{B}{2A\Delta c_{\min}} + \frac{3\gamma_{\alpha\beta}}{2A\varepsilon\Delta c_{\min}}(1-2\phi) \tag{4.15}$$

for $\phi \in (0,1)$. The determinant according to Eq. (4.13) yields with $\frac{\partial^2 f_{\text{pot}}}{\partial \phi^2} = \frac{18\gamma_{\alpha\beta}}{\varepsilon}(6\phi^2 - 6\phi + 1)$ in the double-well case

$$2A\frac{18\gamma_{\alpha\beta}}{\varepsilon}(6\phi^2 - 6\phi + 1) - \left(4A^2[c - c_{\min}(\phi)]\Delta c_{\min} + 2AB\right)\frac{\partial^2 h_{\text{well}}}{\partial \phi^2} \overset{!}{>} 0$$

Investigating the stability of the critical solutions from Eq. (4.15) then leads to

$$\frac{18\gamma_{\alpha\beta}}{\varepsilon} - 12A(c - c^{\beta}_{\min})\Delta c_{\min} + 6B > 0 \qquad \phi = 0, c = c_0 \tag{4.16}$$

$$\frac{18\gamma_{\alpha\beta}}{\varepsilon}(6\phi^2 - 6\phi + 1) - \frac{18\gamma_{\alpha\beta}}{\varepsilon}(1 - 2\phi)^2 > 0 \qquad \phi \in (0,1) \tag{4.17}$$

Evaluating Eq. (4.16) shows that in the case of $\phi = 0$ and $\phi = 1$ a change in the stability behaviour can be observed. The domain of instability is limited by the critical composition

$$c_{\text{crit}}(\phi = 0) = c^{\beta}_{\min} + \frac{B}{2A\Delta c_{\min}} + \frac{3\gamma_{\alpha\beta}}{2A\Delta c_{\min}\varepsilon}, \tag{4.18}$$

$$c_{\text{crit}}(\phi = 1) = c^{\alpha}_{\min} + \frac{B}{2A\Delta c_{\min}} - \frac{3\gamma_{\alpha\beta}}{2A\Delta c_{\min}\varepsilon}. \tag{4.19}$$

In the second case, Eq. (4.17) yields $-\phi(1-\phi) > 0$ which is false $\forall \phi \in (0,1)$. This means the second critical solution is always unstable. To evaluate the stability of Eq. (4.16) for $c_0 < c_{\text{crit}}$ we look at the trace of the system matrix $\text{tr}(H_f) = \lambda_1 + \lambda_2$

$$(\phi_0 = 0) \qquad 2A + \frac{18\gamma_{\alpha\beta}}{\varepsilon} - 12A(c_0 - c^{\beta}_{\min})\Delta c_{\min} + 6B > 0 \tag{4.20}$$

Expression (4.20) holds $\forall c_0 < c_{\text{crit}}$ and therfore is a stable solution of our system (4.12). The two critical values ((4.18) and (4.19)) are symmetric with regard to $c = 0.5(c^{\alpha}_{\text{eq}} + c^{\beta}_{\text{eq}})$, which is due to the choice of $A^{\alpha} = A^{\beta} = A$. The difference in energy height B results in a constant shift of critical concentrations according to the common tangent construction.

Double-obstacle potential

Examination of the stationary solutions of Eq. (4.12) leads to the criterion

$$-\frac{16\gamma_{\alpha\beta}}{\varepsilon\pi^2}(1-2\phi)+\frac{8}{\pi}\sqrt{\phi(1-\phi)}\,(2A\Delta c_{\min}(c-c_{\min}(\phi))-B)\stackrel{!}{=}0. \tag{4.21}$$

which results in

$$c_{\text{stat}}=c_{\min}^{\beta}+\Delta c_{\min}h_{\text{ob}}(\phi)+\frac{B}{2A\Delta c_{\min}}+\frac{\gamma_{\alpha\beta}}{A\varepsilon\pi\Delta c_{\min}}\frac{1-2\phi}{\sqrt{\phi(1-\phi)}} \tag{4.22}$$

The stability criterion Eq. (4.13) with $\frac{\partial^2 f_{\text{pot}}}{\partial\phi^2}=-\frac{32\gamma_{\alpha\beta}}{\varepsilon\pi^2}$ results in

$$\det(H_f)=-2A\frac{32\gamma_{\alpha\beta}}{\varepsilon\pi^2}-4A^2[c-c_{\min}(\phi)]\Delta c_{\min}\frac{\partial^2 h_{\text{ob}}}{\partial\phi^2}+2AB\frac{\partial^2 h_{\text{ob}}}{\partial\phi^2}\stackrel{!}{>}0 \tag{4.23}$$

Inserting the critical points from Eq. (4.22), we get

$$\det(H_f)=-\frac{8\gamma_{\alpha\beta}}{\varepsilon\pi^2}\frac{1}{\phi(1-\phi)}<0 \qquad \forall\phi\in(0,1) \tag{4.24}$$

which means all critical solutions from Eq. (4.22) are instable with respect to small fluctuations.

4.3 Phase separation in a two-phase model system

The first study aims at proving the theoretical predictions in Sec. 4.2 and comparing the simulation results. A set of non-dimensionalised simulation parameters listed in Tab. 4.1 is used for this model system.

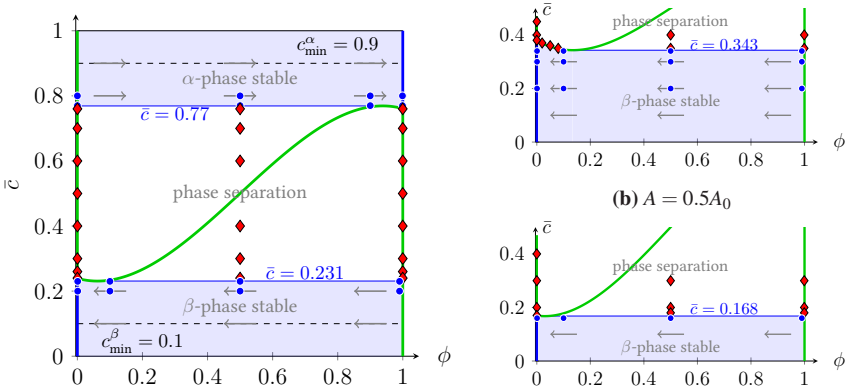
The choice of $A^{\alpha}=A^{\beta}=6.73/\varepsilon$ results in $c_{\text{crit}}(\phi=0)=0.239$ and because of symmetry $c_{\text{crit}}(\phi=1)=1-c_{\text{crit}}(\phi=0)$ applies. The predicted instability ((4.18) and (4.19)) is studied for different initial configurations in the variable

Table 4.1: Input parameters for model validation.

parameter	symbol	value
equilibrium mole fractions	c^{α}_{min}	0.9
	c^{β}_{min}	0.1
interfacial energy	$\gamma_{\alpha\beta}$	0.5
diffusivity	D	1.0

space $\phi \in [0,1]$ and $c \in [0,1]$. Fig. 4.1 shows the results for the double-well potential and three different choices of $A^{\alpha} = A^{\beta}$ while all other parameters are kept constant.

For all cases, three domains with different phase evolution can be identified. All setups with an initial composition above the upper critical one lead to decaying concentration fluctuations and stable α-phase. The phase values in the whole domain trend towards $\phi = 1$, as indicated by the gray arrows. The second stable



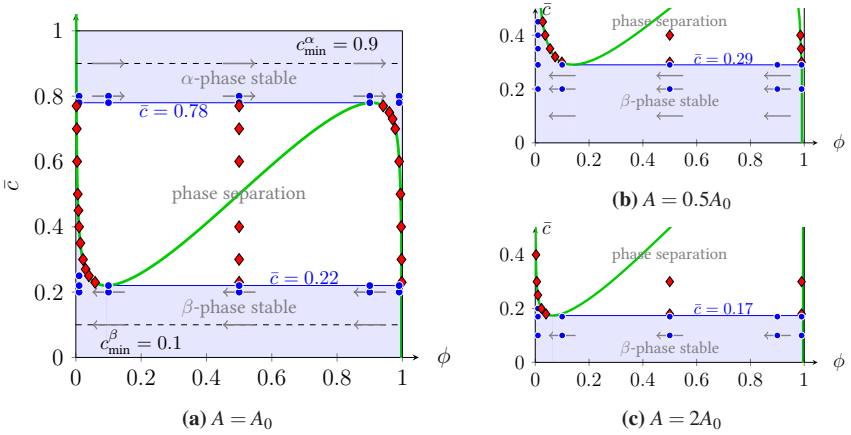
(a) $A = A_0$ **(b)** $A = 0.5A_0$ **(c)** $A = 2A_0$

Figure 4.1: Stability map for well-potential in the variable space $\phi \in [0,1]$ and $c \in [0,1]$. Stationary solutions according to Eq. (4.15) are shown in blue if stable and green for the case of instability. All simulations marked by blue dots feature decaying fluctuations and one stable phase while red diamonds indicate simulations exhibiting phase separation.

domain below the lower critical composition favours the β-phase and ϕ values trend towards zero. The area in between is characterised by unstable amplification of small fluctuations and the formation of regular homogeneous two phase patterns. All simulations are in agreement with the theoretical predictions.

We apply the same procedure to study the stability for the obstacle potential. The results are shown in Fig. 4.2 and once again agreement with the theoretical predictions is observed. The same three domains as before can be identified and are separated by the stationary solution Eq. (4.22). A qualitative difference to the well potential is the non-existence of a stable stationary solution for $\phi = 0$ or $\phi = 1$ due to the shape of the potential. We nevertheless observe stable α- or β-phase within the blue shaded areas as the energy exhibits minimal values at the boundary and ϕ is limited to $\phi \in [0,1]$ by the Gibbs simplex constraint.

The resulting pattern formation during the spinodal decomposition process is highly dependent on the choice of energy density contributions. In Fig. 4.3, the demixing process is compared for the three modeling approaches. The parame-



(a) $A = A_0$ **(b)** $A = 0.5A_0$ **(c)** $A = 2A_0$

Figure 4.2: Stability map for obstacle potential. Stationary solutions according to Eq. (4.22) are always unstable and therfore shown in green. All simulations marked by blue dots feature decaying fluctuations and one stable phase while red diamonds indicate simulations exhibiting phase separation.

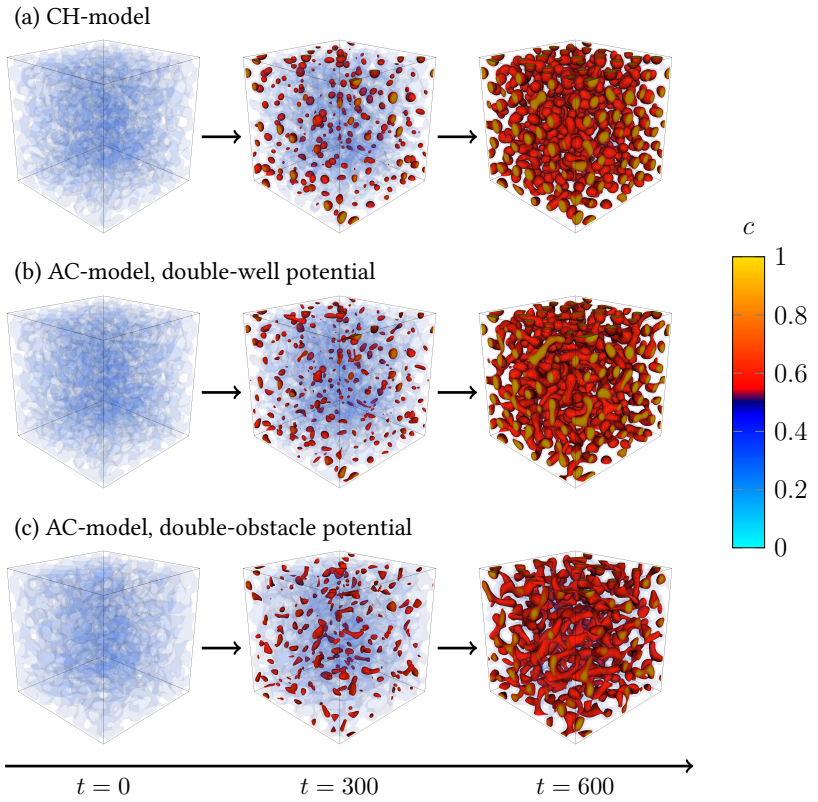


Figure 4.3: Concentration evolution in a 3D domain with $200 \times 200 \times 200$ voxels and initial $c = 0.3$. Opacity of composition below $c = 0.5$ is set to 20 % for better visibility of the phase separation. Three timesteps of temporal evolution are shown for (a) CH-model, (b) AC-model with well potential and (c) AC-model with obstacle potential.

ters were chosen according to Tab. 4.1. The kinetics of the systems are comparable while the structures of the emerging phase are slightly different. While the CH-model tends to form spheroidal precipitates, the AC-model and especially the obstable potential formulation form more entangled structures.«

4.4 Heterogeneous nucleation in pre-existing grain boundaries[2]

We assess the stability of an ϕ_β-ϕ_γ equilibrium interface with regard to the formation of a third phase ϕ_α driven by chemical energies depending on the global initial composition c_0. The initial simulation setup is shown in Fig. 4.4.

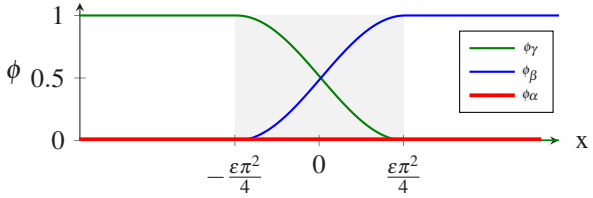


Figure 4.4: ϕ_β-ϕ_γ equilibrium interface

The analysis is based on the chemical energy in Eq. (2.6) and quadratic fitting functions for the phase-dependent contributions (Eq. (2.7)). Based on the assumption that the two present phases β and γ are equal in terms of stoichiometric composition and chemical energies, we set $A^\beta = A^\gamma$, $c^\beta_{\mathrm{min}} = c^\gamma_{\mathrm{min}} = c^{\beta\gamma}_{\mathrm{min}}$ and $B^\beta = B^\gamma$. We further reduce complexity by choice of $A^\alpha = A^{\beta\gamma} = A$ and $B^\alpha = B$, $B^{\beta\gamma} = 0$. The chemical energy Eq. (2.6) can then be re-written as a function of the average composition $c = \sum_\alpha c^\alpha \phi_\alpha$ assuming equal phase diffusion potentials in the interface $\mu = \partial f^\alpha / \partial c^\alpha = \cdots = f^N / \partial c^N$. For three phases and the discussed assumptions, this results in

$$f_{\mathrm{chem}}(\phi, c) = A\left(c - c^{\beta\gamma}_{\mathrm{min}}(1-\phi_\alpha) - c^\alpha_{\mathrm{min}}\phi_\alpha\right)^2 + B\phi_\alpha \tag{4.25}$$

In the following, the abbreviation $\Delta c_{\mathrm{min}} = c^\alpha_{\mathrm{min}} - c^{\beta\gamma}_{\mathrm{min}}$ is used.

[2] This section is an extension of the stability analysis presented in Appendix B of the article Daubner *et al.* [110]. All considerations are applied to the model formulation presented in Chapter 2 for consistency within this work.

We formulate the evolution equations for ϕ_α and ϕ_β based on Eq. (2.15) for a three-phase system

$$\begin{aligned}\dot{\phi_\alpha} =& -\tfrac{M^{\alpha\beta}}{3\varepsilon}\Big[\varepsilon\gamma_{\alpha\beta}\left(\nabla^2\phi_\beta-\nabla^2\phi_\alpha\right)+\tfrac{16}{\varepsilon\pi^2}\gamma_{\alpha\beta}\left(\phi_\beta-\phi_\alpha\right)+\varepsilon(\gamma_{\alpha\gamma}-\gamma_{\beta\gamma})(\nabla^2\phi_\gamma+\tfrac{16}{\varepsilon\pi^2}\phi_\gamma) \\ &+\tfrac{8}{\pi}\sqrt{\phi_\alpha\phi_\beta}\left(-2A\Delta c_{\min}(c-c^{\beta\gamma}_{\min}-\Delta c_{\min}\phi_\alpha)+B\right)\Big] \\ &-\tfrac{M^{\alpha\gamma}}{N\varepsilon}\Big[\varepsilon\gamma_{\alpha\gamma}\left(\nabla^2\phi_\gamma-\nabla^2\phi_\alpha\right)+\tfrac{16\gamma_{\alpha\gamma}}{\varepsilon\pi^2}(\phi_\gamma-\phi_\alpha)+\varepsilon(\gamma_{\alpha\beta}-\gamma_{\beta\gamma})\left(\nabla^2\phi_\beta+\tfrac{16}{\varepsilon\pi^2}\phi_\beta\right) \\ &+\tfrac{8}{\pi}\sqrt{\phi_\alpha\phi_\gamma}\left(-2A\Delta c_{\min}(c-c^{\beta\gamma}_{\min}-\Delta c_{\min}\phi_\alpha)+B\right)\Big]\end{aligned} \tag{4.26}$$

$$\begin{aligned}\dot{\phi_\beta} =& -\tfrac{M^{\alpha\beta}}{3\varepsilon}\Big[\varepsilon\gamma_{\alpha\beta}\left(\nabla^2\phi_\alpha-\nabla^2\phi_\beta\right)+\tfrac{16}{\varepsilon\pi^2}\gamma_{\alpha\beta}\left(\phi_\alpha-\phi_\beta\right)+\varepsilon(\gamma_{\beta\gamma}-\gamma_{\alpha\gamma})(\nabla^2\phi_\gamma+\tfrac{16}{\varepsilon\pi^2}\phi_\gamma) \\ &+\tfrac{8}{\pi}\sqrt{\phi_\alpha\phi_\beta}\left(2A\Delta c_{\min}(c-c^{\beta\gamma}_{\min}-\Delta c_{\min}\phi_\alpha)\right)-B\Big] \\ &-\tfrac{M^{\beta\gamma}}{N\varepsilon}\Big[\varepsilon\gamma_{\beta\gamma}\left(\nabla^2\phi_\gamma-\nabla^2\phi_\beta\right)+\tfrac{16\gamma_{\beta\gamma}}{\varepsilon\pi^2}(\phi_\gamma-\phi_\beta)+\varepsilon(\gamma_{\alpha\beta}-\gamma_{\alpha\gamma})\left(\nabla^2\phi_\alpha+\tfrac{16}{\varepsilon\pi^2}\phi_\alpha\right)\Big]\end{aligned} \tag{4.27}$$

and the evolution of the third phase is given by $\dot{\phi_\gamma} = -\dot{\phi_\alpha} - \dot{\phi_\beta}$. All black terms are related to the mobility $M^{\alpha\beta}$ of the $\alpha\beta$-interface, red terms are scaled with $M^{\alpha\gamma}$ and the blue term with $M^{\beta\gamma}$, respectively.

Under the assumption of coherent nucleation, ϕ_α only grows at the expense of ϕ_β (i.e. $\dot{\phi_\alpha} = -\dot{\phi_\beta}$) while the third phase remains unaffected $\dot{\phi_\gamma} = 0$. This can be implemented wihtin the multiphase-field model by setting the mobilities of neighbouring grains to zero (in this case $M^{\alpha\gamma} = M^{\beta\gamma} = 0$) while coherent variants within one grain can transform into each other with mobility $M^{\alpha\beta}$. This procedure is analogous to the treatment of martensitic variants in a polycrystalline system [140]. Using these assumptions, Eq. (4.26) can be simplified to

$$\begin{aligned}\dot{\phi_\alpha} = -\frac{M^{\alpha\beta}}{3\varepsilon}\Bigg[&\varepsilon\gamma_{\alpha\beta}\left(\nabla^2\phi_\beta-\nabla^2\phi_\alpha\right)+\frac{16}{\varepsilon\pi^2}\gamma_{\alpha\beta}(\phi_\beta-\phi_\alpha) \\ &+\varepsilon(\gamma_{\alpha\gamma}-\gamma_{\beta\gamma})(\nabla^2\phi_\gamma+\frac{16}{(\varepsilon\pi)^2}\phi_\gamma) \\ &-\frac{8}{\pi}\sqrt{\phi_\alpha\phi_\beta}\left(2A\Delta c_{\min}\left(c-c^{\beta\gamma}_{\min}-\Delta c_{\min}\phi_\alpha\right)-B\right)\Bigg].\end{aligned} \tag{4.28}$$

Note that even though ϕ_α grows at the expense of ϕ_β, the driving force for nucleation is still influenced by the third phase ϕ_γ. The effect of this term can

be illustrated for a three phase system of electrolyte, iron-phosphate (FP) and lithium iron-phosphate (LFP). As the interfacial energy between LFP and electrolyte ($\gamma_{\alpha\gamma}$) is smaller than the respective interface between FP and electrolyte ($\gamma_{\beta\gamma}$), there is an additional driving force for the nucleation of LFP (ϕ_α) which lowers the nucleation barrier and leads to wetting of the crystal facets in contact with electrolyte [100]. For simplicity, we neglect the influence of the third phase by setting $\gamma_{\alpha\gamma} = \gamma_{\beta\gamma}$ in the following analysis.

Starting from the equilibrium interface sketched in Fig. 4.4, we assume $\boldsymbol{\nabla}\phi_\alpha$ to be negligibly small initially. From the equilibrium solution $\phi_\gamma = \frac{1}{2} - \frac{1}{2}\sin(\frac{4x}{\varepsilon\pi})$ we derive

$$\frac{\partial^2\phi_\gamma}{\partial x^2} = \frac{8}{\varepsilon^2\pi^2}\sin\left(\frac{4x}{\varepsilon\pi}\right) = \frac{8}{\varepsilon^2\pi^2} - \frac{16}{\varepsilon^2\pi^2}\phi_\gamma. \tag{4.29}$$

Furthermore, we employ $\phi_\beta = 1-\phi_\gamma-\phi_\alpha$ and $\boldsymbol{\nabla}\phi_\beta = -\boldsymbol{\nabla}\phi_\gamma - \boldsymbol{\nabla}\phi_\alpha$. The stationary solutions of Eq. (4.28) are then characterised by

$$\begin{aligned} -\frac{8\gamma}{\varepsilon\pi^2} + \frac{16\gamma}{\varepsilon\pi^2}\phi_\gamma + \frac{16\gamma}{\varepsilon\pi^2}(1-\phi_\gamma-2\phi_\alpha) - \frac{8}{\pi}\sqrt{\phi_\alpha\phi_\beta}\Delta^{\alpha\beta}_{\text{chem}} &\stackrel{!}{=} 0 \\ \frac{8\gamma}{\varepsilon\pi^2}(1-4\phi_\alpha) - \frac{8}{\pi}\sqrt{\phi_\alpha(1-\phi_\gamma-\phi_\alpha)}\left(2A\Delta c_{\min}(c - c^{\beta\gamma}_{\min} - \Delta c_{\min}\phi_\alpha) - B\right) &\stackrel{!}{=} 0 \end{aligned}$$

which yields the criterion for stationary compositions

$$c_{\text{stat}} = c^{\beta\gamma}_{\min} + \Delta c_{\min}\phi_\alpha + \frac{B}{2A\Delta c_{\min}} + \frac{\gamma}{2A\varepsilon\pi\Delta c_{\min}}\frac{1-4\phi_\alpha}{\sqrt{\phi_\alpha(1-\phi_\gamma-\phi_\alpha)}}. \tag{4.30}$$

The system evolution equation can be linearised around stationary point P_0 with the sytem variable vetor $y = [\phi_\alpha, c]^T$. We then transform our system into Fourier space with $\frac{\partial^n y}{\partial x^n} = (ik)^n\hat{y}(k)$ and get

$$\frac{\partial\hat{y}}{\partial t} = -\begin{bmatrix} \frac{M^{\alpha\beta}}{\varepsilon\tilde{N}} & 0 \\ 0 & \frac{Dk^2}{2A} \end{bmatrix}\begin{bmatrix} \varepsilon\gamma k^2 - \frac{16\gamma}{\varepsilon\pi^2} + \frac{\partial}{\partial\phi_\alpha}\Delta^{\alpha\beta}_{\text{chem}} & \frac{\partial}{\partial c}\Delta^{\alpha\beta}_{\text{chem}} \\ \frac{\partial^2 f_{\text{ch}}}{\partial c\partial\phi_\alpha} & \frac{\partial^2 f_{\text{ch}}}{\partial c^2} \end{bmatrix}_{P_0}\hat{y} = -\tilde{M}S_f\hat{y}.$$

with the system matrix $A = -\tilde{M}S_f$. We assume the gradient $\nabla\phi_\alpha$ to be negligibly small, i.e. $k^2 \approx 0$. The mobility matrix $\tilde{M}$ is diagonal and has two constant positive entries. The system is stable if the stability matrix S_f is positive definite. The determinant is given by

$$\det(S_f) = S_{\phi_\alpha\phi_\alpha}S_{cc} - S_{c\phi_\alpha}S_{\phi_\alpha c} = \lambda_1\lambda_2. \tag{4.31}$$

with the single contributions

$$\begin{aligned}
S_{\phi_\alpha\phi_\alpha} =& -\frac{4}{\pi}\frac{1-\phi_\gamma-2\phi_\alpha}{\sqrt{\phi_\alpha(1-\phi_\gamma-\phi_\alpha)}}\left(2A\Delta c_{\min}(c - c^{\beta\gamma}_{\min} - \Delta c_{\min}\phi_\alpha) - B\right) \\
&+ \frac{8}{\pi}\sqrt{\phi_\alpha(1-\phi_\gamma-\phi_\alpha)}2A(\Delta c_{\min})^2 - \frac{32\gamma}{\varepsilon\pi^2} \\
S_{\phi_\alpha c} =& -\frac{8}{\pi}\sqrt{\phi_\alpha(1-\phi_\gamma-\phi_\alpha)}\,(2A\Delta c_{\min}), \quad S_{c\phi_\alpha} = -2A\Delta c_{\min}, \quad S_{cc} = 2A
\end{aligned}$$

which yields

$$\det(S_f) = -\frac{64A\gamma}{\varepsilon\pi^2} - \frac{8A}{\pi}\frac{1-\phi_\gamma-2\phi_\alpha}{\sqrt{\phi_\alpha(1-\phi_\gamma-\phi_\alpha)}}\left(2A\Delta c_{\min}(c - c^{\beta\gamma}_{\min} - \Delta c_{\min}\phi_\alpha) - B\right)$$

Investigating the stability of the stationary solution Eq. (4.30), we derive the criterion

$$\det(S_f) = -\frac{64A\gamma}{\varepsilon\pi^2} - \frac{8A\gamma}{\varepsilon\pi^2}\frac{(1-\phi_\gamma-2\phi_\alpha)(1-4\phi_\alpha)}{\phi_\alpha(1-\phi_\gamma-\phi_\alpha)} \overset{!}{>} 0$$

for stability. Spontaneous nucleation occurs for $\det(S_f) < 0$ which is fulfilled for

$$2\phi_\alpha(1-2\phi_\gamma) > \phi_\gamma - 1$$

As we require $\phi_\alpha < 1-\phi_\gamma$, this criterion is fulfilled for all $\phi_\gamma < 0.75$ and otherwise we require $\phi_\alpha < (\phi_\gamma - 1)/(2-4\phi_\gamma)$.

We now compare the critical composition for homogeneous nucleation according to Eq. (4.22) with the barrier for heterogeneous nucleation in a grain boundary

according to Eq. (4.30). The parameters from Tab. 7.1 are used together with $A^{\alpha} = A^{\beta} = 6.73/\varepsilon$ for an example study. The visualization of analytical predictions in Fig. 4.5 illustrates that the barrier for nucleation of ϕ_{α} is the smallest for values of $\phi_{\gamma} \to 0$ and $\phi_{\alpha} = 0.05$ at around $c_{\mathrm{crit}} = 0.19$ while the minimum for homogenous nucleation (black dashed line) is $c_{\mathrm{crit}} = 0.255$. Thus, we expect nucleation of ϕ_{α} within the diffuse interface but close to the bulk of $\phi_{\beta} = 1$.

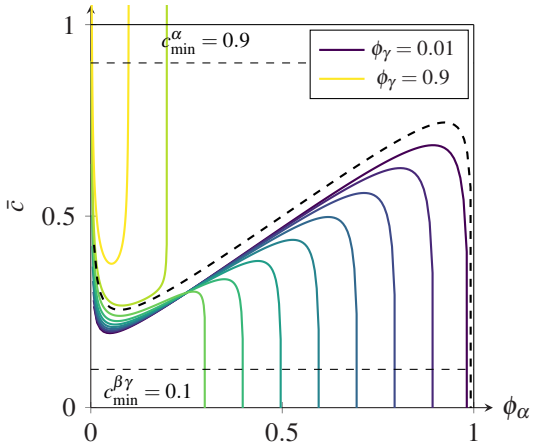


Figure 4.5: Stationary solutions according to Eq. (4.30) shown for discrete values of $\phi_{\gamma} \in [0.01, 0.1, 0.2, \ldots, 0.9]$. The black dashed line represents stationary solutions for homogeneous nucleation in the bulk according to Eq. (4.22).

To prove this analytical prediction, simulations with an initial composition of $c = 0.22$ are conducted which is below the critical value for homogeneous but above the value for heterogeneous nucleation. Various functions to apply the noise in ϕ_{α} are compared in Fig. 4.6. Left subfigures show the initial equilibrium interface with solid lines and the phase fraction after nucleation with dashed lines. The right subfigures show the corresponding driving forces acting on the phase ϕ_{α} where the chemical contribution is shown in purple and the overall $\partial\phi_{\alpha}/\partial t$ as a black line. The diffuse interface (gray shaded area) has been resolved with 25 grid points in this study. As predicted, phase α grows starting from a nucleation

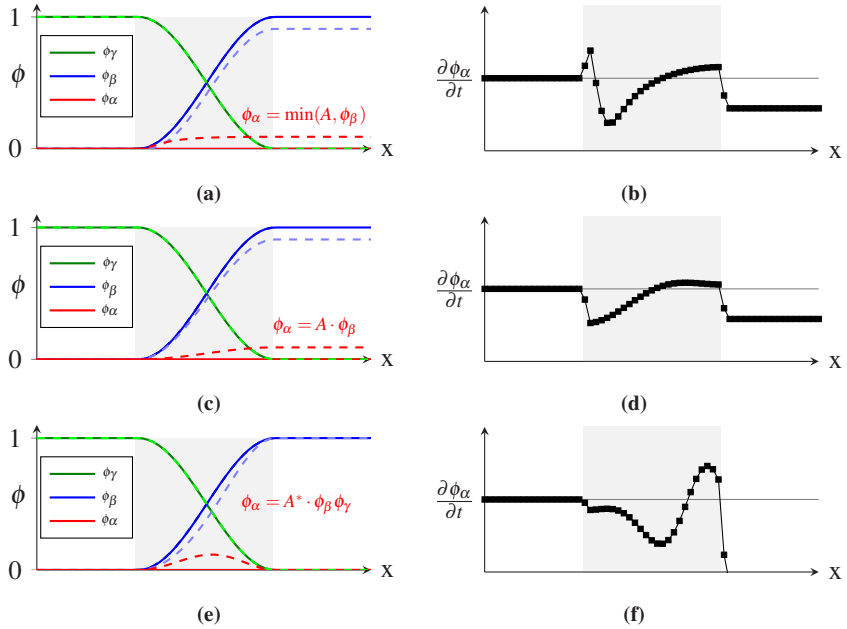


Figure 4.6: Comparison of noise functions for heterogeneous nucleation in a grain boundary. Phase fraction after nucleation are shown in subfigure a,c,e and the corresponding driving force for ϕ_α is shown in b,d, and f.

in the interface. All three cases exhibit a positive driving force for $\phi_\gamma \to 0$ but a negative driving force in the bulk (where $\phi_\gamma = 0$ and $\phi_\beta = 1$ initially).

In polycrystalline battery materials, we expect heterogeneous nucleation at pre-existing grain boundaries as there are typically more defects which facilitate the formation of new phases. This is consistent with the investigated model formulation which has a lower nucleation barrier in grain boundaries and multi-junctions. As we expect heterogeneous nucleation to be dominant in our simulations, it is sufficient to apply the noise term only in diffuse interface regions (see Fig. 4.6 e) which is the reason for formulation (2.21) in Section 2.3.

4.5 Multi-grain intercalation

»In our last example we study the intercalation behaviour of a multi-grain section and, for performance reasons, only employ the obstacle potential. We start from a Voronoi filling of ten phases wich have undergone some volume preserving relaxation to reduce the initially high interfacial energies and reproduce equilibrium angles at triple junctions. Phase pairs are assumed to have the same interfacial energy $\gamma_{\alpha\beta} = 0.072\,\mathrm{J/m^2}$. The diffusivity of lithium ions is asumed to be $D_0 = 10^{-15}\,\mathrm{m^2/mol}$ and the molar volume is $V_m = 4.38 \times 10^{-5}\,\mathrm{m^3/mol}$. The equilibrium composition of the lithium-poor phase is set to $c_{\mathrm{min}}^{\mathrm{FP}} = 0.01$ while $c_{\mathrm{min}}^{\mathrm{LFP}} = 0.99$. We furthermore apply a constant boundary flux corresponding to 1C discharge rate at the left-hand side and no flux BC at the right side of the simulation domain. The phase boundary between FP and LFP is often assumed to be coherent [84] while grain boundaries are non-coherent. This is reflected in the choice of corresponding LFP phases that can only grow at the expense of an FP grain, hence preserving the original grain boundaries.

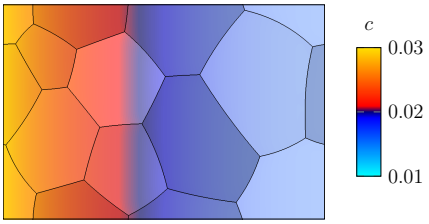
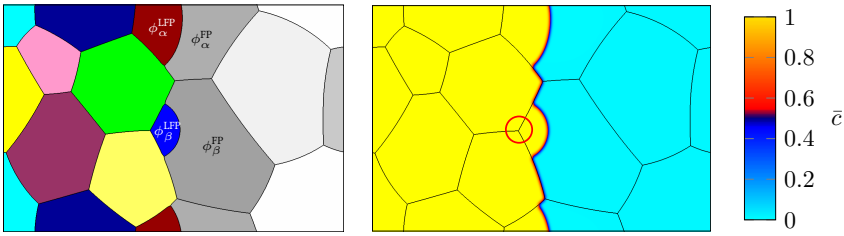


Figure 4.7: Composition gradient within a multi-grain cathode section under CC discharge at $t = 0.01\,\mathrm{h}$.

In Fig. 4.7, the lithium composition is shown at the beginning of the intercalation process at $t = 0.01\,\mathrm{h}$. Composition gradually decays in horizontal direction and the gradient is only weakly influenced by the grain boundaries. Consideration of anisotropic diffusion or grain boundary diffusion would most likely largely influence the transport but both effects are neglected at this point. These are subject to future studies. Phase separation is initiated at interfaces and multiple junctions which lower the nucleation barrier of the LFP phase as discussed in Section 4.4. Higher order junctions most likely lower the nucleation barrier additionally but proving this analytically was out of the scope of this paper. We note however, that in the present simulations nucleation of the LFP phases was always initiated at higher order junctions

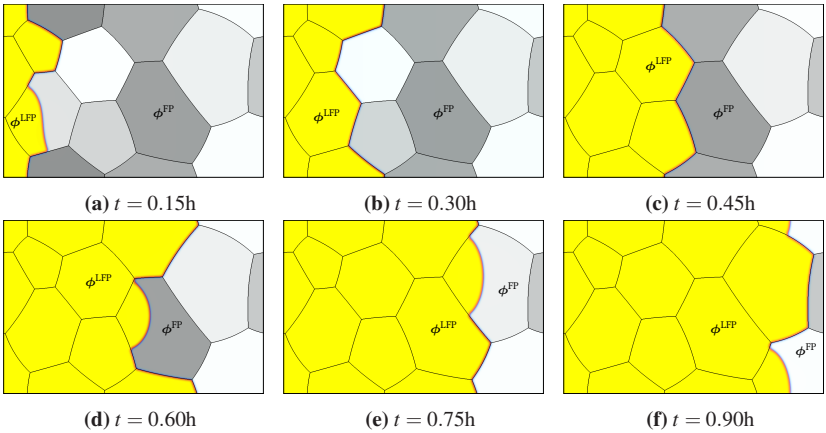


(a) multiphase-field ϕ **(b)** composition c

Figure 4.8: Intercalation in a 2D multi-grain cathode section with 200×300 cells under constant current discharge. Evolution of phases (a) is coupled to composition (b) and displayed here for 1C rate at time $t = 0.5$ h.

which might be due to the fact that less surface is created. These considerations strongly support the choice of the noise term Eq. (2.21), which is only active in the interfacial regions based on the assumption of heterogeneous nucleation.

Once the critical composition has been exceeded and phase separation occurs, grain-by-grain-like filling can be observed. Fig. 4.8a shows two grains in which nucleation has been initiated and LFP phases grow on the expense of the corresponding FP phase. The phase transformation within each grain is triggered at higher order junctions such as that marked by the red circle in Fig. 4.8b, and then proceeds through the grain. If multiple nucleation events happen simultaneously, the energetically more favourable grain will be filled completely by diffusion of ions from the surrounding grains before the next grain will be filled. This illustrates the strong coupling between diffusion and phase transformation. Over time, all grains within the section exhibit phase transformation and a front between LFP phases and FP phases moves through the simulation domain as shown in Fig. 4.9. Neighbouring grains influence the progression of the phase transformation as it is energetically favourable for the intercalation to proceed in a grain-by-grain process. This seems reasonable from a physical point of view as the overall interfacial energy is reduced. From Fig. 4.9, we conclude that the evolving LFP phases form 90° contact angles at the left and right boundary of the domain due to the $\nabla c = 0$ BC, but also at the pre-existent internal grain boundaries. This is in agreement with Young's equation for the wetting angle on



(a) $t = 0.15$h **(b)** $t = 0.30$h **(c)** $t = 0.45$h

(d) $t = 0.60$h **(e)** $t = 0.75$h **(f)** $t = 0.90$h

Figure 4.9: Evolution of FP to LFP phase transformation during intercalation in 2D multi-grain cathode section with 200×300 cells under CC discharge with 1C rate.

a rigid surface where all three phase pairs exhibit the same surface energy $\gamma_{\alpha\beta}$. In this sense, the initial grain boundaries can be interpreted as a rigid substrate because of their immobility. The observed phase front between the LFP and FP phase within each grain then evolves such that curvature and total surface are minimized while keeping 90° contact angles with the grain boundaries.«

4.6 Discussion

»Computation of phase evolution within the Allen-Cahn framework enables the simulation of heterogeneous nucleation of a coherent LFP phase within a multi-grain section of non-coherent FP phases. The model is able to predict composition-dependent phase tranformation nucleating at grain boundaries without making a priori assumtions about the nucleation site. The multiphase-field can be utilised to include lattice orientation information of the respective phases which can be reflected by anisotropy of diffusion and volumetric expansion. The explicit modeling of evolving phases also facilitates the incorporation of mechanical energy contributions.

We also note that this framework is not limited to a one-step phase transition process within the composition range of $c \in [0,1]$ but can easily be extended to a multi-step process as in the $FePO_4 \rightarrow Na_{0.66}FePO_4 \rightarrow NaFePO_4$ phase transformation. To the best of our knowledge, this is the first time a multiphase-field approach has been used to study intercalation in a multi-grain system. Simulations strongly support the assumption of coexistence of fully lithiated and delithiated primary particles as the filling process proceeds stepwise in a grain-after-grain manner through the agglomerate. This result is in agreement with the domino-cascade mechanism proposed by Delmas et al. [121] and the assumption that a core-shell-like intercalation occurs in larger secondary particles. Size and porosity of these secondary structures probably influences the battery performance strongly. The effects of lattice orientation, elastic energy and the electro-chemical reaction at active electrolyte-electrode surfaces on this process should be studied further.«

From Eq (4.15), (4.22) and (4.30) we conclude that the nucleation barrier of a new phase scales with the chemical energy coefficient A, the parameter ε for interfacial width and the interfacial energy $\gamma_{\alpha\beta}$. This stems from the fact that the homogenous free energy landscape is given by the sum of chemical energies and the potential term which imposes the miscibility gap. One of the advantages of formulating the interfacial energy contributions Eq. (2.4) and Eq. (2.5) in terms of $\gamma_{\alpha\beta}$ and ε is that the interfacial width can be re-scaled by changing ε while keeping the physical interfacial energy $\gamma_{\alpha\beta}$ constant. This feature now comes at the price of changing the nucleation barrier when the potential energy is re-scaled while the chemical energy contribution stays constant. In other words, the diffuse interface must be resolved at the physical scale of diffuseness to correctly predict the onset of phase nucleation. If the width of the diffuse interface is enlarged to reduce computation time, nucleation will occur earlier than otherwise expected. However, the stoichiometry of evolving phases is not affected and the ratio of chemical to interfacial forces scales correctly once a diffuse interface is established as the physical value $\gamma_{\alpha\beta}$ remains unchanged.

5 Implementation of anisotropic diffusion

While the formulation of anisotropic diffusion in terms of a partial differential equation is rather straightforward (see Section 2.4), an accurate numerical implementation especially in the non-grid-aligned case, is surprisingly difficult. Strongly anisotropic fluxes also play a role in the simulation of plasma physics [195, 196]. The heat flux in magnetized plasmas exhibits a ratio of heat conductivity coefficients in the order of 10^9. Similarly, the ion flux in layered oxides is mainly restricted to the layers and the direction-dependent diffusivity coefficients span multiple orders of magnitude [10, 13]. The energetic barrier for across-layer hopping is high in a perfect crystal structure which makes it implausible. Larger crystals and agglomerates naturally contain more structural defects which facilitates diffusion in the c-direction but diffusivity is still orders of magnitude smaller compared to the layer direction. Bouwman *et al.* [10] prepared thin film electrodes with the c-axis parallel and, secondly, perpendicular to the charging direction. GITT measurements showed almost 10 orders of magnitude difference between the calculated apparent diffusion coefficients [10, Fig. 13].

5.1 Discretization stencils

Note that the term "cell" is used in the following even though discretization is based on finite differences. The reason is, that the second order, volume conserving stencils employed throughout this work correspond to a cell-centered finite volume scheme on a regular grid (Fig. 2.4). In this sense, cell centers are the

discretization points for the finite difference method and spatial derivatives are computed on a staggered grid which corresponds to computation of fluxes on cell faces. The field variables (ϕ, μ, σ) are stored and computed on cell centers (red squares in Fig. 5.1). The following discussion is based on a two-dimensional grid but extension to 3D is straightforward.

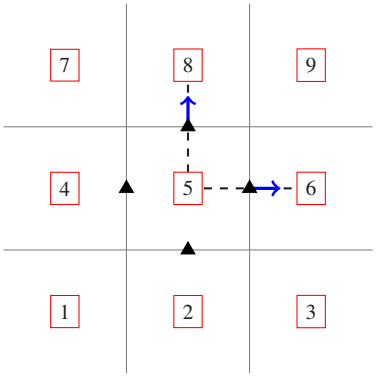


Figure 5.1: Standart isotropic discretisation

The simplest discretization which is typically used to compute gradients or the laplacian of a field (e.g. the contribution stemming from the gradient energy in Eq. (2.16)) is sketched in Fig. 5.1. While spatial derivatives in the x-direction are computed on the left and right side of the cell center, the gradients in y are located at other positions above and below the cell center. This procedure is computationally cheap and, furthermore, able to account for grid-aligned anisotropy. As an example, the fluxes in the mass balance $J = -\mathbb{M}\mu$ could be computed based on different mobilities M_x in the x- and M_y in the y-direction. However, the scheme is insufficient for the investigation of polycrystalline materials as the random orientation of grains within the reference coordinate system cannot be captured.

To inlude full anisotropy, the total spatial gradient needs to be computed at any discretization point. Two possible stencils are shown in Fig. 5.2. The first scheme (Fig. 5.2 a) is called antisymmetric or standard staggered grid (SSG) as the discretization points for spatial gradients are staggered to $(i+\frac{1}{2}, j)$ and $(i, j+\frac{1}{2})$. The second discretization stencil (Fig. 5.2 b) is called symmetric or rotated staggered grid (RSG). Every cell center has a corresponding corner node that is defined by a shift $(i+\frac{1}{2}, j+\frac{1}{2})$. All corner nodes form a grid that is rotated by 45° with regard to the original grid (and thus the naming). The antisymmetric

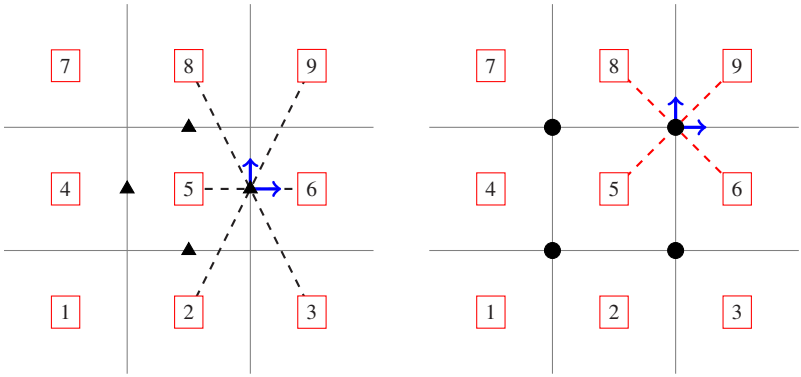


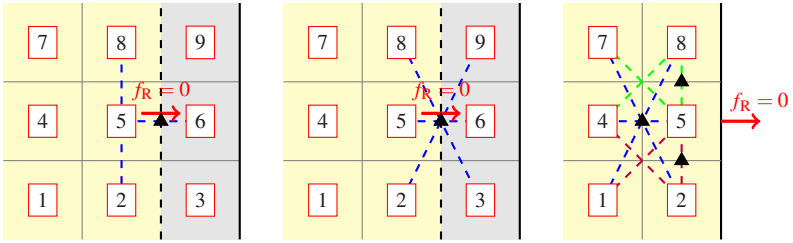
Figure 5.2: Spatial discretization of gradients with the a) antisymmetric and b) symmetric scheme.

scheme shares each discretization point with one neighboring cell, i.e. in the three-dimensional case, there are $6/2 \times N_{\text{cells}}$ gradients that need to be evaluated. The symmetric scheme on the other hand, shares each corner with three other cells in 2D (and eight in 3D). Every cell center can thus be associated with one corner node and there are N_{cells} positions to evalute the spatial gradients which makes this scheme computationally beneficial, especially in 3D.

5.2 Discrete boundary conditions

There are multiple ways to implement flux boundary conditions which influences the simulation outcome crucially. Various options are discussed exemplarily for the right boundary of the spatial domain but results also hold for all other boundaries.

In the antisymmetric approach, fluxes need to be computed on the face between the last inner cell and the adjacent ghost layer. This can either be achieved by setting the ghost layer values such that the resulting fluxes are the ones prescribed (Fig. 5.3a and b) or by directly setting the fluxes (Fig. 5.3c).



(a) 1. order approx. **(b)** 2. order approx. **(c)** 2. order variant

Figure 5.3: No flux (isolate) BC in the antisymmetric scheme

The first order approximation is given as

$$u_{n_x,j} = u_{n_x-1,j} - \frac{\Delta x}{D_{xx}} D_{xy} \frac{u_{n_x-1,j+1} - u_{n_x-1,j-1}}{2\Delta y},$$

where n_x denotes the index of the ghost layer (gray cells). The y-component of the gradient is approximated at $n_x - 1$ such that only inner domain cells are employed for the computation of the BC.

The second order approximation shown in Fig. 5.3b involves three adjacent ghost cells for the computation of the gradient. Solving for the boundary value yields

$$u_{n_x,j} = u_{n_x-1,j} - \frac{\Delta x}{D_{xx}} D_{xy} \frac{u_{n_x-1,j+1} + u_{n_x,j+1} - u_{n_x-1,j-1} - u_{n_x,j-1}}{4\Delta y}$$

which, in the 2D case, leads to a tridiagonal matrix that can be solved via the Thomas algorithm. In the general three-dimensional case, an efficient sparse matrix solver is needed. The last variant does not include a ghost layer such that the index n_x denotes the last cell in the computational domain. Fluxs at the boundary are set to zero. The evolution of composition can be computed as

$$u^{n+1}_{n_x,j} = u^n_{n_x,j} + \Delta t \left(D_{xx} \frac{-u^n_{n_x,j} + u^n_{n_x-1,j}}{(\Delta x)^2} + D_{yy} \frac{u^n_{n_x,j+1} - 2u^n_{nx,j} + u^n_{nx,j-1}}{(\Delta y)^2} \right.$$
$$\left. + D_{xy} \frac{u^n_{n_x,j+1} + 3u^n_{n_x-1,j-1} - 3u^n_{n_x-1,j+1} - u^n_{n_x,j-1}}{4\Delta x \Delta y} \right).$$

One problem that arises is that the derivative ∇_x at the bottom and top side can only be approximated in first order (see green and purple stencils in Fig. 5.3c).

The same procedure can be applied to the symmetric scheme. Again, three variants are introduced as sketched in Fig. 5.4. The corresponding computation procedure for bounday cells is given as

$$u_{n_x,j} = u_{n_x-1,j} - \frac{\Delta x}{D_{xx}} D_{xy} \frac{u_{n_x-1,j} - u_{n_x-1,j-1}}{\Delta y}$$

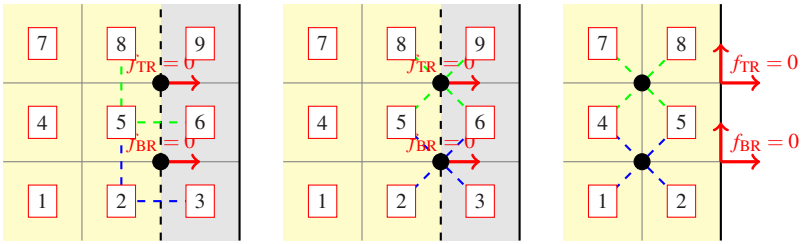
for the first order approximation. The second order approximation based on ghost cells is

$$u_{n_x,j} = u_{n_x-1,j-1} + \frac{D_{xx}\Delta y - D_{xy}\Delta x}{D_{xx}\Delta y + D_{xy}\Delta x}(u_{n_x-1,j} - u_{n_x,j-1})$$

and if the boundary fluxes are directly prescriped instead

$$u^{n+1}_{n_x,j} = u^n_{n_x,j} + \Delta t \Bigg(- D_{xx} \frac{u^n_8 + 2u^n_5 + u^n_2 - u^n_7 - 2u^n_4 - u^n_1}{4(\Delta x)^2} + D_{xy} \frac{2u^n_1 - 2u^n_7}{4\Delta x \Delta y} + D_{yy} \frac{u^n_7 + u^n_8 - 2u^n_4 - 2u^n_5 + u^n_1 + u^n_2}{4(\Delta y)^2} \Bigg).$$

For the last case, fluxes on the boundary in the y-direction are also set to zero as the derivative in y-direction can not be reasonably discretized (see Fig. 5.4c).



(a) 1. order approx. **(b)** 2. order approx. **(c)** 2. order variant

Figure 5.4: No flux (isolate) BC in the symmetric scheme

5.3 Quantifying the numerical error for bulk diffusion

All previously discussed implementations of the isolate BC are tested together with the antisymmetric and symmetric stencils. Problems that may arise with highly anisotropic diffusion on non-aligned meshes are [197]

- significant numerical diffusion perpendicular to the main diffusion direction. This effect depends on grid misalignment and the discretization scheme,
- non-positivity near high gradients, i.e. concentration values become unphysical ($c < 0$).

One possible approach to prevent unphysical concentration values are flux limiters as proposed by Sharma and Hammett [196]. To reduce numerical artefacts due to high gradients, a Dirichlet BC on the left boundary is chosen with a steep but smooth transition between zero and one. The function can be interpreted as a smoothed version of a hat profile and is given as

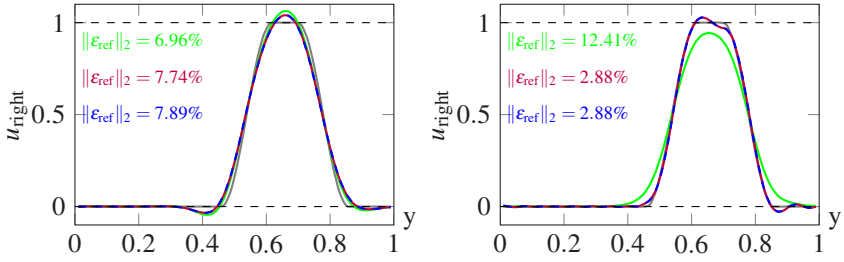
$$u_{\text{left}} = \begin{cases} \frac{1}{2} + \frac{1}{2}\sin(\frac{\pi}{2}\frac{y-0.38}{0.08}) & ,0.30 < y \leq 0.46 \\ 1.0 & ,0.46 < y \leq 0.54 \\ \frac{1}{2} + \frac{1}{2}\sin(\frac{\pi}{2}\frac{y-0.62}{0.08}) & ,0.54 < y \leq 0.70. \end{cases} \tag{5.1}$$

For the anisotropy factor $\zeta = D_{11}/D_{22}$, the limiting case of $\zeta = \infty$ is investigated to yield relevant results for strong anisotropy. The combination of numerical scheme and boundary condition implementation is evaluated by comparison of the transported solution with the analytical profile Eq. (5.1). As the information travels throught the domain, the diffusion anisotropy creates a shift $s_y = L_x \tan(\theta)$. Therefore, the exact solution at the right boundary is known. In

the following, the L^2-norm is introduced and used as a relative error measure by the definition

$$\|\varepsilon_{\text{ref}}\|_2 = \frac{\|u_{\text{right}} - u_{\text{exact}}\|_2}{\|u_{\text{exact}}\|_2} = \sqrt{\sum_0^{n_y}(u_{\text{right}} - u_{\text{exact}})^2 / \sum_0^{n_y}(u_{\text{exact}})^2}. \tag{5.2}$$

Fig. 5.5 illustrates the results for a small misalignment angle $\theta = 9°$ between the diffusion anisotropy direction and the grid. The domain has been discretised by 50×50 cells. All three implementations of the isolate BC are tested for the antisymmetric and the symmetric scheme.



(a) Antisymmetric scheme **(b)** Symmetric scheme

Figure 5.5: Concentration profile at the right domain boundary for various numerical implementations at a rotation angle of $\alpha = 9°$ between the material and spatial coordinate system. The domain has been discretized with 50×50 cells and periodic BCs at bottom and top. The analytical solution is shown in gray. Profiles and L2-errors due to numerical diffusion are compared for the a) antisymmetric and b) symmetric scheme. Green denotes the first order, purple the second order approximation and blue the second order variant of BC implementations as described in Sec. 5.2.

The antisymmetric scheme generally exhibits more numerical diffusion perpendicular to the flux diretion which results in the smoothing of the profiles in Fig. 5.5a. Concentration values exhibit unphysical values of $c < 0$ and $c > 1$ for all cases which has been discussed in literature [196, 197]. For the symmetric scheme, the relative error largely depends on the BC implementation. While the first order approximation introduces strong numerical diffusion which leads to a smoothening of the profile and an increased error measure, the other two

variants yield the exact same result. The error is much lower compared to the antisymmetric scheme.

This study is extended to a set of misalignment angles $\theta \in [-15°, 60°]$. The diffusion length between left and right boundary becomes larger as $L_{\text{diff}} = L_x / \cos(\theta)$, so one expects the error measure to increase with θ. Fig. 5.6 shows the relative error of the six possible combinations as a function of the misalignment angle θ.

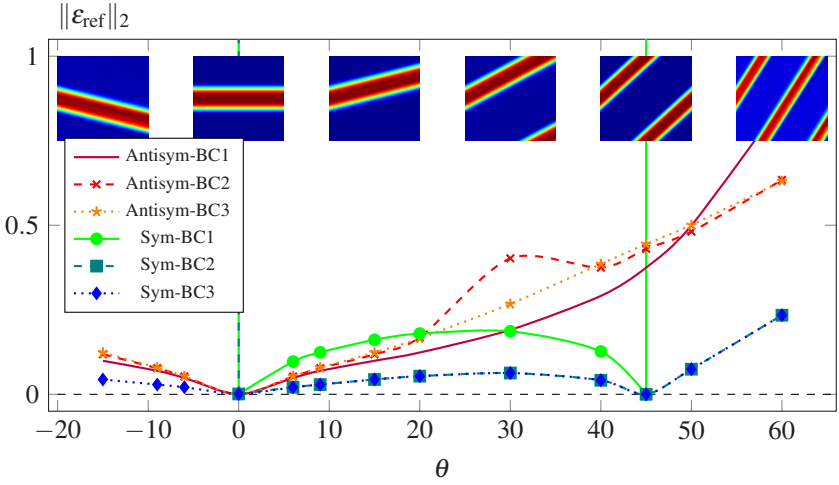
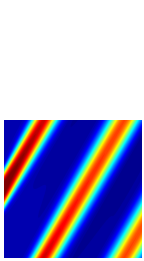


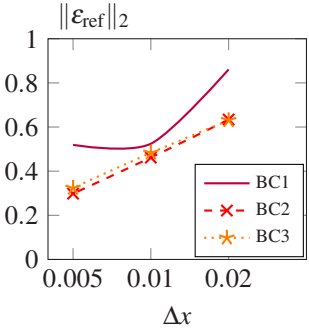
Figure 5.6: Relative error $\|\varepsilon_{\text{ref}}\|_2$ for antisymmetric and symmetric scheme combined with various BC implementations. Domain is discretised with 50×50 cells.

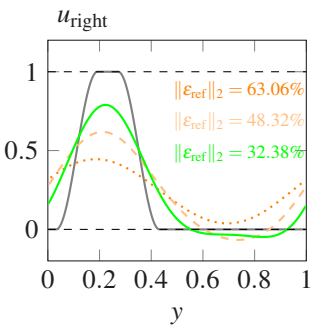
The antisymmetric scheme leads to an increasing error for higher angles which is a combination of two effects. First of all, the misalignment of anisotropy direction and the grid becomes larger and, secondly, the diffusion length increases which results in more numerical diffusion in the perpendicular direction. For angles $\theta < 50°$, the first-order approximation BC features smaller errors while the other two implementations yield better results for higher misalignment. With the symmetric scheme, the first two BC implementations become instable for $\theta < 0$ which disqualifies them for practical usage. Generally the error $\|\varepsilon_{\text{ref}}\|_2$ is smaller for the symmetric scheme in combination with prescribing fluxes (BC

in Fig. 5.4c) compared to all other combinations. Furthermore, the symmetric scheme features the characteristic that the numerical error is zero at $\theta = 0$ and $\theta = 45^\circ$ as both are aligned within the rotated staggered approach.

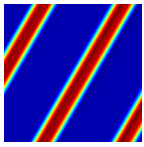
To quantify the effect of discretisation, the case of $\theta = 60^\circ$ is investigated for three discretisations 50×50, 100×100 and 200×200 as shown in Fig. 5.7. The results strongly support the choice of the symmetric finite difference scheme in combination with direct prescription of fluxes for Neumann boundary conditions. The finding is consistent with similar works in the field of strongly anisotropic heat fluxes in magnetized plasmas [195] and anisotropic diffusion [197].

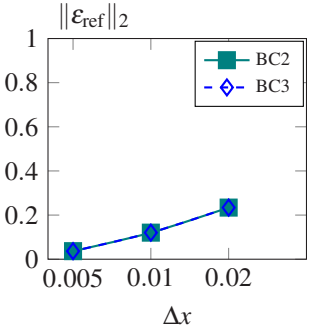


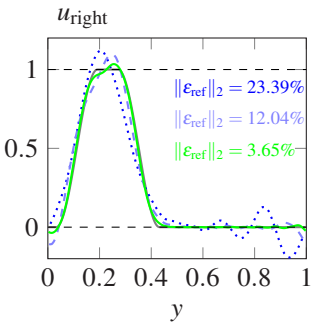




(a) **(b)** **(c)**







(d) **(e)** **(f)**

Figure 5.7: Error of numerical diffusion for antisymmetric (a-c) and symmetric (d-f) scheme at rotation angle $\theta = 60°$. Exemplary field solutions $u(x,y)$ are shown in a) and d). The discretization errors for 50×50, 100×100 and 200×200 cells are compared in b) and e) for various BC implementations. Profiles at the right domain boundary are shown for the second-order variant BC (BC3) in c) and f). The given L2-errors correspond to the three discretizations $\Delta x = [0.02, 0.01, 0.005]$ from top to bottom.

Part II

Application to battery materials

6 Intercalation in $LiFePO_4$[1]

»Phase transformations and ordering effects in cathode materials can lead to a multitude of energetically favourable states marked by coexistence of phases and, thus, plateaus in the open-circuit voltage. A very well-known example is the commercialized, phase separating $LiFePO_4$ (LFP) [198], but also very promising cathode materials for sodium-ion intercalation batteries feature phase separation and pronounced volumetric expansion upon cycling due to the larger ionic radius of sodium [29, 31]. Typically, these materials are based on a reversible intercalation mechanism and have highly anisotropic properties on the crystalline scale. Degradation mechanisms such as fracture and disintegration of agglomerated particles strongly depend on the primary particle size and morphology which is why, in this context, the discussion of particle morphology is crucial for battery performance. Taylored design of agglomerated particles and the overall electrode structure can lead to beneficial multi-particle behaviour and influence overpotential, percentage of active particle population, accessible capacity, rate capability and other kinetic aspects [199]. The strongly coupled effects of electro-chemical and mechanical driving forces on the microscale are difficult to access from experiments but simulations can help to shed some light on the local effects influencing the overall cell behaviour. While this endeavor can surely only be adressed by a combination of simulation approaches across the scales, we want to elaborate on the contribution of the phase-field method and point out links to other methods.

[1] The content of this chapter is taken verbatim from the article Daubner *et al.* [36]. Figures have been adjusted to the format of this dissertation.

Han *et al.* [74] modelled diffusion of intercalated ions employing the phase-field method, motivated by the idea that Fickian diffusion is not sufficient to describe transport inside cathode particles with large concentration gradients as in the phase-separating Li_XFePO_4. This material exhibits a large miscibility gap which results in a voltage plateau over almost the entire composition range of $X \in [0, 1]$ at room temperature [198]. The regular solution free energy introduced in [74] is relatively simple, yet adequate to describe the neighbouring interactions of intercalated ions in the bulk. Following the principle of linear irreversible thermodynamics, the species flux is then driven by the gradient of diffusion potential, hence it could be shown that diffusion coefficients can be reliably determined by GITT measurements [74]. Since then, LFP has become the drosophila of many modeling efforts involving first-principle calculations [9, 24, 43, 48, 49], Kinetic Monte Carlo (KMC) simulations [52, 200, 201] and the phase-field method [82–85, 87, 202].

Density Functional Theory (DFT) is tailored to investigate bulk properties of crystalline materials such as diffusivity, elastic constants, stable phases and the related equilibrium voltage curve. It can furthermore be employed to investigate the chemical interfacial energies between coherent phases as well as surface energies in vacuum. Morgan *et al.* [43] used first-principle calculations to determine the diffusion path and associated energy barrier in LFP, predicting 1D diffusion and kinetic limitation due to electronic conductivity rather than Li diffusivity. This study was later extended to include defects in the crystal, in order to estimate the particle size dependence [9]. The calculation of elastic constants [48] in combination with anisotropic chemical interfacial energies [49] can be used to estimate the thermodynamically stable interface orientation of the phase-separated state. The results are size- and morphology-dependent and based on the assumption of equilibrium, meaning that kinetic effects are neglected. These techniques are very helpful in identifying promising intercalation materials and predicting some of their inherent material properties.

While the above-mentioned material properties of intercalation compounds can be studied using first-principle calculations, there are many relevant phenomena

with time and length scales that are only accessible using continuum methods like the phase-field approach [24]. Nucleation and growth, the interplay of chemical and mechanical driving forces as well as the collective behaviour of many interconnected particles are highly relevant but cannot be investigated by DFT. Efforts to bridge the gap between ab-initio simulations and phase-field studies based on empirical parameter fits have been undertaken using KMC [200]. This approach allows to study bulk and surface effects in small crystalline sections and is able to predict ordering, nucleation and growth behaviour purely based on DFT data. In this work, we want to elaborate if the direct scale bridging between phase-field and ab-initio methods is possible and check if the calculations are consistent with other investigations.

Therefore, we discuss two phase-field approaches and underlying assumptions that can be employed to gain a better understanding of the non-equilibrium behaviour of intercalation compounds. The first is based on the *Cahn-Hilliard equation* [111, 112] and well-suited to model bulk diffusion in single crystals including phase transformations on the same parent lattice (i.e. coherent interfaces between the phases). The second approach is the more general multiphase-field framework [124, 129, 143] based on *Allen-Cahn equations* for the evolution of non-conserved order parameters in combination with the evolution of diffusional potential based on the grand-chemical potential [144, 145]. This framework has been sucessfully combined with elastic driving forces based on jump conditions [165, 167] to model martensitic transformations [140], crack propagation [203–205] and the evolution of electric field to study electromigration [206]. It has further been shown that grain boundary diffusion [207] as well as the instability leading to phase separation in the miscibility gap [110] can be effectively modelled. The aim of this work is to show the potentials of both approaches for the numerical screening of promising intercalation electrode materials while also discussing their complementary range of applicability and their limitations due to modeling assumptions.

6.1 Materials and methods

6.1.1 Material data for $LiFePO_4$

The charge and discharge of $LiFePO_4$ is accompanied by a first-order phase tranformation $FePO_4 \rightarrow LiFePO_4$ between lithium-rich and poor olivine phases exhibiting a large miscibility gap [198]. This leads to a voltage plateau of the open circuit voltage at 3.422V measured against pure metal anode with a residual voltage gap of about 10mV, even after very slow cycling with $C/1000$ [25]. The lattice constants a, b and c of both phases given Tab. 6.1 have been measured in various experimental works [33, 198] with very low variation. Normal eigenstrains ε^0 along the primary crystal axes can be calculated as $\varepsilon_a^0 = (a_{\mathrm{LFP}} - a_{\mathrm{FP}})/a_{\mathrm{FP}}$ and are given in Tab. 6.1.

Table 6.1: Phase characteristics taken from [33]

Parameter		**$FePO_4$**	**$LiFePO_4$**	ε^0
Lattice	a	9.826	10.334	5.2%
constants	b	5.794	6.002	3.6%
in $\mathring{A}$	c	4.784	4.695	−1.9%

The calculated normal strains are equivalent to the values used in other works [85, 107] and are strongly direction-dependent. The orthorombic olivine structure of $LiFePO_4$ is anisotropic in many more properties such as diffusion, surface energies, elastic constants and surface redox potentials. Elastic constants can be gained from DFT calculations [48]. Surface energies are also highly anisotropic and can be computed from DFT simulations [50, 51]. The corresponding Wulff shape shows a crystal with large (010) facets for both FP and LFP. This result is consistent with the nano-platelets gained by hydrothermal synthesis [33, 208].

When phase separation occurs in an Li_XFePO_4 particle with average composition X, an intra-particle interface is present. The energy penalty for this event is given by the combination of chemical intefacial energy $\gamma_{\text{LFP-FP}}$ scaled by interfacial area and the coherency strain accomodated across the particle. The latter is highly dependent on the boundary condition. The chemical interfacial energies for an LFP-FP interface have been computed via DFT [49] and are given in Tab. 6.2. The interplay of anisotropies plays a significant role on the formation of phase

Table 6.2: Interface energies of LFP-FP interface [49]

Orientation	**(100)**	**(010)**	**(001)**
$\gamma_{\text{LFP-FP}}$ in $[\text{J}/\text{m}^2]$	0.115	0.007	0.095

separation, especially as they scale differently with particle size. Regimes where different interfaces are energetically favourable can be predicted.

Diffusion is confined to 1D channels along the b-axis, which has been shown experimentally [33] and through theoretical calculations [9]. The diffusion anisotropy varies with defect concentration and is, therefore, size-dependent. Under the assumption that the diffusivities scale similarly with temperature in all three directions, we use the values at an average defect concentration of $\rho_{\text{defect}} = 0.05$ (and show them for $\rho_{\text{defect}} = 0.005$ for comparison in Tab. 6.3).

Table 6.3: Li-vacancy self diffusion coefficient D_{Li} at $T = 300K$ [9] given in $[\text{m}^2/\text{s}]$

$\rho_{\textbf{defect}}$	$= 0.005$	$= 0.05$
(100)-direction	$3.9 \cdot 10^{-18}$	$3.9 \cdot 10^{-17}$
(010)-direction	$1.3 \cdot 10^{-14}$	$1.3 \cdot 10^{-15}$
(001)-direction	$7.8 \cdot 10^{-19}$	$7.8 \cdot 10^{-18}$

6.1.2 Cahn-Hilliard model

The multiphase-field approach presented in Chapter 2 is compared to a model based on the works of Cahn and Hilliard [111, 112] which has been used in most previous publications modeling LFP with a phase-field approach [82–85, 87, 202]. The total free energy for a nonuniform system can, in first approximation, be expressed as

$$\mathscr{F}^{\mathrm{CH}}(c,\boldsymbol{\nabla} c) = \int_V f^{\mathrm{CH}}_{\mathrm{grad}}(\boldsymbol{\nabla} c) + f^{\mathrm{CH}}_{\mathrm{chem}}(c)\mathrm{d}V \tag{6.1}$$

consisting of two contributions, namely the gradient energy and the free chemical energy. The gradient energy penalizes the gradient of concentration

$$f^{\mathrm{CH}}_{\mathrm{grad}}(\boldsymbol{\nabla} c) = \boldsymbol{\nabla} c \cdot \boldsymbol{\kappa} \boldsymbol{\nabla} c \tag{6.2}$$

and features an anisotropic parameter $\boldsymbol{\kappa}$ in the general case. For lithium iron phosphate as well as other cathode materials that exhibit a miscibility gap, the enthalpic term is usually modelled employing the simplest higher order Redlich-Kister term which leads to a symmetric free energy density with two distinct minima, also called regular solution

$$f^{\mathrm{CH}}_{\mathrm{chem,RS}}(c) = RTc_{\max}\left[c\ln(c) + (1-c)\ln(1-c) + \Omega c(1-c)\right] \tag{6.3}$$

where the parameter Ω is made dimensionless dividing by the thermodynamic pre-factor $RTc_{\max}$ as we will consider constant temperature. The diffusion potential μ can be gained from the free energy by variation $\mu = \delta\mathscr{F}/\delta c$ and is the sum of two contributions

$$\mu = \mu_{\mathrm{grad}} + \mu_{\mathrm{chem}} = -2\kappa\boldsymbol{\nabla}^2 c + \frac{\partial f^{\mathrm{CH}}_{\mathrm{chem}}(c)}{\partial c}. \tag{6.4}$$

Inserting Eq. (6.4) into a reaction-diffusion equation similar to Eq. (2.22) results in a fourth order PDE in c

$$\frac{\partial c}{\partial t} = \boldsymbol{\nabla} \cdot \left[\mathbb{M}(c) \boldsymbol{\nabla} \left(\ln \left(\frac{c}{1-c} \right) + \Omega(1-2c) - 2\kappa \boldsymbol{\nabla}^2 c \right) \right] + R(c,t). \quad (6.5)$$

The ionic mobility is assumed to take the form $\mathbb{M}(c) = \mathbb{D}_0 c(1-c)/RTc_{\max}$. The mass-conserving case without source term is typically referred to as *Cahn-Hilliard equation*. Considerable effort has been undertaken to include concentration dependent eigenstrains and the corresponding elastic energy into this framework. Some works are formulated in the small deformation regime [84, 88, 100, 103, 106] while others account for large deformations [89, 93]. Fracture mechanics has also been sucessfully coupled [93, 103]. Note that a simplified version of coherency strain is used for the 1D analysis in Sec. 6.2.2. while a more sophisticated treatment such as in the above-mentioned works is out of scope if this work.

6.1.3 Modeling assumptions

In the simplest case we investigate a cathode which consists of only one particle which is equivalent to the assumption of many particles that undergo the exact same process simultaneously. We start from the assumption of a platelet-like morphology and conduct two types of simulations:

- **Bulk kinetics:** We investigate the relaxation into the phase-separated state from a solid solution (i.e. spinodal decomposition) which captures the physics of quenching experiments like [209]. This scenario is rather academic but yields valuable insight into the bulk diffusion behaviour decoupled from the effects of electro-chemical reaction. This allows us to test the validity of the phase-field model including strongly anisotropic mobilities and surface enegies. Effects on the nanoscale are captured and discussed to motivate the dimensionality reduction for the following simulations.

- **Charge and discharge:** Charging a battery with constant current is a typical use-case. The applied overpotential and possible phase tranformations are highly dependent on the morphology of primary particles or agglomerates as well as possible diffusion pathways.

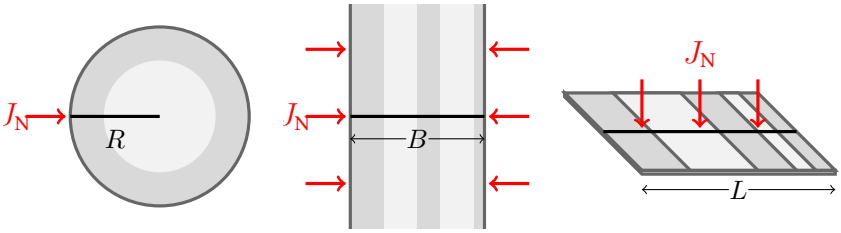
Following [33], only the ac-plane is active for Li extraction and insertion in our simulations. The interface between FP and LFP is assumed to be coherent [85] and, thus, should have an interfacial energy lower than 0.2 J/m [84]. We therefore employ the values presented in Tab. 6.2. For the CH-model, the gradient energy parameter $\boldsymbol{\kappa}$ is also direction-dependent and is fitted to reproduce the chemical interface energies given in Tab. 6.2. The maximal concentration of intercalated ions $c_{\max} = 22809\,[\mathrm{mol/m^3}]$ is computed from the lattice parameters in Tab. 6.1 and accounts for four intercalation sites per unit cell. The enthalpy of mixing $\Omega = 0.115\,e\mathrm{V/Li}$ is taken from Cogswell *et al.* [84].

6.2 Results and discussion

6.2.1 Dimensionality reduction

Dimensionality reduction affects the overall model formulation as the results are heavily influenced by the underlying assumptions. First, we discuss various modeling approaches in one dimension because this type of reduced model is often used in the context of porous electrode modeling (e.g. P2D models like MPET [73]). Typical ways to reduce dimensionality are sketched in Fig. 6.1. The assumption of a particle with spherical symmetry in Fig. 6.1a is quite common in P2D models, but has to be treated with care for materials undergoing phase transformations as it tacitly introduces the notion of a core-shell structure. In a chemo-mechanical model, this automatically leads to high hoop stresses for phase separation during charge and discharge if there is a lattice mismatch between ion-rich and ion-poor phases. Furthermore, material parameters are assumed to be isotropic due to the symmetry condition. The core-shell structure and material isotropy are contradictory to experiments and the known material

parameters, especially for highly anisotropic materials such as $LiFePO_4$, which is discussed here.



(a) 1D spherical particle **(b)** 1D slab **(c)** 1D thin crystal

Figure 6.1: Simulation setup for particle intercalation study.

The 1D slab approach in Fig. 6.1b assumes a finite width B but infinite extension in the other two dimensions. Phase separation occurs as moving planar fronts along the cross-section of the slab. Different directions in the crystal lattice can be investigated in an isolated manner, which allows anisotropies to be studied to some extent. Mechanical stresses are expected to be highly overestimated as the boundary conditions (1D equivalent to plane strain) do not allow for stress relaxation in the tranverse directions. The third approach in Fig. 6.1c is different in the sense that it reduces one dimension by symmetry and the other by volume averaging. The ion composition is averaged in the thin dimension (assuming fast diffusion and filling in that direction) and another dimension is again reduced assuming infinite extension of the plate. The surface flux then turns into a volume source term. Mechanical stresses can be expected to be more realistic as the thin dimension is assumed to be a stress-free surface, thus allowing for some stress relaxation. The correct choice of a reduced model is material specific and should reflect the dominant material anisotropies. A comparison between the different options can be carried out e.g. with the open-source framework MPET [73] which includes the geometries sketched in Fig. 6.1 and, furthermore covers phase-separation.

6.2.2 Bulk kinetics

In their review, Malik *et al.* [199] come to the conclusion that there are three relevant length-scales that need to be considered to accurately model the kinetics in LFP, namely the bulk, the single-particle and multi-particle scales. In this section, we start off with bulk diffusion on the nano-scale to draw first conclusions which are relevant for modeling of the other two scales. The Cahn-Hilliard model presented in Sec. 6.1.2 naturally describes the process of phase separation by diffusion well within the spinodal region, which is why we employ this model throughout this section. Starting from a solid solution with some random fluctuations, we conduct relaxation simulations in three possible 2D cross-cuts, shown in Fig. 6.2. We employ no-flux boundaries and neglect all surface effects at the electrolyte interface. The respective third dimension is reduced assuming symmetry such that the relaxation within planes can be investigated in an isolated manner. The results in Fig. 6.2 suggest that the fastest and thus preferred path to reduce the overall energy in the system is phase separation along the b-axis which leads to very fine striping. The wavelength of fluctuations is in the order of lattice parameters and the predicted interfacial width in the b-direction is $l_{010} = 1.96 \cdot 10^{-10}\,\mathrm{m}$. The spatial scale of striping is below the optical resolution of many experimental works such that the composition would appear homogenous. These simulations qualitatively agree with the finding that there are ordered states of alternating filled and empty ac-planes that minimize the overall energy in comparison with a disordered solid solution [200, 210]. Further reduction of interfacial energies by coarsening of the striped pattern would lead to an ac-interface between lithium-rich and -poor phases over time as has been observed in quenching experiments by Chen *et al.* [209]. The two main reasons for this behaviour are the comparatively small interfacial energy in the b-direction combined with the mobility of ions which is orders of magnitudes higher within the (010)-channels. It should be noted that it is difficult to quantitatively match the reduced energy states for ac-ordering presented in [210] with phase-field simulations. Energy values strongly depend on the free energy function and in this specific case on the choice of the enthalpy of mixing Ω for the regular solution.

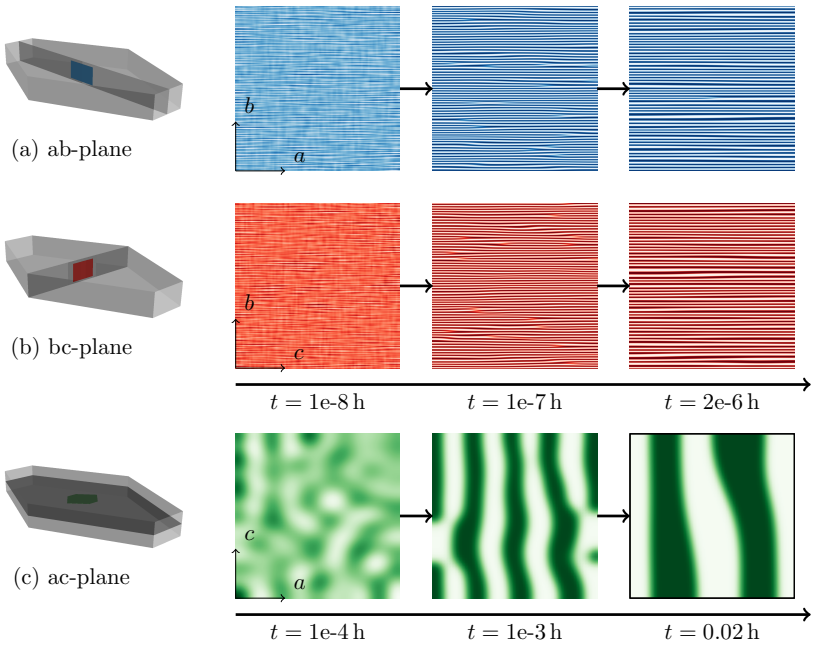


Figure 6.2: Virtual quenching experiment with relaxation from solid solution with $c_{\text{init}} = 0.5$ in 50×50 nm 2D cross-sections. Three timesteps of temporal evolution are shown for (a) the ab-plane, (b) the bc-plane and (c) ac-plane. Both simulations including the b-axis show phase separation on much smaller spatial and time scales compared to the ac-plane. All simulations assume symmetry (infinite extension) in the third dimension and have no-flux boundaries.

The formation energies calculated with DFT refer to 0 K but simple superposition with an ideal solution as in Eq. (6.3) does not reproduce the experimentally observed miscibility gap.

The dynamics of spinodal decomposition in the early stage can be derived using Fourier analysis of fluctuations in the initial solution [113]. The derivations only hold for the one-dimensional case and $\int (c - c_0) \mathrm{d}x = 0$ which basically implies a closed system with no-flux BCs. For a fluctuation of the form $(c - c_0) = A\cos(\frac{2\pi}{\lambda}x)$, we can derive the critical and maximum wavenumber

$$\beta_c = \frac{2\pi}{\lambda_c} = \sqrt{\frac{-\partial^2 f/\partial c^2}{2\kappa}}, \quad \beta_{\max} = \beta_c/\sqrt{2}.$$

To estimate the influence of coherency strain on the resulting pattern formation, we add another free energy contribution $f_{\mathrm{el}}^{\mathrm{CH}}(c)$ to our analysis. Coherency strain due to a change in molar volume is introduced assuming linear dependence of the eigenstrain on the local composition fluctuation $c - c_0$ for orthotropic material properties (which is a generalization of the isotropic case in [112])

$$f_{\mathrm{el}}^{\mathrm{CH}}(c) = \frac{1}{2}\boldsymbol{\sigma} : [\boldsymbol{\epsilon} - \boldsymbol{\epsilon}^*] = \frac{1}{2}\Psi(\boldsymbol{n})(c - c_0)^2. \tag{6.6}$$

The direction-dependent parameter $\Psi(\boldsymbol{n})$ is derived assuming a 1D slab with free ends but infinite extension in the transverse directions (1D equivalent of plain strain). The eigenstrain is modelled assuming linear dependence on the composition fluctuation and the stretch factors are given with reference to the fictitious solid solution $Li_{0.5}FePO_4$ such that

$$\boldsymbol{\varepsilon}^0 = \begin{bmatrix} \eta_a & 0 & 0 \\ 0 & \eta_b & 0 \\ 0 & 0 & \eta_c \end{bmatrix} (c - c_0), \tag{6.7}$$

with $\eta_a = (a_{\mathrm{LFP}} - a_{\mathrm{FP}})/(a_{\mathrm{LFP}} + a_{\mathrm{FP}}) = 2.52\,\%$, $\eta_b = 1.76\,\%$ and $\eta_c = -0.94\,\%$. Stresses are computed assuming linear elasticity and small deformations by employing an averaged stiffness $\mathbb{C} = 0.5(\mathbb{C}_{\mathrm{FP}} + \mathbb{C}_{\mathrm{LFP}})$ from the tensors given in [48].

Following the procedure in [112], we assume stress-free boundaries in longitudinal direction and infinite extension in the other two dimensions. The resulting local elastic strain energy is given examplarily for the a-direction

$$f_{\text{mech}}^{\text{CH}}(c) = \frac{1}{2}\left(\left(C_{22} - \frac{C_{12}^2}{C_{11}} \right) \eta_b^2 + 2 \left(C_{23} - \frac{C_{12}C_{13}}{C_{11}} \right) \eta_b \eta_c + \left(C_{33} - \frac{C_{13}^2}{C_{11}} \right) \eta_c^2 \right) (c - c_0)^2 \tag{6.8}$$

$$= \frac{1}{2} \Psi_a (c - c_0)^2 \tag{6.9}$$

where we introduce the direction dependent elastic factor Ψ_a. Factors for all three lattice directions can be computed with the same procedure and, furthermore, dedimensionalized by dividing with the thermodynamic pre-factor $RTc_{\max}$

$$\tilde{\Psi}_a = 56.37 \text{ MPa}, \quad \tilde{\Psi}_b = 82.89 \text{ MPa}, \quad \tilde{\Psi}_c = 176.30 \text{ MPa}, \tag{6.10}$$

$$\Psi_a = 0.99, \quad \Psi_b = 1.46, \quad \Psi_c = 3.10. \tag{6.11}$$

The second derivative of energy densities with respect to c then reads

$$\frac{\partial^2 f}{\partial c^2} = \frac{1}{c_0(1-c_0)} - 2\Omega + \Psi \tag{6.12}$$

for the initial case of negligibly small ∇c. From this and Eq. (6.5), the exponential factor describing the rate of fluctuation growth $(c - c_0) = \exp[R(\beta)t]\cos(\beta x)$ can be computed depending on the initial concentration c_0 and corresponds to the wavelength of the fastest growing unstable fluctuation $\lambda^{\max}$

$$R_{\max}(c_0) = M \frac{(\partial^2 f / \partial c^2)^2}{8\kappa} = \frac{D c_0 (1-c_0)}{8\kappa} \left(\frac{\partial^2 f}{\partial c^2} \right)^2 \Bigg|_{c_0} \tag{6.13}$$

$$\lambda^{\max}(c_0) = \frac{2\pi}{\beta_{\max}} = \frac{4\pi\sqrt{\kappa}}{\sqrt{2\Omega - \Psi - \frac{1}{c_0(1-c_0)}}}. \tag{6.14}$$

Inserting the values for $LiFePO_4$, we compute the amplification factors for the purely chemical case, where $f = f^{\mathrm{CH}}_{\mathrm{chem}}$, and for the coupled case accounting for coherency strains $f = f^{\mathrm{CH}}_{\mathrm{chem}} + f^{\mathrm{CH}}_{\mathrm{el}}$. The results are plotted in Fig. 6.3.

Generally, we observe negative $R(\lambda)$ for very small wavelengths (which means cancellation), while between the critical wavelengths all fluctuations are amplified. The amplification factor features a distinct peak at $\lambda^{\max}$, indicating that we expect phase separation within a small interval of wavelengths around the peak value. The visualization of $R_{\max}(c_0)$ in the middle row of Fig 6.3 reveals two more details. First, the overall maximal amplification can be found for $c_{\mathrm{init}} = 0.5$ due to the symmetry of f. Secondly, amplification tends towards zero as the initial composition approaches the spinodal. This has been discussed by Cahn [112] and implies that this model cannot describe nucleation as it does not allow for growth of small but finite fluctuations i.e. nuclei. The comparison of lattice directions (100) and (001) clearly shows that amplification factors are higher along the a-axis. In both cases, coherency strain delays phase separation by reducing the amplification factors. Additionally, there is a small shift of the maximal amplification towards higher wavelength as can be seen in the top row for $c_{\mathrm{init}} = 0.5$ and for all $c_{\mathrm{init}} \in [0,1]$ in the bottom row subfigures of Fig. 6.3. Applying the same analysis to the b-axis reveals that the spatial scale as well as the time scales differ drastically. While the exponential growth of fluctuations in the a-axis is in the order of $1/R_{\max} = 1\,\mathrm{s}$, the predicted phase separation along the b-axis is in the order of $10^{-4}\,\mathrm{s}$. Furthermore, much smaller fluctuations are excited, leading to expected wavelengths smaller than 1 nm which is in the order of the lattice parameters (compare Tab. 6.1).

The mechanical contribution generally reduces the amplification of phase separation and in the specific case of the b-direction by a factor of 2.0. However, this reduced value is still four orders of magnitude larger compared to the other

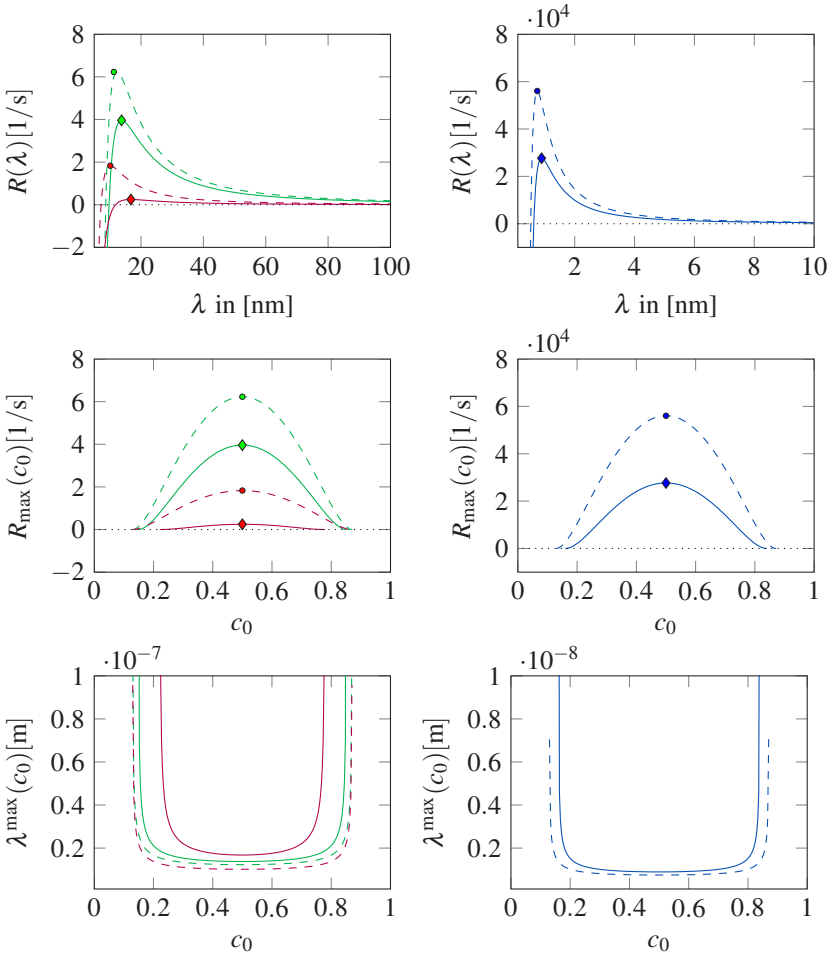


Figure 6.3: Amplification factors for unstable fluctuations in the (100)-direction shown in green and in the (001)-direction shown in red in the left column. Unstable fluctuation in the (010)-direction are shown in the right column in blue. The dashed lines represent the purely chemical case while the solid curves include the additional influence of coherency strain. The top row shows the amplification factor depending on the wavelength of the fluctuation for $c_{\text{init}} = 0.5$.

two directions which means that even with inclusion of coherency strain, ordered states and phase separation in the b-direction will be observed. We conclude that diffusion kinetics has a strong influence on the resulting pattern formation. Quantative phase-field modeling that resolves this smallest scale needs to reflect the strong anisotropies of diffusion, interfacial energies and stiffness to yield meaningful results. Results obtained under the assumption of isotropy, which can either be introduced implicitely by spherical symmetry (see Fig. 6.1a) or explicitly by using a scalar value for the gradient parameter κ, are highly questionable. From a numerical point of view, the strong anisotropy of LFP poses a severe challenge for simulation studies. The small spatial scale of striping limits the overall accessible time and length scales to such an extent that simulation of full or half cycles with technically relevant C-rates becomes infeasible with our code. Furthermore, the chosen simulation setup only captures bulk effects, while the inclusion of surface energy effects at the particle-electrolyte interface is likely to alter the observed phase separation [100]. Surface diffusion and ion exchange with the electrolyte at zero net current enable diffusion across the b-channels which could promote faster phase separation at the particle surface. These could be the thermodynamic reasons for the observation that $LiFePO_4$ forms at the surface while a solid-solution remains within the particle for quenching of Li_XFePO_4 with $X > 0.6$ [209].

The remaining question is: How can homogenization be applied to access larger time and length scales using the phase-field method? We argue that the results in Fig. 6.2 could be interpreted as a solid solution with ordering, coinciding with the results in [200, 210, 211]. The effective, homogenized free energy landscape should be altered compared to the case of a disordered solid solution. However, the phase-field model fails to predict an effective mobility of ions because of its continuum assumptions regarding Fickian diffusion for an ideal solution. A quantitative homogenization should be the goal of future investigations and we are confident that this issue can be addressed by a collaboration of phase-field and KMC methods [200, 201]. While micron-sized particles are likely to be dominated by diffusion limitations [86] and stress effects [114], intermediate solid-solution states have been observed in nano-sized platelets at technically relevant

C-rates [211]. This observation motivates homogenization by depth-averaging in the b-direction for thin platelets as sketched in Fig. 6.1c. Not resolving the atomistic length scale, we neglect ordering effects and phase separation in the 010-direction and replace the local composition variable $c(x,y,z,t)$ with the averaged $\bar{c}(x,y,t) = 1/H \int c(x,y,z,t)\mathrm{d}z$ [82]. This simplification is the basis for the simulation studies in the following section.

6.2.3 Galvanostatic charge and discharge

Based on the assumptions that, first, only (010)-facets are active for the electrochemical insertion reaction [33] and secondly, that phase boundary migration progresses according to the domino cascade mechanism [121], the depth-averaged model sketched in Fig. 6.1c has been formulated [82]. In combination with the boundary condition of galvanostatic (dis-)charge in Sec. 2.6, we can investigate the intercalation behaviour. Due to the depth-averaging, the surface flux turns into a bulk source term $R(c,t)$ with local dependence on filling fraction. There are two possible assumptions for the in-plane diffusion of intercalated ions, namely

- The limit of $D_{\mathrm{Li}}^{(100)} \to 0$ and $D_{\mathrm{Li}}^{(001)} \to 0$ describes a perfect crystal where diffusion is confined to 1D channels along the b-axis. The model reduces to a reaction equation in the ac-plane, which is why this model has been called *Allen-Cahn-reaction model* (ACR model) [82, 99].

- The presence of crystal defects lowers the diffusivity in the b-direction and furthermore allows for diffusion in the ac-plane. The underlying model is a reaction-diffusion equation and can be computed employing the diffusivities in Tab. 6.3 for various defect concentrations. Accounting for surface diffusion, leads to the same evolution equation for ion composition [212]. So in the general sense, the diffusivity in the depth-averaged model could be interpreted as the effective in-plane diffusivity combining bulk and surface effects.

Both cases are simulated and compared in the following. We use a reference cell voltage of $V_{\text{ref}}^{\ominus} = 3.422\,\text{V}$ (see Fig.6.4) and the pre-factor $k_0 = 10^{-2}$ for the Butler-Volmer equation [172] if not stated otherwise.

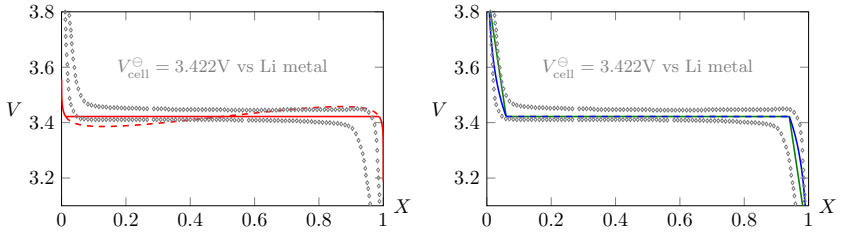


Figure 6.4: Open circuit potential V_{OCV} over filling fraction X in Li_XFePO_4. Gray data points are taken from Dreyer *et al.* [25] at C-rate $1/20$ and mapped to the average filling fracion X under the assumption that all Li can reversibly inserted and extracted. A regular solution fit according to Eq. (6.3) with Ω taken from [84] is shown in a). Quadratic (green) and logarithmic (blue) chemical energy fits for the Allen-Cahn model are shown in b).

Starting from an initially homogenous filling fraction of $c_{\text{init}} = 0.01$ including some random noise with amplitude $A = 0.001$ to account for thermal fluctuations, several C-rates are applied to study the coupled effects of reaction and diffusion. Coherency strains are neglected in this section.

We start with the ACR model and apply C-rates $C \in [2^{-6}, 2^{-5}, ..., 4]$ 1/h. The results in Fig. 6.5 imply that phase separation (which is characterized by a plateau in the voltage plot and a high composition difference $c_{\max} - c_{\min}$ in the domain) can be suppressed for high currents. In the present case, the limit lies around C-rate$= 0.1$, but it should be noted that this value is highly dependent on the choice of the parameters k_0 and the thickness H of the depth-averaged crystal. The critical current to suppress phase separation can be expressed more generally by means of the non-dimensional flux ratio

$$\frac{i}{i_0} = \frac{I}{A_{\text{reac}} i_0} = \frac{\text{C-rate} \times H \times F \times c_{\max}}{2k_0}, \tag{6.15}$$

where I denotes the total flux according to Eq. (2.40) in [mol/s] and A_{reac} is the active surface area (in this case $2LB$). The averaged reaction flux is scaled to the characteristic reaction flux $i_0 = k_0/F$ which is a material surface property. If we allow for bulk diffusion in the simulated plane, the stability limit to suppression of phase separation changes drastically. This can be seen by comparison of the hysteresis for C-rate=1 in Fig. 6.5c. While the assumption of a perfect crystal (ACR limit) predicts suppression of phase separation, the other two cases

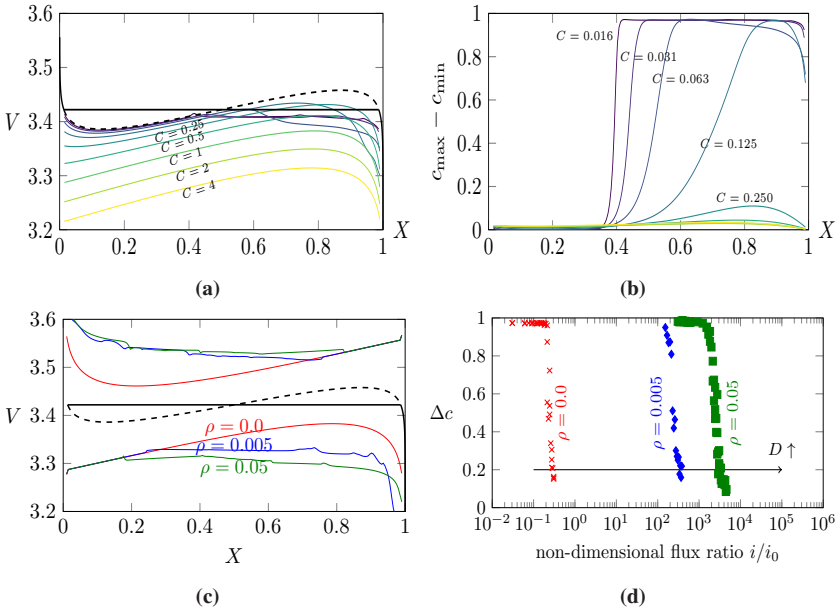


Figure 6.5: Rate-dependent charging behaviour obtained with the Cahn-Hilliard approach (Sec. 6.1.2). Subfigure a) shows the resulting voltage for boundary varying C-rate $C \in [2^{-6}, 2^{-5}, ..., 4]$ 1/h and a constant thickness of $H = 50$ nm. The equilibrium case is drawn in black. The maximal concentration difference over time is shown in b) indicating a transition from phase separation to solid solution around $C = 0.1$. The influence of in-plane diffusion on phase separation is added in c) and d). For C-rate= 1 and defect concentrations $\rho_{\text{defect}} = \{0.0, 0.005, 0.05\}$ the voltage profile V is shown in c). The maximal occuring composition difference $\Delta c = \max(c_{\max} - c_{\min})$ over the non-dimensional flux ratio is given in d) illustrating the transition to solid solution behaviour depending on ρ.

with assumed defect concentrations of $\rho_{\text{defect}} = 0.005$ and $\rho_{\text{defect}} = 0.05$ exhibit large voltage plateaus caused by the two-phase coexistence. There can still be suppression of phase separation but it shifts to higher C-rates (i.e. higher non-dimensional flux ratios) if in-plane ion transport is possible.

The depth-average assumption enforces the same electro-chemical potential in the bulk as on the surface of the active facets, which is why the dynamic suppression of phase separation at high charging rates is very sensitive to the free energy formulation. Employing the experimentally motivated energy fits shown in Fig. 6.4b will consequently alter the onset of phase separation. Another significant difference between the two modelling approaches outlined in Sec. 6.1.2 and Chapter 2 is that within the multi-phase field approach, the phase transition from FP to LFP is modelled as a first-order transformation while the Cahn Hilliard model describes the change of composition as a second-order transformation. As a consequence, the LFP phase occurs once an energetic barrier imposed by the obstacle potential is overcome which is independent of the charging rate. This is confirmed by the results in Fig. 6.6a in which the onset of the first-order phase transformation is initiated at the same average composition but then proceeds at different speeds depending on the imposed charging rate.

Another important factor that alters the observed phase separation is the inclusion of coherency strain. Instead of suppressing phase separation dynamically, the stored elastic energy due to lattice mismatch changes the energetic equilibrium. As can be seen in Fig. 6.6 and Fig. 6.7, a complete demixing into areas of FP and LFP becomes unfavourable while intermediate composition states are promoted. Note that in this study we assumed traction free boundaries such that the nanoparticle can expand freely. Stresses only arise due to phase separation within the computational domain. The evolution of composition and coupled principle stresses is shown exemplarily for a C-rate of 0.25 at a low defect concentration of $\rho = 0.005$ in Fig. 6.7. Due to the influence of coherency strain, larger areas of an intermediate composition form and buffer the lattice mismatch between the end-member phases FP and LFP. Interfaces tend to align with the $\{101\}$ family of crystal planes to reduce the stored elastic energy [84]. Areas with lower Li

content exhibit higher tensile stresses due to the overall lattice strain. In the right column of Fig. 6.7, we display the maximal local tensile stresses as this is the relevant stress measure for fracture in brittle materials.

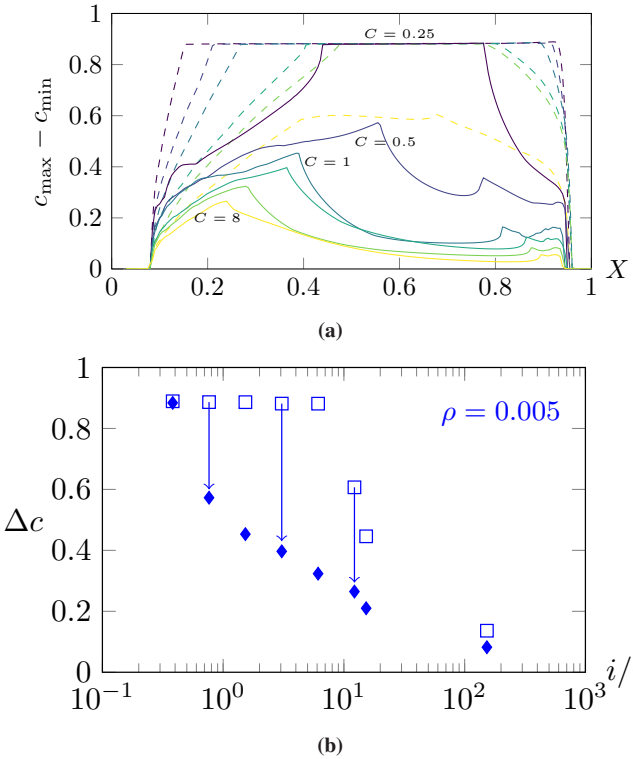


Figure 6.6: Rate-dependent phase separation upon discharge obtained with the multi-phase approach (Chapter 2). The maximal concentration difference over average filling fraction X in Li_XFePO_4 is shown in a) for varying C-rate $C \in [0.25, 0.5, 1, 2, 4, 8]$ 1/h and a constant thickness of $H = 50$ nm. Dashed lines denote simulation neglecting the influence of coherency strain while solid lines include elastic deformation. The effect of in-plane diffusion with assumed defect concentration $\rho_{\text{defect}} = 0.005$ is included. The maximal occuring composition difference $\Delta c = \max(c_{\max} - c_{\min})$ over the non-dimensional flux ratio is given in b) illustrating the transition to solid solution behaviour depending on elastic energy and C-rate. Square symbols represent simulations without elasticity and diamonds show simulations including the influence of elastic deformation.

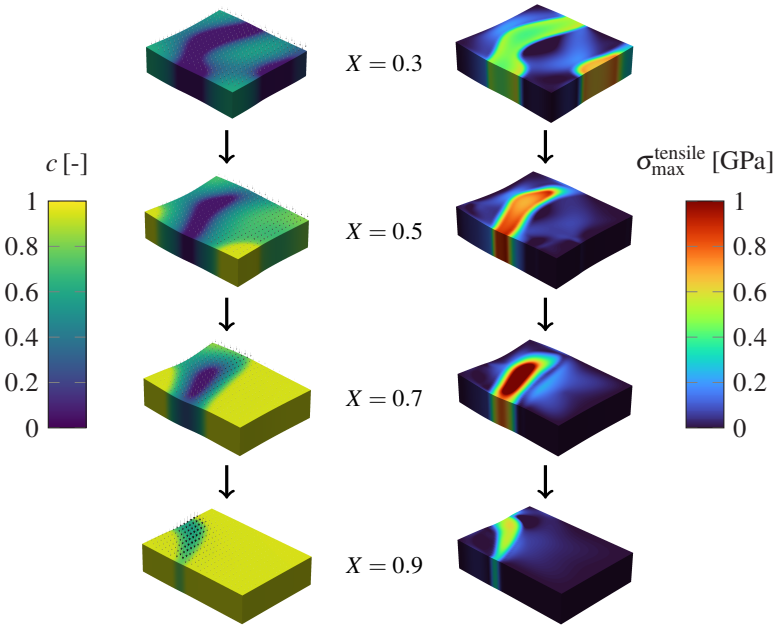


Figure 6.7: Discharge simulation of a thin platelet with dimensions $50 \times 50\,\text{nm}$ under the depth-average assumption using the multi-phase approach including coherency strain. X denotes the average filling fraction in Li_XFePO_4 while the local composition c is indicated by the green color scale in the left column. The arrows indicate the magnitude of reaction flux vectors and illustrate how the reaction flux intensity follows the front of phase transformation. The right column shows the maximum principle stress in GPa. Stresses and strains are computed fully 3D and at all surfaces we apply homogenous Neumann boundary conditions. Displacements resulting from lattice expansion are superposed with a magnification of 5.

Generally, as soon as phase separation occurs, the reaction flux becomes highly non-homogenous across the domain. It can easily be shown that the formulation of the Butler-Volmer equation Eq. (2.36) favours electro-chemical reaction at the phase boundaries between high and low concentration phases [87, 213]. This is also observed in all (dis-)charge simulations exhibiting phase separation and shown exemplarily in Fig. 6.7. Starting from a homogenous flux distribution inside the domain, the flux then concentrates on the interfacial areas as soon as phase separation occurs. The reaction flux intensity follows the phase fronts as

the particle gets filled. In this sense, the suppression of phase separation is not only favourable to avoid high tensile stresses, which likely promote mechanical degradation, but it also leads to a more homogenous flux distribution across the active facet reducing the probability of parasitic side reactions due to high local fluxes and overpotentials. These results illustrate the importance of correct modeling of the electro-chemical reaction at the electrode-electrolyte interface. The assumption of constant flux (locally- as opposed to globally-constant flux which reflects the CC charge) is only valid for non-phase-separated states and small concentration gradients on the surface. Furthermore, it is compliant with the 1D spherical model (see Fig. 6.1a) as the prescribed shrinking core features the same surface concentration.

6.2.4 Multigrain systems

The simulations in the previous sections shed some light on the possible phase transformations and the interplay of electro-chemo-mechanical forces in single crystals. The obtained voltage curves are valid in the limit of a single particle getting charged or many particles undergoing the exact same process. The actual multi-particle behaviour in battery electrodes is, however, much more complicated. In a multi-particle system, the state of charge does not necessarily coincide with the average composition in each particle. Instead, there are many thermodynamic states that minimize energy and the actual ion distribution is history-dependent [199]. It is energetically favourable for the phase transition $FePO_4 \rightarrow LiFePO_4$ to proceed in a particle-by-particle manner, i.e. to have inter-particle instead of intra-particle phase separation [121, 214], sometimes referred to as mosaic pattern [214]. This fact also leads to the non-vanishing hysteresis in the limit of C-rate$\rightarrow 0$ [25]. LFP is mostly produced as single crystals and phase-field simulations thereof have sucessfully shown the current dependency of the active particle population [215]. We investigate the more exotic case of polycrystalline particles [216] to check if the concept of transition from particle-by-particle to concurrent intercalation still applies.

We employ the multiphase-field model described in Chapter 2, still under the assumptions made for the depth-averaging, to extend the previous simulations. Depth-averaging now implies the rather strong assumptions of perfectly interconnected crystals and equal alignment of the b-axis. As the diffusivities in (100)- and (001)-direction are on the same order of magnitude, we neglect in-plane diffusion anisotropy. Note that the inclusion of orthotropic anisotropy in a single crystal simulation is rather straight forward due to grid-aligned discretization (e.g. using finite difference or finite volume schemes). This is, however, not the case for a polycrystalline section with arbitrary lattice orientations. More elaborate handling of the discretization of diffusion is needed to study the full effect of diffusion anisotropy in future works. A noise term enables the simulation of heterogeneous nucleation without making a priori assumptions about the nucleation site. We follow the procedure sketched in [110] to fit the model parameters which leads to $\varepsilon = 2.5\,[\mathrm{nm}]$ and $\gamma_{\text{FP-LFP}} = 0.1\,[J/\mathrm{m}^2]$ for the FP-LFP interface. The pre-existing grain boundaries are assumed to have a higher interfacial energy $\gamma_{\text{FP-FP}} = \gamma_{\text{LFP-LFP}} = 3 \cdot \gamma_{\text{FP-LFP}}$ because they are incoherent. Furthermore, we employ the quadratic chemical energy fits displayed in Fig. 6.4b which are determined by the parameters $A^{\text{FP}} = A^{\text{LFP}} = 150 \cdot RTc_{\max}\,[\mathrm{J/m}^3]$, $c_{\min}^{\text{FP}} = 0.06$, $c_{\min}^{\text{LFP}} = 0.94$ and $B^{\text{FP}} = B^{\text{LFP}} = 0$. As the phase transformations are assumed to be limited by ion kinetics (reaction and diffusion instead of attachment kinetics), we set the mobility of the phase-field evolution to $M_{\alpha\beta} = 5 \cdot D^{(100)}$. A polycrystalline section for the initial simulation setup was prepared by randomized filling employing Voronoi tesselation and subsequent phase evolution under volume conservation [217] such that higher order junctions feature equilibrium angles. We then apply various C-rates to study the influence of particle interaction. First, mechanical influences are neglected and the results for high in-plane diffusion with $\rho = 0.05$ are shown in Fig. 6.8.

For all simulations, we observe that nucleation events occuring during cycling mostly happen at higher-order junctions but also at the pre-existing grain boundaries. This is due to the lower nucleation barrier of new phases at the interface [110]. There is a clear trend that higher C-rates lead to more simultaneous

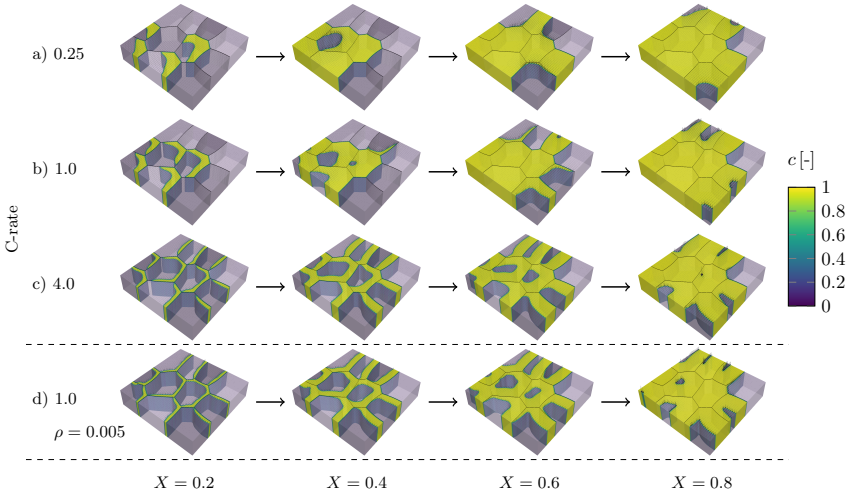


Figure 6.8: Multi-grain platelet with dimensions $250 \times 250 \times 50\,\text{nm}$ during discharge using the depth-averaged model. X denotes the average filling fraction in Li_XFePO_4 while the local composition c is indicated by the colorbar. Arrows indicate the magnitude of reaction flux vectors and are scaled to the average reaction flux. The influence of coherency strain is neglected. The top three rows show simulations based on high defect density $\rho = 0.05$ while the bottom row has $\rho = 0.005$.

nucleation events which is consistent with the observation of higher active particle population in other phase-field studies [212, 215]. At C= 0.25, the filling proceeds in a grain-by-grain manner filling one to four grains at a time. This behaviour reflects the fact that charging particles one-by-one is thermodynamically favourable in the limit of vanishing current [25]. At a C-rate of four, we observe simultaneous nucleation in all but one grain followed by pre-dominantly intra-particle phase separation during the discharging process. In this regime, the diffusivity is high enough for phase separation but not sufficient for relaxation from the intra- to inter-particle phase-separated state. Reducing the in-plane diffusivity by one order of magnitude also leads to more nucleation events. Fig. 6.8 d) shows the composition evolution with $\rho = 0.005$ at C= 1 for comparison. The resulting pattern formation of high- and low-concentration phases is comparable to the case of higher in-plane diffusion together with higher C-rate in Fig. 6.8 c).

As we have already observed in the case of the single platelet in Fig. 6.7, adding the influence of coherency strain stabilizes intermediate composition states to buffer the lattice mismatch between FP and LFP. Nucleation still occurs at multiple junctions and grain boundaries and stress peaks can be observed at the interface of high and low composition regions. In Fig. 6.9, we investigate the influence of texture, i.e. the distribution of crystallographic orientations , in a multi-grain sample. The considered cases range from complete matching of crystal alignment (strong texture) in 6.9 a) to a fully random distribution (no distinct texture)

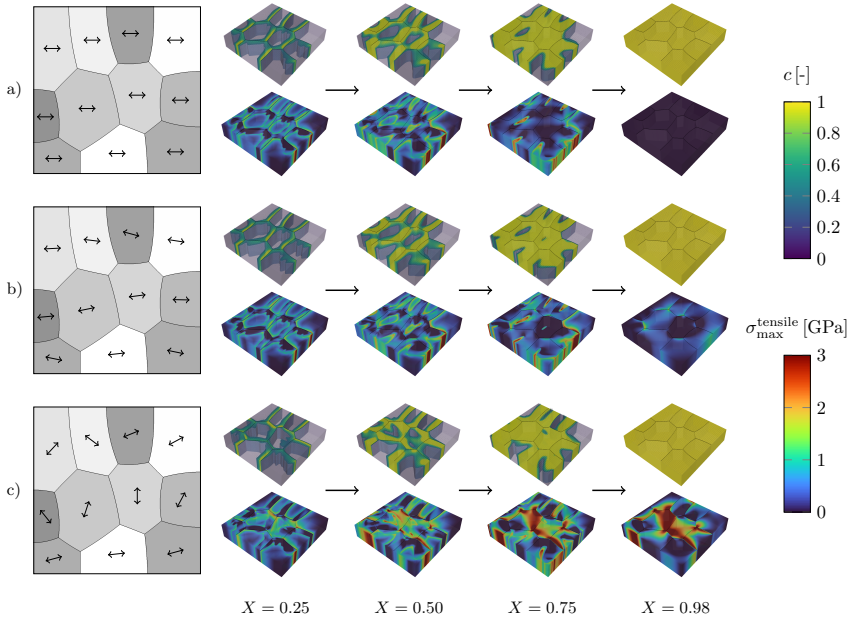


Figure 6.9: Influence of texture on mechanical stresses during discharge using the depth-averaged model. The multi-grain platelet has dimensions $250 \times 250 \times 50$ nm, X denotes the average filling fraction in Li_XFePO_4 while the local composition c is indicated by the colorbar. Arrows in the multi-grain section on the left indicate the orientation of the a-axis. The c-axis is orthogonal to the arrow while the b-direction of all grains is pointing into the sketched plane.

in 6.9 c). In all cases, we compute the fully three-dimensional stress state resulting from the phase-dependent eigenstrain with traction free surfaces as the mechanical boundary condition.

Comparison of the two textured samples (6.9 a) and b)) shows that the concentration and stress evolution is almost identical upon insertion. This stems from the fact that the phase transformation pathway in this regime is predominantly set by the C-rate and in-plane diffusivity. The biggest difference can be observed in the final state where, in the case of complete orientation alignment, all stresses vanish. For the case of small misalignment between the grains, on the other hand, a residual stress is preserved. Stresses accumulate at grain boundaries where the misorientation of neighbouring grains leads to unequal expansion and contraction within the interfacial region. In the third case of fully random crystal orientations, much higher residual stresses are observed. The two inner grains exhibit especially high tensile stresses due to their misalignment. In the final state, larger domains are subject to tensile stresses above 3 GPa and stress hotspots can be found at triple junctions with a maximum principle stress of 7.28 GPa. Hotspots of large tensile stresses are already a good indicator for possible fracture of polycrstalline materials. Future simulations could possibly include explicit modelling of fracture mechanics based on a phase-field approach [103, 104, 218].

6.3 Conclusion

In this Chapter, we discussed a new modeling approach based on the multiphase-field method in the context of previous works and basic modelling assumptions. The multi-grain studies in Sec. 6.2.4 underline the necessity to account for multiple interacting particles, especially in systems featuring phase transformations. Agglomerates and particle ensembles behave differently compared to isolated single crystals which highlights the importance of electrode morphology design for battery performance. An important step to improve the proposed modeling framework is a thermodynamically sound formulation to account for an electrolyte phase and the electro-chemical reaction in the diffuse interface. The

strong ion migration anisotropy of some intercalation compounds needs inclusion of crystal lattice orientation and anisotropic diffusivities to fully capture the occuring transport processes.

We show that the established phase-field models are able to capture spinodal decomposition as a relaxation mechanism and are furthermore able to predict a wide range of strongly coupled effects such as supression of phase separation under sufficient driving force. The newly introduced model extends existing works in the sense that multi-particle interactions including the transition from inter-particle to intra-particle phase separation for increasing C-rates up to complete suppression of phase separation can be modelled. The combination of a thermodynamically consistent model and quantitative material data yields simulation results that are in agreement with experimental observations. LFP has been used as a prominent example in this case but we expect huge potential in the field of post-lithium materials research. Thus, the multi-phasefield approach based on Allen-Cahn equations is reckoned to be promising for the in-depth analysis of phase transformation mechanisms in interacting particle ensembles.

The influence of texture in polycrystalline samples is crucial with regard to mechanical degradation. The simulations performed in Sec. 6.2.4 highlight the dependence of stress hotspots on the misorientation of neighboring grains, especially for strongly anisotropic cathode materials like LFP. The question of nanostructure design to reduce residual stresses is even more relevant for layered-oxide materials such as NMC which are typically produced as polycrystals. Studies have shown that open-pored nanostructuring can, among other benefits, increase cycle life as particle fragmentation is reduced [21]. Many promising sodium ion cathode materials are also layered oxides and produced as polycrystals [219]. Due to the larger atomic radius of sodium, many intercalation compounds undergo phase transformations coupled with large volume changes of the crystal lattice upon cycling which increases the probability of mechanical degradation. Morphology optimization by means of computational studies becomes feasible with the proposed framework.«

7 Phase transitions in the layered oxide $Na_XNi_{1/3}Mn_{2/3}O_2$

Layered oxides based on the structure Na_XTMO_2 are promising candidates for sodium-ion intercalation batteries and have received considerable attention throughout the past couple years. However, first works date back to the emergence of rechargeable batteries [8] as both lithium and sodium intercalation compounds were initially investigated. O3 and P2-type layered oxides are the most common structural polymorphs [220] where O denotes the octahedral and P the prismatic coordination of sodium ions, respectively. The number corresponds to the amount of transition metal layers per unit cell [15]. Transition metals (TMs) can be (Cu, Cr, Fe, Co, Ni, Mn, Ti, V) or combinations thereof [8, 29, 221, 222]. Some of the most promising cathode materials for Na ion batteries are based on a combination of Ni and Mn due to their comparatively high capacity and rate capability [17, 222]. The P2-polymorph of $Na_XNi_{1/3}Mn_{2/3}O_2$ shows high reversibility [29] which matches the previous findings for Na_XCoO_2 [8].

Lu and Dahn [29] first investigated the P2-$Na_XNi_{1/3}Mn_{2/3}O_2$ layered oxide and found high reversibility despite the first order phase transition from O2 to P2 around $x \approx 1/3$ which is accompanied by a significant expansion in the c-axis. Other voltage plateaus were observed below $V = 4.0$ which could later be associated with ion-vacancy orderings within the layers [30]. The cathode material has been modified in several works to increase the cycle stability. Zhang *et al.* [114] investigated Fe doped $Na_XNi_{1/3}Mn_{2/3}O_2$ to stabilize the reversibility at high operating voltage. Furthermore, the stoichiometry was changed to $Na_XNi_{1/4}Mn_{3/4}O_2$ to suppress charge ordering and study the effects on capacity retention and rate capability depending on the voltage range [223, 224].

Very little effort has been addressed to modeling and simulation of this material which is surprising given that it is one of the most experimentally investigated cathode materials for future sodium ion batteries. In the field of lithium-ion material research the amount of simulative works is ever increasing, covering all time- and length-scales from the atomic to the cell level. For investigation of material properties on the atomic level, ab-initio methods such as density functional theory (DFT) have been proven to be important in finding new promising structures [225] and identifying the electro-chemical as well as mechanical properties of known compounds [12, 24, 48, 49]. First-principles calculations are well-established to compute phase diagrams [45], ordering effects [30, 47], diffusion barriers [30], and open circuit voltages (OCV) [169].

DFT is limited to a certain amount of atoms and mostly concerned with bulk properties of crystalline structures. Free surfaces and interfaces are only accessible with high computational effort and under very strong assumptions while phase transformations and the rich interplay of surface reactions, diffusive transport and mechanical deformations are completely out of range [12]. To the best of our knowledge, little effort has been done to bridge the gap between the atomistic to the continuum level which is a crucial factor for the computational screening of cathode materials. Some fundamental aspects are well established, e.g. the relation of energies above hull with electro-chemical potentials and the resulting theoretical voltage profile [12]. The phase-field method is well suited to study intercalation dynamics in single crystals and agglomerates as has been demonstrated in studies on the commercialized $LiFePO_4$ (LFP) cathode material for lithium-ion batteries [84, 87]. This framework is especially useful for the simulation of materials undergoing phase transformations as moving surfaces are inherently difficult to track otherwise. The phase-field method has a strong thermodynamic foundation as the evolution of phases, concentration and stresses is based on minimization of the Gibbs free energy. Multi-physics problems coupling chemical, electrical and mechanical driving forces can be investigated [110, 143]. The transfer of material data from DFT to Cahn-Hilliard-type phase-field methods has been discussed by Hörmann *et al.* [24].

7.1 Material data

$Na_{2/3}Ni_{1/3}Mn_{2/3}O_2$ crystallizes in the hexagonal P63/mmc space group [30]. The primitive hexagonal unit cell contains two formula units (f.u.) as it spans two layers of sodium ions/ trasition metals and its volume is $V = \sqrt{3}/2\, a^2 c = 80.6 \mathring{A}^3$ [30]. Consequently, we compute the reference concentration for the theoretical stochiometry $Na_1Ni_{1/3}Mn_{2/3}O_2$ as $c_{\text{ref}} = 2/(N_A V_{\text{P2-2/3}}) = 41211\ \text{mol/m}^3$. All the initial sodium in $Na_{2/3}Ni_{1/3}Mn_{2/3}O_2$ can be electro-chemically extracted and reversibly inserted in the voltage range $2.0 - 4.5\,\text{V}$ [29]. Charge and discharge are accompanied by three voltage plateaus, two of which can be related to Na-vacancy ordering and the third to a first-order phase transformation [17, 29, 30]. The reversible phase transition from the O2 to P2 phase (crystalline polymorphs with AB-stacking and sodium ions reside in octahedral (O) or prismatic (P) sites) corresponds to a pronounced voltage plateau at $\approx 4.2\,\text{V}$ and has been confirmed by appearance of a new peak in the in-situ XRD [29]. The hypothesis of Na-vacancy orderings has been confirmed by DFT computations [30] and are a result of energetically favored intercalant sites. Low-energy ordered states of $Na_X Ni_{1/3}Mn_{2/3}O_2$ exist for $X = 0.33$, $X = 0.5$ and $X = 0.67$. Furthermore, the existence of these intermediate Na-vacancy ordered phases has been confirmed by in-operando synchrotron XRD [226].

We extract voltage data for $Na_{2/3}Ni_{1/3}Mn_{2/3}O_2$ from three sources [17, 29, 30] and compare the datasets in Fig. 7.1a. The comparison shows that the data from Lee *et al.* [30] exhibits a capacity larger than the theoretical capacity of 173 mAh/g which has been attributed to parasitic side reactions. The other two data sets show a close match. Generally, the charge-discharge data from Mao *et al.* [17] exhibits a smaller voltage hysteresis which could be due to the well-defined, single-crystalline morphology. Other factors such as preparation of the sodium anode, electrolyte or additives could possibly influence the results but are out of scope of this work. The following simulation studies are based on the assumption that all occuring interfaces are coherent with an interfacial energy of $\gamma_{\alpha\beta} \approx 0.1\,\text{J/m}^2$. The mobility of phase transformations is assumed to be in the order of the ionic diffusion.

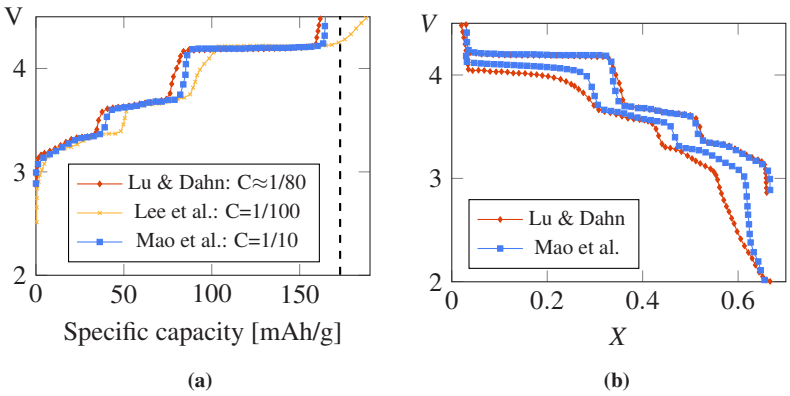


Figure 7.1: Experimental voltage data for $Na_XNi_{1/3}Mn_{2/3}O_2$ at low C-rate. Subfigure a) shows the first charge voltage over specific capacity. On the right, first cycle data from [29] and [17] is shown over the average filling fraction X.

The primary particles of $Na_{2/3}Ni_{1/3}Mn_{2/3}O_2$ exhibit a hexagonal shape and platelet-like morphology with the c-axis oriented along the thin dimension. The morphology can be either single-crystalline with sizes between $1-4\,\mu m$ [17] or larger agglomerates [219]. In this study, we consider a single crystalline platelet with a simplified cuboid shape. Phase evolutions are evaluated in three-dimensional simulations as well as corresponding two-dimensional reductions. The fluxes resulting from the intercalation reaction are applied on all surfaces but bulk diffusion is limited to the layers, i.e. $D_{001} = 0$. Hence, the large crystal facets in the (001)-direction can be charged but the bulk of the crystal is only accessible through insertion at (100)- and (010)-facets followed by bulk diffusion.

7.2 Electro-chemical model

7.2.1 Gibbs free energy fitting

The energetic landscape is approximated by phase-wise fitting functions where we include the O2-phase and three ordered states of P2 ($1/3$: single-row, $1/2$: double-row, $2/3$: large-zigzag). In this work, we employ quadratic fits for computational efficiency on the one hand and logarithmic expressions based on an ideal solution on the other

$$f^{\alpha}_{\text{quad}} = A^{\alpha}(c^{\alpha} - c^{\alpha}_{\text{min}})^2 + B^{\alpha}, \tag{7.1}$$

$$f^{\alpha}_{\text{ideal}} = \mu^{\alpha}_0 c^{\alpha} + K^{\alpha} c^{\alpha} \ln(c^{\alpha}) + K^{\alpha}(c_{\text{max}} - c^{\alpha}) \ln(c_{\text{max}} - c^{\alpha}) + D^{\alpha}. \tag{7.2}$$

The diffusion potential is defined as the derivative with respect to the phase concentration which yields

$$\mu_{\text{quad}} = 2A^{\alpha}(c^{\alpha} - c^{\alpha}_{\text{min}}) \tag{7.3}$$

$$\mu_{\text{ideal}} = \mu^{0,\alpha} + A^{\alpha} \ln\left(\frac{c^{\alpha}}{c_{\text{max}} - c^{\alpha}}\right) \tag{7.4}$$

for the two cases given in Eqs. (7.1) and (7.2). We employ a fit purely based on quadratic functions (7.1) with parameters given in Tab. 7.1 and shown in Fig. 7.2 a). In non-dimensionalized form (using $F/(RT)$ to convert from eV) the functions read

$$\begin{aligned} f_{\text{O2}} &= 500(x - 0.05)^2 - 0.40, \\ f_{\text{P2-1/3}} &= 400(x - 0.33)^2 - 4.00, \\ f_{\text{P2-1/2}} &= 400(x - 0.49)^2 - 2.98, \\ f_{\text{P2-2/3}} &= 500(x - 0.60)^2 - 0.90. \end{aligned}$$

The equilibrium in two-phase regions is given by the tangent construction depicted by dashed lines which results in the voltage plateaus according to Eq. (2.34).

If we replace the energies of the first (O2) and last phase (P2-2/3) with logarithmic functions (Eq. (7.2)) and employ the parameters in Tab. 7.1, the non-dimensional phase energies are given as

$$f_{\mathrm{O2}} = 39.96x + 20x\ln(x) + 20(0.67-x)\ln(0.67-x) + 6.37, \tag{7.5}$$

$$f_{\mathrm{P2\text{-}2/3}} = -9.73x + 15x\ln(x) + 15(0.67-x)\ln(0.67-x) + 12.17. \tag{7.6}$$

As a result, the corresponding voltage curve exhibits more realistic slopes for $X \to 0$ and $X \to 2/3$ as shown in Fig. 7.2.

Table 7.1: Fitting parameters for chemical energies

	O2	P2-1/3	P2-1/2	P2-2/3
$A^\alpha\,[e\mathrm{V}]$	12.93	10.34	10.34	12.93
$c^\alpha_{\min}\,[-]$	0.05	0.33	0.49	0.6
$B^\alpha\,[e\mathrm{V}]$	-0.010	-0.103	-0.077	-0.023
$K^\alpha\,[e\mathrm{V}]$	0.571	-	-	0.388
$\mu_0^\alpha\,[e\mathrm{V}]$	1.033	-	-	-0.252
$D^\alpha\,[e\mathrm{V}]$	0.165	-	-	0.315

Fig. 7.2 shows that both fittings match the experimentally obtained voltage curve [17] quite well. The biggest difference are the chemical potentials obtained at $X \to 0$ and $X \to 2/3$ where the logarithmic fits approach $-\infty$ and ∞ while the derivation of quadratic energies yields a linear relation with respect to c^α. As a consequence, the logarithmic functions are naturally bounded to the interval $c^\alpha \in [0, 2/3]$ while for quadratic functions the concentration values can be negative.

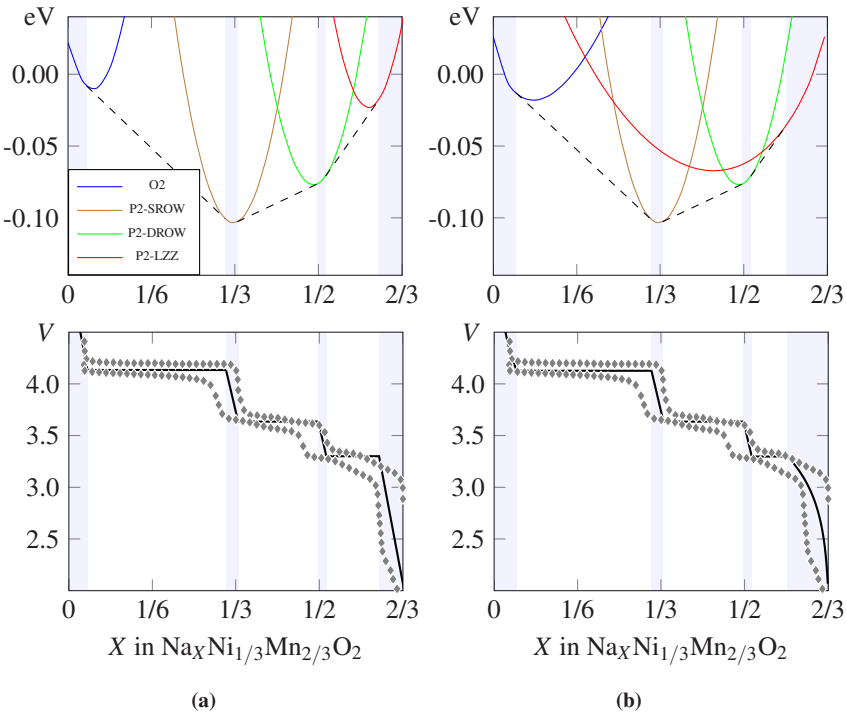


Figure 7.2: Gibbs free energy fittings f_{chem} in the top row and resulting equilibrium voltages below for a) parabolic fitting and b) logarithmic fitting. Black dashed lines depict common tangents indicating two-phase coexistence.Blue shaded areas mark the remaining single phase regions.

7.2.2 Dimensionality study

The chemical energy fits can be used within the framework of the multiphase-field method to study the dynamic behaviour of $Na_XNi_{1/3}Mn_{2/3}O_2$ during charge and discharge. To study the interplay of surface reaction and bulk diffusion, a simulation study with varying C-rates is conducted. In the following, C-rates are varied as powers of 2, e.g. C-rate $\in [2^{-4},\ldots,2] = [C/16, C/8, C/4, C/2, 1C, 2C]$. Diffusivities are assumed to be phase-wise constant. The spread in experimental values is quite large, ranging from $D_{\text{apparent}} = 10^{-8} - 10^{-12}$ [cm^2/s] in the P2

phase. The apparent diffusivity in the O2 phase is two to four orders of magnitude slower. For our reference study, we set the diffusivity in the P2 phase as $D_{P2} = 10^{-11}$ [cm^2/s] [40, 227] and assume the diffusivity in the O2 phase to be three orders of magnitude slower such that $D_{O2} = 10^{-14}$ [cm^2/s]. The rate constant for charge transfer k_0 is assumed to be $\approx 10^{-3}$ A/m^2 [172].

A question that arises due to computational time and also in the context of including small scale models on a larger scale (e.g. particle model in P2D approaches), is finding an appropriate dimensionality reduction. The simplified cuboid particle can be reduced in two ways as sketched in Fig. 7.3. The cross-cut on the left side corresponds to a symmetry reduction assuming c to be constant in the third dimension. This is equivalent to a slab with infinite extension in this direction. The depth-averaged model on the right assumes that composition is mainly a function of x and y while a homogenization by depth-averging can be applied in the z-direction (i.e. c-axis) of the platelet.

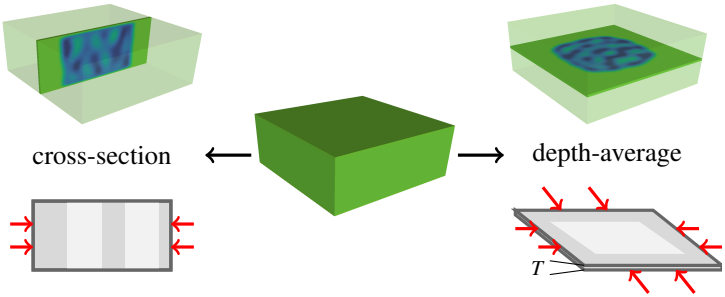


Figure 7.3: Dimensionality reduction from the three dimensional case (middle) to a 2D cross-section (left) or by depth-averaging (right).

The results in Fig. 7.4 a) reveal some fundamental aspects caused by the interplay of surface reaction and bulk diffusion. For any C-rate, the voltage curves deviate from the equilibrium voltage and form a hysteresis between charge and discharge which originates from the fact that the applied potential is determined by the sodium concentration at the surface [228]. The higher the insertion rate in relation to bulk diffusion, the higher are the concentration gradients from the

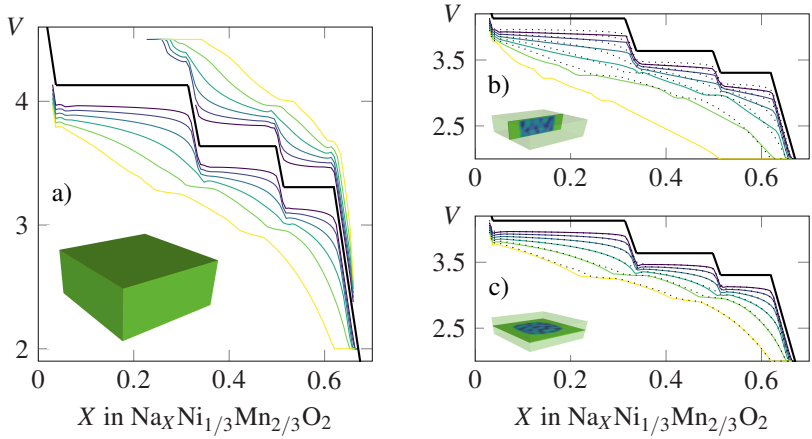


Figure 7.4: Comparison of a) fully resolved particle with b) 2D reduction to cross-section and c) 2D reduction through depth-averaging. For all cases, C-rates $\in [2^{-4}, ..., 1, 2]$ have been computed. The three dimensional results in a) are shown in b) and c) as black dotted lines for reference. Simulations are based on the quadratic energy fit.

surface towards the inner of the particle. The simulated hysteresis also depends on the value of k_0 which scales the energetic barrier for ion desolvation and intercalation. As long as surface reaction is the rate limiting step, the voltage plateaus are simply shifted depending on the C-rate. When bulk diffusion becomes rate limiting, plateaus are sloped and steps in the voltage curve are less pronounced as more than two phases can coexist within one single particle. On discharge, there is a dynamic capacity loss (also called apparent capacity loss [228]) once the P2-LZZ phase has formed on all facets of the crystal. As the surface concentration of sodium approaches $2/3$, the lower cut-off voltage of 2.0 V is reached and the insertion reaction breakes down. The effect is more pronounced during charging due to the slow ion diffusion in the O2 phase. During charging, sodium ions are continuously removed from the crystal which leads to a ring of the O2 phase forming at the active facets of the crystal. This hinders the extraction of ions from the bulk of the particle and causes a blocking effect.

The comparison of dimensionality reductions in Fig. 7.4 b) and c) shows that only the depth-averaged simulations yield similar results to the fully resolved simulations. This can be explained by two factors. The strongly anisotropic diffusion ($D_{001} = 0$) leads to a partial decoupling of the layers. Diffusion processes are not influenced by the gradient of chemical potential in the c-direction. The interfacial energy includes long-range interaction across the layers due to the gradient term (Eq. (2.4)) which causes interfaces to align perpendicular to the diffusion direction. The deviation between the two dimensionality reductions originates from the ratio between surface area to enclosed volume of the active material. For a cuboid particle with lenght L, width L and height H, the volume is $V = L^2H$. As the cross-section corresponds to an infinite slab, the surface to volume ratio is given by $A/V = 2LH/L^2H = 2/L$. For the depth-averaging on the other hand, we get $A/V = (2LH + 2LH)/L^2H = 4/L$ which matches the three dimensional case as the facets at the top and bottom of the crystal do not contribute to intercalation and subsequent bulk diffusion. We conclude that depth-averaging is an appropriate dimensionality reduction for the electro-chemical model employed so far and, thus, the following parameter studies are based on this simplification.

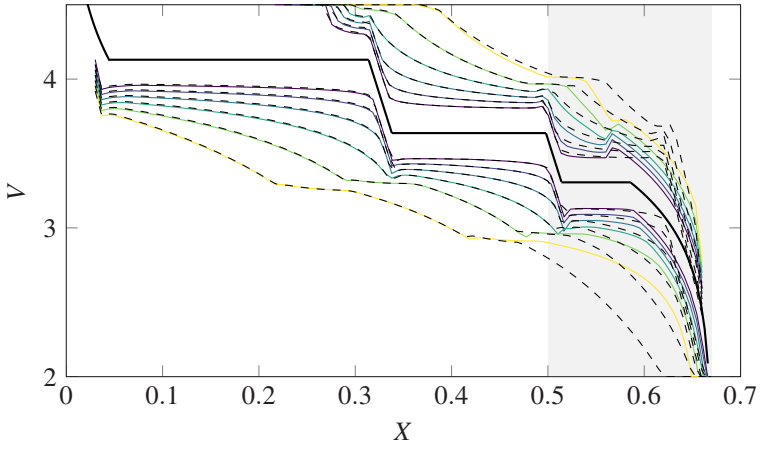


Figure 7.5: Comparison of logarithmic function fit (colored) with quadratic fit (black, dashed lines) for C-rates $\in [2^{-4}, ..., 1, 2]$. The black line represents the fitted equilibrium state.

The comparison of logarithmic function fits for the O2 and P2-2/3 phases with quadratic functions in Fig. 7.5 shows that the resulting voltage profiles only deviate for filling fractions $X \in [0.5, 0.67]$ when the P2-2/3 phase is dominating (gray shaded area). From a computational point of view, the two variants perform similar. Computational times are slighly longer for logarithmic functions as the function evaluation involves more arithmetic operations. From a physical point of view, the logarithmic functions seem more justified as they inhibit unphysical composition values of $c < 0.0$ while the quadratic functions do not. For this reason all following simulations are based on the logarithmic function fit.

7.2.3 Influence of diffusivity and charge transfer

The physical input values of $D_{O2} = 10^{-14}$ cm^2/s and $k_0 = 10^{-3}$ A/m^2 which have been used for simulations in the previous subsection were estimates based on literature [40, 172]. Both parameters are now systematically varied in orders of magnitude ($D_{O2} \in [10^{-14}, 10^{-13}, 10^{-12}]$ cm^2/s and $k_0 \in [10^{-3}, 10^{-2}]$ A/m^2) to quantify their impact on simulated voltage curves.

By first comparing C-rate studies with varying D_{O2} in Fig. 7.6, it becomes evident that the bulk diffusion in the O2-phase only influences the high voltage plateau upon charge. The continuous extraction of sodium ions leads to the formation of a ring of the O2-phase which forms on the active facets and moves towards the center of the particle. Due to the slow ion migration in the O2-phase, the remaining ions in the bulk of the crystal are trapped which results in a fast increase of overpotential until the upper cut-off voltage is reached. Even at very low C-rates of below $C/10$ the upper voltage plateau is not observed for $D_{O2} = 10^{-14}$ and 10^{-13} which contradicts experimental observations [17]. Furthermore, the hysteresis between charge and discharge is larger than expected which indicates that the charge transfer coefficient should probably be larger.

The systematic variation of D_{O2} and k_0 leads to the results shown in Fig. 7.7. As k_0 is increased, the overpotentials at low C-rates become much smaller. For high charging rates, overpotentials are still high due to diffusion limitation.

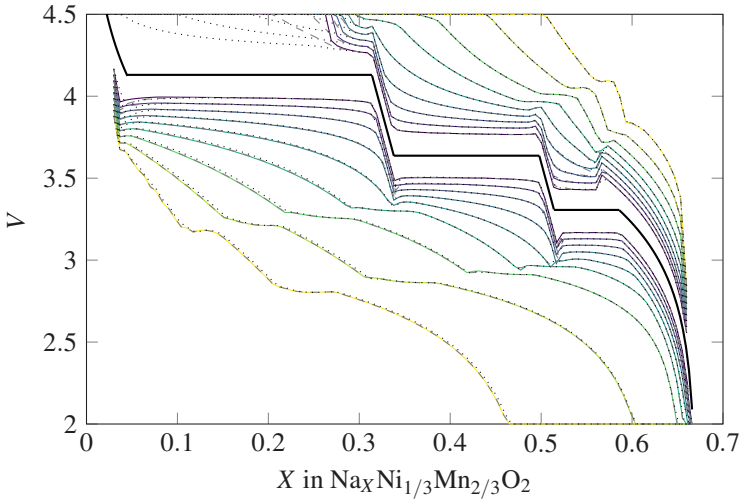


Figure 7.6: Influence of diffusivity in the O2-phase on overpotential for C-rates $\in [2^{-5},...,4,8]$. Colored lines represent simulations with $D_{O2} = 10^{-14}$ cm^2/s where yellow corresponds to 8C and dark violett to C/32. Simulations with $D_{O2} = 10^{-13}$ cm^2/s are drawn as gray dashed lines and $D_{O2} = 10^{-12}$ cm^2/s as black dotted lines, respectively.

Overall, the experimentally observed rate performance in the P2-type layered oxide $Na_XNi_{1/3}Mn_{2/3}O_2$ [17] is much better than the predictions discussed so far from phase-field simulations, even for $D_{O2} = 10^{-12}$ cm^2/s and $k_0 = 0.1$ A/m^2. Possible reasons are

- The diffusivities D_{P2} and D_{O2} might be even higher in single crystals.
- The charge transfer coefficient k_0 might be larger, indicating fast intercalation dynamics.
- Physical effects that have been negleted so far are crucial to fully describe intercalation in the layered $Na_XNi_{1/3}Mn_{2/3}O_2$.

The following studies include the effect of elastic deformations as a result of the anisotropic lattice expansion and contraction upon intercalation to test the third hypothesis.

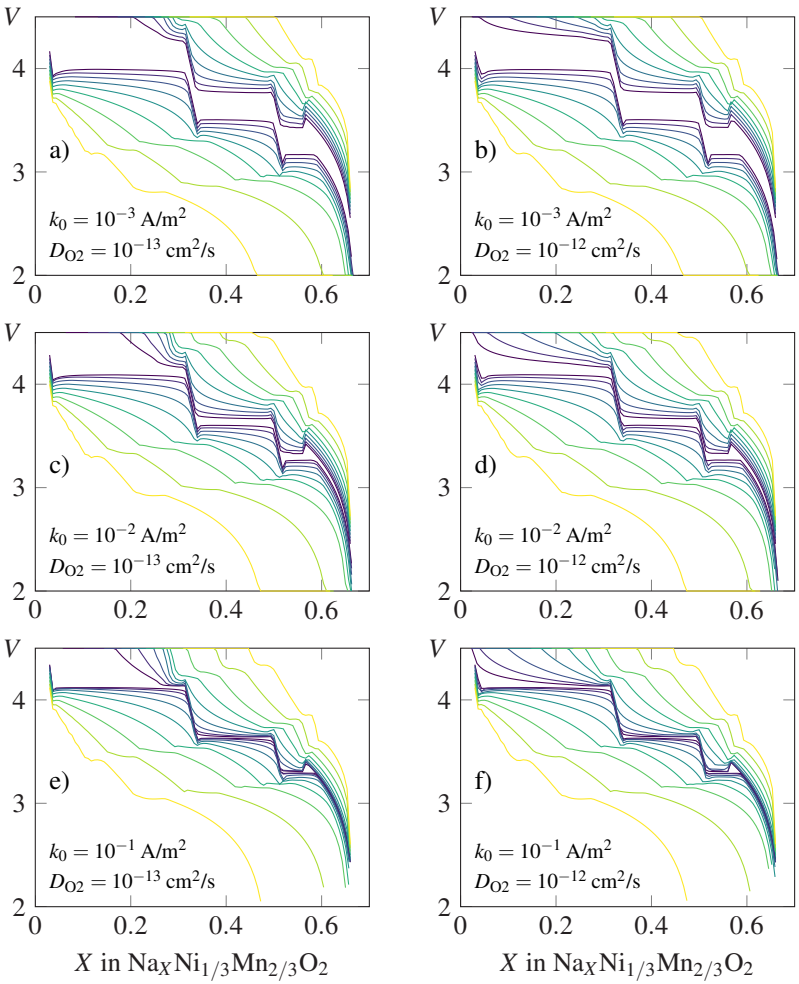


Figure 7.7: Influence of diffusivity in the O2-phase and assumed charge transfer coefficient k_0 on voltage output for C-rates $\in [2^{-5}, ...2, 4, 8]$.

7.3 Electro-chemo-mechanical model[1]

7.3.1 Material-specific input data

The lattice constants of $Na_XNi_{1/3}Mn_{2/3}O_2$ are listed in Table 7.2 for the four stoichiometries that will be modeled as separate phases. They strongly depend on the respective phase and site filling fraction of sodium ions. The normal eigenstrains ε_a^0 and ε_c^0 have been calculated with respect to $Na_{2/3}Ni_{1/3}Mn_{2/3}O_2$, e.g. $\varepsilon_a^0 = (a_{O2} - a_{P2\text{-}2/3})/a_{P2\text{-}2/3}$.

Table 7.2: Phase characteristics of $Na_XNi_{1/3}Mn_{2/3}O_2$

Phases	a [Å]	c [Å]	V [Å^3]	ε_a^0	ε_c^0
(O2) $Ni_{1/3}Mn_{2/3}O_2$	2.835	8.830	61.5	−1.9%	−20.6%
(P2) $Na_{1/3}Ni_{1/3}Mn_{2/3}O_2$	2.848	11.338	79.6	−1.4%	1.9%
(P2) $Na_{1/2}Ni_{1/3}Mn_{2/3}O_2$	2.865	11.241	79.9	−0.8%	1.1%
(P2) $Na_{2/3}Ni_{1/3}Mn_{2/3}O_2$	2.889	11.120	80.4	0.0%	0.0%

Very strong anisotropy becomes obvious from the calculated values. The stiffness tensors computed from DFT [229] are directly included as an input for MPF simulations. The following simulation studies are based on the assumption that all deformations are elastic and occuring interfaces are coherent with an interfacial energy of $\gamma_{\alpha\beta} \approx 0.1\,\mathrm{J/m^2}$ [36] The high resulting stresses are taken as an indicator for degradation but explicit modeling of plasticity, fracture or dislocations is out of scope of this work.

[1] The content of this section is based on the article Daubner *et al.* [229]. Parts that are taken verbatim from the publication have been marked. Note that the fitting parameters for chemical energies are slightly different compared to the previous section as they were fitted to the data from experimental measurements and DFT simulations.

7.3.2 Kinetics of phase transformations

»The chemical energy fits can be used within the framework of the multiphase-field method to study the dynamic behaviour of $Na_X Ni_{1/3}Mn_{2/3}O_2$ during charge and discharge. To study the interplay of surface reaction (Eq. (2.39)) and bulk diffusion (Eq. (2.25)) in combination with elasticity, a simulation study with varying C-rates is conducted. Diffusivities are assumed to be phase-wise constant and are approximated from GITT results in [229, Sec. 3.1] as $D_{O2} = 8 \times 10^{-14}\,cm^2/s$ and $D_{P2} = 2 \times 10^{-10}\,cm^2/s$, respectively. All simulations are based on the function fit including logarithmic terms as the match with experimental results was larger in the equilibrium case.

For comparison, extreme current rate tests without formation cycles have been performed at C/10, C/5, 1C and 5C (Fig. 7.8a-d). At slow rates (C/10 and C/5) the potential profiles run as expected with large initial charge capacities of 172 mAh/g for C/10 and 156 mAh/g for C/5, respectively. Under faster current rates (1C and 5C), the performance drastically decreases to capacities of 113 mAh/g and 86 mAh/g. The electrochemical curves in Fig. 7.8c and d show a drastic increase in overpotential and hysteresis. The poor rate performance, especially at higher potentials can result from the low ionic diffusion coefficient and poor electronic conductivity [230].

The phase transitions are exemplarily shown for 1C in the inset pictures in Fig. 7.8e. The transition between P2 ordered states proceeds through a shrinking core mechanism at 1C and 5C. At low C-rates, the shrinking core is replaced by a wave-like front moving through the crystal in accordance with simulations for LCO [172]. The first order phase transition between the O2 and P2-phase proceeds perpendicular to the layers which is a result of the strong lattice contraction in the c-direction. In simulations where the elastic deformation is neglected, the continuous removal of sodium ions leads to a ring of the O2 phase forming at the active facets of the crystal. This hinders the extraction of ions from the bulk of the particle and results in a blocking effect caused by the slow diffusivity in the

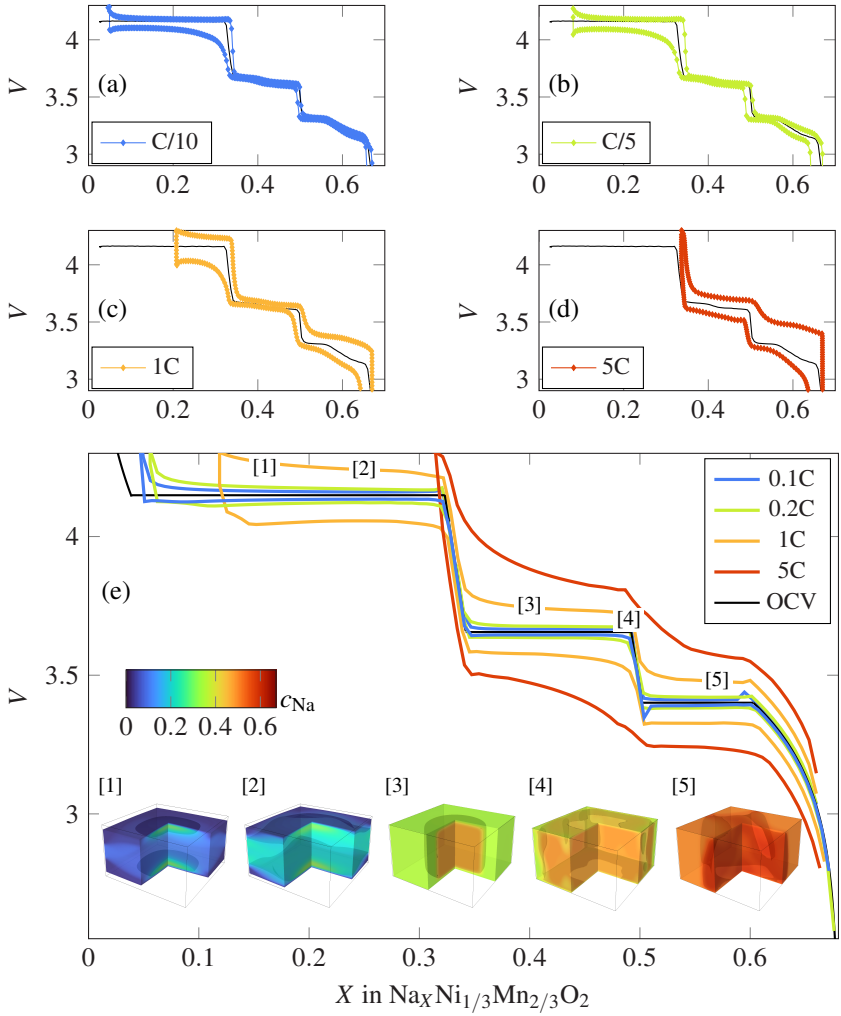


Figure 7.8: C-rate tests performed (a)-(d) experimentally and (e) virtually for C/10, C/5, 1C and 5C. The black solid line in (a)-(d) are the relaxed OCV points from the GITT measurement [229]. The black reference in subfigure (e) is the equilibrium potential. Inset pictures show the local filling fraction of sodium ions for charging with 1C.

O2-phase. As a result, the accessible capacity at all C-rates is heavily underestimated. The experimentally observed capacities can only be achieved through layer-by-layer filling which is preferential for the minimization of stored elastic energy. In all cases, phase transitions are initiated at corners and edges of the crystal where the curvature is high.

The lattice mismatch between phases leads to stress hotspots at locations with high concentration gradients. In brittle materials, the maximum tensile stress can be used as an estimate for possible fracture which is the largest eigenvalue of the local stress tensor. In our simulations, we find high tensile stresses close to the top and bottom facets during charge and in the center of the particle during discharge. The observed stress distributions are consistent with the observation that cracks can form inside the particle and reach the surface through continued cycling [34]. The simulated voltage curves feature strong resemblance with the experimentally obtained ones from which we conclude that the model covers the dominant effects and can be used for predictive material simulation. The differences between the curves in Fig. 7.8a-d and Fig. 7.8e give some hints for further model refinement in future works. Very low overpotentials are observed in the range of $X \in [0.33, 0.5]$ which suggests that the charge transfer coefficient k_0 might be phase-specific. The deviation at high filling fractions $X > 0.6$ results from the energy fit and could be improved by inclusion of the P2'-phase in the model. Furthermore, there is an asymmetry between charge and discharge in the high voltage plateau $\approx 4.16\,\mathrm{V}$ which becomes apparent through the high overpotential in the discharge even at low rates (Fig. 7.8a-b). To the best of our knowledge the reason is not fully understood and could be studied by detailed simulation studies.«

7.4 Conclusion

The dynamic nano-battery model reflects the overall electrode behavior at various C-rates surprisingly well. The inclusion of equilibrium data for phases combined with two kinetic parameters, namely diffusivity and the rate constant for charge transfer k_0, yield a predictive model that covers phase transformations and resulting overpotentials at technically relevant charging rates. The simulation results highlight that the inclusion of elastic deformation is crucial to capture the phase transformation mechanism of the O2-P2 transition. Due to the large lattice mismatch in the c-direction, the phase transformation proceeds perpendicularly to the diffusion direction which enables higher capacity utilization at high rates. Simulations which neglect the elastic energy contribution falsely predict a strong blocking effect upon charge resulting from the slow diffusion in the O2-phase. In future investigations, the established simulation framework could be used to study the multi-particle behaviour during phase transformations to identify the rate limiting step and improve the understanding of GITT measurements.

The detailed investigation of phase transformations in single crystals via the MPF method is computationally challenging and direct inclusion of 3D particle simulations into larger scales would probably not be feasible in terms of computational times. However, the MPF studies can be used to identify regimes where different mechanisms are rate-determining to formulate appropriate reduced particle models. As discussed above the O2-P2 first order phase transformation is strongly influenced by elastic deformation of the host lattice in the c-direction while diffusion proceeds perpendicular. As a consequence this phase transformation must be modeled at least in 2D to capture the relevant effects and get a reliable prediction of overpotential. The regime that is dominated by charge orderings ($0.33 < X < 0.67$ in $Na_XNi_{1/3}Mn_{2/3}O_2$), on the other hand, is sufficiently well described by the model formulation based on depth-averaging and neglecting mechanical contributions. Thus, a one dimensional reduction of a coin shape, reducing the first dimension by depth-averaging and second by rotational symmetry, might be approriate to model hexagonal platelets in P2D models. This discussion is similar to the dimensionality reductions sketched in Fig. 6.1.

8 Anisotropic ion diffusion in polycrystalline battery materials[1]

»Layered oxides are an important material class for lithium as well as sodium ion intercalation batteries [228]. Their stoichiometry is described by the generalized formula $A_X MO_2$, where A is the intercalated ion and M stands for one or various transition metals such as Ni, Mn, or Co [15]. The crystal structure consists of MO_2 sheets with *A*-ions between these layers, thus resulting in strongly anisotropic material properties on the single-crystalline scale. Ion diffusion is limited to the layers in a defect-free structure due to the higher energetic barrier for cross-layer hopping. This effect is mediated through crystal defects; however, diffusivities still vary by orders of magnitude between the directions normal and parallel to the layers in a real system, e.g., in $LiCoO_2$ [10].

Apart from the crystal structure, ion transport in electrode particles is strongly influenced by the morphology (i.e., structural appearance on the microscale). Layered-oxide compounds based on nickel, manganese, and cobalt (NMC) are state-of-the-art cathode materials for commercial lithium-ion cells in high-capacity applications such as electric vehicles [232]. Typically, NMCs form hierarchical structures of hundreds of primary crystals agglomerated in a spherical secondary particle with a diameter in the range of 5–10 µm, sometimes referred to as a meatball structure [18, 19]. Similar secondary morphologies can be obtained for a wide range of layered-oxide cathode materials based on lithium and sodium as the inserting ion [20, 22, 232, 233]. Ionic transport can be altered in polycrystalline materials through microstructure design such as tailoring crystallographic

[1] The content of this chapter is taken verbatim from the article Daubner *et al.* [231].

orientations [22, 233] or introducing nanoporosity [21]. Particles consisting of radially aligned grains show excellent rate performance and improved cyclic stability [22, 233]. This can be attributed to less tortuous pathways for ion transport and the increase of small-angle grain boundaries, which lead to an overall reduction of accumulated stress in grain boundaries. The same applies for the nanoporous particle morphology, as the open-pored structure significantly reduces diffusion paths within the active material compared to close-packed spherical structures.

Secondary particles tend to form intergranular cracks if the primary crystals undergo significant expansion and contraction [18]. This effect is strongly interconnected with the anisotropic nature of these materials because layered oxides typically exhibit much stronger changes in the c-axis (perpendicular to the transition metal oxide sheets). As the primary crystals are typically randomly oriented, stresses arise due to the misorientation of neighboring grains that can lead to fracture and eventually disintegration of the secondary structure [18, 19, 36]. Accordingly, small-angle grain boundaries are not strained as much because neighboring grains expand in a similar way.

NMC agglomerates have been modeled by Xu et al. [19] to study the formation of intergranular cracks. Even though the polycrystalline nature is accounted for, isotropic input parameters for diffusivity, Young's modulus and volumetric expansion, which do not reflect the physical properties on the crystalline scale, were used. Additionally, a detailed investigation of the chemo-mechanical bulk behavior of NMC811 single crystals has been conducted by Lim et al. [234] in which anisotropic stiffness tensors and lattice expansions were computed from density functional theory (DFT) and, subsequently, employed in phase-field simulations. The mechanical properties from DFT [234] were, furthermore, used to study simplified secondary agglomerates consisting of 67 primary particles by Taghikhani et al. [61].

8.1 Materials and Methods

8.1.1 Multi-phase diffusion

In the context of the multiphase-field method, various phases $\alpha \dots N$ are described by their local volume fractions $\phi = \{\phi_\alpha, \phi_\beta, \dots, \phi_N\}$. In this work, ϕ is used to differentiate between grains with different orientations but with equal chemical properties. Interfaces between neighboring grains are represented by diffuse transition regions where the order parameter ϕ_α varies between 0 and 1. The initial polycrystalline microstructures are created by solving the corresponding multiphase-field evolution equations [36, 143, 158] including only interfacial forces to create close-to-equilibrium interfaces. This work is based on a multi-obstacle potential and a gradient formulation based on dual interactions [158]. More details can be found in our previous work [36]. For the remainder of this study, we assume that no phase transformations occur during (dis-)charge. Future works could encompass the effects of cation disorder and surface densification, which has been observed in high-nickel NMCs [232] and $LiNiO_2$ [27]. The ion diffusion in a multi-phase system is given by [145]

$$\frac{\partial c}{\partial t} = \boldsymbol{\nabla} \cdot (\mathbb{M}(c, \phi) \boldsymbol{\nabla} \mu) \tag{8.1}$$

where $\mathbb{M} = \sum_\alpha^N \mathbb{M}^\alpha \phi_\alpha$ denotes the average mobility. The lithium content in interfaces is described by an interpolation of phase-specific concentrations $c = \sum_\alpha^N c^\alpha \phi_\alpha$ [145]. In the bulk of a grain, Eq. (8.1) reduces to

$$\begin{aligned} \frac{\partial c^\alpha}{\partial t} &= \boldsymbol{\nabla} \cdot (\mathbb{M}^\alpha(c^\alpha) \boldsymbol{\nabla} \mu) = \boldsymbol{\nabla} \cdot \left(\mathbb{M}^\alpha(c^\alpha) \frac{\partial \mu}{\partial c^\alpha} \boldsymbol{\nabla} c^\alpha \right) \\ &= \boldsymbol{\nabla} \cdot (\mathbb{D}^\alpha(c^\alpha) \boldsymbol{\nabla} c^\alpha) \end{aligned} \tag{8.2}$$

which yields the relation $\mathbb{M}^\alpha = \mathbb{D}^\alpha / (\partial \mu / \partial c^\alpha)$ between mobility and chemical diffusivity $\mathbb{D}^\alpha$. We employ this relation to correlate the ion mobility in simulations with measured chemical diffusivities as $(\partial \mu / \partial c^\alpha)$, which is given from

the free energy expression Eq. (8.4). For most applications, diffusion is assumed to be ideal and isotropic, which results in a scalar diffusivity D^α that is phase-wise constant. More generally, anisotropic diffusion is described by a second order tensor $\mathbb{D}^\alpha$. Under the assumption that the diffusion potentials of co-existing phases are equal at any point within the diffuse interface (quasi-equilibrium condition [158]), Eq. (8.1) can be re-written in terms of an evolution equation for the diffusion potential [145]

$$\frac{\partial \mu}{\partial t} = \left[\sum_{\alpha}^{N} \frac{\partial c^\alpha}{\partial \mu}\phi_\alpha\right]^{-1} \left(\nabla \cdot (\mathbb{M}(c,\phi)\nabla\mu) - \sum_{\alpha}^{N} c^\alpha \frac{\partial \phi_\alpha}{\partial t}\right) \tag{8.3}$$

which is computationally beneficial. Eq. (8.3) is compatible with the simulation of phase evolution as the last term accounts for mass conservation at moving interfaces. This has been used in our previous study [36] while in this context, all phases and grain boundaries are assumed to be stationary ($\partial\phi_\alpha/\partial t = 0, \forall\alpha$).

8.1.2 Anisotropic diffusion tensor

As discussed in the introduction, layered-oxides exhibit strongly anisotropic properties in terms of diffusivity and lattice expansion. For orthorhombic materials with strong anisotropy, the diffusion tensor in the lattice coordinate system can be described by a diagonal tensor with three independent entries. The layered structure of NMC results in transverse isotropy, i.e., in-plane diffusion is isotropic with a diffusion coefficient of $D_{||}$, while the diffusivity along the c-axis direction $D_\perp$ exhibits a much lower value. The diffusion tensor in material coordinates is given by

$$\mathbb{D}_{123} = \begin{bmatrix} D_{||} & 0 & 0 \\ 0 & D_{||} & 0 \\ 0 & 0 & D_\perp \end{bmatrix}.$$

Every grain α has an individual orientation that can be described by Euler angles or quaternions with respect to the global coordinate system. Rotation of the diffusion tensor from the material to the reference coordinate system can be achieved via rotation matrices, e.g.,

$$\boldsymbol{R}_x^\alpha = \begin{bmatrix} 1 & 0 & 0 \\ 0 & \cos\theta^\alpha & -\sin\theta^\alpha \\ 0 & \sin\theta^\alpha & \cos\theta^\alpha \end{bmatrix},$$

$$\boldsymbol{R}_y^\alpha = \begin{bmatrix} \cos\psi^\alpha & 0 & \sin\psi^\alpha \\ 0 & 1 & 0 \\ -\sin\psi^\alpha & 0 & \cos\psi^\alpha \end{bmatrix},$$

$$\boldsymbol{R}_z^\alpha = \begin{bmatrix} \cos\varphi^\alpha & -\sin\varphi^\alpha & 0 \\ \sin\varphi^\alpha & \cos\varphi^\alpha & 0 \\ 0 & 0 & 1 \end{bmatrix}$$

which, in the XYZ-convention, yields the rotation transformation

$$\mathbb{D}_{xyz}^\alpha = \boldsymbol{R}_z^\alpha \boldsymbol{R}_y^\alpha \boldsymbol{R}_x^\alpha \mathbb{D}_{123} (\boldsymbol{R}_x^\alpha)^T (\boldsymbol{R}_y^\alpha)^T (\boldsymbol{R}_z^\alpha)^T.$$

Alternatively, the rotation can be computed based on quaternions that are more robust for arbitrary rotations [161, 162] and, moreover, allow for the straightforward interpolation of intermediate configurations. Effective material properties are computed by a mixture rule, i.e., interpolation of the phase-specific properties. Throughout this work, we employ a linear interpolation of diffusion tensors $\mathbb{D} = \sum_\alpha^N \mathbb{D}^\alpha \phi_\alpha$ weighted by the local volume fractions ϕ_α. The discretization is based on the finite difference scheme described in more detail in Chapter 5.

8.1.3 Simulation parameters for high-nickel NMC

Lithium layered-oxides with high nickel content, such as NMC811, deliver high capacities but also face stronger capacity fading due to mechanical degradation and surface densification [232]. The cycling of $LiNiO_2$ is accompanied by multiple phase transitions [26, 27] and indications for similar transformations have been observed for NMC811 as well [232], although the voltage curve at low (dis)charge rates does not feature distinct steps and plateaus (see Fig. 8.1). For the purpose of this study, we assume an ideal solution behavior in the voltage range $3.6-4.2$ V. As a consequence, the chemical free energy and the resulting chemical potential are expressed as

$$f_{\mathrm{NMC}} = \mu^{\ominus} c + K\ln(c) + K(1-c)\ln(1-c), \tag{8.4}$$

$$\mu_{\mathrm{NMC}} = \frac{\partial f_{\mathrm{NMC}}}{\partial c} = \mu^{\ominus} + K\ln\left(\frac{c}{1-c}\right). \tag{8.5}$$

The measurable open-circuit voltage (OCV) is related to the difference in chemical potentials between the cathode and the anode [170], which in this case yields

$$V_{\mathrm{OC}} = -\frac{\mu_{\mathrm{Cathode}} - \mu_{\mathrm{Anode}}}{eN_{\mathrm{A}}} = -\frac{\mu_{\mathrm{NMC}} - \mu_{\mathrm{Li}}^{\ominus}}{eN_{\mathrm{A}}} = V^{\ominus} - \frac{K}{eN_{\mathrm{A}}}\ln\left(\frac{c}{1-c}\right) \tag{8.6}$$

where the chemical potential defined in Equation (8.5) is used for the NMC cathode, and we assume a lithium metal counter electrode with constant chemical potential $\mu_{\mathrm{Li}}^{\ominus}$. The reference voltage $V^{\ominus} = (\mu_{\mathrm{Li}}^{\ominus} - \mu_{\mathrm{NMC}}^{\ominus})/(eN_{\mathrm{A}})$ is set to 3.89 V, which results in the blue curve in Fig. 8.1 for the equilibrium electro-chemical potential of the cathode with respect to a lithium metal anode. e denotes the elementary charge and N_{A} the Avogadro constant. The ion mobility is assumed to increase with concentration due to more random hops, while the crowding at high concentrations leads to a decrease such that $M \propto c(1-c)$. The thermodynamic factor $\partial\mu/\partial c^{\alpha}$ calculated based on Eq. (8.5) yields $Kc^{-1}(1-c)^{-1}$. Inserting the mobility and the thermodynamic factor derived from the ideal solution into Eq. (8.2) leads to a chemical diffusivity that is independent of c.

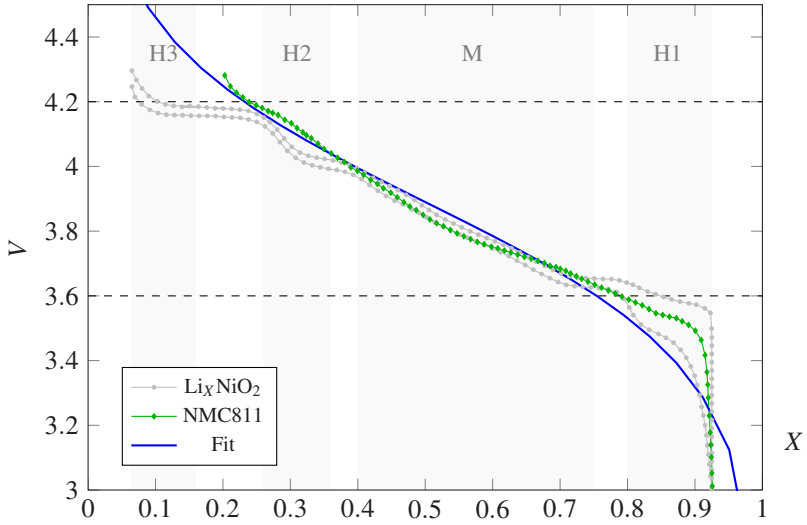


Figure 8.1: Ideal solution fit for the equilibrium electro-chemical potential of NMC811 shown in blue which is based on the datapoints pusblished in Noh *et al.* [232] (green markers). Gray datapoints mark experimental voltage data for Li$_X$NiO$_2$ obtained at $C/10$ [27] for comparison. Gray shaded areas mark the phase transformations observed in Li$_X$NiO$_2$.

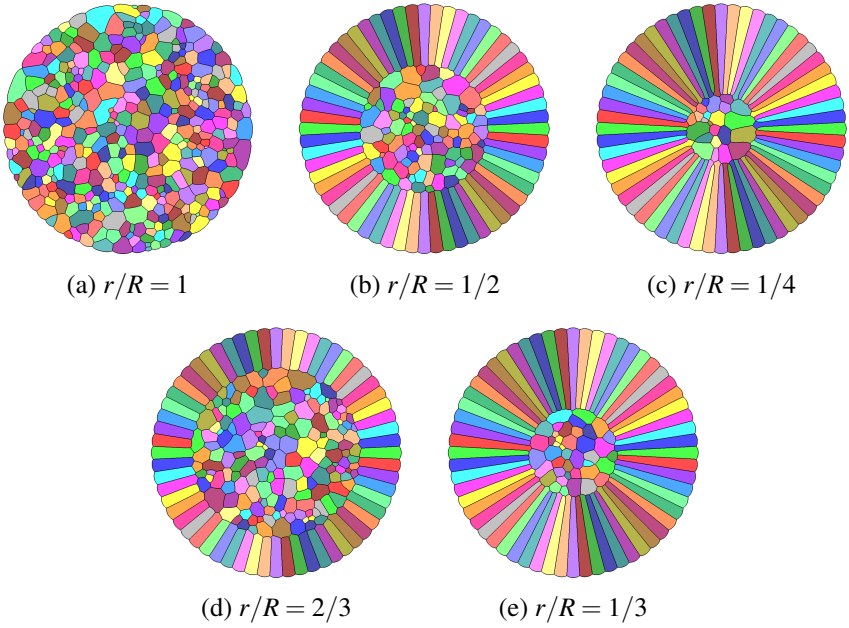
Lithium diffusion is confined to the plane between transition metal oxide sheets in a defect-free structure, and thus, is highly anisotropic. Reported values of the apparent diffusion coefficient in NMC differ by orders of magnitude [16, 232], which stems from the multiple challenges involved in aquiring reliable data. Computation of the apparent diffusion from galvanostatic intermittent titration technique (GITT) relies on the assumption of semi-infinite relaxation that is hard to ensure for small primary crystals and high diffusivities. The fracture of agglomerates and subsequent penetration of electrolytes lead to an increase in surface, and consequently, an overestimation of diffusivities obtained from GITT measurements [16]. Within this study, the in-plane diffusion coefficient is set to $D_{||} = 10^{-10}\,\mathrm{cm}^2/\mathrm{s}$, which is one order of magnitude faster than the apparent diffusion measured in [16]. In the direction perpendicular to the planes, diffusivity is assumed to be negligible ($D_{\perp} = 0$). At grain boundaries, a mixture rule is applied to interpolate diffusion tensors of neighboring grains. To the best of

our knowledge, the influence of grain boundary diffusion on ion transport within polycrystals is not sufficiently understood. Due to a lack of reliable data, no enhanced grain boundary diffusion is modeled although it is technically straightforward in the framework of the multiphase-field method [207].

8.2 Results

Lithium diffusion in NMC811 is simulated in two-dimensional domains for varying microstructures, as shown in Fig. 8.2. All secondary particles in this study are assumed to be spherical with an outer diameter of 10 µm [232] (i.e., $R = 5\,\mu\text{m}$). Inspired by various works with textured, rod-like microstructures [22, 233, 235], we assume a compact core with randomly oriented grains surrounded by a layer of radially aligned grains. The radius r of the inner core is systematically varied, starting from $r/R = 1$ which corresponds to a sphere of randomly oriented grains ("gravel-NMC" [22]), to a ratio of $r/R = 1/4$ where the microstructure is dominated by aligned grains. Randomized grain structures for the inner core are created by Voronoi tesselation. All structures are pre-conditioned by the multiphase-field method, in the sense that diffuse transition regions between order parameters of indiviual grains are established by solving the corresponding phase evolution equations [36, 143, 158]. The grain structures are assumed to be stable at room temperature such that no microstructure evolution occurs during cycling.

All structures are subjected to the same electro-chemical simulation setup where we apply voltage steps of $\Delta V = 0.1\,\text{V}$, followed by a relaxation time of 1 h. The voltage steps are applied via a Dirichlet boundary condition for c at the surface of the particles employing the relation between the voltage and c in Fig. 8.1. The characteristic relaxation time of the model setup is approximately $\tau = R^2/D_{||} = 0.7\,\text{h}$. Due to the different microstructures, diffusional relaxation within the secondary particles varies strongly as can be seen in Fig. 8.3.



(a) $r/R = 1$ (b) $r/R = 1/2$ (c) $r/R = 1/4$

(d) $r/R = 2/3$ (e) $r/R = 1/3$

Figure 8.2: Initial grain structures of secondary particles.

While 1 h of relaxation time is sufficiently long for the strongly textured samples ($r/R = 1/3$ and $r/R = 1/4$) to reach an equilibrium state ($\Delta c = 0$), the other samples are out of equilibrium. Figure 8.3a,d clearly show that the gravel-NMC sample builds up larger concentration gradients over time as a result of slower ion diffusion. This effect is also seen in the shifting of currents for the $r/R = 1$ sample in Fig. 8.4a. The spatial ion distribution is more inhomogeneous as some grains block the direct diffusion path towards the center of the sphere, resulting in a more tortuous pathway. The strongly aligned radial grains, moreover, provide fast ion transport paths towards the inner of the particle. In both cases of aligned grains (Fig. 8.3b,c), we observe an accumulation of ions at the grain boundary that is a result of the tapered shape of these grains. All ions moving through transition metal oxide sheets that end in a grain boundary need to diffuse further

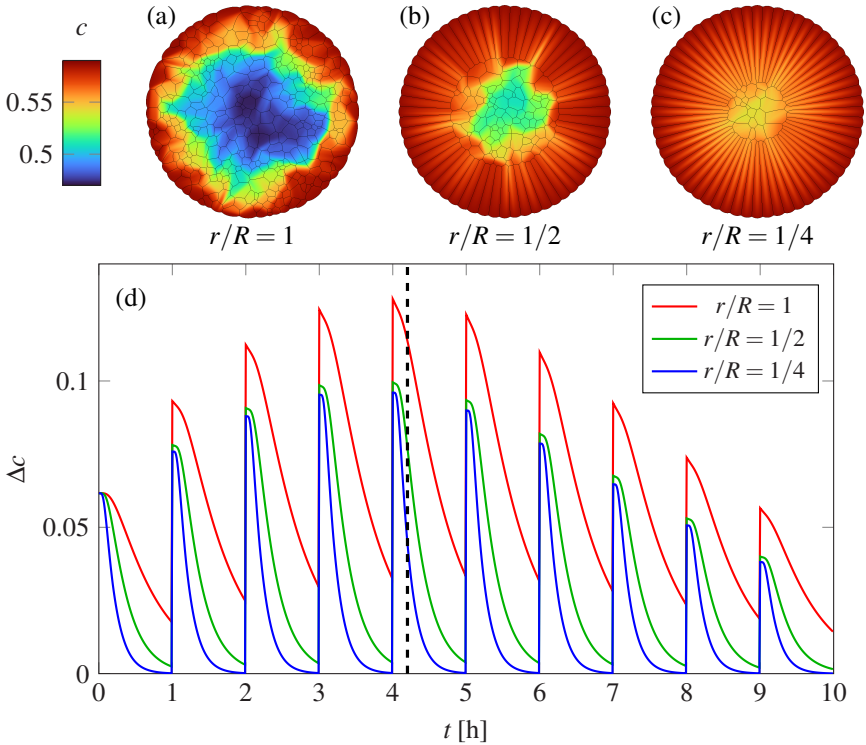


Figure 8.3: Relaxation of concentration gradients in comparison for the three microstructures with $r/R = 1$, $r/R = 1/2$ and $r/R = 1/4$ (Fig. 8.2a-c). The concentration gradient Δc is measured as the difference between maximal and minimal concentration value. Spatial concentration distribution is exemplarily shown for $t = 4.2$ h in subfigure a-c as denoted by the black dotted line in subfigure d.

via the grain boundary. The particle with a ratio of $r/R = 1/2$ exhibits inhomogeneities in the ion diffusion that appear as rays in Fig. 8.3b. The effective ion transport through the radially aligned grains is influenced by the microstructure of the inner core. Strong misalignment at the transition between core and outer ring leads to a blocking of transport routes and as a result some radial grains exhibit stronger concentration gradients. This effect becomes negligible when the textured grains dominate the overall morphology of the particle (Fig. 8.3c).

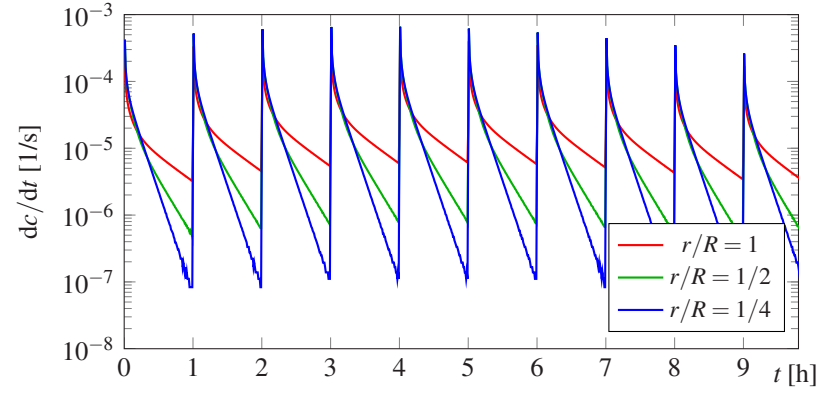
The composition gradients can, furthermore, be evaluated in terms of a virtual potentiostatic intermittent titration technique (PITT) experiment. The non-dimensional current resulting from the applied voltage step is calculated from the change of average concentration in the particle

$$I = \frac{1}{\int \phi_{\mathrm{NMC}} \mathrm{d}V} \int \frac{\partial c}{\partial t} \phi_{\mathrm{NMC}} \mathrm{d}V \tag{8.7}$$

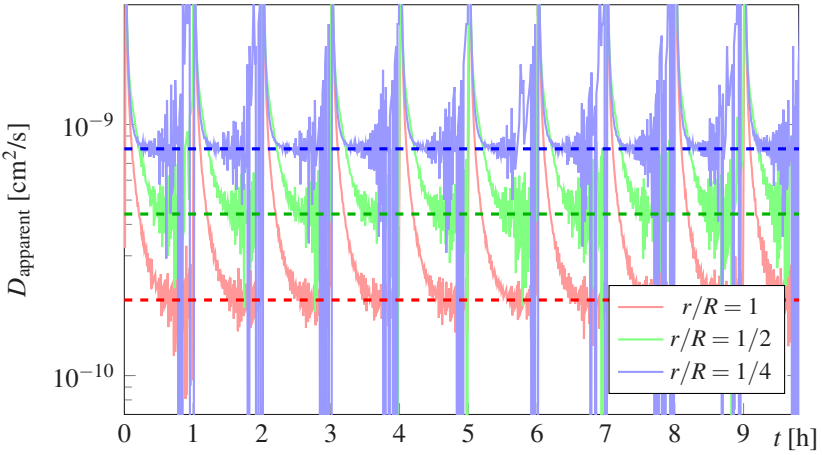
where ϕ_{NMC} denotes the local volume fraction of all NMC grains which is, in this case, identical to $1 - \phi_{\mathrm{electrolyte}}$. After a transient regime, the current follows an exponential decay which can be identified as linear regions in the logarithmic plot Fig. 8.4a. The results in Fig. 8.4a underline that the microstructure influences the global current (i.e. influx of ions in this case). The linear regions of the various samples exhibit different slopes which hints at varying effective diffusion coefficients. Employing a standard equation to compute the apparent diffusion coefficient from PITT experiments [17, Eq. 2]

$$D_{\mathrm{apparent}} = -\frac{\mathrm{d}\ln(I)}{\mathrm{d}t} \frac{16R^2}{\pi^2} \tag{8.8}$$

yields the results shown in Fig. 8.4b. Only regions where the current follows an exponential decay fulfill the assumptions that have been used to derive Eq. (8.8). Over the course of ten potential steps, the computed apparent diffusivities are very reliable and the average values have been marked by dashed lines. It should be noted that the noise in our evaluation becomes larger the faster the average diffusivity is. This is an artefact of the small changes of ion concentration close to equilibrium where the computed diffusivity values are dominated by trunctuation errors.



(a)



(b)

Figure 8.4: Virtual PITT experiment. The total influx of ions corresponding to the current resulting from the potential steps is given in a). Apparent diffusion coefficients calculated with Eq. (8.8) based on these currents are given in b).

8.3 Discussion

The results highlight how crucially ion transport is affected by the microstructure of secondary particles for anisotropic materials. The spatial distribution of composition which is observed in simulations (Fig. 8.5b and Fig. 8.5d) closely resembles the experimentally obtained ion distribution in the work of Xu *et al.* [22]. Especially the ray like ion distribution in [22, Fig. 3a] can now be explained by the interplay of misaligned grains in the randomly distributed core with respect to the outer aligned grains.

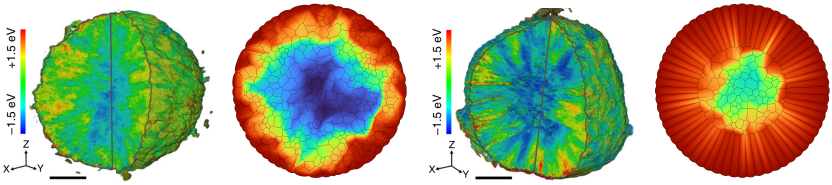


Figure 8.5: Spatial ion distribution in gravel-NMC (a, b) compared to rod-NMC (c, d). Subfigures (a) and (c) are reprinted from Xu *et al.* [22] and have been published under the CC-BY licence.

The evaluation of apparent diffusion coefficients sheds some light on the vast range of values that can be found in literature. In this study, the obtained values for D_{apparent} vary by a factor of 4, even though the input values for $D_{||}$ and $D_{\perp}$ are identical. It should be noted that the apparent diffusion coefficients calculated from Eq. (8.8) are too high in this case. Although $D_{||} = 1 \times 10^{-10}\,\text{cm}^2/\text{s}$ was chosen, the apparent diffusion coefficient for rod-NMC is $D_{\text{apparent}}^{\text{rod-NMC}} = 8 \times 10^{-10}\,\text{cm}^2/\text{s}$, which is physically not possible. This results from the fact that Eq. (8.8) has been derived for spherical particles while the simulations are only a two-dimensional represention of spherical microstructures. This does not change the qualitative differences between the obtained values as all could be corrected by a geometry factor. However, this discussion underlines the importance to question the assumptions that have been used for the derivation of formulas which

are typically used for the evaluation of GITT or PITT experiments. The detailed investigation unravels the influence of microstructure on the effective transport properties which is only one of many parameters influencing experimental results. It should be acknowledged that any experimental measurement of diffusivity can only capture the apparent diffusion in the specific microstructure and, thus, diffusivity values should always be published in combination with a characterization of particle morphology.

Furthermore, the simulation results suggest that grain boundary diffusion could play an important role for the ion transport in dense secondary particles. In the randomly oriented sample, an enhanced grain boundary diffusion would mediate the blocking effect observed at interfaces between strongly misaligned grains. Also in the rod-NMC with strong texture, grain boundaries play a vital role in the overall transport as sketched in Fig. 8.6. Due to the tapered shape of radially

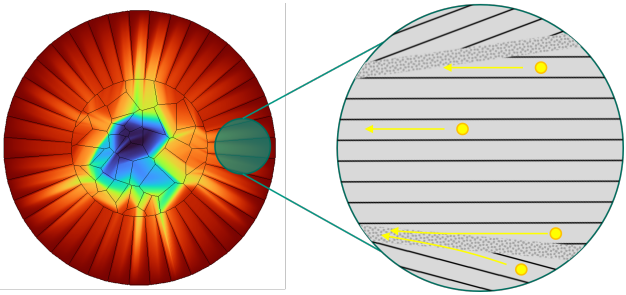


Figure 8.6: Role of grain boundaries in textured secondary particles. Ions travelling through transition metal oxide sheets that end in a grain boundary are forced to diffuse further into the inner of the particle via grain boundary diffsuion.

aligned grains, many layers are cut by grain boundaries and, thus, the migrating ions need to diffuse further into the particle via grain boundary diffusion. An enhanced grain boundary diffusion would lead to faster transport in the whole particle, while sluggish grain boundary diffusion would result in many trapped ions and strong concentration gradients at grain boundaries. To the best of our knowledge, the actual influence of grain boundaries on ion transport is not well understood.

8.4 Conclusion

The presented framework is well-suited to study the influence of particle morphology in terms of size, distribution, and alignment of primary particles on key battery performance measures such as the effective diffusivity. Through a virtual PITT test, we are able to compute an effective diffusivity depending on the actual microstructure.

Within this work, the phase-field method is employed to parametrize the polycrystalline structure of NMC agglomerates. While this study is based on virtually generated structures, the regular grid employed to solve the partial differential equations also enables the straightforward inclusion of image data. Furthermore, the hierarchical particle morphologies investigated in this work are relevant for other layered-oxide cathode materials, such as the P2-type $Na_X Ni_{1/4} Mn_{3/4} O_2$, which is a promising material for sodium intercalation batteries [20]. This material exhibits multiple plateaus in the OCV due to phase transitions. The multiphase-field framework employed throughout this work naturally allows for the computation of phase evolution within the grains such that future investigations will encompass the coupled effects of phase transformations, ion diffusion, and mechanical degradation. A systematic study of electrolyte infiltration after crack formation and the resulting effective diffusion coefficients becomes possible. By explicitly modeling the morphology dependence of ion diffusion, this work contributes to bridging the gap between diffusivity values obtained at different scales, e.g., from first principle methods such as DFT [9, 13], as well as from experimental methods such as GITT [16, 232] and PITT [17]. The proposed framework enables the systematic study of the effective transport properties of secondary particles, which is relevant for Newman-type models in which secondary particles are typically homogenized as isotropic spheres.«

9 Conclusion

9.1 Summary

In this work, I have presented a multiphase-field approach which covers polycrystalline systems on the mesoscopic scale with a system size ranging from 100 nm to 10 µm. The multi-phase formulation is based on the works of Steinbach *et al.* [123], Nestler *et al.* [124] and Eiken *et al.* [158]. The isotropic chemical model is based on the works of Choudhury and Nestler [145] and Aagesen *et al.* [236]. The effective treatment of polycrystalline systems, phase nucleation and coupling with elastic contributions has been adapted from the works of E. Schoof [140, 146]. New aspects in the context of the MPF method are the computation of strongly anisotropic fluxes and the consistent coupling with electrochemistry to describe ion intercalation in terms of measurable quantitites such as the applied current and cell potential.

In summary, the model formulation includes the effects of

- curvature driving forces based on interfacial energies,
- anisotropic ion diffusion driven by electro-chemical potentials,
- ion intercalation described by Butler-Volmer reaction kinetics,
- anisotropic elastic deformation due to a change of the host crystal lattice,
- spontaneous phase nucleation and evolution

which is sufficient and at the same time necessary to describe the relevant processes in intercalation battery materials.

The energy functional as well as evolution equations have a strong thermodynamic foundation which ensures the consistency for bridging from atomic resolution to cell models in a multi-scale approach. All energetic contributions to the energy functional as well as other aspects which are particular to the MPF method have been validated and discussed in the first part of this thesis. The outcomes not only underline the choice of model formulation for this work but might also be helpful as a guidance for model selection and validation in other applications. In the second part, the framework has been applied to three relevant cathode materials, namely Li_XFePO_4, $Na_XNi_{1/3}Mn_{2/3}O_2$ and $Li_XNi_{0.8}Mn_{0.1}Co_{0.1}O_2$.

The study on LFP emphasizes the importance of considering agglomerates and particle ensembles, as they behave differently from isolated single crystals and impact battery performance. The phase-field models successfully capture spinodal decomposition as a relaxation mechanism and predict the suppression of phase separation under sufficient driving force. The new model extends existing works by incorporating multi-particle interactions in an agglomerate which leads to a transition from inter-particle to intra-particle phase separation at increasing C-rates. Furthermore, the influence of texture in polycrystalline samples is crucial for mechanical degradation. Simulations reveal that stress hotspots depend on the misorientation of neighboring grains, especially for strongly anisotropic cathode materials like LFP.

The dynamic nano-battery model effectively represents electrode behavior at various C-rates by incorporating equilibrium data and two kinetic parameters. $Na_XNi_{1/3}Mn_{2/3}O_2$ is used as an example to illustrate the thermodynamically consistent fitting of Gibbs free energies for the phase-field method from DFT calculations and experimentally obtained OCV data. For this material, elastic deformation plays a crucial role in accurately modeling the phase transformation mechanism of the O2-P2 transition, enabling the capacity utilization observed in experiments.

The last application example on NMC highlights the influence of particle morphology, including size, distribution, and alignment of primary particles, on key battery performance metrics such as effective diffusivity. By using a virtual PITT

test, an effective diffusivity can be computed based on the actual microstructure. The framework enables the systematic study of effective transport properties of secondary particles, bridging the gap between diffusivity values obtained from different scales and methods. Furthermore, this allows for morphology optimization through computational studies. In this specific example, the MPF method is employed to parametrize the polycrystalline structure of NMC agglomerates. Future studies could encompass stresses arising due to misorientation of neighboring grains and phase transformations of the active material e.g. for LNO or $Na_X Ni_{1/3} Mn_{2/3} O_2$.

These examples highlight various strengths of the proposed method, namely

- the ability to model polycrystalline agglomerates and
- capture the influence of particle ensembles on phase transformation;
- consistency of thermodynamic equilibrium states with DFT calculations as well as experimental results;
- predictive model for rate performance of intercalation compounds and
- possibility to identify kinetic limitations;
- ability to extract effective properties (e.g. apparent diffusivity) from microstructure simulations.

In accordance with the literature discussed in Sec. 1.3, this works underlines that the phase-field method is the method of choice to model intercalation materials undergoing first-order phase transformations and charge orderings. This is also key to improve Newman-type models for electrode materials with phase transitions.

9.2 Outlook

Like in any research endeavor, the pursuit of answers to specific research questions generates a multitude of new inquiries that emerge during the dedicated examination of the topic. Looking at this thesis, I see many open research questions and challenges which might be addressed in future works.

The combination of the examples explored in the previous chapters would enable detailed insight into the charging of an $Na_XNi_{1/3}Mn_{2/3}O_2$ agglomerate, including the effects of charge ordering, phase transformation, primary particle interaction and stresses arising from grain misorientation. Simulation studies in that regard might help with the interpretation of GITT data for determination of diffusion coefficients for multi-phase materials.

Furthermore, the framework's potential extends beyond the specific materials discussed so far to most intercalation materials and maybe beyond. Advancing thermodynamic understanding and incorporation of quantitative material data is key to the accurate description of many more battery materials such that, ideally, simulation results align closely with experimental observations. This could improve models for graphite, LNO and other compounds.

The numerical implementation employed here is based on finite differences due to the straightforward parallelization of larger simulation domains. Future works might encompass numerically more advanced schemes. Another possible advantage of regular grids is the simple inclusion of image data. Simulation studies based on FIB-SEM data would enhance rate performance predictions for specific material systems. Furthermore, physics-informed neural networks can be employed to solve nonlinear partial differential equations [237]. In combination with experimental image data this can be used for model selection or advanced parameter fitting through PDE-constrained optimization [238]. This becomes especially simple in a framework, where image data and physical simulations are based on the same spatial discretisation, i.e. pixel- or voxel-based data.

Ultimately, the multiphase-field method serves as a valuable tool for comprehending the meso-scale phase transformation mechanisms in battery intercalation materials. This enhanced understanding can guide microstructure design and improve approximations for coarse-grained cell models. While this work has explored connections between simulation methods at different length scales, there is still progress to be made towards a comprehensive description of battery materials through a multi-scale simulation approach. The phase-field method holds significant promise for bridging the scale from atomistic to cell models in the simulation of battery materials. While studying phase transformations in single crystals using the MPF method is computationally challenging, it helps identify regimes where different mechanisms dominate, enabling the formulation of reduced particle models.

In conclusion, the phase-field method offers a powerful tool for investigating battery materials, providing insights into phase transformations, diffusion phenomena, and morphology-dependent performance. Its successful application opens avenues for further research and optimization in energy storage systems, contributing to the development of more efficient and durable battery technologies.

A Phase-field derivations

A.1 Two-phase energy functional

A two-phase system can be described by one order parameter $\phi \in [0,1]$. The corresponding energy functional for interfacial forces can be defined as

$$\mathscr{F}(\phi, \nabla\phi) = \int_V \kappa |\nabla\phi|^2 + f_{\text{pot}}(\phi) \mathrm{d}V.$$

The potential energy is typically formulated in terms of a double-well or double obstacle function

$$\begin{aligned} f_{\text{well}}(\phi) &= \Omega\phi^2(1-\phi)^2 \\ f_{\text{ob}}(\phi) &= \Omega\phi(1-\phi) \quad \forall\phi \in [0,1] \text{ and } \infty \text{ otherwise.} \end{aligned}$$

where the Ω scales the energetic barrier to be overcome. The evolution equation for ϕ is given under the assumption of energy minimization with linear kinetics

$$\dot{\phi} = -L\left(\frac{\partial}{\partial\phi} - \nabla\cdot\frac{\partial}{\partial\nabla\phi}\right)\left(f_{\text{grad}} + f_{\text{pot}}\right)$$

which finally leads to

$$\dot{\phi} = -L\left[-2\kappa\nabla^2\phi + \frac{\partial f_{\text{pot}}}{\partial\phi}\right], \quad \frac{\partial f_{\text{pot}}}{\partial\phi} = \begin{cases} \text{well:} & 2\Omega\phi(1-2\phi)(1-\phi) \\ \text{obstacle:} & \Omega(1-2\phi) \end{cases}$$

A.2 Interfacial properties

Following the procedure in Cahn and Hilliard [111], we can derive the interfacial properties of the diffuse interface. The equilibrium solution is given by $\dot{\phi} = 0$ which yields for a 1D flat interface

$$2\kappa\nabla^2\phi = \frac{\partial f_{\text{pot}}}{\partial \phi} \quad \rightarrow \kappa\left(\frac{\partial \phi}{\partial x}\right)^2 = f_{\text{pot}} \quad \rightarrow \mathrm{d}x = \sqrt{\kappa/f_{\text{pot}}}\mathrm{d}\phi.$$

The surface energy of a flat interface is given by the excess Gibbs free energy across the diffuse region

$$\begin{aligned}\gamma &= \int_{-\infty}^{\infty} \kappa(\nabla\phi)^2 + f_{\text{pot}}\mathrm{d}x = 2\int_{-\infty}^{\infty} f_{\text{pot}}\mathrm{d}x \\ &= 2\int_0^1 \sqrt{\kappa f_{\text{pot}}}\mathrm{d}\phi = \sqrt{\kappa\Omega}\begin{cases}1/3 & \text{(well)} \\ \pi/4 & \text{(obstacle)}\end{cases}\end{aligned}$$

While the obstacle potential leads to a sinus profile which has a finite interfacial width, the well potential leads to a tanh function. For both cases the interfacial width can be defined by the linear tangent fit in $\phi = 0.5$ such that

$$l_{\text{int}} = \frac{1}{\mathrm{d}\phi/\mathrm{d}x}\Big|_{\phi=0.5} = \sqrt{\frac{\kappa}{f_{\text{pot}}(\phi = 0.5)}} = \sqrt{\frac{\kappa}{\Omega}}\begin{cases}4 & \text{(well)} \\ 2 & \text{(obstacle)}\end{cases}$$

A.3 Functional derivatives

Table A.1: Common gradient energy formulations and their variation with respect to ϕ_α

$f_{\mathbf{grad}}$	$\delta f_{\mathbf{grad}}/\delta\phi_\alpha$
$\frac{1}{2}\sum_\alpha \kappa_\alpha \lvert\nabla\phi_\alpha\rvert^2$	$-\kappa_\alpha\nabla^2\phi_\alpha$
$\frac{1}{2}\frac{\sum\sum\kappa_{\alpha\beta}\phi_\alpha^2\phi_\beta^2}{\sum\sum\phi_\alpha^2\phi_\beta^2}\sum_\alpha\lvert\nabla\phi_\alpha\rvert^2$	$\frac{1}{2}\frac{\partial\tilde{\kappa}}{\partial\phi_\alpha}\sum_\alpha\lvert\nabla\phi_\alpha\rvert^2-\nabla\cdot(\tilde{\kappa}\nabla\phi_\alpha)$
$\sum_\alpha\sum_{\beta>\alpha}\kappa_{\alpha\beta}\lvert\phi_\alpha\nabla\phi_\beta-\phi_\beta\nabla\phi_\alpha\rvert^2$	$\sum_{\beta\neq\alpha}2\kappa_{\alpha\beta}\left(2\phi_\alpha\lvert\nabla\phi_\beta\rvert^2-2\phi_\beta\nabla\phi_\alpha\cdot\nabla\phi_\beta+\phi_\alpha\phi_\beta\nabla^2\phi_\beta-\phi_\beta^2\nabla^2\phi_\alpha\right)$
$-\sum_\alpha\sum_{\beta>\alpha}\kappa_{\alpha\beta}\nabla\phi_\alpha\cdot\nabla\phi_\beta$	$\sum_{\beta\neq\alpha}\kappa_{\alpha\beta}\nabla^2\phi_\beta$

$\delta\mathscr{F}/\delta\phi_\alpha$-$\delta\mathscr{F}/\delta\phi_\beta$	use $\phi_\gamma=0$ thus $\phi_\beta=(1-\phi_\alpha)$ and $\nabla^2\phi_\beta=-\nabla^2\phi_\alpha$
$\kappa_\beta\nabla^2\phi_\beta-\kappa_\alpha\nabla^2\phi_\alpha$	$-(\kappa_\alpha+\kappa_\beta)\nabla^2\phi_\alpha$
$\frac{1}{2}\left(\frac{\partial\tilde{\kappa}}{\partial\phi_\alpha}-\frac{\partial\tilde{\kappa}}{\partial\phi_\beta}\right)\sum_\alpha(\nabla\phi_\alpha)^2-\nabla\cdot\left(\tilde{\kappa}\nabla\phi_\alpha-\tilde{\kappa}\nabla\phi_\beta\right)$	$-2\kappa_{\alpha\beta}\nabla^2\phi_\alpha$
very nasty and longish	$-2\kappa_{\alpha\beta}\nabla^2\phi_\alpha$
$\kappa_{\alpha\beta}(\nabla^2\phi_\beta-\nabla^2\phi_\alpha)+\sum_{\gamma\neq\alpha,\beta}(\kappa_{\alpha\gamma}-\kappa_{\beta\gamma})\nabla^2\phi_\gamma$	$-2\kappa_{\alpha\beta}\nabla^2\phi_\alpha$

Table A.2: Common potential term formulations and their variation with respect to ϕ_α

f_{pot}	$\delta f_{\text{pot}}/\delta\phi_\alpha$
$\frac{1}{2}\sum_\alpha\sum_{\beta>\alpha}\Omega_{\alpha\beta}\phi_\alpha^2\phi_\beta^2+\tilde{\Omega}\left(\frac{1}{12}+\sum_\alpha\left(\frac{\phi_\alpha^4}{4}-\frac{\phi_\alpha^3}{3}\right)\right)$	$\phi_\alpha\sum_{\beta\neq\alpha}\Omega_{\alpha\beta}\phi_\beta^2+\tilde{\Omega}(\phi_\alpha^3-\phi_\alpha^2)+\frac{\partial\tilde{\Omega}}{\partial\phi_\alpha}(\frac{1}{12}+\dots)$
$\frac{3}{4}\sum_\alpha\sum_{\beta>\alpha}\Omega_{\alpha\beta}\phi_\alpha^2\phi_\beta^2+\frac{1}{2}\tilde{\Omega}\left(\frac{1}{4}+\sum_\alpha\left(\frac{\phi_\alpha^4}{4}-\frac{\phi_\alpha^2}{2}\right)\right)$	$\frac{3}{2}\phi_\alpha\sum_{\beta\neq\alpha}\Omega_{\alpha\beta}\phi_\beta^2+\frac{1}{2}\tilde{\Omega}(\phi_\alpha^3-\phi_\alpha)+\frac{1}{2}\frac{\partial\tilde{\Omega}}{\partial\phi_\alpha}(\frac{1}{4}+\dots)$
$\sum_\alpha\sum_{\beta>\alpha}\Omega_{\alpha\beta}\phi_\alpha^2\phi_\beta^2+\sum_\alpha\sum_{\beta>\alpha}\sum_{\gamma>\beta}\Omega_{\alpha\beta\gamma}\phi_\alpha^2\phi_\beta^2\phi_\gamma^2$	$2\phi_\alpha\sum_{\beta\neq\alpha}\Omega_{\alpha\beta}\phi_\beta^2+2\phi_\alpha\sum_{\beta\neq\alpha}\sum_{\gamma>\beta}\Omega_{\alpha\beta\gamma}\phi_\beta^2\phi_\gamma^2$
$\sum_\alpha\sum_{\beta>\alpha}\Omega_{\alpha\beta}\phi_\alpha\phi_\beta$	$\sum_{\beta\neq\alpha}\Omega_{\alpha\beta}\phi_\beta$
$\sum_\alpha\sum_{\beta>\alpha}\Omega_{\alpha\beta}\phi_\alpha\phi_\beta+\sum_\alpha\sum_{\beta>\alpha}\sum_{\gamma>\beta}\Omega_{\alpha\beta\gamma}\phi_\alpha\phi_\beta\phi_\gamma$	$\sum_{\beta\neq\alpha}\Omega_{\alpha\beta}\phi_\beta+\sum_{\beta\neq\alpha}\sum_{\gamma>\beta}\Omega_{\alpha\beta\gamma}\phi_\beta\phi_\gamma$

$\delta\mathscr{F}/\delta\phi_\alpha$-$\delta\mathscr{F}/\delta\phi_\beta$
$\Omega_{\alpha\beta}\left(\phi_\alpha\phi_\beta^2-\phi_\alpha^2\phi_\beta\right)+\sum_{\gamma\neq\alpha,\beta}(\Omega_{\alpha\gamma}\phi_\alpha-\Omega_{\beta\gamma}\phi_\beta)\phi_\gamma^2+\tilde{\Omega}\left(\phi_\alpha^3-\phi_\alpha^2-\phi_\beta^3+\phi_\beta^2\right)+\left(\frac{\partial\tilde{\Omega}}{\partial\phi_\alpha}-\frac{\partial\tilde{\Omega}}{\partial\phi_\beta}\right)(\dots)$
$\Omega_{\alpha\beta}(\phi_\alpha\phi_\beta^2-\phi_\alpha^2\phi_\beta)+\sum_{\gamma\neq\alpha,\beta}(\Omega_{\alpha\gamma}\phi_\alpha-\Omega_{\beta\gamma}\phi_\beta)\phi_\gamma^2+\Omega_0(\phi_\alpha^3-\phi_\alpha-\phi_\beta^3+\phi_\beta)$
$2\Omega_{\alpha\beta}(\phi_\alpha\phi_\beta^2-\phi_\alpha^2\phi_\beta)+2\sum_{\gamma\neq\alpha,\beta}(\Omega_{\alpha\gamma}\phi_\alpha-\Omega_{\beta\gamma}\phi_\beta)\phi_\gamma^2+\Omega_{\alpha\beta\gamma}\dots$
$\Omega_{\alpha\beta}(\phi_\beta-\phi_\alpha)+\sum_{\gamma\neq\alpha,\beta}(\Omega_{\alpha\gamma}-\Omega_{\beta\gamma})\phi_\gamma+\Omega_{\alpha\beta\gamma}\dots$
use $\phi_\gamma=0$ thus $\phi_\beta=(1-\phi_\alpha)$ and $\nabla^2\phi_\beta=-\nabla^2\phi_\alpha$
$\left(\Omega_{\alpha\beta}+\tilde{\Omega}\right)\phi_\alpha(1-2\phi_\alpha)(1-\phi_\alpha)$
$(\Omega_{\alpha\beta}+\Omega_0)\phi_\alpha(1-2\phi_\alpha)(1-\phi_\alpha)$
$2\Omega_{\alpha\beta}\phi_\alpha(1-2\phi_\alpha)(1-\phi_\alpha)$
$\Omega_{\alpha\beta}(1-2\phi_\alpha)$

B Gibbs simplex constraint

In multiphase-field models, the phase-field variable ϕ_α corresponds to the volume fraction of the respective phase which makes it necessary to fulfill the Gibbs simplex constraint

$$\boldsymbol{\phi} \in \mathbb{R}^N : \sum_{\alpha=1}^{N} \phi_\alpha = 1, \quad 0 \leq \phi_\alpha \quad \forall \alpha. \tag{B.1}$$

If the sum constraint is fulfilled and all phases fractions are larger than zero, we implicitely ensure $\phi_\alpha \in [0,1]\ \forall \alpha = 1,\ldots,N$. Given that the initial conditions comply with Eq. (B.1), there are two conditions that need to be fulfilled during the evolution of phase-field variables, namely

$$\sum_{\alpha} \frac{\partial \phi_\alpha}{\partial t} = 0 \quad \text{and} \quad 0 \leq \phi_\alpha \quad \forall \alpha.$$

The first conditions is ensured by correct formulation of the evolution equations, either by introducing a Langrange multiplier or by suitable choice of the mobility matrix which results in the sum over dual-interactions in Eq. (2.14). If the choice of energy contributions can lead to nonphysical values of $\phi_\alpha < 0$, this violation of constraint Eq. (B.1) needs to be handled separately. Depending on the discretization of time stepping, there are two possible options

1. **Projection-based approach:** We separate the total problem into two a priori simpler problems where the first one is computation of the evolution equations (e.g. $\phi_\alpha^{\text{new}} = \phi_\alpha^{\text{old}} + \Delta t(\ldots)$) neglecting the additional constraints and thus violation of $\phi_\alpha \in [0,1]$ might occur. In a subsequent step, the tuple of phase variables $\boldsymbol{\phi}$ is projected back onto the admissible set (sort of

"pushed back into the Gibbs triangle"). Differences in pairwise mobilities must be taken into account for this procedure to ensure correct treatment of the underlying physics.

2. **Holistic approach:** The condition $0 \leq \phi_\alpha$ enters the system of equations as an algebraic constraint. For large numbers of phases N the problem growths disproportionally with $\propto N^2$ as for every cell/ grid point $N-1$ evolution equations plus N algebraic constraints must be computed.

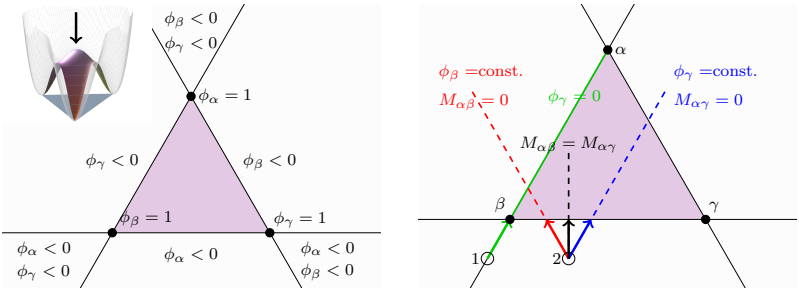
While the projection method can be implemented in a fully explicit and local manner (i.e. cell-wise computation of the prediction ϕ_*^{new} and projection ϕ^{new}), the holistic approach needs global convergence of ϕ-values and all interdependend physical fields (e.g. concentration c).

Projection into the Gibbs triangle

For the binary case of $\phi_\alpha = \phi$ and $\phi_\beta = 1-\phi$, it is sufficient to check for the criterion $\phi < 0$ and, if fulfilled, set $\phi = 0$. Similarly, values of $\phi > 1$ are pushed back to $\phi = 1$. This results in one line of (pseudo-)code

$$\phi^{\text{new}} = \max(0, \min(\phi^{\text{new}}, 1)). \tag{B.2}$$

For the general case of N phases, the procedure is more complicated and will be illustrated over the Gibbs simplex of a triple junction. A detailed discussion of various projection methods can be found in [239]. Far enough from the triple junction (where 'far enough' depends on the width of the diffuse interface), the three-phase system should reduce to a binary interface or bulk ($\phi_\alpha = 1$). Assuming $\phi_\gamma = 0$, any change of phase-variables occurs along the $\alpha\beta$-side of the triangle highlighted in green in Fig. B.1b. A violation of Eq. (B.1), e.g. $\phi_\alpha < 0$ (and thus $\phi_\beta > 1$) as sketched by circle 1, can essentially be handled by Eq. (B.2) and the projection along the green arrow yields $\phi_\alpha = 0$ and $\phi_\beta = 1$. The second scenario is well within the triple junction and again we assume violation of positivity by $\phi_\alpha < 0$. The projection back into the Gibbs triangle now depends on



(a) Gibbs triangle with adjacent domains **(b)** Mobility-weighted projection operation

Figure B.1: Visualization of the Gibbs simplex for a triple junction as the purple triangle while domains fullfilling the sum constraint but violating the positivity constraint $\phi_\alpha \leq 0$ are shown in light gray. The sketch can be interpeted as the top-view onto the energy landscape as shown in a). The mobility-weighted projection into the Gibbs simplex is shown in b) for the case of a binary interface (1) and a general three-phase case (2).

the ratio of pairwise mobilities. In Fig. B.1b, the two limiting cases of $M_{\alpha\beta} = 0$ and $M_{\alpha\gamma} = 0$ are shown together with the case of equal mobilities. The projection algorithm is constructed such that the phase with a negative value will be set to zero $\phi_\alpha = 0$. Incorporation of mobilities is crucial to avoid nonphysically fast evolution of 'slow' phases. Assume that ϕ_γ is a highly immobile phase, any violation of Eq. (B.1) occurs along the blue dashed direction. A projection performed without consideration of mobility ratios results in the operation sketched with a black arrow and would, thus, allow ϕ_γ to zig-zag its way along the lower side of the triangle, resulting in faster kinetics accelerated by the Gibbs simplex algorithm. The general N-dimensional procedure is sketched in the following pseudo-code

Algorithm 1: Gibbs simplex implementation for N phases

```
for α = 1...N do
    if φ_α < 0 then
        activateGibbsSimplex[α] = true;
        count_violations++;
if (count_violations==0) then return;    all phases fulfill φ_α ∈ [0,1]

done=false;
M_red=zeros[N,N];    M_red ∈ ℝ^{N×N}: reduction of M_αβ to phases violating
  φ_α ≤ 0.
b=zeros[N];
while not done do
    for α = 1...N do
        if (!activateGibbsSimplex[α]) then continue;
        b[α]=−φ_α;
        M_red[α,α] = M_αα;
        for β = α+1...N do
            if (!activateGibbsSimplex[β]) then continue;
            M_red[α,β] = M_αβ;
            M_red[β,α] = M_αβ;
    solve(M_red x = b for x);    any vecor-matrix solving algorithm, e.g. Gauss
      elimination.
    done=true;

    for α = 1...N do
        φ_α^new = φ_α^new + M_αβ x_β
        if (φ_α^new < 0) then done=false;
```

C Chemical free energies

The multi-phase field functional presented in Sec. 2.2 contains phase-dependent chemical energies. The grand-potential formulation framework introduced by Choudhury and Nestler [145] is based on the condition of common equilibrium potentials among all phases, i.e. $\mu_i^\alpha = \mu_i^\beta = \cdots = \mu_i$. Direct computation of the evolution of chemical potentials (pds are formulated in terms of K chemical potentials instead of $K \times N$ phase-dependent concentrations with additional constraints) rests on the invertibility of $\mu_i^\alpha(c_i^\alpha)$ to express c_i^α as a function of μ_i. Within this work, only two species are considered, namely charged ions (Li or Na) and the corresponding vacancies. The simplification $K = 2$ leads to $K - 1 = 1$ independent chemical potentials which is the reason that we drop the subscript i. Three possible energy formulations that fullfill the invertibility criterion are

$$\begin{aligned} f_{\text{quad}}^\alpha &= A^\alpha (c^\alpha - c_{\text{min}}^\alpha)^2 + B^\alpha, \\ f_{\text{ideal}}^\alpha &= \mu^{0,\alpha} c^\alpha + A^\alpha c^\alpha \ln(c^\alpha) + A^\alpha (c_{\text{max}} - c^\alpha) \ln(c_{\text{max}} - c^\alpha) + B^\alpha, \\ f_{\text{log}}^\alpha &= (\mu^{0,\alpha} - A^\alpha) c^\alpha + A^\alpha c^\alpha \ln(c^\alpha) + B^\alpha. \end{aligned}$$

The corresponding diffusion potential is defined by $\partial f^\alpha / \partial c^\alpha$ which yields

$$\begin{aligned} \mu_{\text{quad}} &= 2A^\alpha (c^\alpha - c_{\text{min}}^\alpha), \\ \mu_{\text{ideal}} &= \mu^{0,\alpha} + A^\alpha \ln(c^\alpha / (c_{\text{max}} - c^\alpha)), \\ \mu_{\text{log}} &= \mu^{0,\alpha} + A^\alpha \ln(c^\alpha). \end{aligned}$$

Inversion of these functions leads to an expression for the phase-dependent concentrations in terms of the diffusion potential

$$
\begin{aligned}
c^{\alpha}_{\text{quad}}(\mu) &= \frac{\mu}{2A^{\alpha}} + c^{\alpha}_{\text{min}}, \\
c^{\alpha}_{\text{ideal}}(\mu) &= c_{\text{max}} \exp\left(\frac{\mu - \mu^{0,\alpha}}{A^{\alpha}}\right) \Bigg/ \left(1 + \exp\left(\frac{\mu - \mu^{0,\alpha}}{A^{\alpha}}\right)\right), \\
c^{\alpha}_{\log}(\mu) &= \exp\left(\frac{\mu - \mu^{0,\alpha}}{A^{\alpha}}\right).
\end{aligned}
$$

The thermodynamic factor can be expressed as

$$
\begin{aligned}
\left(\frac{\partial c^{\alpha}}{\partial \mu}\right)_{\text{quad}} &= \frac{1}{2A^{\alpha}}, \\
\left(\frac{\partial c^{\alpha}}{\partial \mu}\right)_{\text{ideal}} &= \frac{1}{A^{\alpha} c_{\text{max}}} c^{\alpha}(c_{\text{max}} - c^{\alpha}) \overset{c_{\text{max}}=1}{=} \frac{1}{A^{\alpha}} c^{\alpha}(1 - c^{\alpha}), \\
\left(\frac{\partial c^{\alpha}}{\partial \mu}\right)_{\log} &= \frac{c^{\alpha}}{A^{\alpha}}.
\end{aligned}
$$

The chemical driving force for paiwise phase-transformation is given by

$$
\Delta^{\alpha\beta} = f^{\alpha} - \mu c^{\alpha} - f^{\beta} + \mu c^{\beta}. \tag{C.1}
$$

For the three variants presented above, this yields

$$
\begin{aligned}
\Delta^{\alpha\beta}_{\text{quad}} &= -\left(\frac{1}{4A^\alpha}+\frac{1}{4A^\beta}\right)\mu^2-(c^\alpha_{\text{min}}-c^\beta_{\text{min}})\mu+B^\alpha-B^\beta,\\
\Delta^{\alpha\beta}_{\text{ideal}} &= -c_{\text{max}}A^\alpha\ln\left(1+\exp\left(\frac{\mu-\mu^{0,\alpha}}{A^\alpha}\right)\right)\\
&\quad +c_{\text{max}}A^\beta\ln\left(1+\exp\left(\frac{\mu-\mu^{0,\beta}}{A^\beta}\right)\right)+c_{\text{max}}(A^\alpha-A^\beta)\ln(c_{\text{max}})+B\\
&\overset{c_{\text{max}}=1}{=} -A^\alpha\ln\left(1+\exp\left(\frac{\mu-\mu^{0,\alpha}}{A^\alpha}\right)\right)\\
&\quad +A^\beta\ln\left(1+\exp\left(\frac{\mu-\mu^{0,\beta}}{A^\beta}\right)\right)+B^\alpha-B^\beta\\
&= A^\alpha\ln(1-c^\alpha)-A^\beta\ln(1-c^\beta)+B^\alpha-B^\beta\\
\Delta^{\alpha\beta}_{\text{log}} &= -A^\alpha c^\alpha+A^\beta c^\beta+B^\alpha-B^\beta\\
&= -A^\alpha\exp\frac{\mu-\mu^{0,\alpha}}{A^\alpha}+A^\beta\exp\frac{\mu-\mu^{0,\beta}}{A^\beta}+B^\alpha-B^\beta
\end{aligned}
$$

List of Publications

1. J. Nieschlag, P. Ruhland, **S. Daubner**, S. F. Koch, J. Fleischer. Finite element optimisation for rotational moulding with a core to manufacture intrinsic hybrid FRP metal pipes. Production Engineering 12, 239-247, 2018.

2. **S. Daubner**, P G Kubendran Amos, E. Schoof, J. Santoki, D. Schneider, and B. Nestler. Multiphase-field modeling of spinodal decomposition during intercalation in an Allen-Cahn framework. Physical Review Materials, 5(3):035406, 2021.

3. X. Liu, D. Schneider, **S. Daubner**, and B. Nestler. Simulating mechanical wave propagation within the framework of phase-field modelling. Computer Methods in Applied Mechanics and Engineering, 381:113842, 2021.

4. M. Reder, D. Schneider, F. Wang, **S. Daubner**, and B. Nestler. Phase-field formulation of a fictitious domain method for particulate flows interacting with complex and evolving geometries. International Journal for Numerical Methods in Fluids, 93(8):2486–2507, 2021.

5. J. Santoki, **S. Daubner**, D. Schneider, M. Kamlah, and B. Nestler. Effect of tortuosity, porosity, and particle size on phase-separation dynamics of ellipsoid-like particles of porous electrodes: Cahn–Hilliard-type phase-field simulations. Modelling and Simulation in Materials Science and Engineering, 29(6):065010, 2021.

6. **S. Daubner**, M. Weichel, D. Schneider, and B. Nestler. Modeling intercalation in cathode materials with phase-field methods: Assumptions and implications using the example of LiFePO4. Electrochimica Acta, 421:140516, 2022

7. **S. Daubner**, P. W. Hoffrogge, M. Minar, and B. Nestler. Triple junction benchmark for multiphase-field and multi-order parameter models. Computational Materials Science, 219:111995, 2023.

8. **S. Daubner**, M. Reder, N. Prajapati, D. Schneider, and B. Nestler. Multiphase-field modelling of anisotropic elasticity at finite deformation in Eulerian space. Journal of Computational Science, 66:101930, 2023.

9. Q. Huang, **S. Daubner**, S. Zhang, D. Schneider, B. Nestler, H. Mao, S. Liu, and Y. Du. Phase-field simulation for voltage profile of LixSn nanoparticle during lithiation/delithiation. Computational Materials Science, 220:112047, 2023.

10. **S. Daubner**, M. Weichel, P. W. Hoffrogge, D. Schneider, and B. Nestler. Modeling anisotropic transport in polycrystalline battery materials. Batteries, 9(6), 310, 2023.

11. **S. Daubner**, M. Dillenz, L. Pfeiffer, C. Gauckler, M. Rosin, N. Burgard, J. Martin, P. Axmann, M. Sotoudeh, A, Groß, D. Schneider, and B. Nestler. Combined study of phase transitions in the P2-type $Na_XNi_{1/3}Mn_{2/3}O_2$ cathode material: experimental, ab-initio and multiphase-field results. Submitted.

List of Figures

1 Phase-field simulations applied on the single particle and agglomerate scale vi
1.1 Crystal structure of three canonical intercalation cathodes for LIBs . 3
1.2 Secondary particle morphologies 5
1.3 Methods for battery simulation across the scales 9
1.4 Relevant length scales from single particles to one electrode layer. . 16
2.1 Evolution of a one-dimensional diffuse interface towards the equilibrium solution 29
2.2 Diffuse representation of a sharp interface problem with the phase-field method given exemplarily for a circle 30
2.3 Nano-battery model consisting of a single cathode particle cycled against Na metal anode assuming fast transport in the electrolyte and fast reaction kinetics at the anode side. 43
2.4 Discretisation of spatial domain 45
3.1 Energetic landscape of the multi-well and multi-obstacle potentials shown for a three-phase system over the Gibbs simplex of a triple junction. 53
3.2 Multi-well formulations (3.12) and (3.13) drawn over the Gibbs simplex of a triple junction for different values of χ. 55
3.3 Evolution of phase ϕ_0 towards static equilibrium shown exemplarily for $\gamma_{\alpha\beta} = \gamma_0$ and domain size 100×100. 61
3.4 MPF comparison of metrics for the static triple junction with 100×200 domain size. 63
3.5 Influence of numerical parameter $\Omega_{\alpha\beta\gamma}$ in $f_{\text{well}}^{\text{Garcke}}$ (Eq. (3.11)) on spurious phase generation and model error. 64
3.6 Steady-state triple junction 65
3.7 MPF comparison of metrics for the steady-state triple junction. . . . 66

4.1 Stability map for well-potential. 76
4.2 Stability map for obstacle potential. 77
4.3 Concentration evolution in a 3D domain with $200 \times 200 \times 200$ voxels and initial $c = 0.3$. 78
4.4 ϕ_β-ϕ_γ equilibrium interface 79
4.5 Stationary solutions according to Eq. (4.30) shown for discrete values of $\phi_\gamma \in [0.01, 0.1, 0.2, \ldots, 0.9]$. 83
4.6 Comparison of noise functions for heterogeneous nucleation in a grain boundary. 84
4.7 Composition gradient within a multi-grain cathode section under CC discharge at $t = 0.01$ h. 85
4.8 Intercalation in a 2D multi-grain cathode section with 200×300 cells under constant current discharge. 86
4.9 Evolution of FP to LFP phase transformation during intercalation in 2D multi-grain cathode section with 200×300 cells under CC discharge with 1C rate. 87
5.1 Standart isotropic discretisation 90
5.2 Spatial discretization of gradients with the a) antisymmetric and b) symmetric scheme. 91
5.3 No flux (isolate) BC in the antisymmetric scheme 92
5.4 No flux (isolate) BC in the symmetric scheme 93
5.5 Concentration profile at the right domain boundary for various numerical implementations at a rotation angle of $\alpha = 9^\circ$ between the material and spatial coordinate system. 95
5.6 Relative error $\|\varepsilon_{\text{ref}}\|_2$ for antisymmetric and symmetric scheme combined with various BC implementations. 96
5.7 Error of numerical diffusion for antisymmetric (a-c) and symmetric (d-f) scheme at rotation angle $\theta = 60^\circ$. 98
6.1 Simulation setup for particle intercalation study. 109
6.2 Virtual quenching experiment with relaxation from solid solution with $c_{\text{init}} = 0.5$ in 50×50 nm 2D cross-sections. 111
6.3 Amplification factors for unstable fluctuations in the (100)-direction shown in green and in the (001)-direction shown in red in the left column. 115
6.4 Open circuit potential V_{OCV} over filling fraction X in Li_XFePO_4. . . 118

6.5 Rate-dependent charging behaviour obtained with the Cahn-Hilliard approach 119
6.6 Rate-dependent phase separation upon discharge obtained with the multi-phase approach 121
6.7 Discharge simulation of a thin platelet with dimensions 50×50 nm under the depth-average assumption using the multi-phase approach including coherency strain. 122
6.8 Multi-grain platelet with dimensions $250 \times 250 \times 50$ nm during discharge using the depth-averaged model. 125
6.9 Influence of texture on mechanical stresses during discharge using the depth-averaged model. 126
7.1 Experimental voltage data for $Na_X Ni_{1/3} Mn_{2/3} O_2$ at low C-rate. . . 132
7.2 Gibbs free energy fittings f_{chem} in the top row and resulting equilibrium voltages below for a) parabolic fitting and b) logarithmic fitting. 135
7.3 Dimensionality reduction from the three dimensional case (middle) to a 2D cross-section (left) or by depth-averaging (right). . 136
7.4 Comparison of a) fully resolved particle with b) 2D reduction to cross-section and c) 2D reduction through depth-averaging. . . . 137
7.5 Comparison of logarithmic function fit (colored) with quadratic fit (black, dashed lines) 138
7.6 Influence of diffusivity in the O2-phase on overpotential for various C-rates. 140
7.7 Influence of diffusivity in the O2-phase and assumed charge transfer coefficient k_0 on voltage output for C-rates $\in [2^{-5}, ...2, 4, 8]$. 141
7.8 C-rate tests performed (a)-(d) experimentally and (e) virtually for C/10, C/5, 1C and 5C. 144
8.1 Ideal solution fit for the equilibrium electro-chemical potential of NMC811 shown in blue which is based on the datapoints pusblished in Noh *et al.* [232] 153
8.2 Initial grain structures of secondary particles. 155
8.3 Relaxation of concentration gradients in comparison for the three microstructures with $r/R = 1$, $r/R = 1/2$ and $r/R = 1/4$. . . . 156
8.4 Virtual PITT experiment. 158

8.5 Spatial ion distribution in gravel-NMC (a, b) compared to rod-NMC (c, d). 159
8.6 Role of grain boundaries in textured secondary particles. 160
B.1 Visualization of the Gibbs simplex for a triple junction. 175

List of Tables

3.1 Set of simulation parameters 60
3.2 Overview of MPF model combinations employed in this work with references to original works. All new combinations are marked as such. 62
4.1 Input parameters for model validation. 76
6.1 Phase characteristics taken from [33] 104
6.2 Interface energies of LFP-FP interface [49] 105
6.3 Li-vacancy self diffusion coefficient D_{Li} at $T = 300K$ [9] given in $[\mathrm{m}^2/\mathrm{s}]$ 105
7.1 Fitting parameters for chemical energies 134
7.2 Phase characteristics of $\mathrm{Na}_X\mathrm{Ni}_{1/3}\mathrm{Mn}_{2/3}\mathrm{O}_2$ 142
A.1 Common gradient energy formulations and their variation with respect to ϕ_α 171
A.2 Common potential term formulations and their variation with respect to ϕ_α 172

Bibliography

[1] The Nobel Prize in Chemistry 2019: John B. Goodenough, M. Stanley Whittingham and Akira Yoshino. https://www.nobelprize.org/prizes/chemistry/2019/popular-information, . Accessed: 2023-03-30.

[2] J. Asenbauer, T. Eisenmann, M. Kuenzel, A. Kazzazi, Z. Chen, and D. Bresser. The success story of graphite as a lithium-ion anode material - fundamentals, remaining challenges, and recent developments including silicon (oxide) composites. *Sustainable Energy & Fuels*, 4(11): 5387–5416, 2020.

[3] T. Placke, R. Kloepsch, S. Dühnen, and M. Winter. Lithium ion, lithium metal, and alternative rechargeable battery technologies: the odyssey for high energy density. *Journal of Solid State Electrochemistry*, 21(7): 1939–1964, 2017.

[4] J. W. Fergus. Recent developments in cathode materials for lithium ion batteries. *Journal of Power Sources*, 195(4):939–954, 2010.

[5] D. Larcher and J.-M. Tarascon. Towards greener and more sustainable batteries for electrical energy storage. *Nature Chemistry*, 7(1):19–29, 2015.

[6] Z. Zhao-Karger and M. Fichtner. Beyond Intercalation Chemistry for Rechargeable Mg Batteries: A Short Review and Perspective. *Frontiers in Chemistry*, 6(January):1–12, 2019.

[7] I. Mohammad, R. Witter, M. Fichtner, and M. A. Reddy. Introducing Interlayer Electrolytes: Toward Room-Temperature High-Potential Solid-State Rechargeable Fluoride Ion Batteries. *ACS Applied Energy Materials*, 2(2):1553–1562, 2019.

[8] L. W. Shacklette, T. R. Jow, and L. Townsend. Rechargeable Electrodes from Sodium Cobalt Bronzes. *Journal of The Electrochemical Society*, 135(11):2669–2674, 1988.

[9] R. Malik, D. Burch, M. Bazant, and G. Ceder. Particle size dependence of the ionic diffusivity. *Nano Letters*, 10(10):4123–4127, 2010.

[10] P. J. Bouwman, B. A. Boukamp, H. J. M. Bouwmeester, and P. H. L. Notten. Influence of Diffusion Plane Orientation on Electrochemical Properties of Thin Film LiCoO2 Electrodes. *Journal of The Electrochemical Society*, 149(6):A699, 2002.

[11] M. S. Islam and C. A. Fisher. Lithium and sodium battery cathode materials: Computational insights into voltage, diffusion and nanostructural properties. *Chemical Society Reviews*, 43(1):185–204, 2014.

[12] A. Van Der Ven, Z. Deng, S. Banerjee, and S. P. Ong. Rechargeable Alkali-Ion Battery Materials: Theory and Computation. *Chemical Reviews*, 120(14):6977–7019, 2020.

[13] A. Van der Ven and G. Ceder. Lithium diffusion mechanisms in layered intercalation compounds. *Journal of Power Sources*, 97-98:529–531, 2001.

[14] G. G. Amatucci, J. M. Tarascon, and L. C. Klein. CoO2, The End Member of the Li x CoO2 Solid Solution. *Journal of The Electrochemical Society*, 143(3):1114–1123, 1996.

[15] C. Delmas, C. Fouassier, and P. Hagenmuller. Structural classification and properties of the layered oxides. *Physica B+C*, 99(1-4):81–85, 1980.

[16] E. Trevisanello, R. Ruess, G. Conforto, F. H. Richter, and J. Janek. Polycrystalline and Single Crystalline NCM Cathode Materials—Quantifying Particle Cracking, Active Surface Area, and Lithium Diffusion. *Advanced Energy Materials*, 11(18):2003400, 2021.

[17] J. Mao, X. Liu, J. Liu, H. Jiang, T. Zhang, G. Shao, G. Ai, W. Mao, Y. Feng, W. Yang, G. Liu, and K. Dai. P2-type Na 2/3 Ni 1/3 Mn 2/3 O 2 Cathode Material with Excellent Rate and Cycling Performance for Sodium-Ion Batteries . *Journal of The Electrochemical Society*, 166(16): A3980–A3986, 2019.

[18] A. O. Kondrakov, A. Schmidt, J. Xu, H. Geßwein, R. Mönig, P. Hartmann, H. Sommer, T. Brezesinski, and J. Janek. Anisotropic Lattice Strain and Mechanical Degradation of High- and Low-Nickel NCM Cathode Materials for Li-Ion Batteries. *The Journal of Physical Chemistry C*, 121(6):3286–3294, 2017.

[19] R. Xu, L. S. de Vasconcelos, J. Shi, J. Li, and K. Zhao. Disintegration of Meatball Electrodes for LiNi x Mn y Co z O2 Cathode Materials. *Experimental Mechanics*, 58(4):549–559, 2018.

[20] L. F. Pfeiffer, N. Jobst, C. Gauckler, M. Lindén, M. Marinaro, S. Passerini, M. Wohlfahrt-Mehrens, and P. Axmann. Layered P2-NaxMn3/4Ni1/4O2 Cathode Materials For Sodium-Ion Batteries: Synthesis, Electrochemistry and Influence of Ambient Storage. *Frontiers in Energy Research*, 10(May):1–17, 2022.

[21] M. Müller, L. Schneider, N. Bohn, J. R. Binder, and W. Bauer. Effect of Nanostructured and Open-Porous Particle Morphology on Electrode Processing and Electrochemical Performance of Li-Ion Batteries. *ACS Applied Energy Materials*, 4(2):1993–2003, 2021.

[22] Z. Xu, Z. Jiang, C. Kuai, R. Xu, C. Qin, Y. Zhang, M. M. Rahman, C. Wei, D. Nordlund, C.-J. Sun, X. Xiao, X.-W. Du, K. Zhao, P. Yan, Y. Liu, and F. Lin. Charge distribution guided by grain crystallographic

orientations in polycrystalline battery materials. *Nature Communications*, 11(1):83, 2020.

[23] C. Delmas, M. Ménétrier, L. Croguennec, S. Levasseur, J. Pérès, C. Pouillerie, G. Prado, L. Fournès, and F. Weill. Lithium batteries: a new tool in solid state chemistry. *International Journal of Inorganic Materials*, 1(1):11–19, 1999.

[24] N. G. Hörmann and A. Groß. Phase field parameters for battery compounds from first-principles calculations. *Physical Review Materials*, 3(5):055401, 2019.

[25] W. Dreyer, J. Jamnik, C. Guhlke, R. Huth, J. Moškon, and M. Gaberšček. The thermodynamic origin of hysteresis in insertion batteries. *Nature Materials*, 9(5):448–453, 2010.

[26] W. Li, J. N. Reimers, and J. R. Dahn. In situ x-ray diffraction and electrochemical studies of Li1-xNiO2. *Solid State Ionics*, 67(1-2): 123–130, 1993.

[27] L. de Biasi, A. Schiele, M. Roca-Ayats, G. Garcia, T. Brezesinski, P. Hartmann, and J. Janek. Phase Transformation Behavior and Stability of LiNiO2 Cathode Material for Li-Ion Batteries Obtained from In Situ Gas Analysis and Operando X-Ray Diffraction. *ChemSusChem*, 12(10): 2240–2250, 2019.

[28] T. Ohzuku, Y. Iwakoshi, and K. Sawai. Formation of Lithium-Graphite Intercalation Compounds in Nonaqueous Electrolytes and Their Application as a Negative Electrode for a Lithium Ion (Shuttlecock) Cell. *Journal of The Electrochemical Society*, 140(9):2490–2498, 1993.

[29] Z. Lu and J. R. Dahn. In Situ X-Ray Diffraction Study of P2-Na2/3 Ni1/3 Mn2/3 O2. *Journal of The Electrochemical Society*, 148(11):A1225, 2001.

[30] D. H. Lee, J. Xu, and Y. S. Meng. An advanced cathode for Na-ion batteries with high rate and excellent structural stability. *Physical Chemistry Chemical Physics*, 15(9):3304, 2013.

[31] P. Moreau, D. Guyomard, J. Gaubicher, and F. Boucher. Structure and Stability of Sodium Intercalated Phases in Olivine FePO4. *Chemistry of Materials*, 22(14):4126–4128, 2010.

[32] T. Akçay, M. Häringer, K. Pfeifer, J. Anhalt, J. R. Binder, S. Dsoke, D. Kramer, and R. Mönig. Na3V2(PO4)3 - A Highly Promising Anode and Cathode Material for Sodium-Ion Batteries. *ACS Applied Energy Materials*, 4(11):12688–12695, 2021.

[33] G. Chen, X. Song, and T. Richardson. Electron microscopy study of the LiFePO4 to FePO4 phase transition. *Electrochemical and Solid-State Letters*, 9(6):295–298, 2006.

[34] D. Chen, D. Kramer, and R. Mönig. Chemomechanical fatigue of LiMn1.95Al0.05O4 electrodes for lithium-ion batteries. *Electrochimica Acta*, 259:939–948, 2018.

[35] P.-C. Tsai, B. Wen, M. Wolfman, M.-J. Choe, M. S. Pan, L. Su, K. Thornton, J. Cabana, and Y.-M. Chiang. Single-particle measurements of electrochemical kinetics in NMC and NCA cathodes for Li-ion batteries. *Energy & Environmental Science*, 11(4):860–871, 2018.

[36] S. Daubner, M. Weichel, D. Schneider, and B. Nestler. Modeling intercalation in cathode materials with phase-field methods: Assumptions and implications using the example of LiFePO4. *Electrochimica Acta*, 421(May):140516, 2022.

[37] W. Weppner and R. A. Huggins. Determination of the Kinetic Parameters of Mixed-Conducting Electrodes and Application to the System Li3Sb. *Journal of The Electrochemical Society*, 124(10):1569–1578, 1977.

[38] R. Ruess, S. Schweidler, H. Hemmelmann, G. Conforto, A. Bielefeld, D. A. Weber, J. Sann, M. T. Elm, and J. Janek. Influence of NCM Particle

Cracking on Kinetics of Lithium-Ion Batteries with Liquid or Solid Electrolyte. *Journal of The Electrochemical Society*, 167(10):100532, 2020.

[39] S. Zheng, R. Huang, Y. Makimura, Y. Ukyo, C. A. J. Fisher, T. Hirayama, and Y. Ikuhara. Microstructural Changes in LiNi 0.8 Co 0.15 Al 0.05 O 2 Positive Electrode Material during the First Cycle. *Journal of The Electrochemical Society*, 158(4):A357–A362, 2011.

[40] Y. Zhang, M. Wu, J. Ma, G. Wei, Y. Ling, R. Zhang, and Y. Huang. Revisiting the Na 2/3 Ni 1/3 Mn 2/3 O 2 Cathode: Oxygen Redox Chemistry and Oxygen Release Suppression. *ACS Central Science*, 6(2): 232–240, 2020.

[41] G. Conforto, R. Ruess, D. Schröder, E. Trevisanello, R. Fantin, F. H. Richter, and J. Janek. Quantification of the Impact of Chemo-Mechanical Degradation on the Performance and Cycling Stability of NCM-Based Cathodes in Solid-State Li-Ion Batteries. *Journal of The Electrochemical Society*, 168(7):070546, 2021.

[42] The Nobel Prize in Chemistry 1998: Walter Kohn and John A. Pople. `https://www.nobelprize.org/prizes/chemistry/1998/press-release/`, . Accessed: 2023-04-10.

[43] D. Morgan, A. Van der Ven, and G. Ceder. Li Conductivity in LixMPO4 (M = Mn, Fe, Co, Ni) Olivine Materials. *Electrochemical and Solid-State Letters*, 7(2):A30, 2004.

[44] K. Persson, Y. Hinuma, Y. S. Meng, A. Van der Ven, and G. Ceder. Thermodynamic and kinetic properties of the Li-graphite system from first-principles calculations. *Physical Review B*, 82(12):125416, 2010.

[45] Y. Hinuma, Y. S. Meng, and G. Ceder. Temperature-concentration phase diagram of P2 -Nax CoO2 from first-principles calculations. *Physical Review B*, 77(22):1–16, 2008.

[46] M. E. Arroyo y de Dompablo, A. Van der Ven, and G. Ceder. First-principles calculations of lithium ordering and phase stability on LixNiO2. *Physical Review B*, 66(6):064112, 2002.

[47] J. Vinckevičiūte, M. D. Radin, and A. Van der Ven. Stacking-Sequence Changes and Na Ordering in Layered Intercalation Materials. *Chemistry of Materials*, 28(23):8640–8650, 2016.

[48] T. Maxisch and G. Ceder. Elastic properties of olivine LixFePO4 from first principles. *Physical Review B*, 73(17):174112, 2006.

[49] A. Abdellahi, O. Akyildiz, R. Malik, K. Thornton, and G. Ceder. Particle-size and morphology dependence of the preferred interface orientation in LiFePO4 nano-particles. *Journal of Materials Chemistry A*, 2(37):15437–15447, 2014.

[50] L. Wang, F. Zhou, Y. S. Meng, and G. Ceder. First-principles study of surface properties of LiFeP O4: Surface energy, structure, Wulff shape, and surface redox potential. *Physical Review B*, 76(16):1–11, 2007.

[51] C. Fisher and M. Islam. Surface structures and crystal morphologies of LiFePO4: Relevance to electrochemical behaviour. *Journal of Materials Chemistry*, 18(11):1209–1215, 2008.

[52] C. Hin. Kinetic Monte Carlo Simulations of Anisotropic Lithium Intercalation into LixFePO4 Electrode Nanocrystals. *Advanced Functional Materials*, 21(13):2477–2487, 2011.

[53] T. F. Fuller, M. Doyle, and J. Newman. Simulation and Optimization of the Dual Lithium Ion Insertion Cell. *Journal of The Electrochemical Society*, 141(1):1–10, 1994.

[54] V. Srinivasan and J. Newman. Discharge Model for the Lithium Iron-Phosphate Electrode. *Journal of The Electrochemical Society*, 151 (10):A1517, 2004.

[55] A. Latz and J. Zausch. Thermodynamic consistent transport theory of Li-ion batteries. *Journal of Power Sources*, 196(6):3296–3302, 2011.

[56] S. A. Roberts, V. E. Brunini, K. N. Long, and A. M. Grillet. A Framework for Three-Dimensional Mesoscale Modeling of Anisotropic Swelling and Mechanical Deformation in Lithium-Ion Electrodes. *Journal of The Electrochemical Society*, 161(11):F3052–F3059, 2014.

[57] M. Ender, J. Joos, T. Carraro, and E. Ivers-Tiffée. Three-dimensional reconstruction of a composite cathode for lithium-ion cells. *Electrochemistry Communications*, 13(2):166–168, 2011.

[58] A. H. Wiedemann, G. M. Goldin, S. A. Barnett, H. Zhu, and R. J. Kee. Effects of three-dimensional cathode microstructure on the performance of lithium-ion battery cathodes. *Electrochimica Acta*, 88:580–588, 2013.

[59] S. Han, J. Park, W. Lu, and A. M. Sastry. Numerical study of grain boundary effect on Li+ effective diffusivity and intercalation-induced stresses in Li-ion battery active materials. *Journal of Power Sources*, 240: 155–167, 2013.

[60] J. M. Allen, P. J. Weddle, A. Verma, A. Mallarapu, F. Usseglio-Viretta, D. P. Finegan, A. M. Colclasure, W. Mai, V. Schmidt, O. Furat, D. Diercks, T. Tanim, and K. Smith. Quantifying the influence of charge rate and cathode-particle architectures on degradation of Li-ion cells through 3D continuum-level damage models. *Journal of Power Sources*, 512(April):230415, 2021.

[61] K. Taghikhani, P. J. Weddle, J. R. Berger, and R. J. Kee. Modeling Coupled Chemo-Mechanical Behavior of Randomly Oriented NMC811 Polycrystalline Li-Ion Battery Cathodes. *Journal of The Electrochemical Society*, 168(8):080511, 2021.

[62] T. Hutzenlaub, S. Thiele, N. Paust, R. Spotnitz, R. Zengerle, and C. Walchshofer. Three-dimensional electrochemical Li-ion battery modelling featuring a focused ion-beam/scanning electron microscopy

based three-phase reconstruction of a LiCoO2 cathode. *Electrochimica Acta*, 115:131–139, 2014.

[63] T. Danner, M. Singh, S. Hein, J. Kaiser, H. Hahn, and A. Latz. Thick electrodes for Li-ion batteries: A model based analysis. *Journal of Power Sources*, 334:191–201, 2016.

[64] S. A. Roberts, H. Mendoza, V. E. Brunini, B. L. Trembacki, D. R. Noble, and A. M. Grillet. Insights Into Lithium-Ion Battery Degradation and Safety Mechanisms From Mesoscale Simulations Using Experimentally Reconstructed Mesostructures. *Journal of Electrochemical Energy Conversion and Storage*, 13(3):031005, 2016.

[65] M. E. Ferraro, B. L. Trembacki, V. E. Brunini, D. R. Noble, and S. A. Roberts. Electrode Mesoscale as a Collection of Particles: Coupled Electrochemical and Mechanical Analysis of NMC Cathodes. *Journal of The Electrochemical Society*, 167(1):013543, 2020.

[66] M. Doyle, T. F. Fuller, and J. Newman. Modeling of Galvanostatic Charge and Discharge of the Lithium/Polymer/Insertion Cell. *Journal of The Electrochemical Society*, 140(6):1526–1533, 1993.

[67] D. Grazioli, M. Magri, and A. Salvadori. Computational modeling of Li-ion batteries. *Computational Mechanics*, 58(6):889–909, 2016.

[68] Y. Bai, Y. Zhao, W. Liu, and B.-X. Xu. Two-level modeling of lithium-ion batteries. *Journal of Power Sources*, 422:92–103, 2019.

[69] J. Joos, T. Carraro, A. Weber, and E. Ivers-Tiffée. Reconstruction of porous electrodes by FIB/SEM for detailed microstructure modeling. *Journal of Power Sources*, 196(17):7302–7307, 2011.

[70] PyBaMM: Python Battery Mathematical Modelling. `https://www.pybamm.org`. Accessed: 2023-04-17.

[71] MPET: Multiphase Porous Electrode Theory. `https://bitbucket.org/bazantgroup/mpet/src/master`. Accessed: 2023-04-17.

[72] D. Cogswell and M. Bazant. Size-dependent phase morphologies in LiFePO4 battery particles. *Electrochemistry Communications*, 95:33–37, 2018.

[73] R. Smith and M. Bazant. Multiphase Porous Electrode Theory. *Journal of The Electrochemical Society*, 164(11):E3291–E3310, 2017.

[74] B. Han, A. Van Der Ven, D. Morgan, and G. Ceder. Electrochemical modeling of intercalation processes with phase field models. *Electrochimica Acta*, 49(26):4691–4699, 2004.

[75] J. Guyer, W. Boettinger, J. Warren, and G. McFadden. Phase field modeling of electrochemistry I: Equilibrium. *Physical Review E*, 69(2): 12, 2004.

[76] Y. Shibuta, Y. Okajima, and T. Suzuki. Phase-field modeling for electrodeposition process. *Science and Technology of Advanced Materials*, 8(6):511–518, 2007.

[77] L. Liang, Y. Qi, F. Xue, S. Bhattacharya, S. Harris, and L. Chen. Nonlinear phase-field model for electrode-electrolyte interface evolution. *Physical Review E*, 86(5):1–5, 2012.

[78] D. Cogswell. Quantitative phase-field modeling of dendritic electrodeposition. *Physical Review E*, 92(1):1–5, 2015.

[79] Z. Hong and V. Viswanathan. Phase-Field Simulations of Lithium Dendrite Growth with Open-Source Software. *ACS Energy Letters*, 3(7): 1737–1743, 2018.

[80] V. Yurkiv, T. Foroozan, A. Ramasubramanian, R. Shahbazian-Yassar, and F. Mashayek. Phase-field modeling of solid electrolyte interface (SEI) influence on Li dendritic behavior. *Electrochimica Acta*, 265:609–619, 2018.

[81] K. S. N. Vikrant, E. McShane, A. M. Colclasure, B. D. McCloskey, and S. Allu. Quantification of Dead Lithium on Graphite Anode under Fast

Charging Conditions. *Journal of The Electrochemical Society*, 169(4): 040520, 2022.

[82] G. Singh, G. Ceder, and M. Bazant. Intercalation dynamics in rechargeable battery materials: General theory and phase-transformation waves in LiFePO4. *Electrochimica Acta*, 53(26):7599–7613, 2008.

[83] P. Bai, D. Cogswell, and M. Bazant. Suppression of phase separation in LiFePO4 nanoparticles during battery discharge. *Nano Letters*, 11(11): 4890–4896, 2011.

[84] D. Cogswell and M. Bazant. Coherency strain and the kinetics of phase separation in LiFePO 4 nanoparticles. *ACS Nano*, 6(3):2215–2225, 2012.

[85] M. Tang, J. Belak, and M. Dorr. Anisotropic phase boundary morphology in nanoscale olivine electrode particles. *Journal of Physical Chemistry C*, 115(11):4922–4926, 2011.

[86] L. Hong, L. Li, Y. Chen-Wiegart, J. Wang, K. Xiang, L. Gan, W. Li, F. Meng, F. Wang, J. Wang, Y. Chiang, S. Jin, and M. Tang. Two-dimensional lithium diffusion behavior and probable hybrid phase transformation kinetics in olivine lithium iron phosphate. *Nature Communications*, 8(1), 2017.

[87] L. Hong, K. Yang, and M. Tang. A mechanism of defect-enhanced phase transformation kinetics in lithium iron phosphate olivine. *npj Computational Materials*, 5(1):1–9, 2019.

[88] M. Huttin and M. Kamlah. Phase-field modeling of stress generation in electrode particles of lithium ion batteries. *Applied Physics Letters*, 101 (13), 2012.

[89] A. Walk, M. Huttin, and M. Kamlah. Comparison of a phase-field model for intercalation induced stresses in electrode particles of lithium ion batteries for small and finite deformation theory. *European Journal of Mechanics, A/Solids*, 48(1):74–82, 2014.

[90] T. Zhang and M. Kamlah. Sodium Ion Batteries Particles: Phase-Field Modeling with Coupling of Cahn-Hilliard Equation and Finite Deformation Elasticity. *Journal of The Electrochemical Society*, 165(10): A1997–A2007, 2018.

[91] T. Zhang and M. Kamlah. Phase-field modeling of the particle size and average concentration dependent miscibility gap in nanoparticles of LixMn2O4, LixFePO4, and NaxFePO4 during insertion. *Electrochimica Acta*, 298:31–42, 2019.

[92] Y. Zhao, P. Stein, and B.-X. Xu. Isogeometric analysis of mechanically coupled Cahn–Hilliard phase segregation in hyperelastic electrodes of Li-ion batteries. *Computer Methods in Applied Mechanics and Engineering*, 297:325–347, 2015.

[93] Y. Zhao, B.-X. Xu, P. Stein, and D. Gross. Phase-field study of electrochemical reactions at exterior and interior interfaces in Li-ion battery electrode particles. *Computer Methods in Applied Mechanics and Engineering*, 312:428–446, 2016.

[94] J. Santoki, M. Kamlah, D. Schneider, B. Nestler, M. Selzer, and F. Wang. Phase-field study of surface irregularities of a cathode particle during intercalation. *Modelling and Simulation in Materials Science and Engineering*, 26(6):065013, 2018.

[95] L. Hong, L. Liang, S. Bhattacharyya, W. Xing, and L. Chen. Anisotropic Li intercalation in a LixFePO4 nano-particle: A spectral smoothed boundary phase-field model. *Physical Chemistry Chemical Physics*, 18 (14):9537–9543, 2016.

[96] Y. Zhao. *Phase-Field Modeling of Electro-Chemo-Mechanical Behavior of Li-ion Battery Electrodes*. Dissertation, Technische Universität Darmstadt, 2017.

[97] Y. Zhao, L. De Jesus, P. Stein, G. Horrocks, S. Banerjee, and B.-X. Xu. Modeling of phase separation across interconnected electrode particles in lithium-ion batteries. *RSC Advances*, 7(65):41254–41264, 2017.

[98] L. Wu, V. De Andrade, X. Xiao, and J. Zhang. Phase Field Modeling of Coupled Phase Separation and Diffusion-Induced Stress in Lithium Iron Phosphate Particles Reconstructed From Synchrotron Nano X-ray Tomography. *Journal of Electrochemical Energy Conversion and Storage*, 16(4):041006, 2019.

[99] M. Z. Bazant. Theory of chemical kinetics and charge transfer based on nonequilibrium thermodynamics. *Accounts of Chemical Research*, 46(5): 1144–1160, 2013.

[100] D. A. Cogswell and M. Z. Bazant. Theory of Coherent Nucleation in Phase-Separating Nanoparticles. *Nano Letters*, 13(7):3036–3041, 2013.

[101] M. Klinsmann, D. Rosato, M. Kamlah, and R. McMeeking. Modeling Crack Growth during Li Extraction in Storage Particles Using a Fracture Phase Field Approach. *Journal of The Electrochemical Society*, 163(2): A102–A118, 2016.

[102] C. Miehe, H. Dal, L.-M. Schänzel, and A. Raina. A phase-field model for chemo-mechanical induced fracture in lithium-ion battery electrode particles. *International Journal for Numerical Methods in Engineering*, 106(9):683–711, 2016.

[103] D. O'Connor, M. Welland, W. Kam Liu, and P. Voorhees. Phase transformation and fracture in single LixFePO4 cathode particles: A phase-field approach to Li-ion intercalation and fracture. *Modelling and Simulation in Materials Science and Engineering*, 24(3), 2016.

[104] Y. Bai, D. A. Santos, S. Rezaei, P. Stein, S. Banerjee, and B.-X. Xu. A chemo-mechanical damage model at large deformation: numerical and experimental studies on polycrystalline energy materials. *International Journal of Solids and Structures*, 228:111099, 2021.

[105] M. Tang, W. C. Carter, J. F. Belak, and Y.-M. Chiang. Modeling the competing phase transition pathways in nanoscale olivine electrodes. *Electrochimica Acta*, 56(2):969–976, 2010.

[106] M. J. Welland, D. Karpeyev, D. T. O'Connor, and O. Heinonen. Miscibility Gap Closure, Interface Morphology, and Phase Microstructure of 3D LixFePO4 Nanoparticles from Surface Wetting and Coherency Strain. *ACS Nano*, 9(10):9757–9771, 2015.

[107] M. Fleck, H. Federmann, and E. Pogorelov. Phase-field modeling of Li-insertion kinetics in single LiFePO4-nano-particles for rechargeable Li-ion battery application. *Computational Materials Science*, 153: 288–296, 2018.

[108] N. Nadkarni, E. Rejovitsky, D. Fraggedakis, C. Di Leo, R. Smith, P. Bai, and M. Bazant. Interplay of phase boundary anisotropy and electro-auto-catalytic surface reactions on the lithium intercalation dynamics in LiXFePO4 plateletlike nanoparticles. *Physical Review Materials*, 2(8):1–13, 2018.

[109] G. F. Castelli, L. von Kolzenberg, B. Horstmann, A. Latz, and W. Dörfler. Efficient Simulation of Chemical–Mechanical Coupling in Battery Active Particles. *Energy Technology*, 9(6):2000835, 2021.

[110] S. Daubner, P. G. Kubendran Amos, E. Schoof, J. Santoki, D. Schneider, and B. Nestler. Multiphase-field modeling of spinodal decomposition during intercalation in an Allen-Cahn framework. *Physical Review Materials*, 5(3):035406, 2021.

[111] J. W. Cahn and J. E. Hilliard. Free Energy of a Nonuniform System. I. Interfacial Free Energy. *The Journal of Chemical Physics*, 28(2): 258–267, 1958.

[112] J. W. Cahn. On spinodal decomposition. *Acta Metallurgica*, 9:795–801, 1961.

[113] J. W. Cahn. Phase Separation by Spinodal Decomposition in Isotropic Systems. *The Journal of Chemical Physics*, 42(1):93–99, 1965.

[114] Y. Zhang and M. Tang. Stress-Induced Intercalation Instability. *Acta Materialia*, 201:158–166, 2020.

[115] T. Zhang and M. Kamlah. Microstructure evolution and intermediate phase-induced varying solubility limits and stress reduction behavior in sodium ion batteries particles of NaXFePO4 (0<x<1). *Journal of Power Sources*, 483(October 2020):229187, 2021.

[116] Y. Guo, R. Smith, Z. Yu, D. Efetov, J. Wang, P. Kim, M. Bazant, and L. Brus. Li Intercalation into Graphite: Direct Optical Imaging and Cahn-Hilliard Reaction Dynamics. *Journal of Physical Chemistry Letters*, 7(11):2151–2156, 2016.

[117] M. Chandesris, D. Caliste, D. Jamet, and P. Pochet. Thermodynamics and Related Kinetics of Staging in Intercalation Compounds. *The Journal of Physical Chemistry C*, 123(38):23711–23720, 2019.

[118] M. Rykner and M. Chandesris. Free Energy Model for Lithium Intercalation in Graphite: Focusing on the Coupling with Graphene Stacking Sequence. *The Journal of Physical Chemistry C*, 126(12): 5457–5472, 2022.

[119] J. Steiger, G. Richter, M. Wenk, D. Kramer, and R. Mönig. Comparison of the growth of lithium filaments and dendrites under different conditions. *Electrochemistry Communications*, 50:11–14, 2015.

[120] J. Steiger, D. Kramer, and R. Mönig. Microscopic observations of the formation, growth and shrinkage of lithium moss during electrodeposition and dissolution. *Electrochimica Acta*, 136:529–536, 2014.

[121] C. Delmas, M. Maccario, L. Croguennec, F. Le Cras, and F. Weill. Lithium deintercalation in LiFePO4 nanoparticles via a domino-cascade model. *Nature Materials*, 7(8):665–671, 2008.

[122] S. Bhattacharyya, S. Bandyopadhyay, and A. Choudhury. Phase-field modeling of electrochemical phenomena. *Journal of the Indian Institute of Science*, 96(3):257–268, 2016.

[123] I. Steinbach, F. Pezzolla, B. Nestler, M. Seeßelberg, R. Prieler, G. J. Schmitz, and J. L. Rezende. A phase field concept for multiphase systems. *Physica D: Nonlinear Phenomena*, 94(3):135–147, 1996.

[124] B. Nestler, H. Garcke, and B. Stinner. Multicomponent alloy solidification: phase-field modeling and simulations. *Physical Review E*, 71(4):41609, 2005.

[125] G. Li and C. W. Monroe. Multiscale Lithium-Battery Modeling from Materials to Cells. *Annual Review of Chemical and Biomolecular Engineering*, 11(1):277–310, 2020.

[126] S. Daubner, P. W. Hoffrogge, M. Minar, and B. Nestler. Triple junction benchmark for multiphase-field and multi-order parameter models. *Computational Materials Science*, 219:111995, 2023.

[127] J. W. Cahn and S. M. Allen. A Microscopic Theory for Domain Wall Motion and Its Experimental Verification in Fe-Al Alloy Domain Growth Kinetics. *Le Journal de Physique Colloques*, 38(December):C7–51, 1977.

[128] L.-Q. Chen and W. Yang. Computer simulation of the domain dynamics of a quenched system with a large number of nonconserved order parameters: The grain-growth kinetics. *Physical Review B*, 50: 15752–15756, 1994.

[129] N. Moelans, B. Blanpain, and P. Wollants. An introduction to phase-field modeling of microstructure evolution. *Calphad: Computer Coupling of Phase Diagrams and Thermochemistry*, 32(2):268–294, 2008.

[130] J. D. van der Waals. Thermodynamische Theorie der Kapillarität unter Voraussetzung stetiger Dichteänderung. *Zeitschrift für Physikalische Chemie*, 13U(1):657–725, 1894.

[131] V. L. Ginzburg and L. D. Landau. On the Theory of superconductivity. *Soviet Journal of Experimental and Theoretical Physics*, 20:1064–1082, 1950.

[132] H. Zhang, Y. Wu, F. Wang, F. Guo, and B. Nestler. Phase-Field Modeling of Multiple Emulsions Via Spinodal Decomposition. *Langmuir*, 37(17): 5275–5281, 2021.

[133] D. Jacqmin. Calculation of Two-Phase Navier–Stokes Flows Using Phase-Field Modeling. *Journal of Computational Physics*, 155(1): 96–127, 1999.

[134] R. Kobayashi. Modeling and numerical simulations of dendritic crystal growth. *Physica D: Nonlinear Phenomena*, 63(3-4):410–423, 1993.

[135] J. Hötzer, M. Jainta, P. Steinmetz, B. Nestler, A. Dennstedt, A. Genau, M. Bauer, H. Köstler, and U. Rüde. Large scale phase-field simulations of directional ternary eutectic solidification. *Acta Materialia*, 93: 194–204, 2015.

[136] M. Kellner, J. Hötzer, E. Schoof, and B. Nestler. Phase-field study of eutectic colony formation in NiAl-34Cr. *Acta Materialia*, 182:267–277, 2020.

[137] N. Prajapati, A. Abad Gonzalez, M. Selzer, B. Nestler, B. Busch, and C. Hilgers. Quartz cementation in polycrystalline sandstone: Insights from phase-field simulations. *Journal of Geophysical Research: Solid Earth*, 125(2):e2019JB019137, 2020.

[138] N. Prajapati, M. Spaeth, L. Knecht, M. Selzer, and B. Nestler. Quantitative phase-field modeling of faceted crystal dissolution processes. *Crystal Growth and Design*, 21(6):3266–3279, 2021.

[139] Y. Wang and A. Khachaturyan. Three-dimensional field model and computer modeling of martensitic transformations. *Acta Materialia*, 45 (2):759–773, 1997.

[140] E. Schoof, D. Schneider, N. Streichhan, T. Mittnacht, M. Selzer, and B. Nestler. Multiphase-field modeling of martensitic phase transformation in a dual-phase microstructure. *International Journal of Solids and Structures*, 134:181–194, 2018.

[141] H.-C. Yu, H.-Y. Chen, and K. Thornton. Extended smoothed boundary method for solving partial differential equations with general boundary conditions on complex boundaries. *Modelling and Simulation in Materials Science and Engineering*, 20(7):075008, 2012.

[142] I. Steinbach and F. Pezzolla. A generalized field method for multiphase transformations using interface fields. *Physica D: Nonlinear Phenomena*, 134(4):385–393, 1999.

[143] I. Steinbach. Phase-field models in materials science. *Modelling and Simulation in Materials Science and Engineering*, 17(7), 2009.

[144] M. Plapp. Unified derivation of phase-field models for alloy solidification from a grand-potential functional. *Physical Review E*, 84(3):031601, 2011.

[145] A. Choudhury and B. Nestler. Grand-potential formulation for multicomponent phase transformations combined with thin-interface asymptotics of the double-obstacle potential. *Physical Review E*, 85(2): 021602, 2012.

[146] E. Schoof. *Chemomechanische Modellierung der Wärmebehandlung von Stählen mit der Phasenfeldmethode*. Dissertation, Karlsruhe Institute of Technology (KIT), 2020.

[147] J. S. Langer. Models of Pattern Formation in First-Order Phase Transitions. In *Directions in Concensed Matter Physics: Memorial Volume in Honor of Shang-Keng Ma*, pages 165–186. World Scientific, 1986.

[148] N. Provatas and K. Elder. *Phase-Field Methods in Materials Science and Engineering*. Wiley, 2010.

[149] A. Khachaturyan. *Theory of Structural Transformations in Solids*. John Wiley & Sons Inc, New York, 1983.

[150] K. Ammar, B. Appolaire, G. Cailletaud, and S. Forest. Combining phase field approach and homogenization methods for modelling phase transformation in elastoplastic media. *European Journal of Computational Mechanics*, 18(5-6):485–523, 2009.

[151] P.-C. A. Simon, L. K. Aagesen, A. T. Motta, and M. R. Tonks. The effects of introducing elasticity using different interpolation schemes to the grand potential phase field model. *Computational Materials Science*, 183:109790, 2020.

[152] H. Goldstein, C. P. Poole, and J. L. Safko. *Classical mechanics*. Addison Wesley, 3rd edition, 2002.

[153] G. I. Tóth, T. Pusztai, and L. Gránásy. Consistent multiphase-field theory for interface driven multidomain dynamics. *Physical Review B*, 92(18): 184105, 2015.

[154] R. Folch and M. Plapp. Quantitative phase-field modeling of two-phase growth. *Physical Review E*, 72(1):011602, 2005.

[155] The Pace3D (Parallel Algorithms for Crystal Evolution in 3D) package. `www.iam.kit.edu/mms/english/5317.php`. Accessed: 2023-03-27.

[156] J. Hötzer, A. Reiter, H. Hierl, P. Steinmetz, M. Selzer, and B. Nestler. The parallel multi-physics phase-field framework PACE3D. *Journal of Computational Science*, 26:1–12, 2018.

[157] X. Li, J. Lowengrub, A. Ratz, and A. Voigt. Solving PDEs in complex geometries. *Communications in Mathematical Sciences*, 7(1):81–107, 2009.

[158] J. Eiken, B. Böttger, and I. Steinbach. Multiphase-field approach for multicomponent alloys with extrapolation scheme for numerical application. *Physical Review E*, 73(6):066122, 2006.

[159] J. Tiaden, B. Nestler, H. Diepers, and I. Steinbach. The multiphase-field model with an integrated concept for modelling solute diffusion. *Physica D: Nonlinear Phenomena*, 115(1-2):73–86, 1998.

[160] F. Lin, D. Nordlund, T.-C. Weng, Y. Zhu, C. Ban, R. M. Richards, and H. L. Xin. Phase evolution for conversion reaction electrodes in lithium-ion batteries. *Nature Communications*, 5(1):3358, 2014.

[161] K. W. Spring. Euler parameters and the use of quaternion algebra in the manipulation of finite rotations: A review. *Mechanism and Machine Theory*, 21(5):365–373, 1986.

[162] A. Heinz and P. Neumann. Representation of orientation and disorientation data for cubic, hexagonal, tetragonal and orthorhombic crystals. *Acta Crystallographica Section A*, 47(6):780–789, 1991.

[163] S. Daubner, M. Reder, N. Prajapati, D. Schneider, and B. Nestler. Multiphase-field modelling of anisotropic elasticity at finite deformation in Eulerian space. *Journal of Computational Science*, 66:101930, 2023.

[164] R. Hill. Elastic properties of reinforced solids: Some theoretical principles. *Journal of the Mechanics and Physics of Solids*, 11(5): 357–372, 1963.

[165] D. Schneider, O. Tschukin, A. Choudhury, M. Selzer, T. Böhlke, and B. Nestler. Phase-field elasticity model based on mechanical jump conditions. *Computational Mechanics*, 55(5):887–901, 2015.

[166] J. Mosler, O. Shchyglo, and H. Montazer Hojjat. A novel homogenization method for phase field approaches based on partial rank-one relaxation. *Journal of the Mechanics and Physics of Solids*, 68(1):251–266, 2014.

[167] D. Schneider, E. Schoof, O. Tschukin, A. Reiter, C. Herrmann, F. Schwab, M. Selzer, and B. Nestler. Small strain multiphase-field model accounting for configurational forces and mechanical jump conditions. *Computational Mechanics*, 61(3):277–295, 2018.

[168] W. Schmickler and E. Santos. *Interfacial Electrochemistry*. Springer Berlin Heidelberg, Heidelberg, second edition, 2010.

[169] H. Euchner and A. Groß. Atomistic modeling of Li- and post-Li-ion batteries. *Physical Review Materials*, 6(4):040302, 2022.

[170] A. Van Der Ven, J. Bhattacharya, and A. A. Belak. Understanding Li diffusion in Li-intercalation compounds. *Accounts of Chemical Research*, 46(5):1216–1225, 2013.

[171] J. Lim, Y. Li, D. H. Alsem, H. So, S. C. Lee, P. Bai, D. A. Cogswell, X. Liu, N. Jin, Y.-S. Yu, N. J. Salmon, D. A. Shapiro, M. Z. Bazant, T. Tyliszczak, and W. C. Chueh. Origin and hysteresis of lithium compositional spatiodynamics within battery primary particles. *Science*, 353(6299):566–571, 2016.

[172] D. Fraggedakis, N. Nadkarni, T. Gao, T. Zhou, Y. Zhang, Y. Han, R. M. Stephens, Y. Shao-Horn, and M. Z. Bazant. A scaling law to determine phase morphologies during ion intercalation. *Energy & Environmental Science*, 13(7):2142–2152, 2020.

[173] S. G. Kim, D. I. Kim, W. T. Kim, and Y. B. Park. Computer simulations of two-dimensional and three-dimensional ideal grain growth. *Physical Review E*, 74(6):061605, 2006.

[174] B. Nestler, M. Reichardt, and M. Selzer. Massive multi-phase-field simulations: Methods to compute large grain systems. In *Aluminium alloys : their physical and mechanical properties. Proceedings of the 11th International Conference on Aluminium Alloys*, pages 1251–1255. Wiley-VCH Verlag, 2008.

[175] B. Svendsen, P. Shanthraj, and D. Raabe. Finite-deformation phase-field chemomechanics for multiphase, multicomponent solids. *Journal of the Mechanics and Physics of Solids*, 112:619–636, 2018.

[176] N. Moelans, F. Wendler, and B. Nestler. Comparative study of two phase-field models for grain growth. *Computational Materials Science*, 46(2):479–490, 2009.

[177] H. Garcke, B. Nestler, and B. Stoth. A multiphase field concept: Numerical simulations of moving boundaries and multiple junctions. *SIAM J. Appl. Math.*, 60(1):295–315, 1999.

[178] N. Moelans, B. Blanpain, and P. Wollants. Quantitative analysis of grain boundary properties in a generalized phase field model for grain growth in anisotropic systems. *Physical Review B*, 78(2), 2008.

[179] S. N. Enugala. *Some refinements in the phase-field and sharp interface treatments of eutectic growth*. Dissertation, Karlsruhe Institute of Technology (KIT), 2021. 38.04.04; LK 01.

[180] C. J. Grose and P. D. Asimow. A multi-phase field model for mesoscopic interface dynamics with large bulk driving forces. *Computational Materials Science*, 212(June):111570, 2022.

[181] E. Miyoshi, T. Takaki, M. Ohno, and Y. Shibuta. Accuracy Evaluation of Phase-field Models for Grain Growth Simulation with Anisotropic Grain Boundary Properties. *ISIJ International*, 60(1):160–167, 2020.

[182] W. W. Mullins. Two-dimensional motion of idealized grain boundaries. *Journal of Applied Physics*, 27(8):900–904, 1956.

[183] G. Gottstein and L. S. Shvindlerman. *Grain Boundary Migration in Metals*, volume 31. CRC Press, Boca Raton, Fla., 2nd edition, 2009.

[184] J. Eiken. Discussion of the Accuracy of the Multi-Phase-Field Approach to Simulate Grain Growth with Anisotropic Grain Boundary Properties. *ISIJ International*, 60(8):1832–1834, 2020.

[185] O. Tschukin, A. Silberzahn, M. Selzer, P. G. Amos, D. Schneider, and B. Nestler. Concepts of modeling surface energy anisotropy in phase-field approaches. *Geothermal Energy*, 5(1), 2017.

[186] N. Moelans. A quantitative and thermodynamically consistent phase-field interpolation function for multi-phase systems. *Acta Materialia*, 59(3): 1077–1086, 2011.

[187] L. D. Landau and E. M. Lifšic. *Lehrbuch der theoretischen Physik, Band 5: Statistische Physik Teil 1*. Akademie-Verlag, Berlin, 8. edition, 1979.

[188] H. Jónsson, G. Mills, and K. W. Jacobsen. Nudged elastic band method for finding minimum energy paths of transitions. In *Classical and Quantum Dynamics in Condensed Phase Simulations*, pages 385–404. World Scientific, 1998.

[189] G. Henkelman and H. Jónsson. Improved tangent estimate in the nudged elastic band method for finding minimum energy paths and saddle points. *The Journal of Chemical Physics*, 113(22):9978–9985, 2000.

[190] J. Hötzer, O. Tschukin, M. B. Said, M. Berghoff, M. Jainta, G. Barthelemy, N. Smorchkov, D. Schneider, M. Selzer, and B. Nestler. Calibration of a multi-phase field model with quantitative angle measurement. *Journal of Materials Science*, 51(4):1788–1797, 2016.

[191] Github repository with code used for this publication:. `https://github.com/daubners/triple-junction-benchmark`.

[192] J. Eiken. *A Phase-Field Model for Technical Alloy Solidification*. Dissertation, RWTH Aachen, 2009.

[193] S. Kim, W. Kim, and T. Suzuki. Phase-field model for binary alloys. *Physical Review E*, 60(6):7186, 1999.

[194] M. San Miguel, J. Gunton, G. Dee, and P. Sahni. Theory of spinodal decomposition in relaxational tricritical models. *Physical Review B*, 23 (5):2334–2345, 1981.

[195] S. Günter, Q. Yu, J. Krüger, and K. Lackner. Modelling of heat transport in magnetised plasmas using non-aligned coordinates. *Journal of Computational Physics*, 209(1):354–370, 2005.

[196] P. Sharma and G. W. Hammett. Preserving monotonicity in anisotropic diffusion. *Journal of Computational Physics*, 227(1):123–142, 2007.

[197] B. van Es, B. Koren, and H. J. de Blank. Finite-difference schemes for anisotropic diffusion. *Journal of Computational Physics*, 272:526–549, 2014.

[198] A. Padhi, K. Nanjundaswamy, and J. Goodenough. Phospho-olivines as positive electrode materials for rechargeable lithium batteries. *Journal of the Electrochemical Society*, 144(4):1188, 1997.

[199] R. Malik, A. Abdellahi, and G. Ceder. A Critical Review of the Li Insertion Mechanisms in LiFePO 4 Electrodes. *Journal of The Electrochemical Society*, 160(5):A3179–A3197, 2013.

[200] P. Xiao and G. Henkelman. Kinetic Monte Carlo Study of Li Intercalation in LiFePO 4. *ACS Nano*, 12(1):844–851, 2018.

[201] E. M. Gavilán-Arriazu, M. P. Mercer, D. E. Barraco, H. E. Hoster, and E. P. M. Leiva. Kinetic Monte Carlo simulations applied to Li-ion and post Li-ion batteries: a key link in the multi-scale chain. *Progress in Energy*, 3(4):042001, 2021.

[202] M. Huttin. *Phase-field modeling of the infuence of mechanical stresses on charging and discharging processes in lithium ion batteries*. Dissertation, Karlsruhe Institute of Technology (KIT), 2014.

[203] D. Schneider, E. Schoof, Y. Huang, M. Selzer, and B. Nestler. Phase-field modeling of crack propagation in multiphase systems. *Computer Methods in Applied Mechanics and Engineering*, 312:186–195, 2016.

[204] C. Herrmann, D. Schneider, E. Schoof, F. Schwab, and B. Nestler. Phase-Field Model for the Simulation of Brittle-Anisotropic and Ductile Crack Propagation in Composite Materials. *Materials*, 14(17):4956, 2021.

[205] M. Späth, C. Herrmann, N. Prajapati, D. Schneider, F. Schwab, M. Selzer, and B. Nestler. Multiphase-field modelling of crack propagation in geological materials and porous media with Drucker-Prager plasticity. *Computational Geosciences*, 25(1):325–343, 2021.

[206] S. Chakraborty, P. Kumar, and A. Choudhury. Phase-field modeling of grain-boundary grooving and migration under electric current and thermal gradient. *Acta Materialia*, 153:377–390, 2018.

[207] P. Hoffrogge, A. Mukherjee, E. Nani, P. K. Amos, F. Wang, D. Schneider, and B. Nestler. Multiphase-field model for surface diffusion and attachment kinetics in the grand-potential framework. *Physical Review E*, 103(3):033307, 2021.

[208] S. Yang, P. Y. Zavalij, and S. Whittingham. Hydrothermal synthesis of lithium iron phosphate cathodes. *Electrochemistry Communications*, 3 (9):505–508, 2001.

[209] G. Chen, X. Song, and T. Richardson. Metastable Solid-Solution Phases in the LiFePO4/FePO4 System. *Journal of The Electrochemical Society*, 154(7):A627, 2007.

[210] R. Malik, F. Zhou, and G. Ceder. Kinetics of non-equilibrium lithium incorporation in LiFePO4. *Nature Materials*, 10(8):587–590, 2011.

[211] A. Abdellahi, O. Akyildiz, R. Malik, K. Thornton, and G. Ceder. The thermodynamic stability of intermediate solid solutions in LiFePO4 nanoparticles. *Journal of Materials Chemistry A*, 4(15):5436–5447, 2016.

[212] Y. Li, H. Chen, K. Lim, H. D. Deng, J. Lim, D. Fraggedakis, P. M. Attia, S. C. Lee, N. Jin, J. Moškon, Z. Guan, W. E. Gent, J. Hong, Y.-S. Yu, M. Gaberšček, M. S. Islam, M. Z. Bazant, and W. C. Chueh. Fluid-enhanced surface diffusion controls intraparticle phase transformations. *Nature Materials*, 17(10):915–922, 2018.

[213] M. Z. Bazant. Thermodynamic stability of driven open systems and control of phase separation by electro-autocatalysis. *Faraday Discussions*, 199:423–463, 2017.

[214] W. C. Chueh, F. El Gabaly, J. D. Sugar, N. C. Bartelt, A. H. McDaniel, K. R. Fenton, K. R. Zavadil, T. Tyliszczak, W. Lai, and K. F. McCarty. Intercalation Pathway in Many-Particle LiFePO 4 Electrode Revealed by Nanoscale State-of-Charge Mapping. *Nano Letters*, 13(3):866–872, 2013.

[215] Y. Li, F. El Gabaly, T. R. Ferguson, R. B. Smith, N. C. Bartelt, J. D. Sugar, K. R. Fenton, D. A. Cogswell, A. L. D. Kilcoyne, T. Tyliszczak, M. Z. Bazant, and W. C. Chueh. Current-induced transition from particle-by-particle to concurrent intercalation in phase-separating battery electrodes. *Nature Materials*, 13(12):1149–1156, 2014.

[216] J. Zhu, J. Fiore, D. Li, N. M. Kinsinger, Q. Wang, E. DiMasi, J. Guo, and D. Kisailus. Solvothermal Synthesis, Development, and Performance of LiFePO 4 Nanostructures. *Crystal Growth & Design*, 13(11):4659–4666, 2013.

[217] B. Nestler, F. Wendler, M. Selzer, B. Stinner, and H. Garcke. Phase-field model for multiphase systems with preserved volume fractions. *Physical Review E*, 78(1):011604, 2008.

[218] M. Klinsmann, D. Rosato, M. Kamlah, and R. McMeeking. Modeling crack growth during Li insertion in storage particles using a fracture phase field approach. *Journal of the Mechanics and Physics of Solids*, 92: 313–344, 2016.

[219] H. Hu, K. Tang, S. Cao, X. Yang, and X. Wang. Synthesis and electrochemical properties of P2–Na2/3[Ni1/3Mn2/3]O2 microspheres as cathode materials for sodium-ion batteries. *Journal of Alloys and Compounds*, 859:157768, 2021.

[220] X. Qi, L. Liu, N. Song, F. Gao, K. Yang, Y. Lu, H. Yang, Y.-S. Hu, Z.-H. Cheng, and L. Chen. Design and Comparative Study of O3/P2 Hybrid Structures for Room Temperature Sodium-Ion Batteries. *ACS Applied Materials & Interfaces*, 9(46):40215–40223, 2017.

[221] Y. Zhao, L. Peng, B. Liu, and G. Yu. Single-Crystalline LiFePO4 Nanosheets for High-Rate Li-Ion Batteries. *Nano Letters*, 14(5): 2849–2853, 2014.

[222] R. J. Clément, P. G. Bruce, and C. P. Grey. Review—Manganese-Based P2-Type Transition Metal Oxides as Sodium-Ion Battery Cathode Materials. *Journal of The Electrochemical Society*, 162(14): A2589–A2604, 2015.

[223] P. Manikandan, D. Ramasubramonian, and M. M. Shaijumon. Layered P2-type Na0.5Ni0.25Mn0.75O2 as a high performance cathode material for sodium-ion batteries. *Electrochimica Acta*, 206:199–206, 2016.

[224] A. Gutierrez, W. M. Dose, O. Borkiewicz, F. Guo, M. Avdeev, S. Kim, T. T. Fister, Y. Ren, J. Bareño, and C. S. Johnson. On Disrupting the Na+-Ion/Vacancy Ordering in P2-Type Sodium-Manganese-Nickel Oxide Cathodes for Na+-Ion Batteries. *Journal of Physical Chemistry C*, 122 (41):23251–23260, 2018.

[225] H. Euchner, O. Clemens, and M. A. Reddy. Unlocking the potential of weberite-type metal fluorides in electrochemical energy storage. *npj Computational Materials*, 5(1):31, 2019.

[226] N. Tapia-Ruiz, W. M. Dose, N. Sharma, H. Chen, J. Heath, J. W. Somerville, U. Maitra, M. S. Islam, and P. G. Bruce. High voltage structural evolution and enhanced Na-ion diffusion in P2-Na2/3Ni1/3-xMgxMn2/3O2 ($0 \leq x \leq 0.2$) cathodes from diffraction, electrochemical and ab initio studies. *Energy and Environmental Science*, 11(6):1470–1479, 2018.

[227] P.-F. Wang, H.-R. Yao, X.-Y. Liu, Y.-X. Yin, J.-N. Zhang, Y. Wen, X. Yu, L. Gu, and Y.-G. Guo. Na+/vacancy disordering promises high-rate Na-ion batteries. *Science Advances*, 4(3):1–10, 2018.

[228] M. D. Radin, S. Hy, M. Sina, C. Fang, H. Liu, J. Vinckeviciute, M. Zhang, M. S. Whittingham, Y. S. Meng, and A. Van der Ven. Narrowing the Gap between Theoretical and Practical Capacities in Li-Ion Layered Oxide Cathode Materials. *Advanced Energy Materials*, 7(20):1602888, 2017.

[229] S. Daubner, M. Dillenz, L. F. Pfeiffer, C. Gauckler, M. Rosin, N. Burgard, J. Martin, P. Axmann, M. Sotoudeh, A. Groß, D. Schneider, and B. Nestler. Combined study of phase transitions in the P2-type NaxNi1/3Mn2/3O2 cathode material: experimental, ab-initio and multiphase-field results. Submitted.

[230] Y. Liu, Z. Yao, P. Vanaphuti, X. Yang, L. Mei, X. Zhu, S. Liu, and Y. Wang. Stable fast-charging sodium-ion batteries achieved by a carbomethoxy-modified disodium organic material. *Cell Reports Physical Science*, 4(2):101240, 2023.

[231] S. Daubner, M. Weichel, P. W. Hoffrogge, D. Schneider, and B. Nestler. Modeling Anisotropic Transport in Polycrystalline Battery Materials. *Batteries*, 9(6):310, 2023.

[232] H.-J. Noh, S. Youn, C. S. Yoon, and Y.-K. Sun. Comparison of the structural and electrochemical properties of layered Li[NixCoyMnz]O2 (x = 1/3, 0.5, 0.6, 0.7, 0.8 and 0.85) cathode material for lithium-ion batteries. *Journal of Power Sources*, 233:121–130, 2013.

[233] U.-H. Kim, G.-T. Park, B.-K. Son, G. W. Nam, J. Liu, L.-Y. Kuo, P. Kaghazchi, C. S. Yoon, and Y.-K. Sun. Heuristic solution for achieving long-term cycle stability for Ni-rich layered cathodes at full depth of discharge. *Nature Energy*, 5(11):860–869, 2020.

[234] J.-M. Lim, H. Kim, K. Cho, and M. Cho. Fundamental mechanisms of fracture and its suppression in ni-rich layered cathodes: Mechanics-based multiscale approaches. *Extreme Mechanics Letters*, 22:98–105, 2018.

[235] C. S. Yoon, K.-J. Park, U.-H. Kim, K. H. Kang, H.-H. Ryu, and Y.-K. Sun. High-Energy Ni-Rich Li[Ni x Co y Mn 1 –x–y]O 2 Cathodes via Compositional Partitioning for Next-Generation Electric Vehicles. *Chemistry of Materials*, 29(24):10436–10445, 2017.

[236] L. Aagesen, Y. Gao, D. Schwen, and K. Ahmed. Grand-potential-based phase-field model for multiple phases, grains, and chemical components. *Physical Review E*, 98(2):1–16, 2018.

[237] M. Raissi, P. Perdikaris, and G. Karniadakis. Physics-informed neural networks: A deep learning framework for solving forward and inverse problems involving nonlinear partial differential equations. *Journal of Computational Physics*, 378:686–707, 2019.

[238] H. Zhao, B. D. Storey, R. D. Braatz, and M. Z. Bazant. Learning the Physics of Pattern Formation from Images. *Physical Review Letters*, 124 (6):060201, 2020.

[239] A. Reiter. *Some Impliciations of Constraints in Phasefield Models*. Dissertation, Karlsruhe Institute of Technology (KIT), 2020.